



FAST AND FURIOUS

EXPLORING THE POTENTIAL OF ULTRA-HIGH DOSE RATE HEAVY ION IRRADIATION



CELINE KARLE

CONDUCTED AT:

German Cancer Research Center (DKFZ)
Heidelberg, Germany

UNDER SUPERVISION OF:

Prof. Dr. Dr. Jürgen Debus,
head of Clinical Cooperation Unit Radiation Oncology

Prof. Dr. Dr. Amir Abdollahi
head of Clinical Cooperation Unit Translational Radiation Oncology

AS A MEMBER OF:

German Cancer Research Center (DKFZ)
National Center for Tumor Diseases (NCT)
Heidelberg University Hospital (UKHD)

WHILE ENROLLED AT:

the Heidelberg Graduate School for Physics (HGSFP)
Department of Physics and Astronomy
of the Heidelberg University

THE AUTHOR RECEIVED FINANCIAL SUPPORT FROM:

the Helmholtz International Graduate School of Cancer Research (HIGS)
Doctoral Fellowship

the National Institutes of Health (NIH)
Program Number: NIH-1P01CA257904-01A1

the National Center for Tumor Diseases (NCT)
Program Numbers: NCT-PRO 1030000042 and Biodose 1030000043

the Particle Therapy Co-Operative Group (PTCOG)
PTCOG Travel Fellowship

TYPESETTING:

L^AT_EX by the author

FIGURES DESIGN:

by the author and, when required, with acknowledgement and references to original data sources.

DISSERTATION

submitted to the

Combined Faculty of Mathematics, Engineering and Natural Sciences
of Heidelberg University, Germany

for the degree of

Doctor of Natural Sciences

Put forward by

Celine Karle

born in: Mannheim, Germany

Oral examination: 04.12.2025

FAST AND FURIOUS:
EXPLORING THE POTENTIAL OF
ULTRA-HIGH DOSE RATE
HEAVY ION IRRADIATION

REFEREES:

Prof. Dr. Dr. Jürgen Debus

Prof. Dr. Michael Hausmann

ABSTRACT

Radiation therapy is a cornerstone of cancer treatment, though its effectiveness is limited when treating radio-resistant, hypoxic, and motion-affected tumors, including pancreatic ductal adenocarcinoma (PDAC). To overcome these obstacles, heavy-ion irradiation emerges as a promising alternative to conventional radiotherapy for treating hypoxic and radio-resistant cases due to its favorable physical and biological properties. Simultaneously, delivering radiation over a short time frame, at so-called ultra-high dose rates (UHDR), offers the potential to mitigate intra-fractional motion and to enhance the therapeutic ratio by sparing healthy tissue. Combining these two advanced modalities to heavy-ion UHDR irradiation may therefore be of particular benefit when treating these challenging tumor instances.

The objective of this work was to establish the technical basis for exploring heavy-ion UHDR irradiation and to determine its clinical potential. Firstly, the technical feasibility and dosimetric prerequisites were systematically assessed. Diamond detectors were characterized under densely ionizing carbon and oxygen ion irradiation at UHDR. The results confirmed their suitability for dosimetry in heavy-ion UHDR beams. Subsequent mechanistic studies were conducted to examine the radiochemical processes after various particle beam deliveries, followed by the first preclinical experiments with oxygen-ion UHDR to evaluate the biological response in PDAC models. Herein, this radiation quality proved iso-effective in vitro cell killing and in vivo tumor growth delay compared to conventional dose rates. Survival benefits of oxygen-ion UHDR have been demonstrated and support future investigations of this modality.

Collectively, these results provide methodological and physical groundwork as well as the first biological evidence endorsing the clinical exploration of heavy-ion UHDR irradiation, particularly for tumors with limited therapeutic options.



ZUSAMMENFASSUNG

Die Strahlentherapie ist eine tragende Säule in der Krebsbehandlung, stößt jedoch bei der Therapie von radio-resistenten, hypoxischen und bewegungsbeeinflussten Tumoren wie dem duktalem Adenokarzinom der Pankreas (engl. PDAC) an ihre Grenzen. Um diese Hindernisse zu überwinden, bietet sich die Schwerionenbestrahlung als vielversprechende Alternative zur konventionellen Strahlentherapie für die Behandlung hypoxischer und strahlen-resistenter Fälle an, aufgrund ihrer günstigen physikalischen und biologischen Eigenschaften. Gleichzeitig bietet die Strahlenabgabe über einen kurzen Zeitraum mit sogenannten ultrahohen Dosisraten (UHDR) das Potenzial, intrafraktionelle Bewegungen zu mildern und zudem möglicherweise ein besseres Schonung des umliegenden gesunden Gewebes zu erzielen. Die Kombination dieser beiden Modalitäten zur Schwerionen-UHDR-Bestrahlung könnte daher bei der Behandlung dieser schwierigen Tumorfälle von besonderem Nutzen sein.

Das Ziel dieser Arbeit war es, die technischen Grundlagen für die Erforschung der UHDR-Bestrahlung mit Schwerionen zu schaffen und ihr klinisches Potenzial zu untersuchen. Zunächst wurden die technische Machbarkeit und die dosimetrischen Voraussetzungen systematisch geprüft. Diamantdetektoren wurden in dicht ionisierender UHDR Bestrahlung mit Kohlenstoff- und Sauerstoffionen charakterisiert und ihre Eignung für die Dosimetrie bestätigt. Anschließend wurden mechanistische Studien zur Untersuchung der zugrunde liegenden radiochemischen Prozesse durchgeführt, gefolgt von den ersten präklinischen Experimenten an PDAC-Modellen mit Sauerstoff-UHDR-Bestrahlung. Diese Behandlung erwies sich im Vergleich zur Bestrahlung mit konventionellen Dosisraten sowohl in Zell-Experimenten in vitro als auch in der Verzögerung des Tumorwachstums in vivo als isoeffektiv. Der gezeigte Überlebensvorteil nach Sauerstoff-UHDR-Bestrahlung stützt zukünftige Untersuchungen dieser Modalität im klinischen Kontext.

Insgesamt liefern diese Ergebnisse sowohl die methodischen und physikalischen Grundlagen als auch die ersten biologischen Belege für eine weitere klinische Erforschung der UHDR-Bestrahlung mit Schwerionen, insbesondere für Tumore mit begrenzten Behandlungsmöglichkeiten.

CONTENTS

Acronyms

xii

INTRODUCTION

1

CHAPTER 1

Evolution of Radiotherapy Towards Heavy Ion Treatment

1

THEORETICAL BACKGROUND

2

CHAPTER 2

Along the Particle's Path: From Acceleration to Biological Effects

7

- 2.1 Particle Acceleration at the Heidelberg Ion Beam Therapy Center *7*
 - 2.1.1 Sources *7*
 - 2.1.2 LINAC and Synchrotron *8*
 - 2.1.3 Beam Delivery *9*
- 2.2 Initial Particle Interaction with Matter *11*
 - 2.2.1 Physical Description of the Energy Loss Process *13*
 - 2.2.2 Longitudinal Spread of the Depth Dose *15*
 - 2.2.3 Lateral Scattering of a Pencil Beam *15*
- 2.3 Radiochemistry *16*
- 2.4 Biological Effects *18*

3

CHAPTER 3

Strategic Use of Heavy Ion Therapy

21

- 3.1 Advantages Across Scales: Physical, Chemical, and Biological *21*
 - 3.1.1 More Conformal Dose Distribution *21*
 - 3.1.2 More Intra-Track Interactions *23*
 - 3.1.3 More Abbreviations: OER and RBE - Biological Implications of High LET *24*
- 3.2 Recognizing the Limitations *27*
- 3.3 Clinical Indications for High-LET Irradiation *28*
 - 3.3.1 A Case in Focus: Pancreatic Cancer *29*

4	CHAPTER 4	
	Tracing the Effects of UHDR	31
4.1	Revival of the FLASH Effect	31
4.2	Significance of the Temporal Beam Structure	33
4.3	Towards a Mechanistic Understanding	34
	4.3.1 Oxygen Dynamics	34
	4.3.2 Radical-Radical Interactions	35
	4.3.3 Biological Factors	36
4.4	Advantages Beyond the Sparing Effects	37

STATE OF THE ART

5	CHAPTER 5	
	Combining the Potential of Heavy Ion & UHDR Irradiation	39
5.1	State of the Art: Particle UHDR Irradiation	39
5.2	From Standard to UHDR at HIT	40
	5.2.1 Hardware Adaptations	40
	5.2.2 Irradiation Plan Adjustments	42
5.3	Assuring the Correct Dose	42
	5.3.1 Detectors for High LET and UHDR Dosimetry	43
	5.3.2 Monte Carlo Simulation for high LET	44
5.4	Rationale for Pancreatic Cancer as Target	46

RESULTS

6	CHAPTER 6	
	Bottom Up Approach: From Setup to First Experiments	47
6.1	“Characterizing Diamond Detectors for Various Dose and Dose Rate Measurements in Scanned Carbon and Oxygen Beams”	53
6.2	“Oxygen Consumption Measurements at Ultra-High Dose Rate over a Wide LET Range”	67
6.3	“First In Vitro and In Vivo Experiments with Ultra High-Dose Rate Oxygen Ion Radiotherapy”	81

DISCUSSION

7	CHAPTER 7	
	Heavy Ion UHDR Towards Clinical Implementation	87
7.1	Technical Implementation of Heavy Ion UHDR Therapy at HIT	87
7.2	Dosimetric Protocol for Heavy Ion UHDR at HIT	89
	7.2.1 Advanced Temporal Dosimetry with Diamond Detectors	90
	7.2.2 Detector Response and Correction Strategies	93

7.3	Mechanistic Insights into UHDR Effects	94
7.3.1	Impact of Solution Composition	94
7.3.2	Hypothetical ODH Mechanism	95
7.3.3	Dose Rate Effects in Pancreatic Cancer Models	95
7.4	Future Directions for Biological Investigations	96
7.4.1	Pathway to Clinical Translation	97

CONCLUSION

8	<div style="display: inline-block; width: 10px; height: 20px; background-color: #ccc; margin-right: 5px;"></div> <div> <div>CHAPTER 8</div> <div>A FLASH-Debate: Is Heavy-Ion UHDR Needed?</div> </div>	99
---	---	----

APPENDIX

A	<div style="display: inline-block; width: 10px; height: 20px; background-color: #ccc; margin-right: 5px;"></div> <div> <div>CHAPTER A</div> <div>List of Scientific Contributions</div> </div>	103
A.1	Peer-Reviewed Publications	103
A.2	Conference Contributions	104
B	<div style="display: inline-block; width: 10px; height: 20px; background-color: #ccc; margin-right: 5px;"></div> <div> <div>CHAPTER B</div> <div>List of Figures</div> </div>	105
C	<div style="display: inline-block; width: 10px; height: 20px; background-color: #ccc; margin-right: 5px;"></div> <div> <div>CHAPTER C</div> <div>List of Tables</div> </div>	107
D	<div style="display: inline-block; width: 10px; height: 20px; background-color: #ccc; margin-right: 5px;"></div> <div> <div>CHAPTER D</div> <div>Bibliography</div> </div>	109
E	<div style="display: inline-block; width: 10px; height: 20px; background-color: #ccc; margin-right: 5px;"></div> <div> <div>CHAPTER E</div> <div>Supplementary Material</div> </div>	127
E.1	Supplementary - 2 nd Paper	127
E.2	Supplementary - 3 rd Paper	129
	<div style="display: inline-block; width: 10px; height: 20px; background-color: #ccc; margin-right: 5px;"></div> <div>Acknowledgements</div>	131

ACRONYMS

2DRM 2D Range Modulator

3DRM 3D Range Modulator

AMC Advanced Markus Chamber

BAMS Beam Application Monitoring System

BP Bragg Peak

BSA Bovine Serum Albumin

CO₂ Carbon Dioxide

CSDA Continuous Slowing Down Approximation

CT Computer Tomography

DDD Depth Dose Distribution

DNA Desoxyribonucleic Acid

\bar{D} averaged Dose Rate

\dot{D}_{inst} instantaneous Dose Rate

DSB Double-Strand Breaks

ECRIS Electron Cyclotron Resonance Ion Source

fd flashDiamond

FMF FLASH Modifying Factor

FWHM Full Width Half Maximum

GI Gastrointestinal Tract

HEBT High Energy Beam Transport

HIT Heidelberg Ion Beam Therapy Center

IC Ionization Chamber

IEL Iso-Energy Layer

LBL Lawrence Berkley Laboratories

LEM Local Effect Model

LET Linear Energy Transfer

LETd dose-averaged LET

LINAC Linear Accelerator

MC Monte Carlo Simualtion

MCS Multiple Coulomb Scattering

mD microDiamond

MKM Microdosimetric Kinetic Model

MWPC Multi-Wire Proportional Chambers

NT Normal Tissue

OAR Organ At Risk

ODH Oxygen Depletion Hypothesis

OER Oxygen Enhancement Ratio

PBS Pencil Beam Scanning

PDAC Pancreatic Ductal Adenocarcinoma

PMMA Polymethylmethacrylate

QA Quality Assurance

RBE Relative Biologic Effectiveness

RFQ Radio Frequency Quadrupole

RiFi Ripple Filter

ROS Reactive Oxygen Species

SDR Standard Dose Rate

SF Survival Fraction

SOBP Spread-Out Bragg Peak

SSB Single-Strand Break

TPS Treatment Planning System

TT Tumor Tissue

UHDR Ultra-High Dose Rate

ZFE Zebra Fish Embryos

EVOLUTION OF RADIOTHERAPY TOWARDS HEAVY ION TREATMENT

Cancer has been a part of human civilization since its earliest days. One of the oldest known reports of this disease is in the Edwin Smith Papyrus, an Egyptian medical text dating to approximately 1600 BCE, which contains a description of breast cancer. [1] The presence of this particular condition has even been depicted in a manneristic painting from the 1550s (Fig. 1.1). [2]



Figure 1.1.: “The Night” – Oil painting by Michele di Rodolfo del Ghirlandaio, circa 1550s: The woman is a reinterpretation of a marble statue originally created by Michelangelo Buonarroti. In contrast to the statue, the woman’s health condition is emphasized by the colored representation. [2] Image from [3].

While ancient healers attempted to identify treatments for these kinds of devastating diseases, they could hardly have imagined that a possible solution would emerge from an invisible radiation that surrounds us daily in the form of cosmic rays, naturally decaying elements in soil, or even in our fruits, like bananas.¹ The radiation remained undetected until 1895, when Wilhelm C. Röntgen’s coincidental discovery of ionizing radiation opened the door to an entirely new field of research and subsequently for cancer treatment. [5]

¹Indeed, the following discovery refers to X-rays. X-rays can also be produced as a byproduct of radioactive decay. For instance, this can be observed in the decay of potassium-40 (^{40}K) in bananas, following electron capture. [4]

The so-called “X-rays” initially revolutionized both shoe shopping [6] (Fig. 1.2) and medical imaging, as it allowed examination of internal structures without surgical intervention.

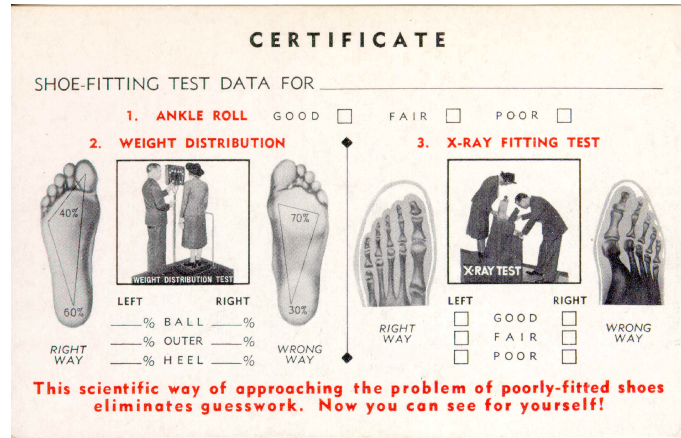


Figure 1.2.: Certificate for a Shoe Fitting Test: In the 1940s, X-ray tubes operating at peak voltages of 53 kV were employed in commercial shoe-fitting fluoroscopes to visualize customers’ feet inside shoes for optimal fit. A dedicated button reduced exposure for children. This practice exemplifies the widespread and uncritical use of X-rays at the time, showing a limited awareness of their potential health risks. Image from [7].

The therapeutic potential of X-rays was recognized by Emil Grubbé, who served as his own test subject. On his own body, he recognized the radiation’s ability to cause tissue damage and radiation burn. Witnessing these effects, Dr. Gilman noted, “any physical agent capable of doing so much damage to normal cells and tissues might offer possibilities, if used as a therapeutic agent”. [8] Since then, radiotherapy has been known as the use of ionizing radiation to damage the irradiated target volume, like tumors, by depositing energy – or dose – to the target structure and therewith harming the encasing cells. [9] After designing and building the first X-ray machines, Emil Grubbé used this ability of ionizing radiation to treat one of the first radiotherapy patients: Rose Lee was treated for a recurrence of her breast cancer, the same illness depicted in Michele di Rodolfo del Ghirlandaio’s painting from the 1550s. [8]

The overall treatment goal of radiotherapy is to conformally target the tumor tissue with a high dose, while sparing the surrounding healthy tissue from the dose. [10] X-ray or photon treatment technologies have improved drastically since Emil Grubbé’s first trials, with Volumetric-Modulated Arc Therapy (VMAT) or high precision Cyberknife devices being particularly notable examples. [10, 11] However, the physically feasible optimum in dose conformity is nearly reached with conventional Intensity-Modulated Radiation Therapy (IMRT) photon systems. [10] Given the depth dose distribution of photons in tissue, a full sparing of the surrounding tissue is not possible due to the constant decrease in dose with depth following a small build-up (Fig. 1.3).

In 1903, William H. Bragg described the distinctive inverse dose profile of low-energy alpha particles, which can be seen in Fig. 1.3. [12] The inverse Depth Dose Distribution (DDD) of particles has a finite range, which enabled both a more conformal tumor irradiation and, crucially, a sparing of Organ At Risk (OAR) beyond the target volume – an achievement impossible with conventional photon therapy (Fig. 1.3). This finding, combined with new developments in particle acceleration technology, laid the groundwork for a more precise treatment option in radiotherapy: In 1946, Wilson investigated the use of the proton Bragg Peak (BP) in cancer treatment. This theoretical foundation was put into practice in 1954, when the first clinical trials with protons and deuterons commenced at the Lawrence Berkley Laboratories (LBL). [13]

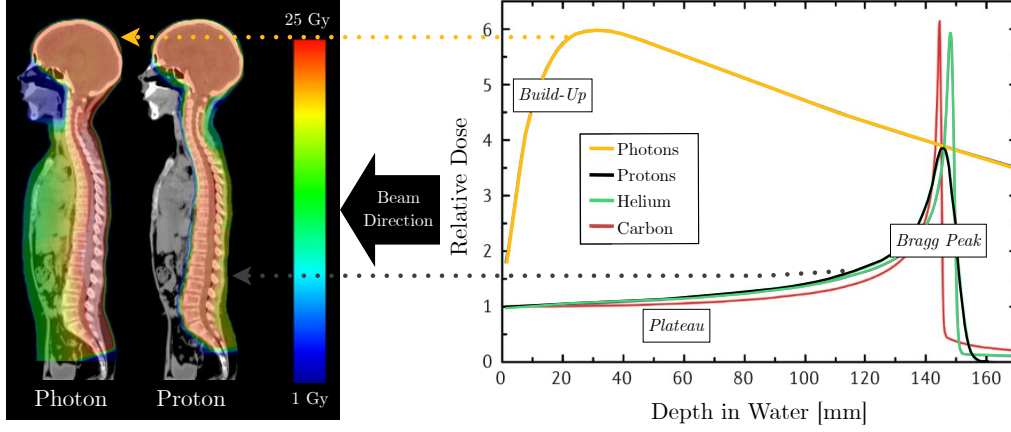


Figure 1.3.: On the right side of the picture, the Depth Dose Distribution (DDD) for photons, protons, helium, and carbon ions are displayed in water: The photon distribution can be characterized by a small build-up area until the maximum is reached, which is followed by a gradual decrease in dose. In comparison, the particles demonstrate a low-dose plateau at the start of the "tissue mimicking" - water block, and then delivering a large part of their dose within a limited region, called Bragg Peak (BP). Subsequently, the dose for protons approaches zero, while a dose tail is evident for heavier ions. The inverse DDD facilitates a more conforming irradiation of the tumor borders in the longitudinal direction, thereby sparing the tissue behind the tumor compared to photons. This is emphasized on the left side of the image by two comparative treatment plans, one using photons and the other using spot scanning protons for an 11-year-old child with medulloblastoma. The beam direction is indicated by the arrow in the bottom center. With the finite range of protons, the Normal Tissue (NT) after the spinal cord can effectively be spared, while the depth dose curve of photons exposes the adjacent organs. [14] Image adapted and taken from [14, 15].

In the following years, it was experimentally demonstrated that while protons offered superior dose conformity through the BP, their biological effectiveness remained comparable to photons at equivalent doses. The pursuit of enhanced therapeutic efficacy led to investigations of heavier ions², which demonstrated not only increased biological effectiveness [16] but also superior physical characteristics, including an even more precise DDD and improved OAR sparing (Fig. 1.3). [18] Therewith, the potential of heavy ions started to be explored by Cornelius A. Tobias and colleagues [13], whose work at the Berkeley BEVALAC accelerator enabled pioneering experiments with various ions, from carbon to argon, with energies approaching 1 GeV/u. [18, 19]

However, argon (atomic number $Z = 18$) treatments at LBL induced long-term toxicities in the NT and were not continued. [20, 21] The same result was obtained with silicon ($Z = 16$) treatments, which demonstrated several adverse effects. Therefore, for medical physics, "extremely" heavy ions were excluded, and patients were treated with particles up to neon ($Z = 10$) in the periodic table. [22] Back then, through systematic investigation, researchers identified ions between carbon and oxygen as optimal candidates, offering an effective balance between therapeutic efficacy and minimizing complications and side effects in NT. [23]

In the following years, carbon ions were extensively investigated and have emerged as a particularly promising choice due to their favorable peak-to-plateau ratio and numerous biological advantages, compared to protons and photons. These include enhanced effectiveness against hypoxic tumors, reduced cell cycle dependence, decreased fraction effects, potential inhibition of angiogenesis and cell migration, and possible enhancement of immune responses. [24]

²It should be noted that, in the world of medical physics, the term "heavy ions" is used liberally to describe any ion heavier than a proton [16], equivalent to the use of the word "metal" in astronomy [17] – both definitions that would surely make a nuclear physicist raise an eyebrow.

Following the pioneering experiments at LBL Berkley, the clinical translation of heavy ion therapy began in 1994 at the Heavy Ion Medical Accelerator (HIMAC) in Chiba, Japan, establishing the first dedicated medical carbon ion facility. [25] Following the HIMAC's commencement, the GSI (Helmholtzzentrum für Schwerionenforschung) in Darmstadt, Germany initiated carbon-ion trials. [26]

Currently, particle therapy has grown to include approximately 120 facilities offering proton treatment; however, only about 17 facilities worldwide provide carbon ion therapy. [27]

Despite the possible advantages of heavy-ion treatment, the limited availability of heavy ion facilities, just 17, has constrained clinical trials.

Approaching higher mass ions, oxygen ions showed particular promise in overcoming the radioreistance of severely hypoxic tumors in experiments. Nonetheless, this approach and higher mass ion irradiation in general remain in the research phase.

Leading research centres worldwide are working to demonstrate the superiority of particle and especially heavy ion therapy, while also exploring innovative novel treatment approaches to further enhance the therapeutic outcome. Among these novel approaches is the so-called “FLASH” irradiation, during which the radiation delivery time is drastically abbreviated to achieve high dose rates classically above 40 Gy/s, which is named Ultra-High Dose Rate (UHDR). “FLASH” represents a promising frontier that could enable higher-dose tumor treatments, while sparing the NT significantly. [28]

The Heidelberg Ion Beam Therapy Center (HIT) stands at the forefront of these developments since it came into clinical operation in 2009. With its possibilities of delivering ions from proton to oxygen, the facility serves as a hub for advancing our understanding and application of heavy ion therapy. [29]

Before a novel treatment modality can be clinically applied, its mechanisms should be understood and quantified to enable its safe and effective use in Treatment Planning System (TPS) and, ultimately, for patient treatment. Max Planck aptly stated [30]:

“Dem Anwenden muss das Erkennen vorausgehen”
(Recognition must precede application)

A principle that guides the methodical progression from fundamental research to clinical implementation in general.

This quote reflects **the essence of this thesis**. The conducted research is aimed at establishing a new synergy of two modalities: heavy ion and UHDR irradiation. After validating the dosimetric foundations, the fundamental reactions and mechanisms behind this joint irradiation were investigated. With this foundation, the world's first in vitro and in vivo experiments with oxygen ion UHDR irradiation were conducted at HIT. These experiments suggest a potential clinical advantage of this radiation modality for highly resistant pancreatic cancer.

Although clinical application of this new treatment technique will require further development, the first technical and methodological steps have been taken, and the results of this thesis may be used to justify future investigations with this “*fast and furious*” irradiation technique.

This research journey, from confirming the feasibility of oxygen-ion UHDR irradiation to conducting the first experiments, is documented in three peer-reviewed papers published in internationally acclaimed scientific journals. Consequently, this thesis is written as a **cumulative thesis** following the regulations of the *Department of Physics and Astronomy of Heidelberg University*. The publications included in this thesis are outlined in Chapter 6, while all additional contributions are listed in Chapter A.1.

The structure of this thesis is as follows: The fundamental interactions of particles with matter, essential for understanding the physical and biological characteristics of particle therapy, are described in Chapter 2. Chapter 3 delves into the unique properties of heavy ion radiation. The innovative concept of UHDR irradiation is introduced in Chapter 4. The following Chapter 5 discusses the synergy between heavy ion radiation and UHDR, exploring how their combination could enhance therapeutic outcomes. The core findings from the establishment to the first biological experiments with this irradiation modality are presented in Chapter 6, including the three peer-reviewed publications. Finally, Chapter 7 provides a comprehensive discussion of the results, their implications for future research, and potential clinical applications, concluding with a FLASH-debate on the future of heavy-ion FLASH in Chapter 8.

ALONG THE PARTICLE'S PATH: FROM ACCELERATION TO BIOLOGICAL EFFECTS

To demonstrate the possibilities of particle therapy and ultimately the advantages of heavy ions, this chapter explains the technical requirements for delivering heavy-ion therapy and the subsequent interaction of particles in matter with the induced chemical and biological effects. The path of the particles is traced from their production and acceleration, through transport and beam shaping, to their delivery and the resulting microscopic and molecular interactions within tissue. The focus is on the specific capabilities and technologies available at Heidelberg Ion Beam Therapy Center (HIT), where these studies were conducted.

2.1 Particle Acceleration at the Heidelberg Ion Beam Therapy Center

In 2003, construction began of Germany's first dedicated clinical heavy ion therapy facility – HIT – following promising preliminary clinical studies on carbon ion therapy at GSI. [29, 31] Clinical operations commenced in 2009, offering both proton and carbon ion radiotherapy treatment to patients. In 2021, helium ion therapy was introduced into clinical routine, and the first individual clinical trials started. [29] A notable feature of the facility is its pioneering heavy ion gantry, enabling 360° irradiation of patients (Fig. 2.1). [32]

2.1.1 Sources

The starting point of each particle is the ion source that can be seen on the left side in Fig. 2.1. Currently, four different ion species are available for irradiation: proton (^1H), helium (^4He), carbon (^{12}C), and oxygen (^{16}O) ions. The first three are used for clinical treatment, while oxygen ions are solely used for research purposes. [29]

The ions are produced in Electron Cyclotron Resonance Ion Sources (ECRISs), which are stable sources with low maintenance requirements. [31] Within the ECRIS, electrons are trapped by a static magnetic field with an energy of approximately 100 keV. This energy is sufficient to ionize atoms that are injected into the ECRIS electron cloud. [34]

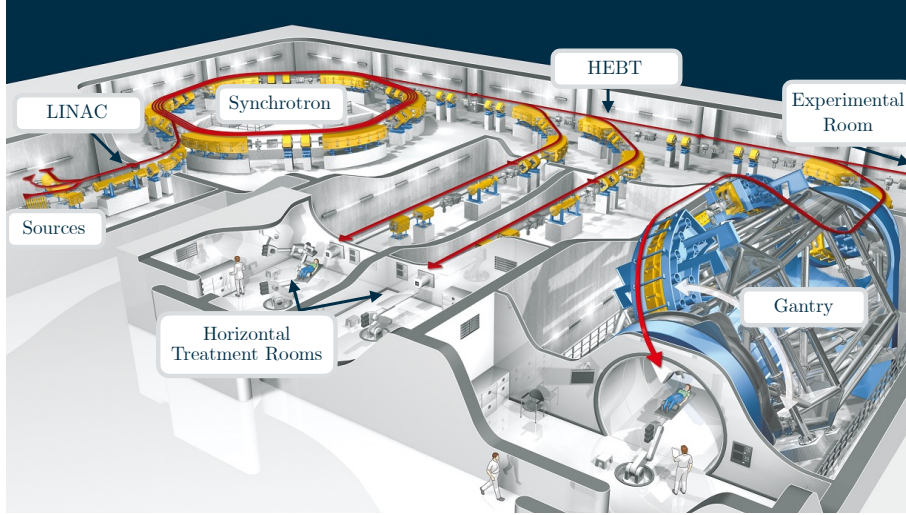


Figure 2.1.: HIT Accelerator Complex: The particles are generated at the three sources on the left of the image. The following Linear Accelerator (LINAC) leads to the synchrotron. The High Energy Beam Transport (HEBT) transports and distributes the particles to the two horizontal treatment rooms, the gantry irradiation room, or the experimental room. Additionally, a beam dump can be targeted, which is not included in this image. Image adapted from [33].

In the electron cloud, ions at different charge states are produced due to the stochastic nature of electron-particle interactions. [35] The produced ions are extracted by applying a voltage, and the desired ion charge state is filtered afterwards by a bending magnet acting as a mass spectrometer. [36]

The four ion species are produced in three separate ECRISs. One source is designated for proton extraction, one for helium ion production, and one for the formation of carbon and oxygen ions. [37, 38] The gases injected into the proton and helium ECRIS are pure hydrogen and helium gases, respectively. From the resulting ion spectrum, H_3^+ and $^4\text{He}^{2+}$ ions are selected for the beam. By employing Carbon Dioxide (CO_2) as the primary feed gas for carbon ion generation, oxygen ions can also be efficiently extracted by simply adjusting the extraction voltage without modifying the plasma conditions. The resulting ion spectrum includes $^{12}\text{C}^{4+}$ and $^{16}\text{O}^{6+}$ ions, which are subsequently separated by the bending magnet. Consequently, switching between carbon and oxygen ions only requires adjustment of the ECRIS extraction voltage and the bending magnet. [38]

2.1.2 LINAC and Synchrotron

After the ECRIS, a Radio Frequency Quadrupole (RFQ) bunches and accelerates particle from 8 keV/u up to 400 keV/u. In the subsequent LINAC, the particles are pre-accelerated up to 7 MeV/u. [36] Afterwards, a 100 μm stripping foil removes unwanted electrons to get fully ionized atoms. The resulting $^1\text{H}^+$, $^4\text{He}^{2+}$, $^{12}\text{C}^{6+}$ and $^{16}\text{O}^{8+}$ ions are injected into the synchrotron. [38] Within the synchrotron, an ultra-high vacuum ($\approx 1.3 \times 10^{-9}$ mbar) is maintained to minimize loss by electron capture processes and to avoid interferences with the beam particles. [32] The acceleration cycle in the synchrotron starts as follows [39]:

During the multiturn injection scheme, three bump magnets change the position of the injected particles to fill the whole phase space of the synchrotron to maximize the number of particles in the synchrotron. [32, 40]

The synchrotron's acceleration cavities accelerate the particles to the desired energy, reaching up to 35 cm in water, which corresponds to kinetic energies of 220 MeV for protons and 430 MeV/u for carbon ions. [29] During the acceleration, horizontal and vertical dipole magnets guide and correct the trajectories of the particles, while quadrupole magnets focus the beam and modulate the tune. [32, 39] Additionally, sextupole magnets are employed for chromatic correction and the extraction process. [39]

The particles are extracted via third-order resonance extraction. [39] The machine tune is gradually adjusted by changing the strengths of the quadrupole to approach a third-order resonance with the particles' betatron oscillation frequency. During the RF-knockout extraction, the oscillation amplitudes progressively increase until the particles reach the extraction point. [41] Varying the phase space with sextupole magnets and the knock-out exciter amplitude achieves the extraction of all particles. For clinical applications, a slow extraction lasting around 1-10 s is required for the beam delivery (Sec. 2.1.3). [32]

The desired beam intensity is often not constant for clinical field applications. Additionally, potential fluctuations in the extraction process can occur from one day to the next, and even from one cycle to the next. Therefore, it is imperative to implement active regulation and compensation mechanisms to ensure the correct delivery of beam intensity. The process is facilitated by a feedback loop, which collects the information about the applied intensity with the monitoring chambers located at the beam exit and compares it with the planned intensity. In the event of any detected deviations, the extraction process is modified accordingly. [39]

Such a synchrotron offers the flexibility to deliver beams containing different ions with a wide range of energies tailored to specific clinical or experimental requirements. [39] This level of versatility is not achievable with other accelerator types, such as cyclotrons, which are limited to providing a fixed energy output. [16]

2.1.3 Beam Delivery

After the synchrotron, the focus width of the beams is adjusted in the HEBT line and the extracted particles distributed to either one of the two horizontal treatment rooms, the gantry room, the experimenters' natural habitat, the experimental room on the right in Fig. 2.1, or a beam dump. All rooms have a beam exit equipped with a set of monitoring devices collectively referred to as the Beam Application Monitoring System (BAMS), which can be seen in Fig. 2.2. This system ensures precise supervision of beam properties during irradiation. The nozzle includes two Ionization Chamber (IC) filled with 80 % argon and 20 % CO₂ [42], which are used to count the number of particles delivered and measure the applied dose.

Additionally, Multi-Wire Proportional Chambers (MWPC) are employed to monitor the beam position and width. These measured beam parameters are supervised and processed by the therapy control system and compared to the planned properties. This process lasts ≈ 1 ms, establishing a minimum irradiation time per raster point to allow for real-time corrections via the aforementioned feedback loop. [39] The BAMS system also includes a third IC, referred to as IMON, which uses an alternative electronic readout with a frequency converter to measure the integrated signal rather than the current directly. Therefore, the IMON provides redundant and independent dose monitoring. At the exit window (Fig. 2.2), various interchangeable ripple filters are installed to extend longitudinally the pristine Bragg Peak (BP) mainly used for high mass particles.

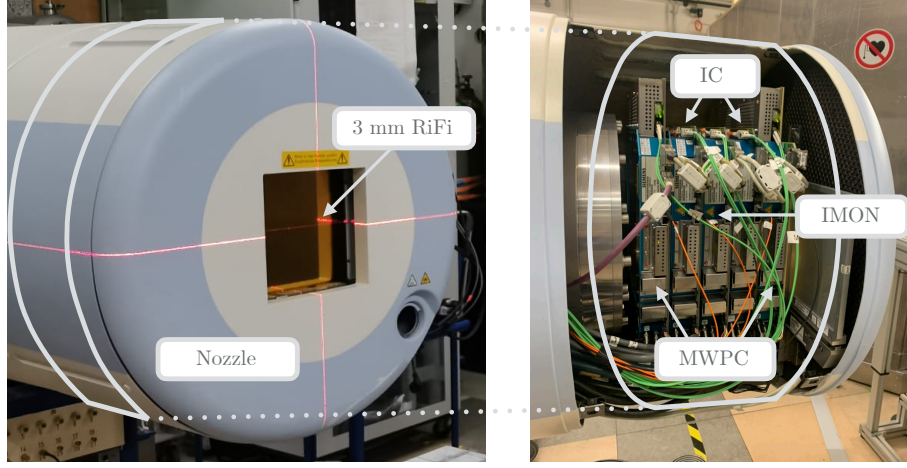


Figure 2.2.: Beam Exit Nozzle at HIT: The left side of the image shows the closed nozzle, while the right side reveals the inner Beam Application Monitoring System (BAMS) system. Particles traverse two Multi-Wire Proportional Chambers (MWPC), two Ionization Chamber (IC), and one additional IC, called IMON, integrated within the nozzle. The exit window, visible on the left, is equipped here with a 3 mm Ripple Filter (RiFi), typically employed for heavy ion experiments.

To effectively irradiate a three-dimensional tumor volume, the active raster Pencil Beam Scanning (PBS) technique is employed at HIT, which combines variable particle beam energies with precise lateral magnetic deflection seen in Fig. 2.3. [26]

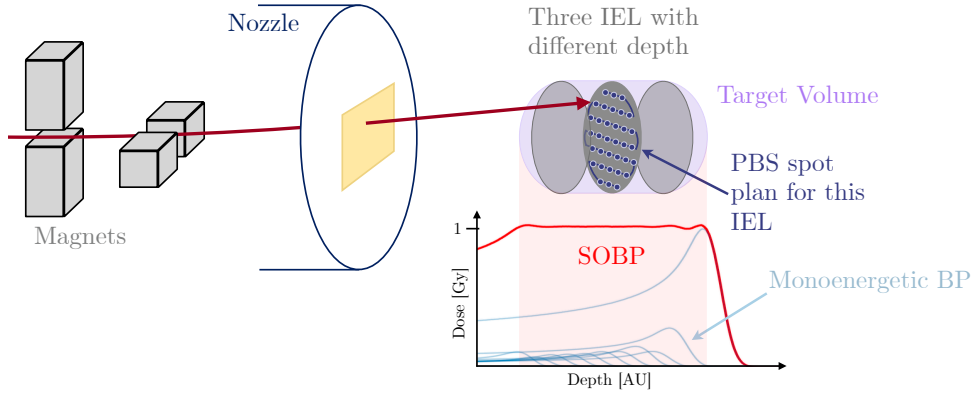


Figure 2.3.: Active Raster Scanning at HIT: The red particle beam is moved in x and y directions by magnets in the beam line, indicated by the grey blocks on the left side, in order to cover the target volume (purple ellipsoid) laterally. One slice of the target volume, here the darker grey slice, is covered laterally following a predefined Pencil Beam Scanning (PBS) pattern (blue spots and lines). To achieve in-depth coverage, the target is divided into multiple Iso-Energy Layer (IEL) along the beam direction, here marked with grey circles, each corresponding to a specific tissue depth and corresponding beam energy. Sequential irradiation of these mono-energetic beams forms a Spread-Out Bragg Peak (SOBP) region (red), achieving uniform longitudinal dose coverage of the full target volume. In the lower diagram, the light blue lines indicate the monoenergetic Bragg Peak (BP) correspond to one IEL, and in red, the formed SOBP is indicated. After completing the irradiation of one IEL, the beam energy is adjusted to irradiate the next layer. Image inspired by [26] with the SOBP diagram from [43].

Based on the prescribed tumor dose, the Treatment Planning System (TPS) calculates the required IEL to cover the tumor in depth, as well as the necessary number of spots, their sizes, and their spacing within each layer for lateral coverage (Fig. 2.3). The active PBS irradiation allows sub-millimetre resolution and thus enables a volume coverage with high spatial accuracy. [16]

In addition to the high conformity, the active PBS technique offers several advantages over passive beam delivery systems, where the energy of the beam is not adapted in the acceleration process,

but degraded with additional modulators. Therefore, passive approaches require patient-specific hardware, such as apertures and range modulators, to shape the beam laterally and to degrade its energy for longitudinal dose coverage. [16] The modulation components can cause nuclear fragmentation, leading to beam contamination [26, 31] by secondary particles and additional scattering. In contrast, active PBS achieves precise dose conformation without the need for patient-specific hardware. [16]

In summary, the HIT accelerator complex provides light proton and helium beams, as well as heavier carbon and oxygen ions. These particle beams are delivered with the requisite energy and spatial distribution.

2.2 Initial Particle Interaction with Matter

After exiting the beam nozzle, the particle beam crosses the air and enters the patient. Here, the particles interact with matter in a series of processes where the particle successively deposits its energy. [44] Two types of two-particle collisions are distinguished: electromagnetic and nuclear interactions, which themselves can be subdivided into elastic and inelastic interactions [45], as displayed in Fig. 2.4.

Elastic scattering is characterized by the interaction products being identical to the initial particles. The total kinetic energy and the momentum are conserved. However, a change in the direction of motion occurs, e.g., with the scattering angle Φ for the projectile and Θ for the targets, as in Fig. 2.4. This interaction occurs in electromagnetic or nuclear processes.

In **inelastic electromagnetic collisions**, the projectile and target nuclei are identical before and after the collision, but the projectile transfers energy to the target atom not only in the form of kinetic energy. Three major processes can occur (Fig. 2.4):

- During **excitation**, a bound electron is transferred into a higher energy level in the atom or molecule, indicated by the asterisk (*) in Fig. 2.4. [44] To return to the energetically favored ground state, the additional energy is emitted in the form of a photon. [45]
- During **ionization**, electrons bound in an atom or molecule are liberated in a collision with an incoming particle, leaving the atom in an ionized state indicated by a plus (+) in Fig. 2.4. [44] Due to the ionization processes, lots of secondary electrons are emitted along the primary particle track. After ionization, the inner-shell vacancy is filled by an outer-shell electron. The resulting liberated energy is either emitted by a photon or transferred to another electron, causing its emission. The latter is known as the Auger-Meitner effect, which presents an additional electron source. All those “convoy” electrons follow the primary particle and contribute to the energy deposition in the material. [16]
- Thirdly, when a projectile particle experiences an acceleration, part of its kinetic energy is released via the emission of **bremsstrahlung**, shown on the bottom of Fig. 2.4. [45]

The traversing particle may also undergo a nuclear interaction, which can be either elastic or inelastic. [16] During **elastic nuclear interactions**, the projectile and target nuclei remain unaltered. Merely their momenta and directions are changed.

Nuclear fragmentation occurs at energies of several tens of MeV/u. [46] **Inelastic nucleus-nucleus collisions** change the atomic composition of the projectile and target, resulting in the production of various fragments, displayed on the right side of Fig. 2.4.

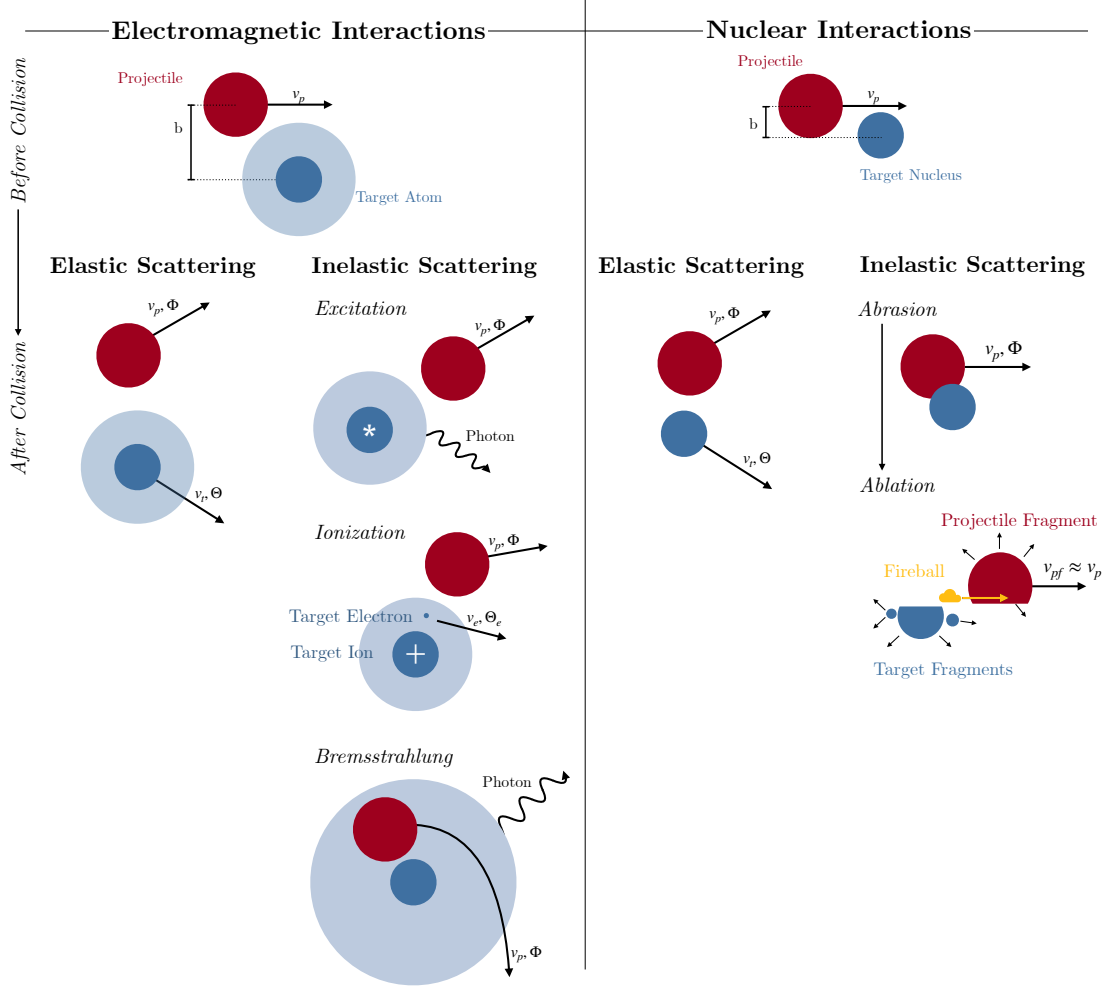


Figure 2.4.: Particle Interactions: Before the collision, the red-marked projectile approaches a target with velocity v_p and impact parameter b . The target's electron cloud is shown in light blue, and its nucleus in dark blue. After the collision, possible emission directions are shown with solid arrows, defined by the angles (Φ, Θ) and the resulting particle's velocity v . Photon emissions are indicated by curved arrows labeled accordingly. The index p belongs to properties of the projectile, t to the target atom, e to the target electron, and pf to the projectile fragments. The interactions are detailed in this section.

This process can be described by the abrasion-ablation model. The projectile particle abrades the target nucleus, forming a highly excited reaction zone (“fireball”). In this region, the nuclei are left in excited states and decay to the ground state, e.g., by emission of γ -rays. In the ablation phase, projectile-like secondary fragments are predominantly emitted in the forward direction, sharing the initial velocity vector of the primary ion. [16, 46] In contrast, target-like fragments tend to exhibit lower velocities compared to their projectile-like counterparts. [46, 47] In general, peripheral projectile-target collisions cause only minor mass removal and are the most likely. [16] Less frequent central collisions can lead to the complete disintegration of both nuclei involved. [24]

These physical interactions are statistical in nature and depend on the properties of the particles, including their mass, charge, and energy. The cross section of a process provides the probability of a specific interaction based on the particle and target properties. Therefore, which interaction occurs is not deterministic but rather follows a statistical distribution. [45]

For reaching deep-seated tumors, protons require a kinetic energy of approximately 230 MeV, while carbon ions require an energy of 430 MeV/u. [29] The particles are therefore moderately relativistic with a relativistic velocity β of around 0.6-0.7. [24]

At these energies, generally electromagnetic interactions are dominated by inelastic collisions with the target's electrons, [16] thus the majority of the energy is deposited via ionization and excitation. For heavier ions, nuclear interactions gain importance, which is discussed in Chapter 3. [24]

2.2.1 Physical Description of the Energy Loss Process

The mentioned interactions deposit energy in the tissue. To quantify the energy deposition and correlate it with biological effects, several quantities are needed.

Mathematically, all energy depositions along the particle's path are summed up to yield the mean energy imparted $\bar{\epsilon}$. Therewith, the **absorbed dose** represents $\bar{\epsilon}$ deposited per unit mass of the target material m :

$$D = \frac{d\bar{\epsilon}}{dm} \quad (2.1)$$

given in SI units [J/kg]. In medical physics, the SI unit of the dose is renamed to Gray [Gy]. [44] For a thin absorber, the dose can be approximated by

$$D = \Phi \cdot 1.6 \cdot 10^{-9} \cdot \frac{1}{\rho} \cdot \frac{dE}{dx}. \quad (2.2)$$

The dose therefore depends on the particle fluence Φ in [1/cm²], which describes the amount of particles per area and the density of the material ρ in [g/cm³]. The last factor in Eq. 2.2 represents the so-called stopping power S , here in [keV/μm]. [16] The **stopping power** describes the energy loss per unit length [44]

$$S = \frac{dE}{dx}. \quad (2.3)$$

The total stopping power can be expressed as the sum of its distinct contributions [44]

$$S = S_{\text{el}} + S_{\text{rad}} + S_{\text{nuc}}, \quad (2.4)$$

namely the electronic stopping power S_{el} , the radiation stopping power S_{rad} , and the nuclear stopping power S_{nuc} .

The **electronic stopping power** S_{el} refers to inelastic Coulomb interactions with an atomic electron, resulting in ionization or excitation. [16] When considering the Continuous Slowing Down Approximation (CSDA), in which it is assumed that the particle loses energy continuously along its path, rather than in discrete, random collisions, the mean electronic stopping power is given by the Bethe-Bloch equation:

$$\langle -S_{\text{el}} \rangle = K \cdot \rho \cdot \frac{Z_t}{A_t} \frac{Z_p^2}{\beta^2} \left\{ \frac{1}{2} \ln \left(\frac{2m_e c^2 \beta^2 \gamma^2 W_{\text{max}}}{I^2} \right) - \beta^2 - \frac{\delta(\beta\gamma)}{2} - \frac{C(\beta)}{Z} \right\}, \quad (2.5)$$

with the constant factor $K = 0.307 \text{ MeV cm}^2/\text{mol}$, Z_t the atomic number of the target material and A_t the mass number, Z_p is the effective charge of the projectile and β its relativistic velocity. m_e is the mass of the electron, c the speed of light, γ the Lorentz factor, W_{max} the maximum energy transfer to an electron in a single collision, and I the mean excitation energy [48, 49], which for liquid water is 78 eV. [50] The additional terms after the β^2 in the brackets are correction terms:

- For highly relativistic particles, the Lorentz boost of the Coulomb field increases the cross section with increasing energy. However, this relativistic rise is limited by the polarization of the target material traversed by the charged particle. The density effect correction factor $\delta(\beta\gamma)$ incorporates this polarization effect, which is only important for high energies. [48]
- Lastly, the shell correction $\frac{C}{Z}$ should be considered for slow particles with $\beta < 0.3$. [49] Initially, the Bethe-Bloch formula for the stopping power was based on the assumption that the incoming particles have higher velocities than the atomic orbital electrons, which are therefore considered stationary. This assumption breaks down at low energies when the velocity of the shell electrons and the incoming particle are similar. The orbital electrons are fast, so their probability of participating in interactions with the charged particle decreases. Thus, the correction factor depends on the atomic electronic structure of the target (C). [48]

The **radiation stopping power** S_{rad} includes the inelastic interaction where bremsstrahlung is emitted. In comparison to the electronic stopping power, the bremsstrahlung cross section is inversely proportional to the projectile's mass m_p squared and proportional to its energy E_p and charge Z_p [49]

$$\sigma_{\text{rad}} \propto \left(\frac{E_p \cdot Z_p^2}{m_p^2} \right). \quad (2.6)$$

Due to the $\frac{1}{m^2}$ dependency, the energy loss via bremsstrahlung is negligible for heavier particles, like ^1H , ^4He , ^{12}C and ^{16}O in the clinically relevant energy ranges. [45]

Compared to the discussed electromagnetic interactions, **nuclear interactions** considered in S_{nuc} are rare events, but have to be considered at energies exceeding tens of MeV and for heavy particles as discussed in Chapter 3. [46] Elastic interactions impart recoil energy to target nuclei [44] and the angular distribution of the particle. [16] Generally not included in conventional stopping power calculations are inelastic nuclear interactions, which play a distinct role in heavy ion irradiation. [44] The nuclear-fragmentation cross section σ_{nuc} at high energies can be described by the geometric Bradt-Peters approximation

$$\sigma_{\text{nuc}} = \pi r_0^2 \left(A_p^{\frac{1}{3}} + A_t^{\frac{1}{3}} - b \right)^2 \quad (2.7)$$

with the nuclear radius r_0 , the impact parameter b (see Fig. 2.4) and the atomic number A for the projectile p and the target t . [15]

The total stopping power shapes the Depth Dose Distribution (DDD) of the particles, concentrating the energy deposition in a small region called the BP, depicted in Fig. 1.3. [9]

In medical physics, instead of the stopping power, the **Linear Energy Transfer (LET)** is used to quantify the radiation quality. In its unrestricted form, the LET is equal to the electronic stopping power. The restricted form of the LET is defined as follows:

$$\text{LET} = S_{\text{el}} - \frac{dE_{\text{ke}\Delta}}{dx}, \quad (2.8)$$

where the total kinetic energy loss $dE_{\text{ke}\Delta}$ per length considers the energy carried away from the regarded volume by the emission of secondary electrons with energies above a certain threshold Δ . [44] The restricted LET, typically expressed in $[\text{keV}/\mu\text{m}]$ [9], quantifies the local energy deposition and is relevant for the biological effects. [15]

2.2.2 Longitudinal Spread of the Depth Dose

The pristine BP of a multiple particle beam is spread in depth due to two mechanisms: random variations in particle range, known as longitudinal straggling [24], and the extended range of secondary fragments produced in nuclear interactions. **Longitudinal straggling** arises from statistical fluctuations in the energy-loss interactions as the particles slow down. [24] Since each particle undergoes a unique sequence of random interactions, their ranges differ. This leads to a spread in the position of the BP around its average location and exhibits a smeared-out BP seen in Fig. 1.3. This effect is further enhanced in inhomogeneous tissues due to increased interaction variability. [16]

In addition to straggling, the various nuclear fragments contribute to the longitudinal dose spread. The **range R of a particle** can be determined by integrating the total stopping power (Eq. 2.3). For two projectile particles with identical velocities in the same material, the ratio of their ranges depends on both mass M and charge Z [24]:

$$\frac{R_2}{R_1} = \frac{M_2}{M_1} \cdot \frac{Z_1^2}{Z_2^2}. \quad (2.9)$$

This implies that lighter projectile fragments, which are mostly emitted in the forward direction and possess the same velocity as the incident particle, can travel farther in tissue than the actual heavier primaries because of the squared charge dependency. As a result, heavy ion beams, which have a higher fragment production rate than light ion beams, produce a characteristic dose-“fragmentation tail” beyond the BP (Fig. 1.3). [46]

2.2.3 Lateral Scattering of a Pencil Beam

The lateral dose distribution of a beam results partially from the **angular dispersion of secondary fragments** produced through nuclear interactions. Although the angular distribution of nuclear fragments is generally narrow and forward-focused, lighter fragments in particular may exhibit larger deflection angles and thus diverge from the initial beam axis. [24]

Another dominant driver of lateral spread is the elastic Coulomb interactions between the incoming particles and target nuclei, which typically experience small deflection angles. As particles traverse thicker targets, they undergo numerous small-angle deflections described as **Multiple Coulomb Scattering (MCS)**. According to the central limit theorem, the cumulative result of many such small-angle scatterings leads to a lateral displacement that can be approximated by a Gaussian distribution with the standard deviation σ_{lateral} :

$$\sigma_{\text{lateral}} = K \cdot \frac{Z_p}{\beta \cdot p \cdot c} \cdot D(L, L_{\text{rad}}), \quad (2.10)$$

with a constant factor $K = 14.1 \text{ MeV}$ the particles momentum p and a function D , which depends on the total mass thickness L and the radiation length L_{rad} . [24]

The extent of lateral scattering is influenced not only by the patient’s tissue but also by all materials the beam passes through before reaching the target, including measurement chambers and beam shaping elements. This upstream scattering distinctly shapes the lateral beam profile before it reaches the region of interest. [16]

2.3 Radiochemistry

The primary physical particle interactions occur within ≈ 1 fs after irradiation. The following chemical stage, during which the products interact and diffuse throughout the cell, typically lasts up to 1 μ s. [45]

The aim of the radiotherapy is to damage the **Desoxyribonucleic Acid (DNA)** of tumor cells, since DNA damage can cause cell sterilization or cell death. The helical structure of the DNA has a backbone made of alternating sugar and phosphate groups, which are connected by four paired bases. [9] The entire structure is surrounded by water molecules and tightly packed around with structural proteins like histones, making it difficult to access it from the outside (Fig. 2.5). [51]

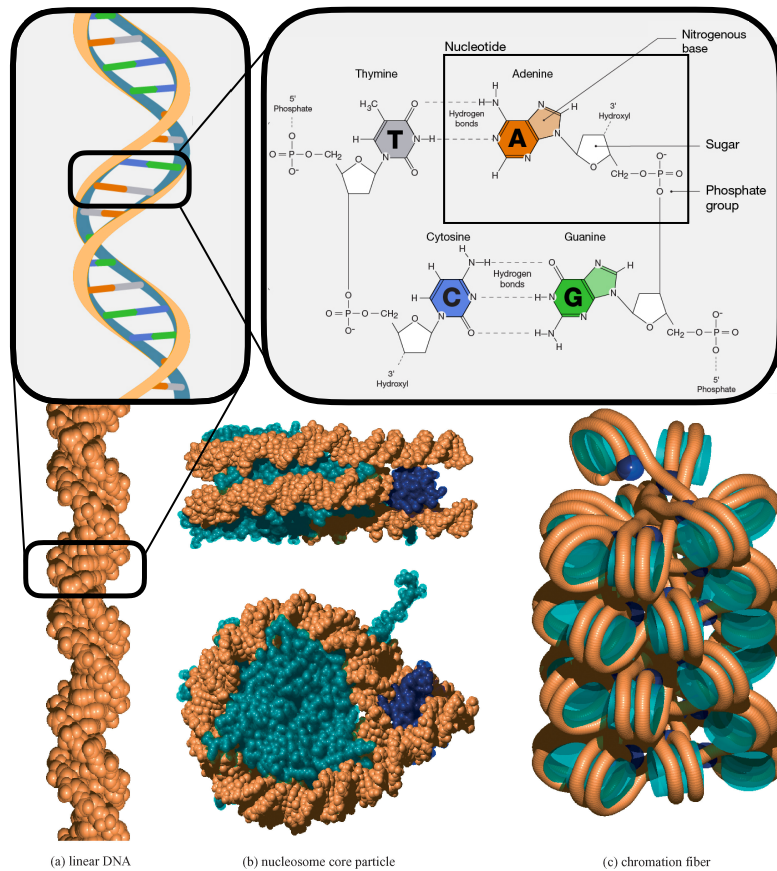


Figure 2.5.: DNA Model: The linear DNA form is shown on the lower left. Next to this, the turquoise structure represents the histone octamer around which the DNA is wrapped, while the blue element represents the globular core of a linker histone. On the right side, the DNA is shown in its condensed form. As seen in the zoom plot on the top left, the DNA consists of two strands composed of alternating sugar (deoxyribose), phosphate groups, and four types of nitrogenous bases – adenine (A), thymine (T), cytosine (C), and guanine (G) – which are displayed on the right top. The lower image is from Bernhardt et al.[52] and the structure figures from [53].

Damages to the DNA structure can be induced in two different ways [54]:

Direct Damage: The incident particle interacts directly with the DNA biomolecules, forming radicals through physical interactions described in Sec. 2.2. [55] These interactions can induce covalent bond breakage of the DNA strands. The estimated ionization threshold of a DNA molecule ranges from 7 eV to 10.5 eV. [56]

Indirect damage: Since 70 % of the cellular mass is water, an incoming particle is more likely to interact with a water molecule than a DNA molecule. This interaction is called water radiolysis and marks the starting point of a highly complex and versatile chemical cascade. The resulting products can contribute substantially to damage the DNA. [51, 54, 56] Fig. 2.6 displays a small section of this cascade, highlighting the most relevant pathways for this thesis.

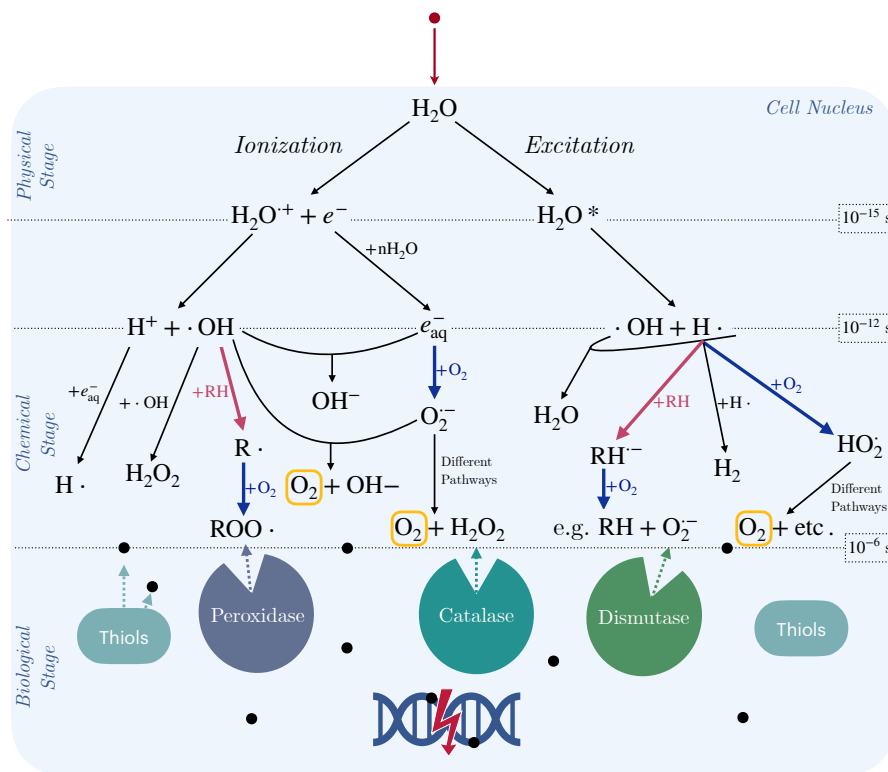


Figure 2.6.: Radiochemical Cascade: The incoming particle (indicated by the red dot) interacts with water molecules through either ionization (left pathway) or excitation (right pathway). These initial events in the physical stage trigger a cascade of radiochemical reactions as the resulting species begin to diffuse. Reactions involving organic substances (RH) are shown in red [57], while oxygen-consuming reactions are indicated in dark blue. The oxygen-producing mechanisms are highlighted with yellow boxes around the oxygen molecule and are further discussed in Subsection 3.1.3. [58] The remaining Reactive Oxygen Species (ROS) after the chemical stage are indicated by the black dots, which diffuse to the DNA. The various cell defense mechanisms against these chemical products are indicated in the lower part of the image in the biological stage. The relevant time scales of these processes are marked by dotted black lines. The reactions are selected from [51, 54, 56–58].

After the ionization (seen on the left side of Fig. 2.6), the resulting water radical cation is a very strong acid and can lose its proton by forming hydroxyl radical $\cdot OH$ radicals and a free H^+ . The free electron is often hydrated by water molecules e_{aq}^- .

The excited water molecules, on the upper right side of Fig. 2.6, decompose into a hydroxyl radical $\cdot OH$ and a hydrogen radical $H\cdot$.

Already at this early stage – lasting only 1 ps [45] – three **different radicals** ($H\cdot$, $\cdot OH$, e_{aq}^-) of which one is a highly reactive Reactive Oxygen Species (ROS) ($\cdot OH$), are produced. [59]

Over time, the different reaction products start to diffuse from their point of origin and interact further. [51] With a diffusion coefficient in cytoplasm of $2\mu m$ in 1 ms, the time and distance towards the DNA can be challenging for some of the short-lived products to overcome. [54] For example, $\cdot OH$ is highly reactive and travels a maximum of 2 \AA before interacting again. [51]

Many hydroxyl radicals can be produced along the particle track, since both excitation and ionization lead to hydroxyl radical production (Fig. 2.6). In subsequent self-interactions hydrogen peroxide H_2O_2 can be produced. This uncharged, low-weighted molecule can easily diffuse through membranes and reach the DNA, where it induces Single-Strand Break (SSB) or oxidizes nucleobases. Additionally, hydroxyl radicals are an important starting point in the generation of primary carbon-centered, organic radicals $\text{R}\cdot$. Under the consumption of molecular oxygen, carbon-centered radicals can produce peroxy radicals ($\text{ROO}\cdot$), which are highly efficient at inducing DNA damage by oxidizing the DNA bases [51] and damaging other cell organelles, such as lipids. [54, 60]

Another key contributor to DNA damage is the superoxide radical ($\text{O}_2^{\cdot-}$), which is a small and mobile species thus capable of diffusing through the cellular environment. [51] As illustrated in Fig. 2.6, the formation of this radical depends on the presence of both organic molecules (RH) and molecular oxygen (O_2), highlighting their central role in the radiochemical cascade. H_2O_2 , $\text{ROO}\cdot$, and $\text{O}_2^{\cdot-}$ are a few products demonstrating how intricately the organic composition of the medium and the local oxygen concentration shape the outcome of radiation-induced processes. [57, 61]

Oxygen is crucial in various radical interactions as shown in Fig. 2.6 for the efficacy of the indirect DNA damage induction [9]. Additionally, molecular oxygen may play an important role in fixing the damage. The DNA can be damaged indirectly or directly by inducing DNA radicals $\text{DNA}\cdot$. This reduced form can be restored through a reaction with a sulfhydryl (SH) group, a process called chemical repair. However, before repair occurs, oxygen molecules can interact with DNA radicals to form an organic peroxide $\text{DNA} - \text{O}_2\cdot$. These organic peroxides represent a nonrestorable permanent DNA damage, because the chemical composition is fully changed, which is why this is called the “oxygen fixation hypothesis”. [9, 51]

Furthermore, since these interactions require the presence of oxygen immediately when the DNA damage is produced and the radicals interact, the precise temporal distribution of oxygen is crucial. [51] Understanding the oxygen dynamics is vital for interpreting cellular radiation responses. [57, 62]

2.4 Biological Effects

Cells are not unarmed against damaging interactions, radicals, and ROS. Our body is constantly exposed to ROS, since they are produced, among other places, in the mitochondria as a byproduct of energy production. [63] Therefore several **guard mechanism** are active within a cell, shown in Fig. 2.6: Superoxide dismutases can theoretically degrade the $\text{O}_2^{\cdot-}$ concentration. However, its effectiveness as a scavenger is limited by its heavy mass of 32.5 kDa, which restricts its accessibility and mobility. Catalase degrades H_2O_2 to water and molecular oxygen, and peroxidases scavenge ROS like $\text{ROO}\cdot$. [54, 63] Thiols, such as glutathione, act as antioxidants in the nucleus, neutralizing further ROS species (Fig. 2.6). [61] Therewith, the cell can protect itself from the indirect damage.

All of the different molecules of the DNA shown in Fig. 2.5 can be harmed directly or indirectly. The various chemical damages to DNA are categorized as base damage, SSB, or Double-Strand Breaks (DSB).

Repairing base damages and **SSBs** is a relatively straightforward process due to the use of the complementary DNA side as a template. Nonetheless, there exists a possibility of a misrepair, which could result in a mutation and could lead to cell death.

Single **DSBs** can theoretically be repaired through different mechanisms depending on the phase of the cell cycle. However, DSB are generally more detrimental to cells than SSBs, because DSBs are less likely to be repaired effectively and correctly. As a result, DSBs are more likely to be lethal to cells. [9]

The most lethal for cells are **complex DNA** damages, which contain several lesions in close proximity of 20 base pairs. [64] These clustered lesions can undergo recombination in various ways, e.g., leading to chromosomal aberrations that are often irreparable. Such complex lesions and resulting aberrations are mainly formed on the basis of DSB. [9]

Depending on the severity of the damage, the harmed cells undergo **cell death mechanisms**, such as apoptosis or autophagic cell death, or die during attempted cell division through mitotic cell death. [9] Successful radiotherapy treatment does not require tumor cells to undergo cell death. It is sufficient for the targeted tumor cells to permanently lose their ability to proliferate or become sterile. However, a proportion of sterile cells may retain metabolic activity and thus be capable of producing growth factors.

Dying cells release signals that can influence the immune system. [65] These signals can either have tolerogenic or immunogenic effects on the local environment, thereby affecting the post-treatment anti-tumor response. Ideally, the immune system mediates the suppression of tumor growth, but also vice versa effects have been reported. [66]

The biological mechanisms underlying radiation-induced cell death, cellular signalling, and the reaction of the body are highly complex and depend on multiple factors such as dose, fractionation scheme, radiation type, and tissue characteristics. [63] Despite extensive research, these processes are not yet fully understood. [66]

STRATEGIC USE OF HEAVY ION THERAPY

Having outlined the fundamental processes governing general particle irradiation from acceleration to their physical, chemical, and biological effects, the following comparison is made between different particle species.

For treating deep-seated tumors in clinical settings, the particles have to reach around 35 cm in water equivalent depths. Therefore, light protons require a kinetic energy of 230 MeV and thus have an average Linear Energy Transfer (LET) in the Spread-Out Bragg Peak (SOBP) of around 5 keV/μm. The elevated proton LET is only relevant for the last few millimeters of the particle range. [24] Heavier ions, such as carbon ions, need an energy of around 430 MeV/u to reach the same depths and possess average LET values of around 60 keV/μm. With oxygen ions, values of above 100 keV/μm are possible depending on the SOBP and depth. [67]

This raises the question: What makes heavy ions, with their characteristically high-LET values, particularly advantageous for clinical applications?

3.1 Advantages Across Scales: Physical, Chemical, and Biological

The answer is found in the unique physical, chemical, and biological advantages of heavy ion irradiation, which enable more precise dose delivery, fundamentally alter radiochemical processes, and enhance biological effectiveness. The subsequent sections elucidate how these multi-scale advantages render heavy ions a **more** efficacious modality compared to lighter proton therapy.

3.1.1 More Conformal Dose Distribution

Heavy ions offer several physical advantages compared to lighter particles. One major benefit lies in their **reduced longitudinal straggling** (Sec. 2.2.2). The variance of the resulting range distribution, and thus the width of the Bragg Peak (BP), depends on the mass M of the particles (Eq. 2.9). For two particles, the ratio of their range straggling widths σ_{long} is given by [24]:

$$\frac{\sigma_{\text{long}_1}}{\sigma_{\text{long}_2}} = \sqrt{\frac{M_2}{M_1}}. \quad (3.1)$$

Given the $\frac{1}{\sqrt{M}}$ dependency, heavier particles experience less straggling and form a sharper BP when applied as a multiple particle beam. For instance, the range straggling of carbon ions is 3.5 times less than that of protons. [16] The more defined BP enable precise dose localization at the tumor's rear edge [15], as seen in Fig. 1.3 and in the Depth Dose Distribution (DDD) in Fig. 3.1.

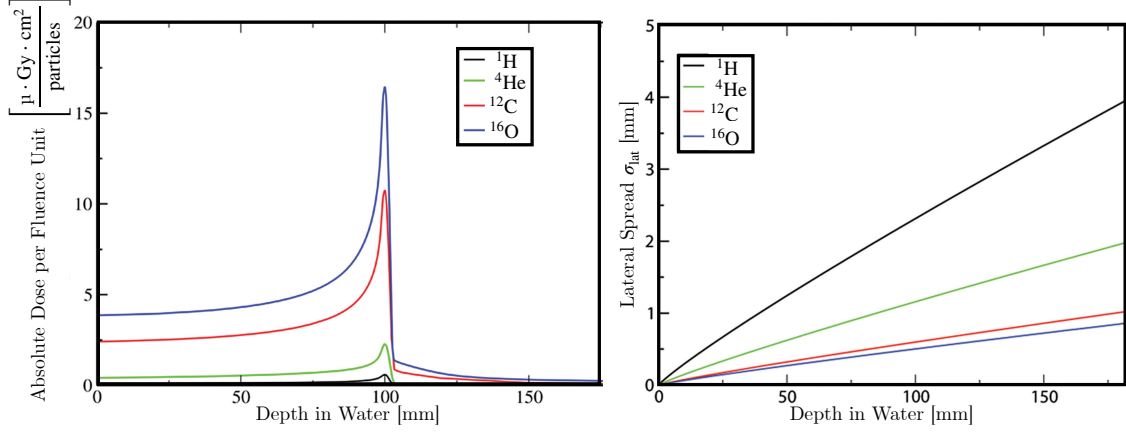


Figure 3.1.: Depth Dose Distribution (DDD)(on the left side) and the Corresponding Lateral Spread (on the right side) for ^1H , ^4He , ^{12}C and ^{16}O Ions in Water: The energies of the ions were matched to result into the same BP depth of 10 cm in water. The DDD emphasizes that heavier ions deposit more dose per particle. On the right, the corresponding lateral spread of these ions is shown. Protons tend to diverge considerably laterally. The four times higher helium mass serves to reduce this divergence (Eq. 2.10). The difference between carbon and oxygen is smaller. In general, this highlights the benefits of reduced lateral scattering of heavy ion irradiation. Image adapted from [68].

In addition to improved longitudinal precision, heavy ions also experience **less lateral scattering**. This is due to the inverse dependence on momentum and velocity $\frac{1}{\beta \cdot p \cdot c}$ (as per Eq. 2.10). Therefore, heavier particles at the same range exhibit smaller lateral deflections, as seen in Fig. 3.1. [16] However, while for protons the lateral spread is predominantly influenced by Multiple Coulomb Scattering (MCS), for heavier ions the lateral broadening arises primarily from nuclear fragmentation processes. [16] This process will be addressed in a subsequent section (Sec. 3.2).

The combination of reduced lateral and longitudinal spread enables **more conformal dose distributions** in all three directions. [69]

Furthermore, heavy ions exhibit higher stopping powers, as described by the Bethe-Bloch equation (Eq. 2.5), which scales with $\propto \frac{Z^2}{\beta^2}$. [15] A higher stopping power is correlated with **higher-LET** values (Eq. 2.8), which is displayed in Fig. 3.2. This means that heavy ions deposit more energy and thus more dose per unit length than protons (Eq. 2.2), as shown in the DDD in Fig. 3.1. As seen in Fig. 3.2, protons also reach slightly elevated LET values at the end of their range. Since they possess slow velocities in this region, the area of potentially harmful high LET is limited to a small area. For heavier ions, this region is extended, and it can be seen that, e.g., with oxygen ions, even the target region is exposed to an dose-averaged LET (LET_d) over 100 keV/ μm . This is a major advantage for tumor treatment.

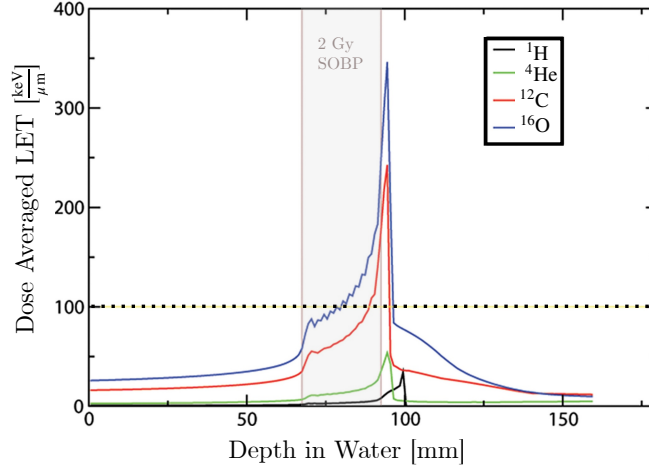


Figure 3.2.: Dose-averaged LET (LETd) Distributions over Depth for ^1H , ^4He , ^{12}C and ^{16}O Ions: The generated SOBP was optimized to deliver 2 Gy physical dose to the grey marked target area of 2.5 cm. The maximum LETd for higher mass ions is closer to the target region edge. Nuclear fragmentation results in an increased LET tail, especially pronounced for high ion masses. 100 keV/ μm is marked with a dashed line for orientation. Image adapted from [68].

3.1.2 More Intra-Track Interactions

At this high LET, ionizing interactions occur in close spatial proximity, resulting in **dense ionization tracks**, often referred to as spurs, as illustrated in Fig. 3.3. The following reactions of diffusing radiolysis products generated by a single primary particle within its track are referred to as intra-track interactions.

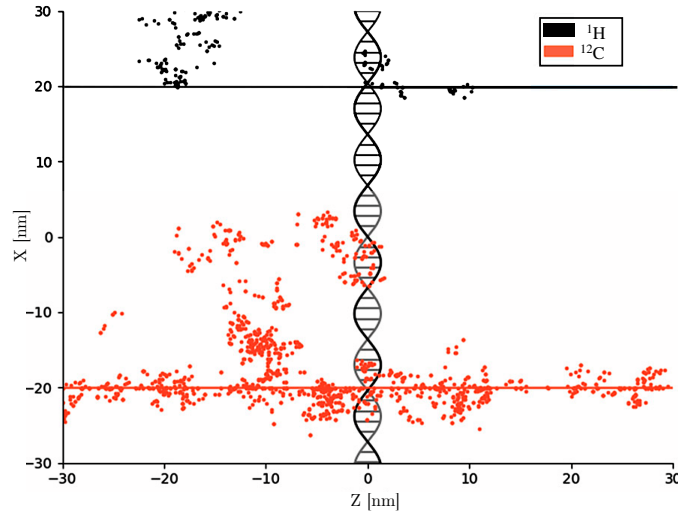


Figure 3.3.: Illustration of Proton and Carbon Trackstructure: The upper track represents a 10 MeV proton track in black with an LET of approximately 5 keV/ μm , while the lower track in red shows a 200 MeV carbon ion with an LET of 100 keV/ μm . The DNA strand is depicted for scale, and energy deposition events are marked with dots. Whereas the proton deposits energy sparsely along its path, the carbon ion produces a much denser pattern of ionizations, which results in more intra-track interactions. Image adapted from [70].

The consequences of the close proximity of interactions are manifold.

Firstly, in the subsequent chemical stage, the reduced spatio-temporal distance between radiation-induced species enhances the probability of **radical-radical interactions**. This high density promotes self-reactions, such as $\text{H}\cdot + \text{H}\cdot$ and $\text{HO}\cdot + \text{HO}\cdot$ [71], leading to the formation of more molecular species like H_2 and H_2O_2 . [72]

In contrast, the concentrations of other radicals, such as HO^- [71], e_{aq}^- , H_3O^+ , and peroxy radicals, are lower in high-LET compared to low-LET tracks, due to the amplification in chemical reactions. [73–75] These radiochemical changes due to the intra-track interactions underscore the profound impact of high-LET irradiation on the chemical environment, which also affects the subsequent biological response. [72]

While indirect damage induction may also be amplified due to the intra-track interactions and to the higher concentration of harming molecular species (e.g. H_2O_2), the great advantage of high-LET irradiation lies in the **direct damage** component. High-LET radiation, such as carbon ions, induces a greater proportion of direct Desoxyribonucleic Acid (DNA) damage compared to low-LET radiation due to the higher ionization density along the particle track (Fig. 3.3). [71, 76, 77] The close spatial clustering of ionization events increases the frequency of DNA lesions, resulting in a higher proportion of complex Double-Strand Breaks (DSB) damage [77] and significantly more chromosomal aberrations, particularly reciprocal exchanges. [78] Such complex lesions are repaired more slowly, less accurately, and often incompletely, increasing the likelihood of cell death. [79] This dense damage pattern underlies the enhanced biological effectiveness of the densely ionizing high-LET radiation. [9, 70]. At the cellular level, high-LET irradiation has been shown to induce various forms of **cell death** more effectively, including apoptosis, mitotic catastrophe, autophagy, and senescence. Although the precise signaling pathways remain to be fully elucidated, increasing LET is associated with a more pronounced activation of cellular inactivation mechanisms. [80]

Beyond direct tumor cell killing, heavy ion irradiation also appears to influence the **tumor microenvironment and immunogenicity**. Studies suggest that carbon ions may contribute to the formation of a distinct tumor microenvironment [81], reduce the risk of metastasis [82], and enhance T-cell activation. However, the LET dependence of these immunomodulatory and inflammatory responses in tissue remains incompletely understood. [80]

Another biological implication of high-LET irradiation and the resulting **complex DNA damage** is reduced sensitivity to the cell cycle phase. [83] The effectiveness of damage repair is strongly influenced by the cell cycle stage, since various DNA repair pathways are active during specific phases. However, high-LET radiation induces more complex and irreparable DNA lesions than low-LET irradiation, reducing the relevance of cell cycle-dependent repair mechanisms for determining cell fate. [9]

Similarly, the benefit of dose fractionation diminishes with increasing LET. Low-LET irradiation typically causes a higher proportion of sublethal damage, which cells can repair between fractions, justifying dose fractionation as a radiobiological strategy. In contrast, high-LET radiation produces fewer sublethal lesions, reducing the opportunity for inter-fraction repair. [24]

3.1.3 More Abbreviations: OER and RBE - Biological Implications of High LET

The consequences of the direct damage induction extend beyond the diminished cell cycle phase and fractionation dependencies. An additional major biological implication of this phenomenon is the reduced dependency on the oxygen concentration. [84]

For low-LET radiation, the presence of molecular oxygen plays a critical role in mediating indirect DNA damage, as discussed in Section 2.3 and illustrated in Fig. 2.6. In contrast, direct DNA damage occurs independently of the local oxygen concentration, which renders high-LET irradiation damage less dependent on the oxygen concentration for indirect damage.

To describe this oxygen dependence of different radiation qualities, the **Oxygen Enhancement Ratio (OER)** is defined as the ratio of iso-effective doses under hypoxic and normoxic conditions [9], demonstrated in Fig. 3.4

Therefore, the OER indicates the dose needed under hypoxic conditions to yield the same biological effect as under normoxic conditions.¹

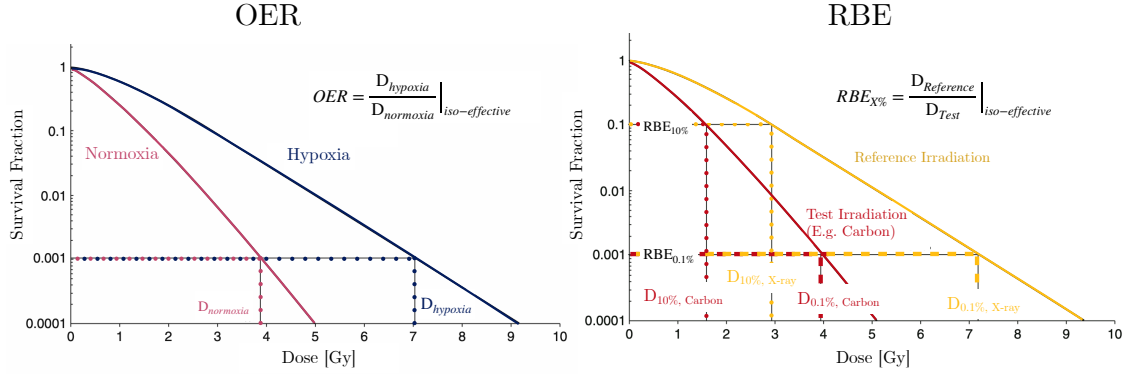


Figure 3.4.: Oxygen Enhancement Ratio (OER) and Relative Biologic Effectiveness (RBE) Calculation: On the left side, the OER is demonstrated with two Survival Fraction (SF) curves, where one is obtained under hypoxic and the other under normoxic conditions. The corresponding OER is determined at a specific SF level (e.g., 0.1 % marked with a dotted line). For the Relative Biologic Effectiveness (RBE) calculation on the right side of the figure, the required dose for a given SF is compared between a reference irradiation (typically X-rays) and the test irradiation (e.g. carbon ions), shown here for 10 % (dotted lines) and 0.1 % (dashed lines) survival. Images adapted from [85].

The OER is a dose-modifying factor, yielding that high-LET irradiation has the potential to more effectively target and eradicate hypoxic tumors in comparison to low-LET irradiation. [84, 86] Therewith the OER decreases with increasing LET demonstrated in Fig. 3.5.

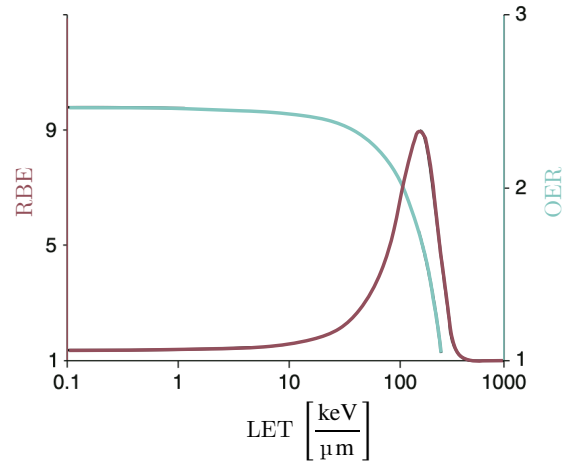


Figure 3.5.: OER and RBE over LET: The RBE values are depicted on the red left scale and the quantitative OER values on the green right scale. Images adapted from [85].

¹In general, hypoxic conditions have an oxygen concentration of below 5 %, while normoxic atmospheric conditions have approximately 20 %.

The reduction in OER is most pronounced for heavy ions with high LET, such as carbon or neon. [16] Aside from the mentioned factors, this phenomenon could also be partially attributed to the so-called **oxygen-in-track hypothesis**. [87] According to this theory, the high local density of ionizations within the track core temporarily produces local oxygen in radiolytic reactions. [87, 88] Some of these oxygen-producing interactions are included in Fig. 2.6. Monte Carlo Simulations (MCs) support this hypothesis by demonstrating that the calculated in-track oxygen concentrations correspond well with the amounts needed to explain the observed reduction in OER under high-LET conditions. [74]

Regardless of the exact underlying chemical mechanisms, the reduced OER associated with high-LET particle therapy makes it a promising approach for treating hypoxic and therefore conventionally radioresistant tumors (Fig. 3.5). [89]

The concept of **Relative Biologic Effectiveness (RBE)** is used to quantify and compare the biological impact of high-LET irradiation to that of conventional photon radiation. The RBE value is calculated by dividing the reference dose from X-ray irradiation D_x by the dose needed with another radiation quality to achieve iso-biological efficacy (Fig. 3.4). The RBE depends on many parameters, including the physical properties of the beam, the survival fraction, or the dose analysis point. As visualized in Fig. 3.4, the quantitative RBE value heavily depends on the chosen SF value. Generally, RBE increases with LET, as higher ionization densities enhance biological effectiveness, as shown in Fig. 3.5. However, beyond a certain LET threshold, the energy deposition per particle becomes so intense that a single traversal can severely reduce cell survival. At the same time, fewer particles are needed to deliver the same dose (Fig. 3.6). The decreased fluency ultimately leads to a decrease in RBE at very high-LET values. [9]

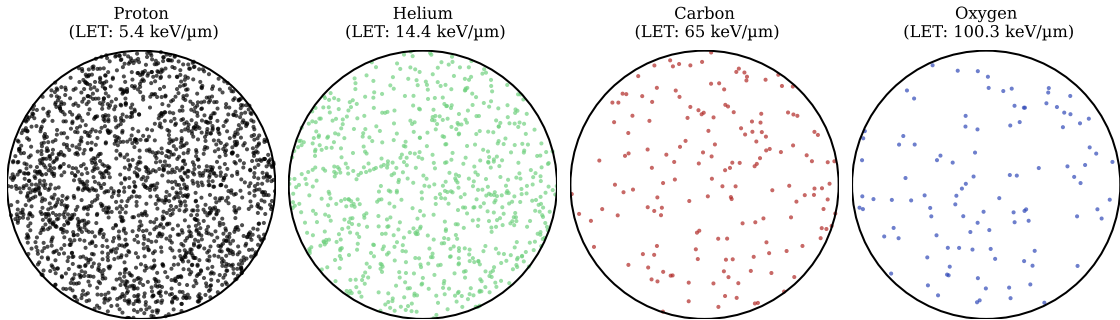


Figure 3.6.: Particle Fluence for Various LET: The displayed circle indicates the scale of a cell nucleus ($r = 6 \mu\text{m}$). In this example, a dose of 15 Gy is applied with the corresponding LET values for the particle.^a The fluence is calculated with Eq. 2.2. This nucleus cross-section illustrates the reduced number of particles required to deliver the same dose with high-LET irradiation.

^aThe dose and LETd values match the experiments conducted in Sec. 6.2.

Unlike the schematic drawing of the RBE distribution in Fig. 3.5, the maximum RBE shifts in accordance with the particle's mass. Specifically, for higher mass particles, the maximal RBE value shifts to higher-LET values [84, 90], which can be seen in Fig. 3.7.

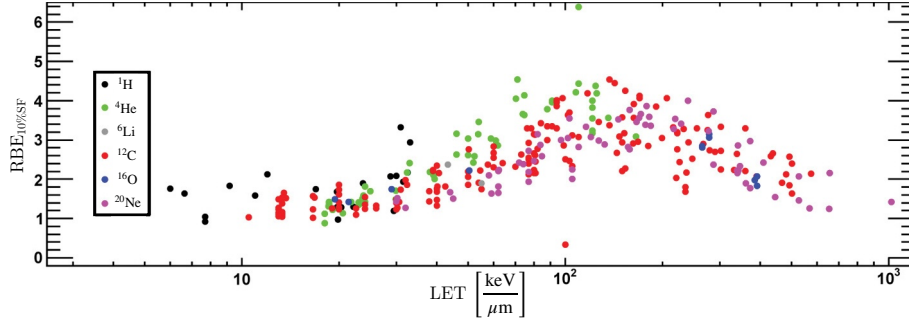


Figure 3.7.: RBE over LET for Various Ions: RBE was measured at 10 % Survival Fraction (SF) for several ions over LET. Image adapted from [68].

This can be attributed to differences in particle velocity: for an equivalent LET, a proton travels at a lower velocity than a carbon ion due to its smaller mass. (Eq. 2.5). This lower velocity results in a more concentrated energy deposition in a narrower track core, promoting clustered damage along the track. In contrast, the faster-moving carbon ion creates a broader track with lower central energy deposition compared to a proton. Consequently, the damage is less centralized. As a result, the biological effectiveness per LET is lower for carbon ions compared to protons. [16]

Aside from physical factors, biological factors such as repair capacity of the cell line, the microenvironment, and the level of oxidative stress play a major role in determining the overall biological response and, consequently, the RBE. [91, 92]

The biological evaluation point for calculating the RBE does not necessarily have to be the in vitro cell survival fraction. Furthermore, it can be assessed for in vivo endpoints, such as those observed in rat spinal cords, in order to more accurately reflect tissue responses. [93] In vivo investigations are of crucial importance for elucidating the effects of irradiation in complex biological systems, thereby providing more reliable insights into the responses observed in patients. Moreover, their significance lies in the fact that the majority of patients are treated with fractionated irradiation, a process which exerts a considerable influence on the RBE. [9] Notably, the in vivo RBE tends to increase with the number of fractions, as this corresponds to a lower dose per fraction, where differences in biological effectiveness become more pronounced. [16]

Since the RBE quantifies the relative biological effectiveness of an irradiation compared to a reference X-ray exposure, it is used to convert the physically applied dose D into a **biological dose** D_{bio} :

$$D_{\text{bio}} = D \cdot \text{RBE}(E, \text{LET}, b), \quad (3.2)$$

which highlights the RBE dependencies on the energy E , the LET, and several biological factors b . [15] The biological dose more accurately reflects the damaging capacity of the irradiation and makes the ion irradiation comparable to the well-known photon world.

3.2 Recognizing the Limitations

The physical, chemical, and biological advantages of heavy ion irradiation are very promising. However, as indicated by Eq. 2.7, the probability of **nuclear interactions** increases with the atomic number of the ion, making such interactions more prominent for heavy ions. Additionally, to reach clinically relevant tumor depths, heavy ions require higher energies than protons, as indicated by Equation 2.9, which amplifies further nuclear interactions.

The more prominent nuclear **fragmentation** severely reduces the fluence of primary ions reaching the BP. For example, in typical carbon ion treatments with 400 MeV/u only about 50 % of the ions reach the BP; for neon, this number drops to around 38 %. [24] Fragmentation diminishes the primary beam and therefore produces light fragments that can deposit energy even beyond the BP (Section 2.2.2). The sharp distal BP fall-off has an attachment of a low-dose tail composed of secondary particles, called “fragmentation tail” [69], seen in Fig. 3.1.

Although the physical dose contribution of these fragments appears small, their high LET (Fig. 3.2) and corresponding RBE can lead to severe biological damage in tissues adjacent to the tumor.

At larger depths of above 20 cm in water, the contribution of laterally scattered fragments from carbon ions increases, eventually making their lateral dose profiles comparable to proton irradiation. [15]

Therefore, careful consideration must be given to nuclear fragmentation, which generates a biologically potent fragmentation tail beyond the target and introduces lateral dose broadening at greater depths.

A technical challenge of heavy ion therapy is the acceleration process. Since heavy ions require higher kinetic energies, the synchrotrons magnetic fields must be reinforced, which imposes substantial **engineering and cost constraints**. [15] While light protons can also be accelerated in commercially available cyclotrons, one potential solution for more compact heavy ion synchrotrons could be the use of superconducting magnets, which can achieve higher magnetic fields and thus reduce the accelerator size needed for heavy ion therapy. [94]

3.3 Clinical Indications for High-LET Irradiation

The clinical value of heavy ion therapy is rooted in its superior physical dose conformity, enhanced RBE, low OER, and therefore the unique ability to treat challenging tumors. Despite the aforementioned limitation, the use of heavy ions remains clinically justified, particularly for **hypoxic or radio-resistant tumors**, for which there are no effective treatment alternatives. [24]

A key clinical advantage is the spatial variation in LET along the beam path. As shown in Fig. 3.2, heavy ions deliver a low-LET plateau in the entrance region, followed by a sharp LET increase at the BP. This ensures that normal tissue is exposed mainly to low LET, while the tumor receives harmful high-LET irradiation, maximizing tumor control and minimizing collateral damage.

Despite these benefits, there are important clinical limitations. The high precision and steep dose gradients can become a clinical dilemma if the **target moves** during treatment or **tissue inhomogeneities** change slightly, potentially shifting the BP. This can result in unintended Normal Tissue (NT) exposure. [15] This highlights the need for advanced motion management strategies in clinical applications of heavy-ion therapy. Currently, however, no particle therapy facility is tracking the internal tumor motion during irradiation to prevent intra-fractional movement. In contrast, such machines are available in the photon world; for example, the CyberKnife (Accuray, Sunnyvale, CA, USA). [11] Online-adaptive planning is under development for particle therapy [95], whereby treatment plans are adapted to daily tumor conditions to mitigate inter-fractional changes. In contrast, current clinical practice relies on motion mitigation rather than plan adaptation to prevent intra- and inter-fractional motion. [96]

Proton therapy remains the most widely established form of particle therapy, with established protocols and over 400 000 patients treated worldwide. [97] Protons are recommended by the American Society for Radiation Oncology (ASTRO) for tumor targets, where precise dose deposition is needed to spare critical structures or previously irradiated areas. [98] However, protons are not considered high-LET radiation, and their RBE is conservatively set to 1.1. [99]

Approaching higher mass ions: **helium ions** offer a compromise between dose precision and a smaller fragmentation tail compared to heavier carbon ions (Fig. 3.1). Early clinical trials at Lawrence Berkley Laboratories (LBL) showed low complication rates and favorable physical properties. [100] At Heidelberg Ion Beam Therapy Center (HIT), the clinical implementation started in 2021, with the first patients treated. [101, 102] Nevertheless, LET within the SOBP for helium typically remains below 40 keV/ μm .

To reach the wanted high LET in the target volume for the discussed clinical benefits, heavier ions, such as **carbon or oxygen**, are required. Therewith, LET values above 100 keV/ μm are achievable. [102]

To date, no clinical trials have investigated SOBP oxygen ions, but carbon ion therapy has been administered to about 63 000 patients worldwide. [97] Despite the absence of standardized treatment guidelines, the “4 Rs” of hadron therapy highlight the efficacy of carbon ions for rare, radioresistant, recurrent, and radiation-induced tumors. [103] High dose conformity enables hypofractionation and high-LET application without exceeding Organ At Risk (OAR) tolerance, which is especially important for radioresistant tumors. [104] A recent review from 2024 by Yun et al. reported improved toxicity profiles, local tumor control, overall survival, and prolonged progression-free survival with carbon ion in comparison to conventional therapies. [105] Particularly for head and neck tumors such as skull base chordoma, sacral chordoma, meningioma, and adenoid cystic carcinoma, there is substantial evidence for the high-LET therapeutic efficacy. [104]

Nevertheless, more randomized phase III clinical trials are needed to fully quantify the benefits of heavy-ion therapy and to determine the optimal particle type for specific clinical scenarios. [104]

3.3.1 A Case in Focus: Pancreatic Cancer

Pancreatic Ductal Adenocarcinoma (PDAC) is one of the few tumors fulfilling partially the “4R” criteria – being both rare and radioresistant – and exhibits the **lowest 5-year survival rate** among all cancer instances. It is frequently diagnosed at an advanced stage, often resulting in unresectable and bulky tumors. [106] Aside the late diagnosis, it presents considerable therapeutic challenges due to its anatomical location near **critical OAR** such as the Gastrointestinal Tract (GI) [107], its highly **hypoxic** microenvironment [108], and the **motion** of surrounding tissues [109], which can be seen in Fig. 3.8.

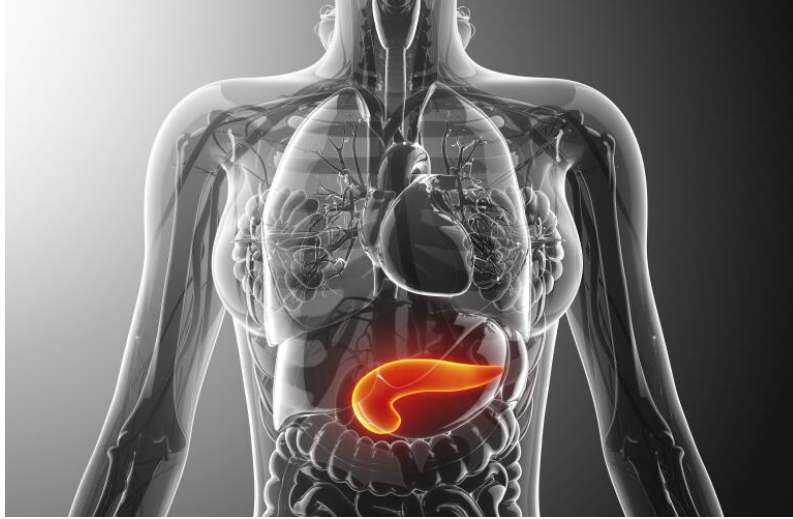


Figure 3.8.: Anatomical Location of the Pancreas: The pancreas, here marked in orange, is important for the digestive system by having both endocrine and exocrine functions. However, its delicate location within the bowl, adjacent to the highly radiosensitive GI, poses a challenge in the context of radiotherapy. Image from [110].

The unwanted exposure of the GI and the spinal cord constitutes a major limiting factor for the maximum dose that can be applied to the PDAC tumor. However, a dose escalation would be necessary to address its radioresistance. [109]

To deliver higher doses without exceeding NT tolerances, heavy ion radiation presents a promising alternative, offering superior dose conformity with enhanced OAR sparing, as well as reduced oxygen dependence due to the high LET, thereby mitigating PDAC radioresistance. [111]

Carbon-ion irradiation has already been studied for this purpose, and safer dose escalation while minimizing collateral damage to adjacent OAR has been demonstrated. [109] Indeed, several studies have suggested that carbon ions have been more efficient than photons in this setting, improving both local control and survival outcomes. [112, 113] A Japanese Phase I study reported a promising five-year survival rate of 42 %, which increased to 48 % in the high-dose arm of a subsequent Phase III trial. [113, 114] Additional encouraging outcomes have been published by the heavy ion facilities GUNMA, CHIBA, and HIT with the ongoing PACK trial. [109, 111, 115]

Interestingly, preclinical in vitro and in vivo experiments have shown that carbon ion irradiation could enhance immune activation in the pancreatic tumors, including increased antigen presentation compared to X-rays. [81] Together, these findings highlight the potential of high-LET radiation to overcome the intrinsic challenges of pancreatic cancer treatment and improve patient outcomes.

TRACING THE EFFECTS OF UHDR

In typical clinical particle therapy settings, the total prescribed dose is administered in several fractions. This allows the Normal Tissue (NT) to recover and repair sublethal damage in between the treatments, which are usually scheduled one day apart. Each fractionated dose of approximately 2 Gy is applied at dose rates ranging from 0.001 to 0.5 Gy/s. Interestingly, when high-dose, single-fraction treatments are delivered at dose rates exceeding 40 Gy/s, a regime commonly referred to as Ultra-High Dose Rate (UHDR), certain new biological effects are becoming apparent. [116]

4.1 Revival of the FLASH Effect

The earliest evidence of high-dose-rate-dependent radiobiological effects was reported in the late 1950s. In vitro experiments yielded enhanced cell survival following iso-dose irradiation at Ultra-High Dose Rate (UHDR) compared to Standard Dose Rate (SDR). [117] These preliminary experiments yielded the first evidences of the **in vitro UHDR sparing** effect. Notably, the sparing effect was more pronounced under lower oxygen concentrations, highlighting the important role of oxygen availability in modulating cellular responses in conjunction with UHDR. [117–119]

Following years of research in this field, in 1974 Weiss et al. [119] concluded:

“The effect must be regarded as unexplained requiring further investigation.”

Nonetheless, the research into the UHDR sparing effect remained largely dormant for nearly four decades.

In 2014, a study on UHDR irradiation was published with novel in vivo evidence: Lung tumor-bearing mouse models were irradiated with electrons at dose rates exceeding 40 Gy/s. The UHDR treatment achieved iso-effective tumor control in comparison to SDR irradiation. Yet, additionally, UHDR significantly enhanced NT preservation, as evidenced by a reduction in lung fibrosis, an improvement in the sparing of smooth muscle, and protection of epithelial cells from acute radiation-induced apoptosis. [120] The phenomenon of NT protection without compromising tumor control has since been widely termed the **FLASH effect**. [64, 121, 122] Over the next two decades, the majority of UHDR research has been conducted with low-Linear Energy Transfer (LET) irradiation, predominantly electron and proton, given the more straightforward technical implementation of delivering light particles at UHDR.

Until today, the superiority in NT sparing of UHDR over SDR at iso-doses has been demonstrated in Zebra Fish Embryos (ZFEs) and mice, where protective effects were observed in blood, intestinal, brain, and lung tissues, as well as in larger animals, including mini pigs, cats, and dogs. Detailed references in the reviews [28, 64, 122, 123] and a summary of the in vivo findings for different LET ranges and various in vivo models can be seen in Fig. 4.1.

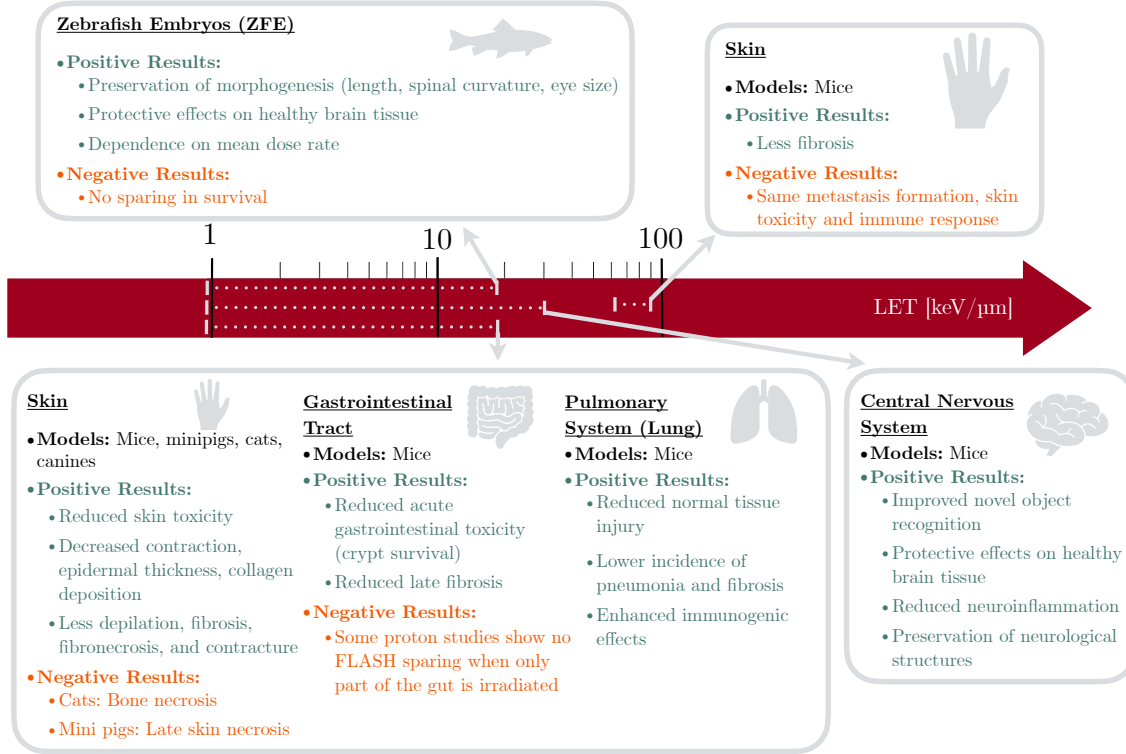


Figure 4.1.: Summary of In Vivo Results and the Corresponding LET Range: Positive and non-finding “negative” results are included. Information summarized from Review [123] with adding [124] for the ZFE, [125, 126] for the brain tissue, [127] for lung tissue and the high-LET study from [128].

These promising preclinical findings have paved the way for the first clinical applications of UHDR irradiation. In a case study, a 75-year-old male patient with treatment-resistant lymphoma received electron UHDR irradiation at a total dose of 15 Gy in 1 μ s. This treatment resulted in complete regression of the tumor. [129] The following FAST-01 non-randomized clinical trial investigated the use of transmission-proton¹ UHDR for palliative treatment of extremity bone metastases. Patients received a single fraction of 8 Gy at 60 Gy/s, achieving therapeutic efficacy comparable to conventional proton therapy. [130] A prospective FLAST-02 trial is now following up on this trial to assess the efficacy and safety of transmission proton FLASH for palliative bony metastases irradiation in the thorax. [131]

Despite promising in vivo findings and first clinical applications, the underlying mechanisms of the in vitro UHDR sparing and the in vivo FLASH effect remain largely unknown. In vitro results for low-LET irradiation have shown considerable variability. For electron irradiation, diverse cell lines have exhibited a UHDR sparing effect under varying oxygen concentrations, though no consistent trend has emerged. Proton irradiation under normoxic conditions has generally shown no UHDR sparing effect, while under oxygen-deprived conditions, few cell lines have been spared with UHDR irradiation. [132]

¹In transmission irradiation, the Bragg peak is not positioned within the target volume. Instead, the dose is delivered using the low-LET plateau region of the depth-dose distribution.

In 2023, Böhlen et al. stated that the data is highly heterogeneous, thereby preventing the formulation of broad conclusions at this stage [133], similar to Weiss et al. in 1974. [119]

4.2 Significance of the Temporal Beam Structure

To properly investigate the mechanisms behind dose rate effects, it is essential to identify their triggers. Various studies have shown that changes in the **temporal dose patterns** result in significant variations in outcomes. [134, 135] Consequently, a novel substantial degree of freedom must be considered: the temporal beam structure.

Complex treatment units, such as synchrotrons or pulsed dose applications, necessitate a detailed characterization of the beam time structure. Parameters such as pulse length, inter-pulse interval, and pulse repetition frequency essentially influence the effective dose rate at different temporal scales, demonstrated in Fig. 4.2. [136]

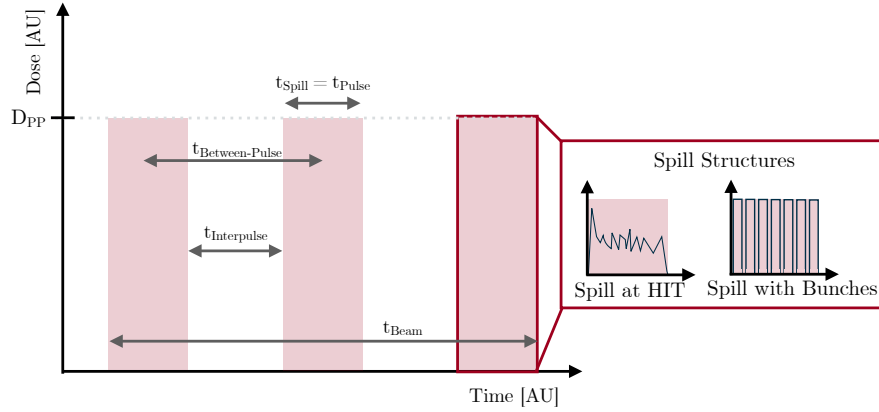


Figure 4.2.: Temporal Beam Structure Characterization: A schematic beam profile with pulsed dose application, so-called “spills”, is depicted. D_{PP} is the dose per pulse. The various spills are marked in red, with different types of spill structure shown at the bottom. At HIT, we have a continuous spill application in one pulse, whereas other accelerator machines produce bunched pulses, as indicated in the zoom plot on the right side. It is imperative to determine all the different time structures of the spill time t_{Spill} , the pause between spills $t_{Interpulse}$, the time between the midpoints of pulses $t_{Between-Pulses}$, and the total beam time t_{Beam} . Image inspired by [136].

With the various time structures and time spans emphasized in Fig. 4.2, different dose rate parameters can be determined: The most commonly used method is the **averaged Dose Rate** (\bar{D}), which involves dividing the total dose by the overall irradiation time. In Fig. 4.2, this corresponds to the total dose of $3 \cdot D_{PP}$ divided by t_{beam} . However, the \bar{D} is insufficient to fully describe complex beam structures [136], although some studies suggest that a high average dose rate is the main trigger for UHDR effects. [134, 135, 137] For pulsed dose applications, the **instantaneous Dose Rate** (\dot{D}_{inst}) should also be reported, which refers to the dose rate within a single pulse. [136] As illustrated in Fig. 4.2, the \dot{D}_{inst} would be a constant value of D_{PP}/t_{spill} for such a fixed-dose application, but would be more complex for spills like the one at Heidelberg Ion Beam Therapy Center (HIT) (Sec. 7.2.1). Depending on the overall dose pattern, these two dose rate measures can differ drastically.

The full temporal characterization is of special importance for Pencil Beam Scanning (PBS) systems, where the dose is delivered spot-by-spot in a sequential manner, potentially resulting in high intra-voxel dose rates despite a modest average dose rate.

Therefore, for PBS another measure – called the $\dot{D}_{5\%-95\%}$ – is suggested, which only considers the time during which 5 % and 95 % of the corresponding dose are applied in this time span. [138] Comprehensive reporting of all temporal parameters facilitates inter-institutional and inter-experimental comparisons, which are essential for identifying the critical temporal factors triggering UHDR effects.

4.3 Towards a Mechanistic Understanding

The causes of the sparing effects are currently the subject of intense discussion. While it is evident that the radiochemical cascade is altered under UHDR conditions, the exact pathways and qualitative and quantitative dependencies are still under investigation.

4.3.1 Oxygen Dynamics

Since the early investigations in the 1950s, the strong dependence of UHDR effects on the oxygen concentration has been well supported by both in vitro [117, 139, 140] and in vivo studies. [141, 142] Therefore, a leading hypothesis for the UHDR sparing effect concerns the oxygen dynamics: The **Oxygen Depletion Hypothesis (ODH)** states that during the brief pulse of dose, oxygen is rapidly consumed by radiochemical reactions, leading to a transient hypoxic state that reduces the radio-sensitivity. The oxygen consumption reaction also occurs during SDR, but for UHDR, the rate of oxygen consumption is thought to exceed the tissue’s capacity for reoxygenation via diffusion, leaving cells in a temporarily oxygen-deficient environment during the critical physical and chemical stages of damage induction. [9, 117, 143] The time scale for the reoxygenation process is approximately 10 ms in monolayer cell cultures. [139] In vivo, additional oxygen delivery delays are introduced by the oxygen unloading from hemoglobin and the diffusion from distant vasculature, which occur on a timescale of around 50 ms [55] and in the seconds-range [141], respectively. Therefore, at SDR (approx. 0.1 Gy/s), the application of dose matches the range of reoxygenation processes, so the oxygen consumption can be compensated. Consequently, the oxygen consumption was only measured during UHDR irradiation and not during SDR due to the reoxygenation compensation. [55, 144, 145] However, this hypothesis was already challenged in [143] when Berry et al. reported sparing with 7 ns pulses but not after 50 ns. Given that reoxygenation occurs on the microsecond timescale, ODH alone could not account for these single study findings. [143] In addition to this, the impact of oxygen consumption on the UHDR effects remains a **subject of active debate**, for two main reasons:

Firstly, several studies have demonstrated that UHDR irradiation consumes lower quantities of oxygen than SDR. [57, 67, 144, 146] This phenomenon could be attributed to the increased local density of reactive species, which reduces the likelihood of interactions with molecular oxygen, thereby lowering net oxygen consumption. [57, 147] Although UHDR irradiation consumes slightly less oxygen quantitatively, the reoxygenation process timescale stays unaltered, and the transient oxygen-deprived state may still persist.

Secondly, it has been argued that the absolute amount of oxygen consumed may be insufficient to cause meaningful hypoxia and therefore radioresistant. [146] However, even small reductions in oxygen tension can substantially impact radiosensitivity [148], indicating that complete depletion to hypoxia might not be necessary to observe biological effects. At this point, the initial oxygen concentration of the cells is the important parameter. [55] In many tumors, a median oxygen concentration ranges from 0.3 % to 4.3 %. [149]

Following the ODH, hypoxic tumors would show limited FLASH sparing because their oxygen levels are already minimal, whereas NT in a physioxic state may experience increased radioresistance due to further transient oxygen consumption. [150] Especially the typically high total doses used in UHDR regimens may further enhance the overall oxygen consumption, which would support the ODH. [140]

However, the extent to which oxygen consumption can induce the necessary change in oxygen concentration to induce radioresistance in tissue remains a subject of debate. A recent comprehensive study from Grilj et al. reported actual oxygen consumption values in vivo and concluded that the measured consumption via ODH could not fully explain the detected in vivo FLASH sparing effect, which was quantified by novel object recognition. [145] However, predictions based on FLASH data have yielded support for the ODH in vivo. [141, 151]

To investigate the mechanisms behind the ODH and to elucidate its predictive value for the FLASH effect, oxygen consumption studies with model solutions were conducted. [57, 67, 144, 146] It is important to acknowledge that extrapolating results from model solutions to cellular environments and especially complex biological species is non-trivial. Intracellular factors such as radical scavengers, metabolic pathways, and blood vessel architecture are not included in model solution studies but strongly influence oxygen availability. [61]

Based on these results, it remains uncertain whether the ODH can fully or partially account for the observed UHDR effects. Nevertheless, in vivo observations and Monte Carlo Simulation (MC) simulations support a potential role of the ODH in UHDR effects [140, 141, 151], although contradictory findings have also been reported. [145, 146]

These discrepancies have led to the proposal and ongoing investigations of an additional mechanism involving radical-radical interactions.

4.3.2 Radical-Radical Interactions

UHDR irradiation not only alters the oxygen consumption, but also has a drastic impact on the entire radiochemical cascade. For a given absorbed dose, the total number of ionization events is on average the same between UHDR and SDR irradiation. However, during UHDR, these events occur over a much shorter time span, resulting in markedly higher instantaneous radical concentrations. [54]

The reaction rate of radicals is directly proportional to radical concentration, whereas radical-radical recombination scales with the square of the radical concentration. [54] Consequently, the closer spatio-temporal proximity of radicals leads to an **acceleration in radical-radical recombination**, resulting in self-scavenging, and fewer interactions with surrounding molecules. This results in different steady-state levels of radiolytic Reactive Oxygen Species (ROS) even when irradiated at iso-doses for both dose rates. [55, 143] A lower radical yield correlates with reduced biological damage, offering a complementary explanation for the UHDR sparing effect. [143]

While high LET primarily amplifies intra-track reactions, where species from a single track interact, UHDR conditions favor **inter-track interactions**. At UHDR, multiple primary tracks are generated within a short time frame, allowing their radiolysis products to interact with one another. The occurrence and impact of these inter-track reactions are still under debate and not yet fully quantified. Some MC studies have suggested that inter-track interactions can occur under specific conditions, such as high doses and low LET. [152, 153]

Especially in the context of low-LET electron irradiation, the spatial overlap of track structures may serve as a catalyst for the enhancement of radical-radical recombination events [154] and also for PBS systems where single spots are irradiated. [155] Other MC studies have indicated that the distance between the tracks is insufficient for the interaction of radicals [72, 156, 157] and therefore inter-track interactions can be neglected, especially for high LET. [54, 72] This decreased fluency for high LET is shown in Fig. 3.6.

However, investigations of radio-chemical interactions with **modelling approaches** like MCs are confined to simulating a pure water environment and single-track simulations, thereby constraining our theoretical comprehension. [73] Additionally, experimental investigation of these processes is challenging due to the extremely short lifetimes of some radicals involved. For this reason, more stable species, such as H_2O_2 , and residual oxygen can serve as surrogates to estimate radical production and elucidate radiochemical mechanisms behind the UHDR effects. For H_2O_2 specifically, it has been reported that the production decreases slightly under UHDR conditions, which could hint at a potential sparing mechanism. [55, 158]

Amplified radical-radical interactions and altered radiochemical pathways pose a major challenge to the cell [55], highlighting the need for further research to understand and quantitatively assess radical production and interactions under UHDR conditions.

4.3.3 Biological Factors

Moving from radiochemical considerations to Desoxyribonucleic Acid (DNA) damage, several studies have reported lower levels of cellular markers of DNA **Double-Strand Breaks (DSBs)**, such as 53BP1 [159] and γH2AX foci [160, 161], following UHDR irradiation. This corresponds to reduced DNA damage [162, 163], fewer dicentric and centric rings [164], and a lower incidence of micronuclei. [165] The reduction in complex chromosomal aberrations may be attributed to a lower number of DNA-damaging radicals, due to enhanced radical-radical scavenging under UHDR conditions.

Interestingly, the UHDR sparing effect has been observed in vitro for both certain normal and tumor cell lines. [162, 166]

A general overview of the in vitro data is provided by Friedl et al. [64] and Adrian et al. [132].

However, the capacity to manage, detoxify, and eliminate ROS is cell-specific. [167, 168] Normal cells have a superior **enzymatic capacity** to reduce hydrogen peroxide H_2O_2 [167, 168], allowing them to efficiently eliminate this ROS. [55, 122] Additionally, the repair mechanisms are intact, and thus, the cell can repair some of the DNA damage induced by radicals. In contrast, tumor cells often lack sufficient repair mechanisms and antioxidant defenses to remove harmful chemical products. As a result, they are more vulnerable to cytotoxic products and the broad spectrum of radicals. [55, 169] This redox stress is further compounded by the fact that tumor cells frequently exhibit a more hypoxic microenvironment, which further modulates their redox and metabolic status. [54]

Therefore, the **differential response of NT and Tumor Tissue (TT)** to UHDR and the FLASH effect may additionally be amplified due to the cell-type dependent biochemical and physiological microenvironment differences.

Moving from in vitro to in vivo systems, so from the UHDR sparing effect to the FLASH effect, the additional involvement of the **immune system** reactions must be regarded.

Radiation-induced immune activation and inflammation can differ depending on the type and extent of cellular damage. [122] The importance of this was shown when there was no UHDR effect, neither in survival nor in acute side effects for immunocompetent rats. [170] However, it was also reported that there was a decrease in T-cell infiltration after UHDR irradiation [171] and less inflammation in mice after proton FLASH. [125]

One other factor for UHDR irradiation might be that lymphocytes are more effectively spared due to the shorter overall irradiation time. [150]

These findings underscore the complexity of biological responses to UHDR irradiation, which involves DNA repair processes, immune modulation, and tissue-specific susceptibility, and therefore highlight the need for further research to elucidate their contributions to UHDR effects.

4.4 Advantages Beyond the Sparing Effects

In addition to the potential, though still not fully understood, biological advantages of UHDR irradiation, there are practical benefits related to the accelerated treatment delivery. The extremely short treatment time frame reduces the possibility of patient motion during irradiation, called **intra-fractional movements**.

The patient's position is typically verified at the start of each treatment session using an imaging technique. However, the internal tumor motion is mostly not monitored in real-time during dose delivery. As a result, unrecognized tumor movement, especially in anatomically mobile regions like the abdomen, may occur. When the interval between imaging and irradiation ending is minimized, the tumor is more likely to remain in the imaged position. This reduction in intra-fraction motion could ultimately allow for smaller treatment margins, thereby improving targeting precision and potentially reducing radiation exposure to surrounding healthy tissue. [150, 172]

COMBINING THE POTENTIAL OF HEAVY ION & UHDR IRRADIATION

Building on the previous chapters, both high Linear Energy Transfer (LET) and Ultra-High Dose Rate (UHDR) independently provide substantial advantages. Heavy ion irradiation has demonstrated great potential in the treatment of highly hypoxic radioresistant tumors, and UHDR has been shown to mitigate intrafractional motion problems and to potentially offer additional normal tissue sparing in vivo. The combination of these elements into a “*fast and furious*” modality would be the logical step.

5.1 State of the Art: Particle UHDR Irradiation

Due to technical difficulties and the limited number of heavy ion centers, most of the UHDR studies were conducted with **low-LET** photons, electrons, or proton irradiation. With particle irradiation, the FLASH effect has been demonstrated several times for protons, for example, in the neuroprotective effects and reduced Double-Strand Breaks (DSB) after UHDR in mice with brain tumors. [125] Even the first clinical trial, FAST-01, was conducted with proton transmission irradiation. [130] However, as the review from Diffenderfer et al. showed, the in vitro UHDR sparing effect is not reproducible for proton experiments, and multiple studies have shown only a little or even no difference in tumor growth delay compared to Standard Dose Rate (SDR). [166]

For **high-LET** irradiation, available studies are limited for both in vitro and in vivo. In the case of in vitro studies, one single study from Heidelberg Ion Beam Therapy Center (HIT) reported UHDR sparing after Spread-Out Bragg Peak (SOBP) helium ion irradiation in tumor cells under both hypoxic conditions for LET values up to 16 keV/μm. [161] Going higher in mass to carbon ions, Tinganelli et al. reported an UHDR sparing effect in Chinese hamster ovary cells irradiated under hypoxia. Although the LET in the transmission carbon beam was relatively low at 13 keV/μm. [173] In contrast, studies employing higher LETs up to 50 keV/μm have not demonstrated a consistent sparing effect across various cell lines, including both tumor and normal tissue cells, for the investigated dose region. [174–176] In instances in which an in vitro sparing effect was observed, it was exclusively at doses of above 7 Gy, which is typically beyond the range of clinical treatment doses. [173, 176]

The first **high-LET in vivo** studies by Tinganelli et al. with up to $80 \text{ keV}/\mu\text{m}$ reported a FLASH sparing in reduced fibrosis and collagen production after UHDR irradiation of the hind limbs, yet no difference in tumor control, lung metastasis formation, and immune response. [128] For their low-LET carbon ion study, they found a significant difference in UHDR and SDR in the metastasis formation. [127]

Overall, the current literature on proton in vitro studies investigating the FLASH effect remains highly variable, and for high-LET irradiation is limited to a single study with an LET of $80 \text{ keV}/\mu\text{m}$. Preliminary evidences suggest that LET may play an important role in modulating the FLASH response; however, its possible advantages remain to be elucidated. This underscores the urgent need for more systematic and mechanistic research in this field. [64]

5.2 From Standard to UHDR at HIT

At HIT, we have the unique opportunity to investigate this largely uncharted research field. In order to facilitate UHDR irradiation, a large amount of particles is needed, since the full dose must be administered in a single spill, and the particles must be extracted rapidly in order to achieve target dose rates of around 100 Gy/s .¹

5.2.1 Hardware Adaptations

To achieve a high particle number, the maximum number of particles is extracted from the Electron Cyclotron Resonance Ion Source (ECRIS) and accelerated with minimal losses, which is also possible with conventional settings. Subsequently, for UHDR irradiations, the beam current is increased by a factor of approximately 100 compared to clinical SDR. [41]

Light ions, such as ^1H and ^4He , are accelerated for UHDR using standard beam optics, whereas, heavier ions like ^{12}C and ^{16}O require adapted beamline settings. Three main aspects of the **acceleration process** are modified to meet UHDR requirements: First, the synchrotron extraction tune is shifted closer to the third-order resonance via the quadrupole magnets. Secondly, the sextupole magnets are strengthened, and lastly, the RF-knockout exciter amplitude is increased to facilitate a faster particle extraction. [41] These parameters are optimized by the accelerator team for specific particle energies and must be reloaded individually for each experiment. The settings used in this research are summarized in Table 5.1.

Particle	Extraction Energy [MeV/u]	FWHM [mm]	Ripple Filter	Spot Spacing [mm]
^1H	146.56	11.4	-	3
^4He	145.74	6.8	3 mm	2
^{12}C	275.98	4.1	3 mm	1.5
^{16}O	325.98	3.3	3 mm	1.5

Table 5.1.: UHDR Settings at HIT: The beam focus width is given as Full Width Half Maximum (FWHM) and the type of ripple filter (Ripple Filter (RiFi)) used for each particle species is listed. These settings were employed in the present work.

¹Although certain studies have previously investigated UHDR effects at dose rates already above 40 [120], our approach was to amplify the UHDR mechanisms by applying the highest possible dose rates.

To maintain functional raster scanning and an effective intensity feedback loop, the processing time of approximately 1 ms per spot must be exceeded, which is the case even for UHDR and the Beam Application Monitoring System (BAMS) must be capable of accurately recording the high particle flux of the UHDR beam. [41] To avoid detector saturation, the monitoring BAMS Ionization Chamber (IC) is flushed with a gas mixture of 96 % **helium** and 4 % CO_2 instead of the standard argon- CO_2 mixture. Helium's lower density and faster drift times reduce the risk of detector saturation under high particle flux conditions, making it more suitable for accurate measurements in UHDR scenarios. [42] With these BAMS adaptations the UHDR spills can be recorded (Fig. 5.1).

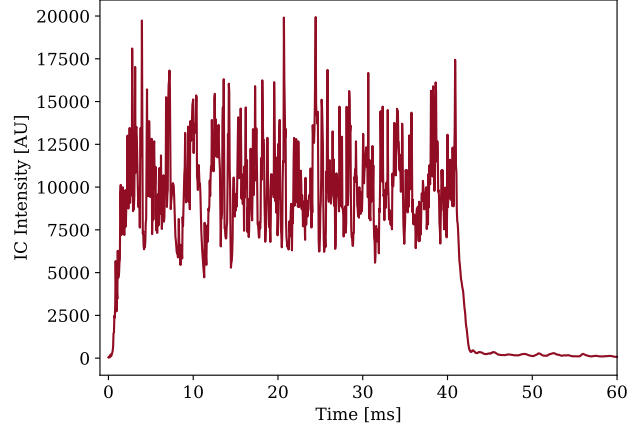


Figure 5.1.: Carbon-Ion UHDR Spill at HIT Recorded by the BAMS.

Typically, energy layer switching is required to cover the target volume longitudinally (Sec. 2.1.3). However, this process necessitates a new accelerator cycle, therefore a second spill, which normally requires 5 s. Research at HIT has demonstrated the feasibility of multi-energy extraction. However, this approach may also be constrained by particle number limitations and thus might not permit irradiation of the entire target volume at UHDR conditions. [177]

Currently **2D Range Modulators (2DRMs)** are used to passively create a SOBP and achieve in-depth coverage of the target (Fig. 5.2).

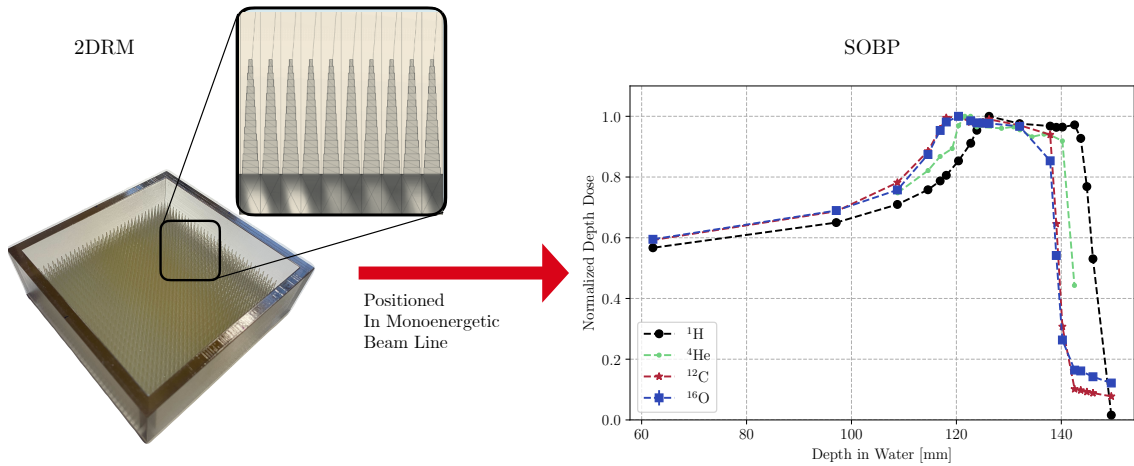


Figure 5.2.: 2DRM Example and SOBP: The picture of the hedgehog 2DRM and its zoomed-in structure was kindly provided by Sae Hyun Ahn. The SOBP on the right side was produced by another 2DRM and recorded with a PinPoint chamber for the given beam parameter from Tab. 5.1. The measurements are detailed in Sec. 6.2. [67]

The current technical limit of the extraction rate and thus the intensity at UHDR is determined by the maximum amplitude of the RF-knockout exciter. [41]

5.2.2 Irradiation Plan Adjustments

The available number of parties per spill limited the maximum field sizes depending on the required dose. With the active Pencil Beam Scanning (PBS), the **field sizes** to achieve 15 Gy were relatively small with below 1.5 cm length² (see Sec. 6.2 [67]). Continuous improvements of the UHDR settings by the accelerator team enlarge the achievable field sizes over time.

The **spot spacing** (Tab. 5.1) is selected to provide homogeneous field coverage while maximizing the distance between the spots, therefore simultaneously maximizing the field size. As explained, the field is irradiated with a monoenergetic beam and is covered with the usual active PBS, which can be seen in Fig. 5.3.

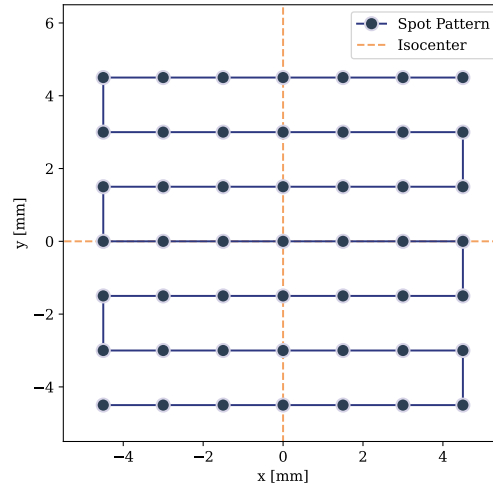


Figure 5.3.: Exemplary PBS Spot Pattern: The spot spacing of 1.5 mm is applied for heavy ion UHDR dose application (Tab. 5.1). This specific plan with a dose of 15 Gy was used in the investigation of the oxygen consumption in Sec. 6.2.

5.3 Assuring the Correct Dose

Accurate dose determination is a fundamental aspect of radiotherapy, typically ensured through established quality assurance protocols. However, due to the high ionization density of this combined high-LET and UHDR irradiation, conventional dosimeters often encounter major challenges. Therefore, the selection of appropriate detectors is crucial for precise dose measurements in this context. Additionally, accurate dose calculations are essential for Treatment Planning Systems (TPSS) and quality assurance, a context in which MC simulations are utilized.

²The field size was measured from the first to the last spot (see Fig. 5.3). It should be noted that this measurement does not take into account the FWHM of the beams in order to report a particle-independent measure.

5.3.1 Detectors for High LET and UHDR Dosimetry

High-LET ion beams at UHDR present major challenges for conventional dosimeters, due to the densely ionizing tracks and the additional need for high temporal and spatial resolution for precise characterization of the beam structure, as discussed in Sec. 4.2. Accurate dosimetry in this context requires precise dosimeters [178], additionally applicable in small field scenarios given field limitations, and sufficient radiation hardness to withstand the high doses and dose rates.

Currently, **no primary standard protocol** exists specifically for heavy ion dosimetry. In general, water calorimetry is recommended as a primary standard for absolute dose measurements [179], and the clinical reference dosimetry relies on calibrated IC. [180]

Table 5.2 summarizes currently available detectors and categorizes them according to their potential to provide reliable readout for high-LET and UHDR dosimetry, based on reported time resolution and performance characteristics under these conditions.

Detector	Temporal Information	High LET Independence	UHDR Independence
<i>Passive Detectors</i>			
Alanine			
Fricke Gel			
OSLD			
Radiochromic Film			
TLD			
<i>Active Detectors</i>			
Calorimeter			
Diamonds			
IC			
Scintillator			
Si-Diodes			

Table 5.2.: Detector Performance Comparison: Evaluation is based on temporal resolution, high-LET suitability, and UHDR capability: Cell background colors denote performance status: **Green** for confirmed suitability, **red** for insufficient or non-viable performance, and **yellow** for technologies under active research and development to address current limitations. Information summarized from [179, 181, 182].

All **Passive detectors**, like alanine pellets, gels, stimulated luminescence detectors (OSLD), films, and thermoluminescent detectors (TLD) are unsuitable for UHDR studies, because they are unable to provide the temporal information of the beam, which is why they are marked with a red cell in Tab. 5.2. [136, 181]

The primary standard **calorimeters** provide direct dose-to-water measurement by measuring directly the temperature change induced by the ionizing radiation in a water phantom. [182] However, their complex setup renders them impractical for experiments, and the millisecond-scale temporal resolution is insufficient for sub-millisecond UHDR beam characterization. [181] There are current investigations to make a small portable graphite calorimeter suitable for UHDR and high-LET absolute dosimetry. The first proof-of-principle test was conducted with a laser-driven proton irradiation, but these detectors are not yet clinically established. [182]

In **scintillators**, light is emitted upon dose deposition, therewith the resulting signal is proportional to the absorbed dose. However, under high-LET and UHDR, scintillators suffer from Cherenkov contamination in the optical fibers [183] and quenching. The local energy deposition is sufficient to cause excited molecules to interact with each other, thereby promoting non-

radiative de-excitation and reducing their accuracy. [184, 185] Since scintillator materials are tissue-equivalent and therefore are particularly well-suited for clinical applications that require accurate dose determination in tissue, ongoing research aims to mitigate these effects. [181]

Regarding Tab. 5.2, aside from temperature-based calorimeters, detectors with charge-based readout are currently viable for high-LET dosimetry. However, the charge readout can exhibit firstly initial recombination, where ion-electron pairs neutralize each other in dense tracks, inducing LET-dependence, and secondly volume recombination, which describes recombination during charge drift from different origins, resulting in a dose rate-dependence. [42, 155]

Gas-filled **ICs** are recommended for high-LET dosimetry [179], with plane-parallel chambers used for large fields and thimble or small cylindrical chambers for small fields. [180] At HIT, the PinPoint Ion Chamber (PTW Freiburg GmbH, Type:31015) [186] is used in experiments for absolute dose measurements without receiving temporal information. However, in normal ICs, UHDR conditions can cause significant ion recombination [179, 187] and polarity effects. [188] Mitigation strategies include the use of alternative gases [42] and thin-gap designs [189] to decrease the readout time or correction models. [190] However, the ICs limited spatial in the millimeter-range and temporal μ s-resolution makes them suboptimal for UHDR beam structure analysis. [181]

Therefore, **semiconductor** detectors are promising for combined high-LET and UHDR dosimetry. Due to their higher-density solid-state material, they can be manufactured in a compact size to achieve high spatial resolution. Additionally, they can provide a high temporal resolution and radiation hardness. [45, 181] Conventional **Silicon (Si) diodes**, however, have been shown to be energy-dependent and inaccurate at high LET. [191] Novel Silicon-Carbide (SiC) detectors are under development to overcome these limitations, but are not yet established. [182, 192]

Diamond as semiconductor material combines several advantages: The wide bandgap of 5.45 eV leads to reduced leakage current compared to Si-diodes with a 1.14 eV band gap. [45] The material shows excellent radiation hardness, and with its atomic number of $Z = 6$, the material is closer to tissue equivalence compared to silicon ($Z = 14$). Additionally, the high charge carrier mobility enables a fast readout and thus a high temporal resolution. [193, 194] Such diamond detectors are already commercially available. PTW manufacture the microDiamond (mD)[195], which was recently refined into the flashDiamond (fD)[196] to overcome UHDR saturation effects.

A comprehensive summary about the detectors is provided in Marinelli et al. [197] and in Sec. 6.1. In short, the fD enhancements were achieved by reducing the sensitive area to limit detection current and increasing boron doping concentration to reduce series resistance. [198] Therewith, the reliability of the fD in UHDR conditions with electrons [199] and helium [200] has already been demonstrated. Diamond detectors currently represent a promising solution for high-LET and UHDR dosimetry, combining robustness, high spatial and temporal resolution, and clinical applicability.

5.3.2 Monte Carlo Simulation for high LET

In addition to accurate dose measurements, Depth Dose Distribution (DDD) predictions are also essential for clinical radiotherapy for the TPS and Quality Assurance (QA). Initially, dose distributions were computed using analytical transport equations. This approach is adequate for photons and light particles. However, for heavy ions, the more complex interaction schemes necessitate the use of more accurate predictive models. Nowadays, with advancements in computational hardware and algorithms, Monte Carlo Simulations (MCs) have become the **gold standard**,

especially for heavy-ion irradiations because of their accuracy. [43] In a MC, the particle transport is modeled by simulating the physical interactions of individual particles with matter based on probabilistic sampling. [201]

A primary particle with defined energy is launched into a medium, typically a patient-specific geometry derived from Computer Tomography (CT) voxel data. As the particle traverses the medium, firstly, the step length until the next interaction point is probabilistically sampled based on the given interaction probabilities. Then the type of interaction (Sec. 2.2) is sampled based on pre-tabulated cross sections.

The outcomes (e.g., energy loss, scattering angles, secondary particle production) are determined from cross-section data, either experimentally measured or derived from first principles. The secondary particles generated are tracked until they fall below a predefined energy threshold.

During this tracking process, several quantities, like the energy deposition and stopping power, can be recorded per voxel, enabling the construction of detailed DDD and LET maps of the given geometry. This process is repeated for each particle history until all primary and secondary particle transports are complete.

Since MCs rely on statistical methods, achieving low uncertainty requires simulating a large number of events. Advances in computational power have made MC methods feasible for routine clinical applications, including treatment planning, detector response modeling, commissioning support, and dose verification. [202]

The **accuracy** of MCs depends on the implemented physics models and available cross-section data. Although MCs offer high precision calculations for known interactions in benchmarked regions, several challenges remain, especially for hadronic interactions relevant in heavy-ion particle therapy. [24, 201] While electromagnetic interaction models are well described, hadronic physics models are still incomplete, under development, and subject to higher variability. [203, 204] The implemented nuclear-interaction cross sections carry significant uncertainties, since experimental data for clinically relevant energies and projectiles is sparse. [204]

Detailed cross-section measurements are essential not only for optimizing the MC itself but also for benchmarking the hadronic models, which is vital for validating MCs. [24, 201]

Despite these limitations, MCs remain indispensable in heavy ion radiotherapy for precise dose predictions.

Several MC packages go beyond modeling the physical stage, and also predict the complex kinetics of **radiolysis**, including species diffusion and reactions along the particle tracks. TRAX-CHEM[73] or Geant4-DNA[205] extend the physical stage of MC to the chemical stage. Therewith, the production of chemical species, their interactions, and their diffusion with time (Fig. 5.4). [73]

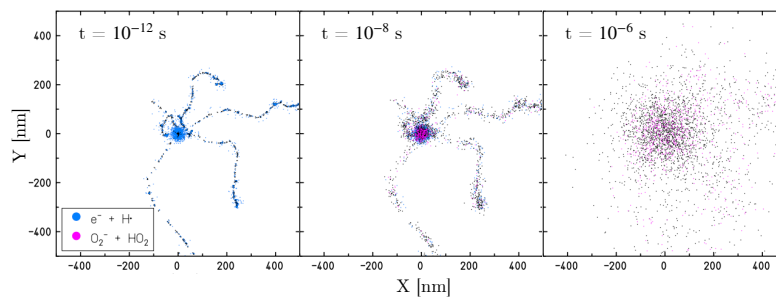


Figure 5.4.: Chemical Track MC: The temporal evolution of several radiolysis species in normoxic water after a 10 MeV carbon ion traverses the material, simulated using the TRAX-CHEM code. Image from Boscolo et al. [147]

These simulations can provide insights into the molecular mechanisms underlying radiation damage, such as DSB and oxidative stress, which are essential for evaluating the biological effectiveness of different radiation modalities. Therefore, the simulations must be benchmarked against experimental data with radiation-induced chemical yields to validate the accuracy of the models. [205] More radiochemical data sets are required to improve and extend the capabilities of radiochemical MCs.

Currently, these simulations are limited to a pure water environment and to single-track consideration, which limits their applicability for high-LET UHDR due to the amplified intra- and inter-track interactions. [62, 73] Therefore, these results must be interpreted with caution.

5.4 Rationale for Pancreatic Cancer as Target

As explained in Section 3.3.1, the rationale behind classifying Pancreatic Ductal Adenocarcinoma (PDAC) as a potentially effective target for high-LET irradiation is its hypoxic microenvironment and its intrinsic radioresistance. [108]

In Chapter 4, the potential Normal Tissue (NT) sparing effect of UHDR irradiation is discussed, along with the general advantages of UHDR for treating moving targets. Given the anatomical location of the pancreas situated near the highly mobile Gastrointestinal Tract (GI) tract, below the lungs, and within the general dynamic abdominal region (Fig. 3.8), a rapid dose delivery would be particularly advantageous to mitigate intra-fractional changes. The addition of a FLASH sparing effect could provide even greater benefits.

These considerations suggest a beneficial synergy between high-LET and UHDR irradiation, making their combined application especially compelling for PDAC.

BOTTOM UP APPROACH: FROM SETUP TO FIRST EXPERIMENTS

The aim of this thesis was to systematically explore the integration of Ultra-High Dose Rate (UHDR) delivery with high-Linear Energy Transfer (LET) particles at the Heidelberg Ion Beam Therapy Center (HIT), with a particular focus on pancreatic cancer treatment applications. The research pursued three primary objectives: (1) establishing and validating the technical feasibility of this novel combined modality in the form of a dosimetric investigation, (2) examining the underlying mechanisms, and (3) evaluating potential therapeutic directions.

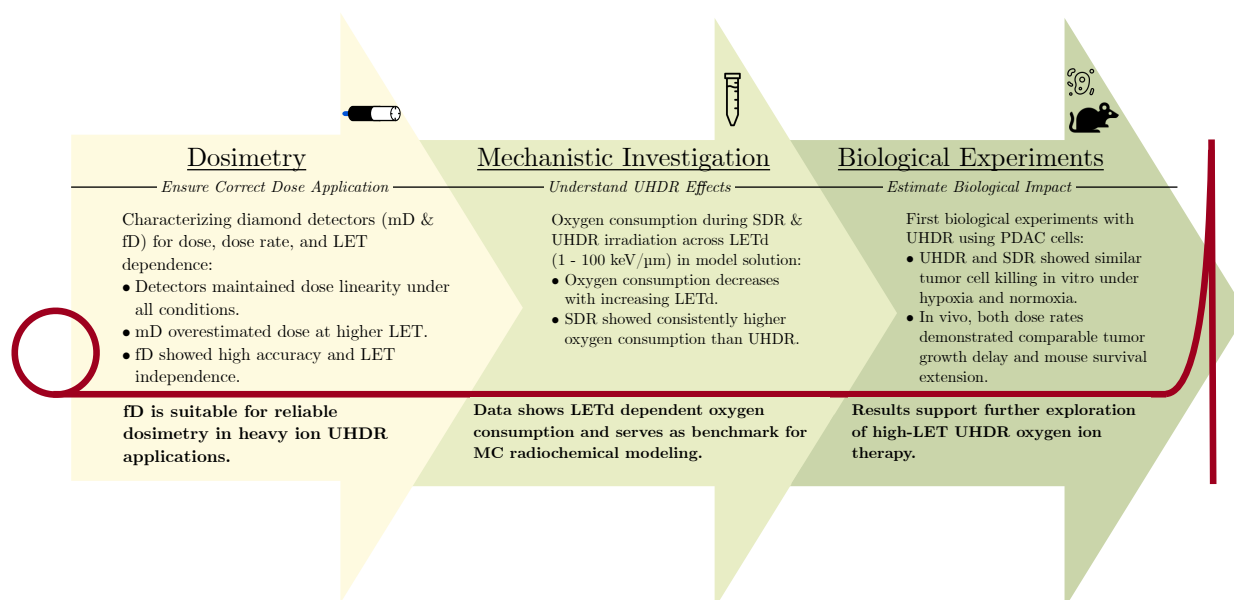


Figure 6.1.: Structure of This Research Project.

The starting point was therefore to verify the dosimetry for high-LET UHDR irradiation, as conventional detectors often exhibit limitations due to saturation and recombination effects (Sec. 5.3.1). Building upon previous results for lower-LET helium ions by Tessonnier et al. [200], diamond detectors emerged as promising candidates for this challenging dosimetric environment.

Consequently, these detectors were used in the study:

Celine Karle, Gianluca Verona-Rinati, Stephan Brons, Rainer Cee, Stefan Scheloske, Christian Schömers, Rafael Kranzer, Thomas Haberer, Marco Marinelli, Andrea Mairani, Thomas Tessonier. **“Characterizing diamond detectors for various dose and dose rate measurements in scanned carbon and oxygen beams”**. *Medical Physics* (2025); DOI: <https://doi.org/10.1002/mp.17893>. [206]

One microDiamond (mD) [195] detector from PTW Freiburg and a flashDiamond (fD) prototype were tested for their dose, dose rate, and dose-averaged LET (LET_d) dependencies in carbon and oxygen ion beams. Their performance was benchmarked against a standard Ionization Chamber (IC) (Advanced Markus Chamber (AMC) [180]) and Monte Carlo Simulations (MCs). The evaluation included the complete assessment of the Depth Dose Distribution (DDD) under Standard Dose Rate (SDR) irradiation with mD, fD, and for comparison, the AMC as well as targeted Bragg Peak (BP) measurements under UHDR conditions with the diamond detectors alone. Lastly, dose linearity was systematically investigated through dose escalation measurements across both particle types irradiated with both dose rates. The corresponding setup exemplary with the mD is shown in Fig. 6.2.

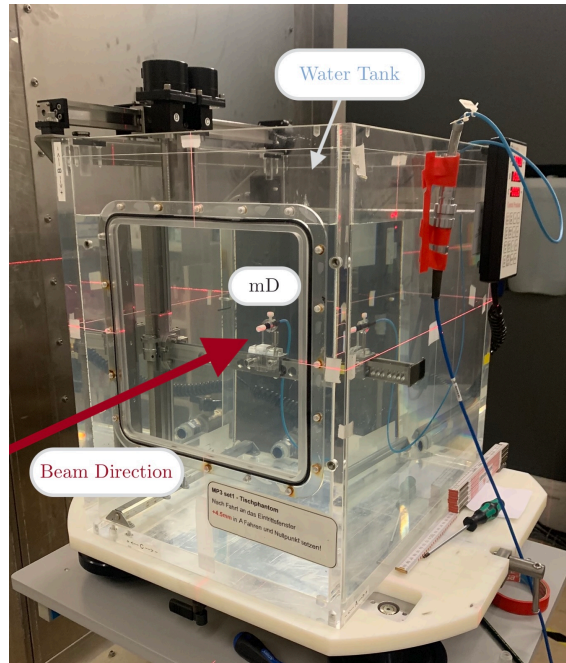


Figure 6.2.: Experimental Setup for Dosimetric Validation of the Diamond Detectors: Here, the microDiamond (mD) detector is mounted in the motorized water tank.

The experimental results revealed concordance between both diamond detectors and the simulated DDD for oxygen and carbon irradiations. However, the mD showed a small systematic dose overestimation that increased with LET_d under SDR conditions for both particle types. The overestimation remained $\approx 5\%$ under UHDR conditions. However, increased uncertainties under UHDR could mask any trends. The fD demonstrated superior performance with discrepancies below 5% across all modalities in both plateau and BP regions. In the BP fall-off, both detectors exhibited an expected increase in deviations compared to MC simulations, while they maintained a strong correlation with AMC measurements. The mD and fD demonstrated excellent dose linearity across all investigated conditions, varying dose rate and LET_d.

In conclusion, both detectors maintained dose-rate independence under heavy-ion irradiation within the investigated dose ranges. The key difference emerged in their LET response: while the mD showed a slight LETd-dependent overestimation, the fD maintained consistent accuracy independent of LETd. These characteristics establish the fD as the preferred dosimetric tool for UHDR heavy ion experiments. This dosimetric validation, coupled with the demonstration of reliable UHDR heavy ion beam delivery at HIT, established the technical foundation for the following mechanistic and biological experiments.

Subsequently, we examined the mechanistic aspects of UHDR heavy ion irradiation, with particular focus on radiolytic oxygen consumption. Despite ongoing scientific debate about the quantitative impact of the oxygen consumption in the context of the Oxygen Depletion Hypothesis (ODH), these parameters are hypothesized to be central to the UHDR sparing effect and FLASH phenomenon (Sec. 4.3). However, the quantification of the oxygen consumption rates in representative model solutions with dependence on radiation quality was limited in the literature (Sec. 5.3.2).

In the following study, we addressed this data gap [67]:

Celine Karle, Hans Liew, Thomas Tessonier, Stewart Mein, Kristoffer Petersson, Christian Schömers, Stefan Scheloske, Stephan Brons, Rainer Cee, Gerald Major, Thomas Haberer, Amir Abdollahi, Jürgen Debus, Ivana Dokic, Andrea Mairani. **“Oxygen consumption measurements at ultra-high dose rate over a wide LET range”.** *Medical Physics* (2024); DOI: <https://doi.org/10.1002/mp.17496>. [67]

The experimental setup utilized a Bovine Serum Albumin (BSA) 5% solution as a surrogate for the extracellular environment. The sealed BSA samples were exposed to 15 Gy delivered by various particles (electrons, protons, helium, carbon, and oxygen ions) spanning LETd values from 1 keV/ μm to 100.3 keV/ μm . Irradiations were performed at SDR (0.3 Gy/s - 0.4 Gy/s) and UHDR (approximately 100 Gy/s), during which the oxygen concentration was monitored using the OxyLiteTM system (Oxford Optronics), which can be seen in Fig. 6.3. Using these measurements, the oxygen consumption rates were calculated, fitted, and compared across particle types and dose rates.

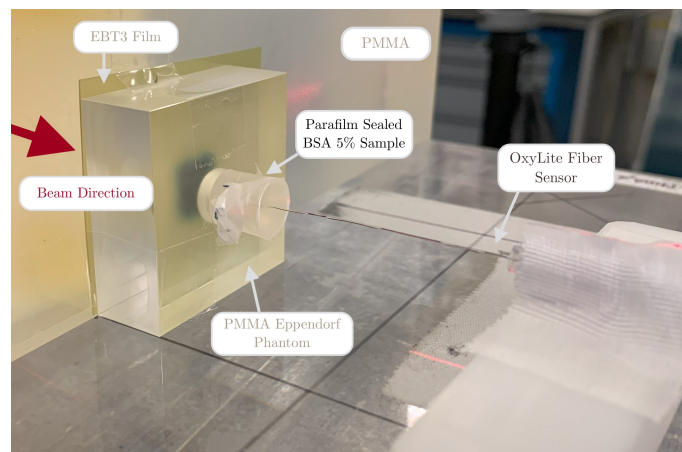


Figure 6.3.: Experimental Setup for Oxygen Consumption Measurements: The Polymethylmethacrylate (PMMA) phantom holds an Eppendorf tube containing BSA 5%, which was sealed with parafilm. The bare-fiber OxyLiteTM oxygen sensor is inserted into the tube. Directly behind the PMMA phantom, an irradiated EBT3 film is positioned. Further downstream along the beam path, additional PMMA material is placed, followed by a 2D Range Modulator (2DRM), which is not visible in this image.

The results revealed an inverse relationship between oxygen consumption rates and LETd. Under SDR conditions, consumption rates decreased from (0.351 ± 0.007) mmHg/Gy for low-LET electrons to (0.1796 ± 0.0022) mmHg/Gy for high-LET oxygen ions. Similar trends were observed under UHDR conditions, with rates ranging from (0.317 ± 0.007) mmHg/Gy to (0.1556 ± 0.0022) mmHg/Gy. Notably, SDR irradiation consistently resulted in higher consumption rates than UHDR across all particle types, suggesting a potential mechanism for the UHDR sparing effect at high LET. The experimental setup (Fig. 6.3) used in this mechanistic study was designed to align with the subsequent biological experiments. By utilizing the same Eppendorf tubes, consistent and verified experimental conditions were ensured across the studies.

Building upon our dosimetric validation and the setup from the mechanistic studies, we conducted the first biological investigation focusing on UHDR oxygen ion irradiation across multiple levels of biological complexity in the following study. [207] This systematic approach was designed to assess the feasibility of in vitro and in vivo experiments and to find first response patterns with potential therapeutic implications of this novel irradiation modality:

Celine Karle, Domenico I. Filosa, Mahdi Akbarpour, Nora Schuhmacher, Stephan Brons, Rainer Cee, Christian Schömers, Stefan Scheloske, Kristoffer Petersson, Thomas Haberer, Amir Abdollahi, Jürgen Debus, Thomas Tessonier, Mahmoud Moustafa, Andrea Mairani, Ivana Dokic. **“First in vitro and in vivo experiments with ultra high-dose rate oxygen ion radiotherapy”**. *Physics and Imaging in Radiation Oncology* (2025); DOI: <https://doi.org/10.1016/j.phro.2025.100803>. [207]

Firstly, we extended the oxygen consumption evaluation for the oxygen ion irradiation using higher initial oxygen concentrations in the BSA solution to include oxygen levels later used in the in vitro study. Under these conditions, consumption rates saturated at (0.0205 ± 0.0003) %/Gy (UHDR) and (0.0235 ± 0.0003) %/Gy (SDR), consistent with our earlier results when applying the conversion factor of ≈ 7.7 from [%] to [mmHg]. The discrepancy between UHDR and SDR remained minimal (< 0.003 %/Gy).

For the in vitro investigations (Fig. 6.4), we examined Pancreatic Ductal Adenocarcinoma (PDAC) cell survival using the KPC cells, which closely mirror human disease characteristics. [208, 209] The cells were irradiated with 8 Gy at LETd of $100.3 \text{ keV}/\mu\text{m}$ at UHDR (170 Gy/s) and SDR (0.19 Gy/s) under both normoxic (20 % O_2) and hypoxic (1 % O_2) conditions. The dose rates produced comparable cytotoxic effects for both oxygen concentrations.

In the in vivo phase, the same KPC cells were injected into the hind limbs of mice to form subcutaneous PDAC tumors. Single-fraction treatments of 10 Gy at $134 \text{ keV}/\mu\text{m}$ were administered under both dose rate conditions ($n=6$ per group)¹, with the irradiation setup shown in Fig. 6.4. Both UHDR and SDR treatments induced significant tumor growth delay and modest survival benefits compared to the control group, with median survival extending by 4 and 3 days for UHDR and SDR, respectively. These encouraging results with this aggressive tumor model highlight the potential for further investigation of oxygen ion therapy for PDAC treatment.

¹The study involved the administration of SDR and UHDR to six mice, with a non-irradiated control group serving as a comparison.

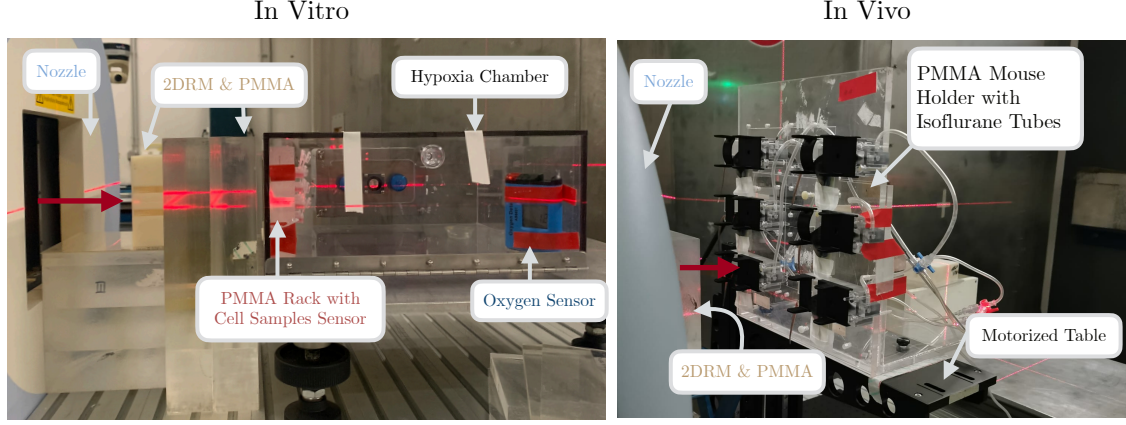


Figure 6.4.: Experimental Setup for In Vitro and In Vivo Oxygen UHDR Experiments: The in vitro configuration is shown on the left, with the 2DRM and PMMA slabs ensuring correct Spread-Out Bragg Peak (SOBP) positioning onto the cell samples. The cells were placed in Eppendorf tubes within a dedicated rack holder. For hypoxia experiments, the entire setup was housed in a hypoxia chamber equipped with an oxygen sensor for continuous oxygen-concentration supervision. The in vivo configuration depicted on the right, where the 2DRM and PMMA are positioned but concealed behind the nozzle. Anesthetized mice were secured in a 3D-printed holder, with their legs extending outside the fixture for irradiation. A motorized table allowed for slow vertical and horizontal positioning, enabling efficient irradiation while the animals remained under anesthesia with isoflurane, supplied via the visible tubing.

6.1 “Characterizing Diamond Detectors for Various Dose and Dose Rate Measurements in Scanned Carbon and Oxygen Beams”

Authors	<u>Celine Karle</u> , Gianluca Verona-Rinati, Stephan Brons, Rainer Cee, Stefan Scheloske, Christian Schömers, Rafael Kranzer, Thomas Haberer, Marco Marinelli, Andrea Mairani, Thomas Tessonnier
Publication Status	Published - 02 June 2025
Journal	Medical Physics
DOI	https://doi.org/10.1002/mp.17893
Contribution	<u>CK</u> and TT led the conceptualization and methodology of the study. GVR, RK, and MM supplied the detector and the software. SB, RC, SS, and CS provided the resources and technical support at the HIT facility. Data were acquired by <u>CK</u> , with initial assistance from TT, and subsequently curated and analyzed by <u>CK</u> . The data interpretation was conducted by <u>CK</u> , TT, and AM. All visualizations and the original draft were prepared by <u>CK</u> . The manuscript was reviewed and edited by <u>CK</u> , SB, RC, SS, CS, RK, AM, and TT. Supervision was provided by AM and TT, with TH and AM contributed to funding acquisition and clinical guidance.

©2025 The Author(s). Medical Physics published by Wiley Periodicals LLC on behalf of American Association of Physicists in Medicine. This is an open access article under the terms of the Creative Commons Attribution License, which permits use, distribution and reproduction in any medium, provided the original work is properly cited.

RESEARCH ARTICLE

MEDICAL PHYSICS

Characterizing diamond detectors for various dose and dose rate measurements in scanned carbon and oxygen beams

Celine Karle^{1,2} | Gianluca Verona-Rinati³ | Stephan Brons⁴ | Rainer Cee⁴ |
 Stefan Scheloske⁴ | Christian Schömers⁴ | Rafael Kranzer⁵ | Thomas Haberer⁴ |
 Marco Marinelli³ | Andrea Mairani^{1,4,6,7} | Thomas Tessonier^{4,8}

¹Clinical Cooperation Unit Translational Radiation Oncology, National Center for Tumor Diseases (NCT), Heidelberg University Hospital (UKHD) and German Cancer Research Center (DKFZ), Heidelberg, Germany

²Department of Physics and Astronomy, Heidelberg University, Heidelberg, Germany

³Industrial Engineering Department, University of Rome "Tor Vergata", Rome, Italy

⁴Heidelberg Ion-Beam Therapy Center (HIT), Department of Radiation Oncology, Heidelberg University Hospital, Heidelberg, Germany

⁵PTW-Freiburg, Freiburg, Germany

⁶Department of Radiation Oncology, Heidelberg University Hospital, Heidelberg Institute of Radiation Oncology (HIRO), National Center for Tumor Diseases (NCT), University Hospital Heidelberg (UKHD), Heidelberg, Germany

⁷National Center for Oncological Hadrontherapy (CNAO), Medical Physics, Pavia, Italy

⁸Clinical Cooperation Unit Radiation Oncology, National Center for Tumor Diseases (NCT), Heidelberg University Hospital (UKHD) and German Cancer Research Center (DKFZ), Heidelberg, Germany

Correspondence

Andrea Mairani, Clinical Cooperation Unit Translational Radiation Oncology, National Center for Tumor Diseases (NCT), Heidelberg University Hospital (UKHD) and German Cancer Research Center (DKFZ), Heidelberg, Germany.

Email:

andrea.mairani@med.uni-heidelberg.de

Thomas Tessonier, Heidelberg Ion-Beam Therapy Center (HIT), Department of Radiation Oncology, Heidelberg University Hospital, Heidelberg, Germany.

Email:

Thomas.Tessonier@med.uni-heidelberg.de

Funding information

German Research Council, Grant/Award Number: DFG-Unite: SFB1389/2C05; National Center for Tumor Diseases; NIH-P01CA257904

Abstract

Background: The emerging FLASH radiotherapy technique employs "Ultra-High Dose Rate" (UHDR) irradiations and offers the potential to spare normal tissue while maintaining iso-effective tumor treatment. Given the physical and biological advantages inherent to high "Linear Energy Transfer" (LET) particles, the combination of UHDR and high LET has the capability to enhance the normal tissues sparing, as indicated by initial in vivo trials. However, to ensure a safe implementation of this combined modality, it is essential to establish robust dosimetric protocols utilizing dose-, dose rate-, and LET-independent detectors.

Purpose: The objective of this study is to characterize the dose, dose rate, and LET dependency of two diamond detectors with high LET carbon and oxygen ion irradiation under "Standard Dose Rate" (SDR) and UHDR conditions.

Methods: The "microDiamond" (mD) and a "flashDiamond" (fD) prototype were benchmarked against measurements with a monitoring ionization chamber, Advanced Markus chamber (AMC), and simulations for carbon and oxygen irradiation, with energies of 274.98 MeV/u and 325.98 MeV/u under SDR and UHDR conditions. First, the entire depth-dose profiles obtained during SDR

Andrea Mairani and Thomas Tessonier contributed equally to this study.

Statistical Analyses were performed by C.K. (celine.karle@dkfz.de, +49 (0)6221-56-39391).

This is an open access article under the terms of the [Creative Commons Attribution](https://creativecommons.org/licenses/by/4.0/) License, which permits use, distribution and reproduction in any medium, provided the original work is properly cited.

© 2025 The Author(s). *Medical Physics* published by Wiley Periodicals LLC on behalf of American Association of Physicists in Medicine.

irradiations and the partial in-depth profiles of the Bragg peak region in UHDR were compared to the corresponding simulation values. Secondly, the linearity of the diamond detector response during dose escalation measurements was investigated for both dose rates.

Results: The two detectors exhibited alignment with the simulated depth-dose distributions for oxygen and carbon irradiations across both dose rate conditions. The mD overestimated the dose values for carbon and oxygen measurements. This overestimation increased with “dose-averaged LET” (LET_d) during SDR irradiation and maintained a stable value of 5% for UHDR. Meanwhile, the fD demonstrated a high degree of agreement with the simulation, with a maximum discrepancy of 5% across all irradiation modalities in the plateau and “Bragg Peak” (BP). Deviations were observed in the BP fall-off region, while both diamond detectors exhibited a strong alignment with the AMC measurements. Furthermore, both detectors exhibited dose linearity under SDR and UHDR irradiation for both carbon and oxygen irradiation, with a coefficient of determination (R^2) above 0.99.

Conclusion: In the context of heavy ion carbon and oxygen irradiation in UHDR and SDR, the two diamond detectors demonstrated dose-rate independence. While the mD exhibited a tendency to overestimate dose values with increasing LET_d, the fD was found to be LET-independent. The fD appears to offer accurate and reliable dose assessments for UHDR heavy ion experiments.

KEYWORDS

diamond detector, high LET, UHDR

1 | INTRODUCTION

“Ultra-high Dose Rate” (UHDR) irradiation offers a promising new avenue for treatment modalities. As early as the 1960s, irradiation with dose-rates exceeding 40 Gy/s, classified as UHDR, have been found to spare cells to a greater extent than “Standard Dose Rate” (SDR) irradiation when the same dose is applied.¹ The general cell sparing ability of UHDR irradiation has been the subject of extensive investigation for electrons and light ion, such as protons² and helium ions.³ Furthermore, in vivo irradiation at UHDR reduces normal tissue toxicity while maintaining effective tumor control, which is termed as “FLASH effect”.^{4,5} Promising in vitro and in vivo results led to the first clinical trials with patients receiving electron⁶ and proton⁷ UHDR irradiation.

In comparison to light ions, heavier particles like carbon ions, exhibit both physical advantages in providing more precise dose profiles, as well as biological advantages due to their increased “Linear Energy Transfer” (LET) in the “Bragg Peak” (BP) region. The higher LET aids in eradicating radioresistant and hypoxic tumors, which makes the use of even higher mass particles, such as oxygen, attractive.^{8–10}

Combining UHDR treatment with heavy ions could allow to take advantage of both approaches.^{11,12} A recent study by Tinganelli et al. showed promising results for carbon UHDR irradiations in both low LET entrance¹³ and high LET BP region.¹⁴

While, the precise mechanism responsible for this phenomenon remains unclear, the temporal structure of the dose delivery might play an important role in the FLASH effect,^{15,16} for instance as demonstrated by Ruan et al., who examined the impact of altering the beam pause between two pulses and the mean dose rate on crypt survival.¹⁶ Similarly, Karsch et al. investigated the impact of different temporal settings on zebra fish embryo lengths.¹⁷ These are merely two illustrations of the significance of precise temporal recording to enhance understanding of the FLASH effect. Concerning the temporal beam delivery, the beam time structure of the diverse FLASH delivery systems, such as isochronous cyclotrons and synchrotrons, differs¹⁸ and especially for inter-institutional comparison the logging of all the parameters, like spill time, interspill pauses, and pulse frequencies is crucial.¹⁹ Temporal monitoring is of particular interest in the context of scanned ion beams, where instantaneous dose rates can reach exceptionally high levels.^{20,21} Consequently, the analysis of spatio-temporal dose distribution is crucial and demonstrates the necessity of suitable detectors that can provide time-resolved measurements while remaining independent of dose, dose rate, and LET.

Passive dosimetric systems, such as alanine detectors, thermoluminescence detectors, or radiochromic films, may be suitable for the assessment of absolute dose; however, they do not permit active temporal monitoring of the dose during the course of the

experiments.^{22,23} This can only be evaluated through the use of active real-time systems with a small time resolution.

The conjunction of UHDR and high LET necessitates the implementation of dosimetric systems that circumvent the physical demands of these radiation modalities, such as saturation and recombination effects.¹² In the case of high LET, the resulting recombination charge loss can be attributed to two principal factors: volume recombination, where ions from different primary particles recombine, and initial recombination, where ions produced by the same primary particle interact.²⁴ Although the volume recombination appears to be insignificant in the context of high LET irradiation and heavy ions, the intra-track effects are amplified.^{12,24}

“Ionization Chambers” (IC) are recommended by the IAEA as a reference for high LET irradiation dosimetry.²⁵ However, ICs are susceptible to saturation in the context of rapid charge releases following UHDR irradiation, due to the influence of recombination^{22,26,27} and polarization effects.²⁸ Despite the existence of methodologies for modelling ion recombination within an IC, this approach is not applicable to synchrotron beams, due to their non-reproducible intensity fluctuations and heterogeneous high instantaneous dose rates.¹⁸ To circumvent the application of numerous correction factors,^{22,29} hardware adaptations have been investigated, including the use of alternative gas mixtures in the chamber³⁰ or the reduction of the gap between the electrodes.³¹ Despite these promising advancements in signal acquisition, the response time of available ICs is around 300 μ s, which is too slow to resolve the single-digit microsecond beam time structure of certain isochronous and synchrotron delivery systems.¹⁸ Furthermore, the low spatial resolution due to significant volume averaging effects poses major challenges for UHDR applications, which often involve small fields with large dose gradients.²³

A preferable higher resolution and thus smaller sensitive volumes can be achieved with more dense solid-state detectors.³² High spatial resolution in the nano- to micrometer range can thus be attained.¹⁸ In the context of solid state detector materials, scintillators are inherently constrained by their dead times due to the nature of their scintillation centers and optical contamination by Cherenkov light in the optical fibers.²³ These factors could result in unintended LET and dose rate-dependent effects.^{22,27} Additionally, high LET irradiation has been observed to cause ionization quenching in scintillators, necessitating additional corrections to be made.^{33–35} Furthermore, scintillators can experience radiation damage, leading to a decrease in light output and a shift in spectra.³⁶

Regarding radiation hardness, semiconductors are highly resistant to radiation damage and additionally offer the advantage of a direct charged based read out that should not be less affected by high LET and dead times.^{23,22} Their small active volume and resulting high axial resolution allows for the assessment of

detailed lateral and “Depth Dose Distributions” (DDD).³⁷ Thus, semiconductors have a high sensitivity due to the charge-based signal, a high spatial resolution, and thus are suitable for monitoring the temporal application of UHDR small fields.^{18,23}

Silicon (Si) diodes represent a class of semiconductor detectors that are currently available. However, the high-Z material results in considerable variation of mass energy absorption coefficient and electronic stopping power when compared to tissue equivalent materials. This leads to an energy-dependent outcome and introduces general uncertainties.³⁸ Radiation damage can also be expected for Si diodes under UHDR conditions, especially in combination with high LET, albeit to a lesser extent than scintillators.³⁹

These disadvantages are avoided when diamond is selected as a sensitive component for the semiconductor detector. The diamond crystal is near tissue equivalent and resistant to radiation damage.^{23,40} Diamonds as semiconductor material exhibit a wider band gap. Consequently, this results in reduced leakage currents and an enhanced charge collection efficiency compared to silicon-based semiconductors.⁴¹ Currently available diamond-based detectors are the “microDiamond” (mD)⁴² and “flashDiamond” (fD) both from PTW.⁴³

Recent advancements in the field have seen the development of silicon carbide (SiC) detectors, which combine the industrial maturity of silicon and the robustness of diamonds. Initial studies have demonstrated the potential of SiC detectors in the context of electron UHDR irradiation, yielding results that are comparable to those observed in fD.⁴⁴ However, further research is required in the characterization of SiC detectors under high LET irradiation.

The commercially available mD from PTW⁴² has already been tested and found to be dose rate independent for photon, electron, and helium irradiation.^{45,46} Furthermore, the mD was benchmarked for scanned carbon ions during SDR irradiation, confirming a negligible LET dependence for this range.³⁷ However, in the course of investigating unmodulated beams, Rossomme et al.⁴⁷ found an LET dependency of low-energy carbon and oxygen ions with 62 MeV/u. This discrepancy could be attributed to the presence of a border LET spectrum in beams with modulators, such as a ripple filter, beam monitoring systems, and so forth.⁴⁷

Due to its promising characteristics for UHDR real-time beam monitoring, the mD was therefore tested in this study. Given indications that the mD might be affected by high LET and UHDR irradiation,⁴⁸ additionally, a prototype of a “fD” from PTW was investigated. The fD uses the base of an mD, but was developed to fulfill the UHDR requirements with modifications made to the sensitive area and the diamond-doped area.⁴⁹ In order to guarantee that the diamond Schottky diode provides a linear response at high dose per pulse without saturating, two approaches were employed: the first is

to limit the detection current, thereby reducing sensitivity; the second is to decrease the series resistance. The detection current can be reduced by decreasing the sensitive area, while the series resistance is minimized by increasing the boron concentration in the doped diamond layer.⁴⁹ These modifications introduced have enabled the fD to record a reliable signal under electron and helium UHDR irradiation^{45,46} and thus showcased its potential to serve potentially as a secondary standard instrument for absolute dose measurements in water for UHDR beams.⁴⁸

The objective of this study was to investigate whether these UHDR adaptations are also appropriate for heavy particle UHDR irradiation. Accordingly, the mD and fD were analyzed regarding their dose linearity and depth dose response under SDR and UHDR irradiation with carbon and oxygen ions at the “Heidelberg Ion beam Therapy facility” (HIT) to evaluate the detectors’ reliability for combined high LET and high dose rate irradiation.

2 | MATERIALS AND METHODS

2.1 | Detectors and electronic chains

Two diamond detectors were tested using different dose rates and LET: the commercially available “mD” (TM60019, PTW Freiburg)⁴² and a “fD” prototype, while the latter has been optimized for UHDR applications. Both detectors contain an active volume comprising a pure intrinsic diamond layer mounted on top of a conductive p-type boron doped diamond layer.^{49,50} The detectors differ mainly in their boron concentration in the p-type layer and the size of the active volume.⁴⁹ The mD has an active layer with a diameter of 2.2 mm and a thickness of 1 μm ,³⁷ while the fD prototype has a similar geometric structure but a 1.5 smaller active area (diameter 1.4 mm).⁴⁵ Both detectors have a similar construction and are encapsulated, resulting in a measurement point situated at a water equivalent depth of 1 mm. Due to their intrinsic build-up potential, no external voltage needs to be applied.^{37,49} The response signal of the mD remained stable when rotated around the azimuthal axis. However, it was necessary to maintain the detectors’ polar angle at 0° in order to circumvent any potential uncertainties.⁴⁰

The mD demonstrated reliable signal generation under conditions of SDR high-LET irradiation,³⁷ as well as for UHDR eletrons,⁴⁵ proton²⁶ and helium⁴⁶ irradiation. Under these conditions, the signal linearity, as specified by PTW, was achieved. Similarly, the fD prototype was validated for UHDR irradiation with electrons and helium ions.^{45,46}

In accordance with the recommendations set forth in TRS-398, SDR measurements were additionally conducted with a plan-parallel “Advanced Marcus Chamber”

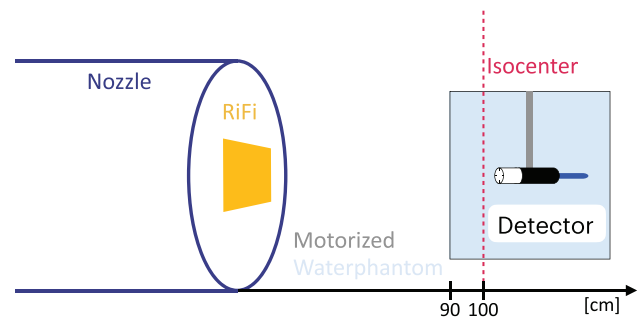


FIGURE 1 Setup at the HIT experimental room: The beam exit nozzle is equipped with a 3 mm ripple filter (“RiFi”). A motorized water phantom is positioned with its entrance window 10 cm before the isocenter, marked with a red line. All three detectors are positioned with dedicated holders into the moving metal arms of the water phantom.

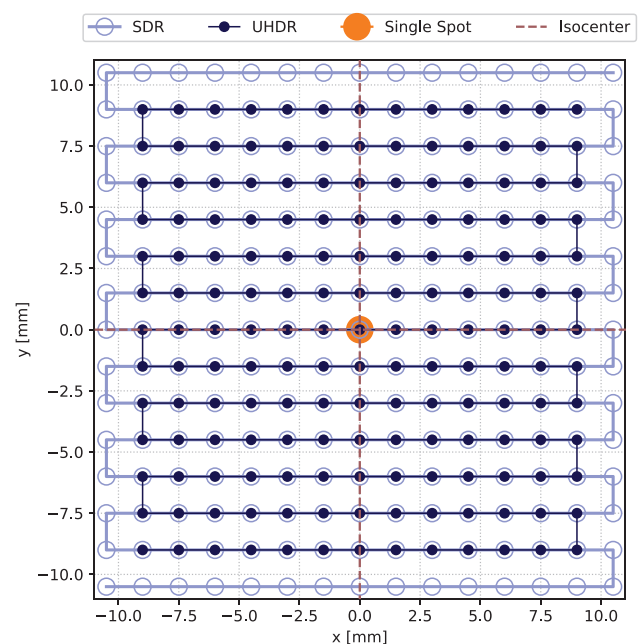


FIGURE 2 “PBS” patterns of the fields in beam’s eye view. All fields for carbon and oxygen irradiations were centered in the isocenter, indicated by the dashed red lines, and had a spot spacing distance of 1.5 mm. The PBS direction is depicted by solid lines. For all SDR experiments, the $21 \times 21 \text{ cm}^2$ field was used (marked as light blue). The fields employed for the UHDR DDD measurements were of a slightly reduced size in comparison to those utilized in SDR, with the objective of increasing the dose rates (dark blue). The single spot plans, displayed as orange spot, were used for the dose escalation experiment with UHDR. The varying spot sizes have been selected for enhanced visualization. DDD, depth dose distributions; PBS, pencil beam scanning; SDR, standard dose rate; UHDR, Ultra-High Dose Rate.

(TM34045, PTW Freiburg) (AMC) in axial orientation.²⁵ The AMC has a sensitive volume with a radius of 2.5 mm and a depth of 1 mm. To compare the values of the three detectors, “Monte Carlo” (MC) FLUKA (Version 2021.2.9) simulations were conducted to obtain DDD and LET distributions in a water tank using a detailed geometry of the HIT beamline.^{51,52}

For the electronic readout, prior studies demonstrated that the diamond detectors offer a reliable readout during SDR and UHDR irradiation when coupled with the PTW UNIDOSE^{webline} electrometer.^{37,45,46} The charge was recorded for the diamond detectors, whereas for the AMC, the dose was calculated directly using the calibration factor of the chamber and the correction factor for radiation quality with an applied temperature and pressure correction.

2.2 | Experiments and evaluation

Two key experiments were carried out to assess the dose, dose rate, and LET dependencies of the two diamond detectors. The first experiment involved measuring the entire DDD under SDR irradiation and focusing on the BP region under UHDR irradiation. The second experiment evaluated the linearity of the dose response during dose escalation measurements for the diamond detectors in both SDR and UHDR settings.

2.3 | Setup

The three different detectors were positioned with their designated holders inside a motorized water tank. The phantom was positioned at approximately 10 cm in front of the iso center at the “Heidelberg Ion Beam Therapy Center” (HIT) experimental room (Figure 1).

2.4 | Depth dose distribution

The delivered dose or charge was measured from irradiated fields (Figure 2 and Table 1) along the central axis 4 cm up to ~ 17 cm in water depth with all three detectors in SDR. The BP region was the focus of the UHDR measurements. For each depth point, three measurements were averaged, and the standard deviation was calculated. The dose or charge values were normalized to the “Area Under the Curve” (AUC). The AUC was calculated by interpolating the measured values and then integrated using the trapezoidal rule to obtain the total AUC. For the UHDR measurements, where only the Bragg peak was acquired, the values from these measurements were normalized to those from the SDR measurements and subsequently divided by the SDR AUC value. The standard deviations were determined through Gaussian error propagation. Subsequently, the local deviation from the MC values was calculated with a symmetric percentage change formula.

2.5 | Dose response linearity

To determine the linearity of the SDR dose response for carbon and oxygen, field plans (Figure 2) were cal-

ibrated to deliver doses of 1, 1.5, 2, 2.5, 5, and 10 Gy using the AMC (Table 1) in the plateau region. During the calibration process, the AMC doses were recorded a total of three times. Similarly, the charge from the diamond detectors was recorded three times for each dose in each plan, with the resulting values averaged. The charges and their standard deviations were then fitted linearly using an orthogonal distance regression accounting for the x-deviation provided by the AMC dose measurement.

The slope of this fit represents a sensitivity factor that correlates the dose obtained by the AMC to the charges from the diamond detectors. The factors for carbon and oxygen were then applied to convert the charges for the different UHDR experiments into dose, allowing the calculation of the dose and dose rate.

In order to achieve high doses and dose rates at UHDR, a single spot on the central axis was irradiated in opposition to the conventional approach of using a large field (Figure 2). Given the relatively small field size, the actual number of particles delivered was used as the reference for linearity rather than the AMC. A single spot with the desired quantity of particles was delivered for carbon with approximately 2.5×10^8 , 2×10^8 , 1.5×10^8 , 1×10^8 , 0.5×10^8 and 0.1×10^8 particles and for oxygen with approximately 1×10^8 , 0.9×10^8 , 0.7×10^8 , 0.5×10^8 , 0.3×10^8 and 0.1×10^8 particles. The “Beam Application and Monitoring System” (BAMS) system at HIT recorded the actual number of particles delivered, which differed from the requested amount due to the instability of the synchrotron settings. Consequently, the charge was normalized to the actual number of particles delivered. As the variation in particle delivery was already accounted for, the data was fitted by a linear function using the least squares method.

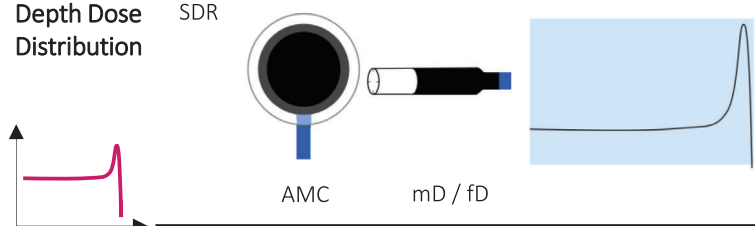
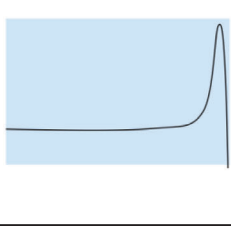
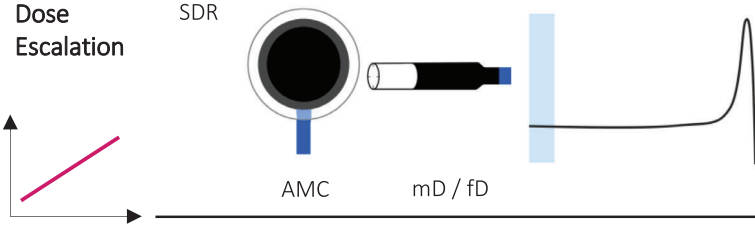
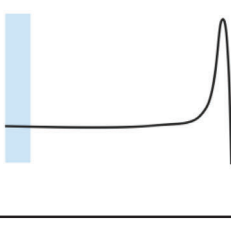
2.6 | Dose rate calculation

In the case of the SDR irradiations, the dose values were provided by the AMC. Conversely, for the UHDR experiments, the sensitivity factor was employed to convert the charges to dose values. The irradiation times were determined using the recorded BAMS files, and the average dose rate was calculated by dividing the dose by the total irradiation time.¹⁹ The reported dose rate values are based on at least three different BAMS recordings and corresponding dose measurements (Table 1).

2.7 | Film analysis

Given that the irradiation was conducted with an active “Pencil Beam Scanning” (PBS) system, it is essential to ascertain the level of flatness exhibited by the field in the region of the detectors. Therefore, EBT3 Gafchromic Films (Ashland) were placed in front of the water tank during irradiation. Each film was scanned with an Epson

TABLE 1 The various experimental settings.

Experiment	Mode	Detector	Measurement Depth	Carbon (274.98 MeV/u)	Oxygen (325.98 MeV/u)
Depth Dose Distribution	SDR			21 x 21	
				Field Size [mm ²]	
				Focus [mm]	4.16.4
				Nr. of Particles	~2.3E8~1E8
				Spill Time [s]	~3~2
				Dose Rate [Gy/s] Plateau – BP	0.34 -1.330.35 -1.29
UHDR				Field Size [mm ²]	18 x 18
				Focus [mm]	4.13.3
				Nr. of Particles	~2.3E8~1E8
				Spill Time [s]	~0.05~0.1
				Dose Rate [Gy/s] Plateau - BP	30.8 - 120.29.6 – 35.9
Dose Escalation	SDR			21 x 21	
				Field Size [mm ²]	
				Focus [mm]	4.16.4
				Dose [Gy]	1, 1.5, 2, 2.5, 5, 10
				Dose Rate [Gy/s]	< 0.27< 0.34
UHDR				Field Size [mm ²]	Single Spot
				Focus [mm]	4.13.3
				Nr. of Particles [•1E8]	2.5, 2, 1.5, 1, 0.5, 0.11, 0.9, 0.7, 0.5, 0.3, 0.1
				Dose [Gy] Plateau - BP	1 to 18 – 3 to 501 to 7 – 2 to 17
				Dose Rate [Gy/s] Plateau - BP	163 to 211 – 433 to 105838 to 50 – 101 to 150

Note: The blue area in the measurement depth column indicates the location of the detectors. The plan details include field size and focus, expressed as the full width at half maximum. Depending on the experiment, the number of particles applied, or the dose is provided. The dose rate given represents the mean dose rate, which was calculated by dividing the total dose applied by the irradiation time. For the dose escalation for SDR the highest and for UHDR the lowest reached dose rate is provided.

Perfection V850 Pro at a resolution of 1200 dpi. Horizontal and vertical line profiles through the center of the film were extracted with ImageJ. The resulting data were then subjected to further processing in Python, whereby the profile was normalized to the maximum greyscale value and smoothed with a Gaussian filter. From the central point of the profile, we identified a region spanning 50% of the total area under the curve (highlighted in green in Figure 3) to exceeds the dimensions of the sensitive areas of all detectors. Within this central region, we calculated a flatness index (F):

$$F = 100 * \frac{Y_{\max} - Y_{\min}}{Y_{\max} + Y_{\min}}$$

with Ymax and Ymin being the maximum and minimum normalized grey scale value in the 50% area.

3 | IRRADIATION DETAILS

3.1 | Irradiation facility

The HIT provides intensity-controlled raster scanning pencil beams consisting of proton, helium, carbon, and oxygen ions with energies between 50 and 430 MeV/u.⁵³ A third-order resonant RF knock-out extraction system is responsible for the selective extraction of the requested number of particles from the synchrotron. The extracted particles are then transported to the dedicated room, for this study the experimental room. During the extraction phase, the dynamic intensity controller modulates the amplitude of the RF-knockout exciter in response to detected deviations.⁵⁴ To extract carbon and oxygen ions with UHDR at HIT, it was necessary to implement a series of adaptations with the objective of increasing

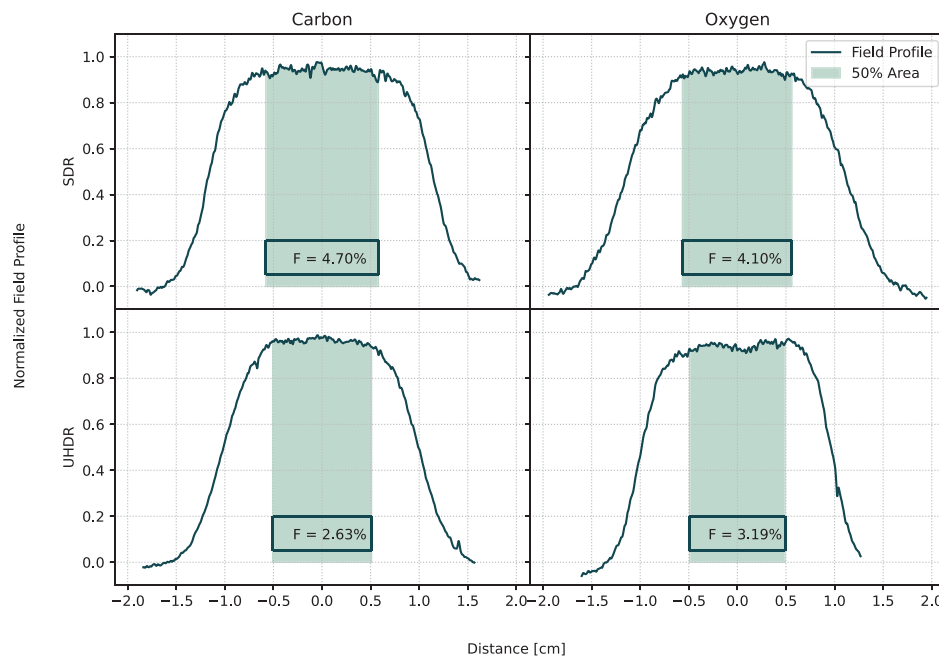


FIGURE 3 Normalized field profiles of the EBT3 films. The evaluated 50% area is displayed as green shaded region, in which also the flatness index is given.

the number of particles and reducing the extraction time. Consequently, the synchrotron was filled with a certain number of particles that can be extracted in one spill, which was 2.5×10^8 and 1×10^8 for carbon and oxygen ions respectively. The extraction tune was adjusted to a position closer to the resonance, and the field strength of the sextupole magnets was enhanced to facilitate a more rapid extraction. These modifications did not affect the operational status of the PBS and intensity control systems, which remained functional for UHDR irradiation.⁵⁵

Additionally, the nozzle was equipped with a 3 mm ripple filter to broaden the pristine BP for both carbon and oxygen beams and with a BAMS containing several IC and multi-wire chambers (Figure 1). These chambers are employed for the control of beam delivery,⁵⁴ the assessment of the spill length, and the number of particles that were delivered.

3.2 | Irradiation parameters

The HIT accelerator provided carbon ions with an energy of 274.98 MeV/u or oxygen ions with 325.98 MeV/u for both SDR and UHDR irradiations. For the beam application at HIT, active PBS is used, and the spot spacing between the pencil beams was 1.5 mm for both particles and dose rates. The various experiment settings and irradiation parameters for the DDD and dose escalation experiments at SDR and UHDR are presented in Table 1.

4 | RESULTS AND DISCUSSION

4.1 | Field homogeneity

The field homogeneity was evaluated by analyzing irradiated EBT3 films. The extracted profile lines and the central 50% area are shown in Figure 3. Despite the active PBS application of the fields, the small flatness factor below 5% indicates that the irradiation in the area considered was homogeneous. As this area extended beyond the sensitive area of the detectors, the detectors were adequately covered by both SDR and UHDR fields.

4.2 | Depth dose response

Depth dose profiles were recorded in SDR for the AMC, mD, and fD, and in UHDR for the diamond detectors in both the plateau and BP regions. Dose rates for carbon UHDR irradiation ranged from 30.8 to 120.2 Gy/s in the plateau and the BP respectively, while for oxygen UHDR, even in the BP region the dose rate did not exceed 35.9 Gy/s (Table 1). It is important to note that the average dose rate is not the sole indicator of dose rate, particularly for PBS systems.^{19,46} Due to the raster scanning process, only a few surrounding spots contribute to the local dose, meaning that the actual irradiation time locally may be much shorter than the total field irradiation time. This effect has been previously demonstrated for helium,⁴⁶ highlighting the need for further time-resolved studies to accurately

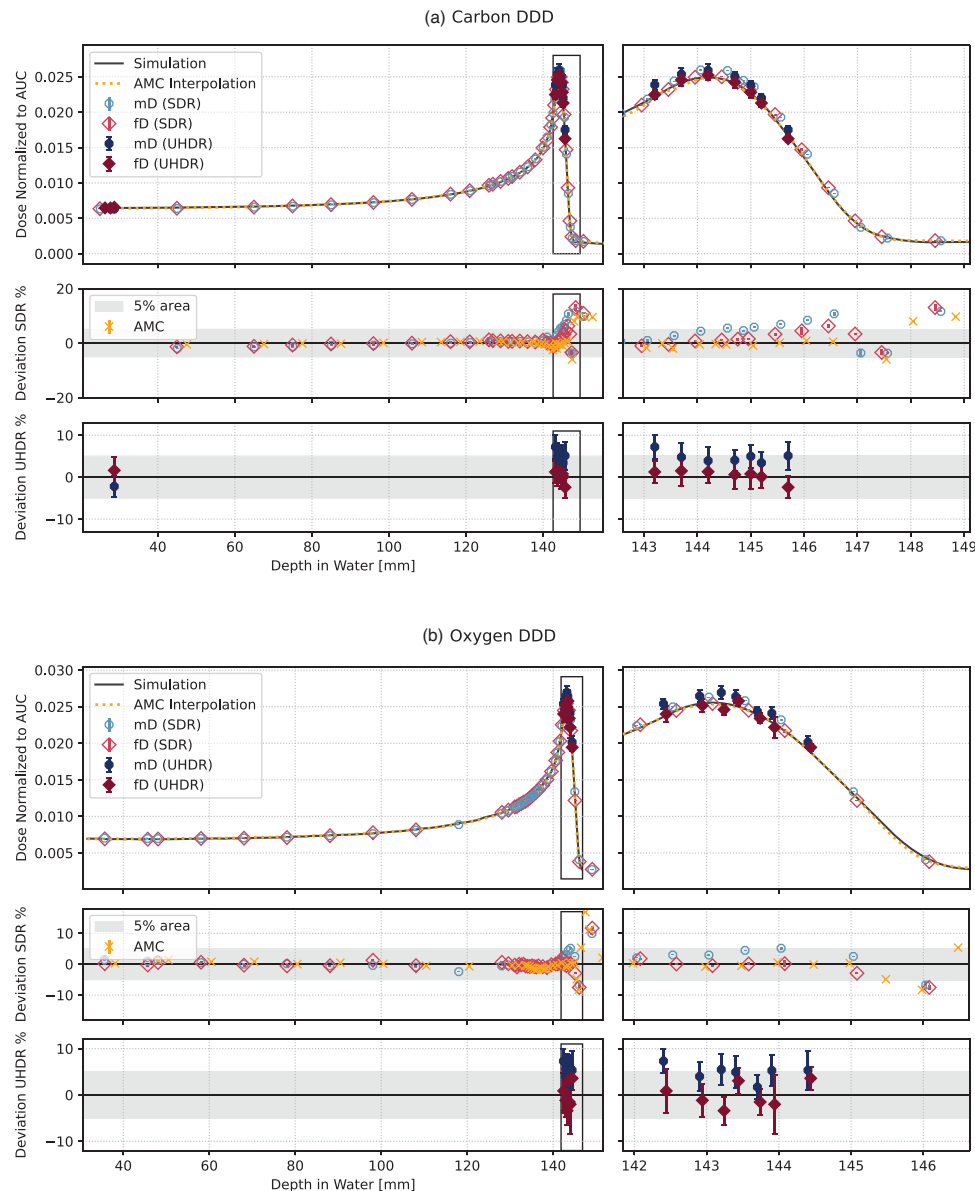


FIGURE 4 Carbon and oxygen DDD normalized to the AUC. The upper plot A displays the carbon data, while the lower panel B contains the data from oxygen irradiations. For each individual panel, the left side displays the full DDD, and the right side specifically focuses on the BP and BP fall off region. The first plot depicts the dose values normalized to the AUC, the middle plot illustrates the percentage local deviation from SDR measurements in relation to FLUKA simulation, shown as back lines, and the bottom graph represents the deviations from UHDR diamond measurements in comparison to the simulations. The AMC values are shown as dotted orange line resulting from a quadratic interpolation of the individual values for better visibility in the DDD plots, and for the deviation plots, the individual measurement points are marked with orange crosses. The data points for the mD (blue circle) and fD (red diamond) are shown individually. The UHDR measurements are marked by a darker color and a filled marker symbol. Additionally, the 5% deviation area is marked with a grey band. AUC, Area Under the Curve; BP, Bragg Peak; DDD, depth dose distributions; fD, flashDiamond; mD, microDiamond; UHDR, Ultra-High Dose Rate.

determine the instantaneous dose rate pattern and other indicators.²¹

The recorded DDD were normalized to the AUC and are displayed in Figure 4. In addition to the individual deviations shown in Figure 4, the average deviations from the simulations in the BP region for all detectors at SDR and UHDR are given in Table 2.

In general, while the standard deviations for SDR measurements for all detectors were below 1%, the standard deviations of UHDR measurements were around 3%, due to the variability of the delivery (Figure 4). This can also be seen by the variability of the average deviation, which was for SDR below 0.2% and for UHDR around 2.5% (Table 2). The adjustment of the synchrotron to deliver UHDR

TABLE 2 Average percentage deviation in the BP region from the FLUKA simulation: Values are given with their standard deviation.

Particle	Dose Rate	Detector	Average Deviation \pm Standard deviation [%]
Carbon	SDR	AMC	0.81 ± 0.08
		mD	4.53 ± 0.29
		fD	2.5 ± 0.4
	UHDR	mD	3.9 ± 2.2
		fD	0.6 ± 2.2
Oxygen	SDR	AMC	-0.08 ± 0.15
		mD	2.1 ± 0.3
		fD	-1.0 ± 0.4
	UHDR	mD	3.4 ± 2.4
		fD	-1.0 ± 2.6

Abbreviations: BP, Bragg Peak; fD, flashDiamond; mD, microDiamond; SDR, standard dose rate; UHDR, ultra-high dose rate.

results in the particles being moved closer to the extraction tune. This adaptation can lead to more variable dose delivery compared to the normal particle delivery.

It is noteworthy that the average deviation of all detectors in the BP region remained below 5% (see Table 2), indicating a high degree of agreement with the simulations, even at this high LET and UHDR. The observed consistency in the average deviation of the diamonds between SDR and UHDR (see Table 2) suggested a dose rate independence for the conducted high LET carbon and oxygen irradiations.

The AMC dose values corresponded to the simulation values and resulted in individual deviations below 2%, except for a few measurement values at the distal part of the BP. Several factors may be responsible for this partial discrepancy. First, the nuclear model of FLUKA may have limitations in reproducing the depth dose distribution, which is of particular relevance for carbon and oxygen beams, due to a lack of experimental fragmentation data.^{56,57} Second, the AMC dose measurements were affected by the experimental conditions with dose variations in the order of 0.4%, but in general, uncertainties in the dosimetry of heavy ions may reach 3.4% in the absorbed dose in water due to uncertainties in the stopping power ratio.²⁵

The mD displayed around 4% overestimation of the dose compared to the simulation in the BP region for both SDR and UHDR and both particles (Table 2). This is consistent with the findings found by Tessonnier et al⁴⁶ for helium irradiation. As shown in Figure 5b, the deviation to the simulation for carbon and oxygen irradiations tended to increase for SDR irradiations with “dose-averaged LET” (LET_d), indicating an LET_d dependency. However, the largest variations up to 15% for carbon and 12% for oxygen (Figure 5b, black box) were at an LET_d of about 30 keV/μm and 60 keV/μm for carbon and oxy-

gen respectively, which corresponded to the tail of the DDD (Figure 5a). This region is highly influenced by the nuclear model used in FLUKA, as evidenced by the fact that all detectors show similar deviations from the simulation in this area. The consistency between the AMC, mD, and fD detectors further supported this observation.

For the UHDR irradiations with both ions, deviations of the mD were around +5% for all LET_d within the BP region, without a possibility to observe the trends shown in SDR due to the larger uncertainty of the measurements (Figure 5b). When considering the consistency of the average deviation of the mD for SDR and UHDR for both particle types (Table 2), this suggested that the mD may have an LET_d but no dose rate dependency.

The deviations of the fD for carbon and oxygen in UHDR and SDR were below 5% until the fall-off of the BP. For carbon ions, the dose was generally slightly overestimated, though the deviations were less than half of those seen for the mD values. This overestimation was not observed in the oxygen DDD. As shown in Figure 5, for oxygen no clear LET_d trend was apparent for both SDR and UHDR, indicating that the detector was independent of LET_d and dose rate. Moreover, the average deviation for the fD in the BP region was 2.5% at most, which was generally smaller than the mD deviations (Table 2). Furthermore, it is noteworthy that the discrepancies from the simulation were consistent between UHDR and SDR, indicating a dose rate independence.

4.3 | Dose response linearity SDR

The detector charge was benchmarked against the AMC dose values of the irradiated PBS fields to evaluate the linearity of the detector response in the SDR irradiations within the plateau region (Figure 6). The detectors demonstrated an overall dose linearity, as indicated by coefficients of determination (R^2) of the linear fit exceeding 0.99. The mD demonstrated a sensitivity of $1.509^{nC}/Gy$ for carbon and a marginal increase in sensitivity for oxygen, reaching $1.5316^{nC}/Gy$. This value was threefold higher than those observed for the fD, which yielded $0.501^{nC}/Gy$ for both particle types within the standard deviation. Therefore, neither of the diamond detectors exhibited dose dependence during SDR irradiation.

4.4 | Dose linearity UHDR

For the UHDR dose response linearity, the detector response was compared to the delivered particles applied to a single spot on the central axis (Figure 7).

Similarly to the SDR results, the diamonds demonstrated satisfactory linearity during UHDR dose escalation measurement within both plateau and BP region.

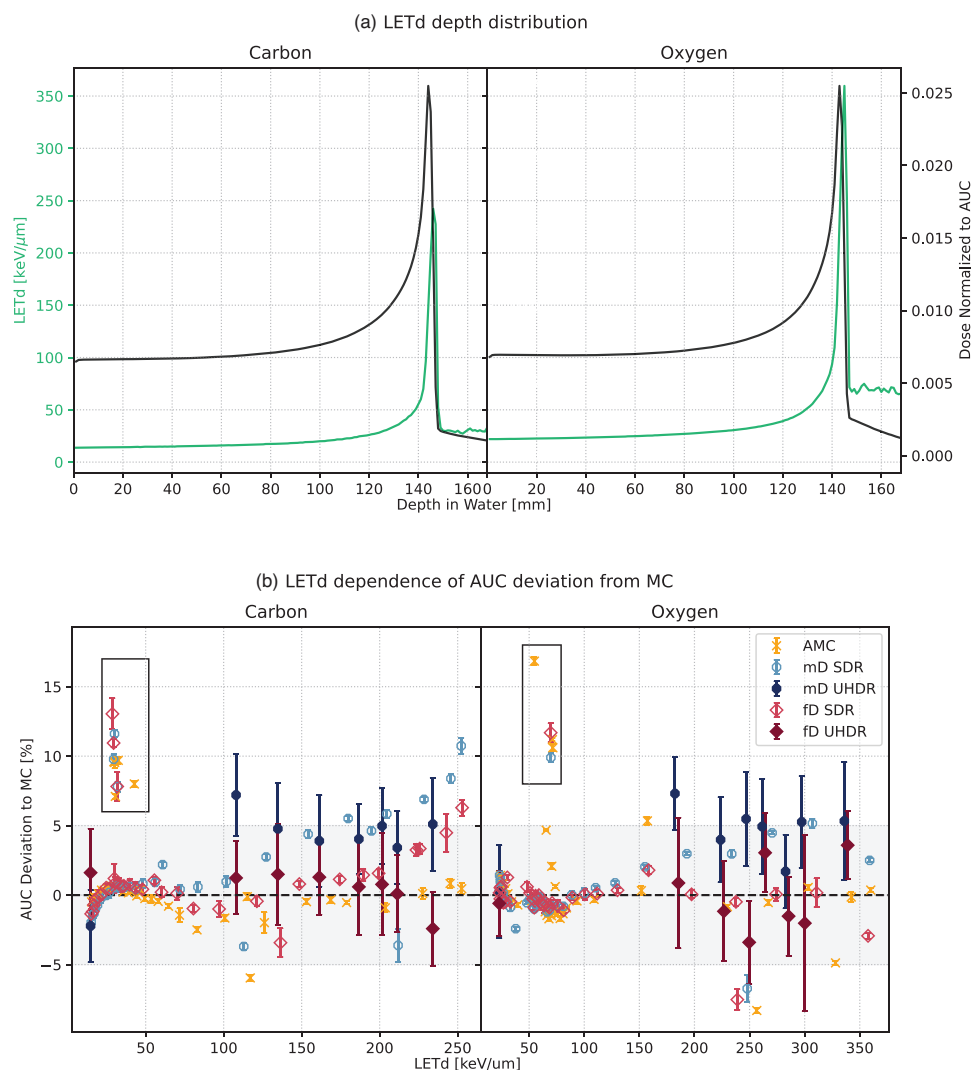


FIGURE 5 LETd dependency of the AUC deviation with respect to the MC. The data related to carbon is displayed on the left-hand side of the panels, while the data pertaining to oxygen is displayed on the right-hand side. Panel A depicts the LETd distribution (green solid line) alongside the AUC distribution (black solid line). Panel B illustrates the resulting correlation between AUC deviation and MC, as well as LETd at varying depth values. As previously, AMC values are represented by orange crosses, mD by blue circles, and fD by red diamonds. Hollow markers indicate SDR irradiation data, while filled markers represent UHDR measurement points. The black boxes surround the values from the fragmentation tail. AUC, Area Under the Curve; AMC, Advanced Markus chamber; LETd, dose-averaged LET; MC, Monte Carlo; mD, microDiamond; SDR, Standard Dose Rate.

Particularly the coefficient of determination for the various linear fits exceeded 0.99.

The elevated UHDR standard deviations in comparison to the SDR measurements can be explained by the beam fluctuations, due to UHDR delivery conditions.

5 | CONCLUSION

The two diamond detectors exhibited reliable and accurate dose measurements during heavy ion irradiations, thereby confirming their strong potential for use in UHDR dosimetry. While the mD showed an increasing deviation with higher LETd, the fD prototype demon-

strated superior accuracy and an absence of dose, dose rate, and LET dependency, making it an appropriate choice for the assessment of the absolute dose in high-LET irradiations at UHDR. In comparison with other detector candidates that might be suitable for these radiation modalities, such as SiC detectors, the fD is commercially available and can be integrated into normal dose-metric routines by being connected to standard electrometers.^{44,45,58} Consequently, the fD is readily available for research in this area and might be suitable as a secondary standard.⁴⁸

A fundamental concern in the investigation of the FLASH effect and its clinical applicability is the deciphering the temporal effects of beam application.

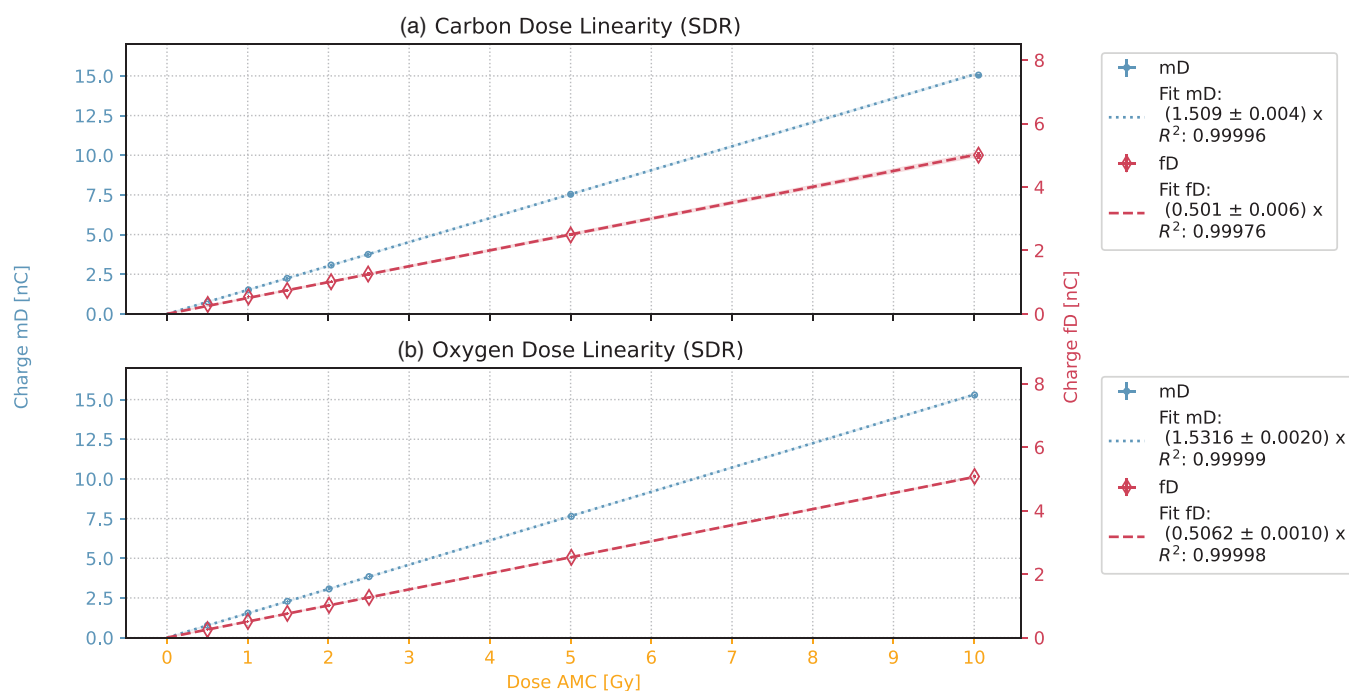


FIGURE 6 Dose linearity for SDR field irradiation for carbon in the upper plot and for oxygen in the lower plot. The data points for mD and fD are presented with their respective standard deviations. The right-hand side legends provide the fit parameter value, its standard deviation, and the R^2 for the fit. The 1σ standard deviation is included in the plots as a shaded area. mD, microDiamond; fD, flashDiamond.

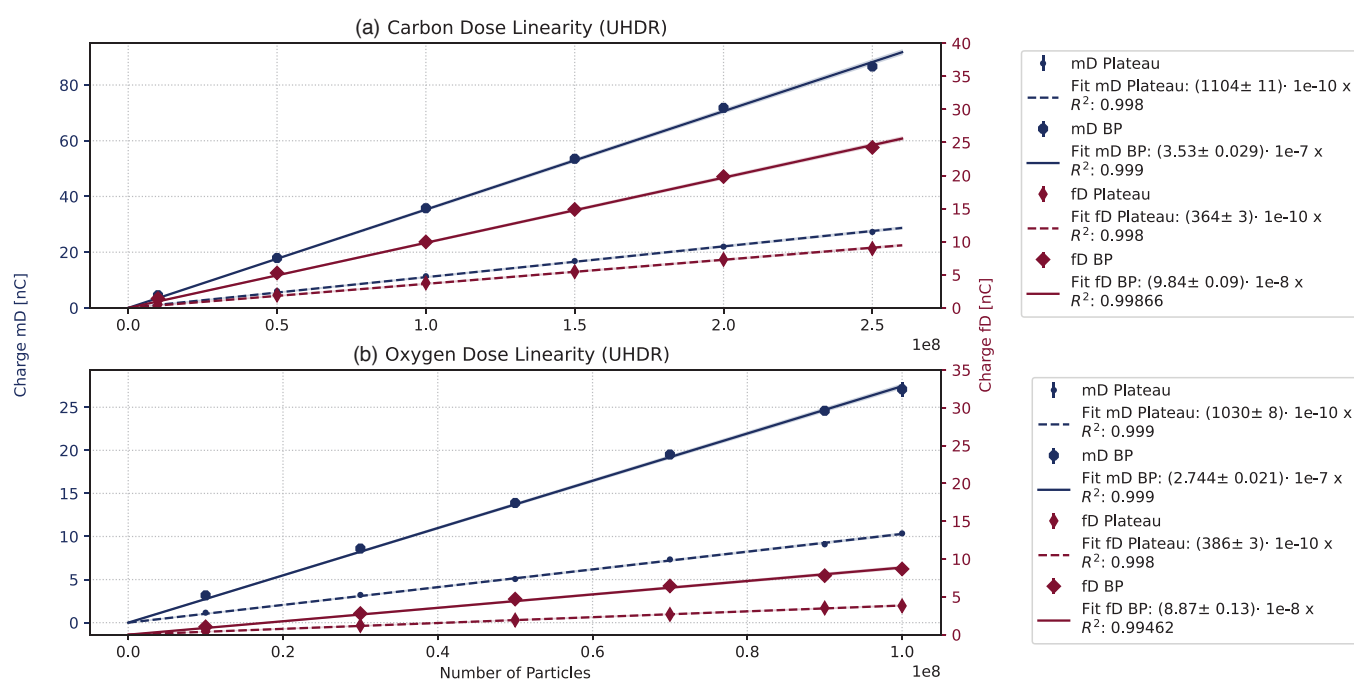


FIGURE 7 Dose linearity after UHDR single spot irradiation for carbon in the upper plot and for oxygen in the lower plot. The data points for mD and fD are presented with their respective standard deviations. The measured values for the plateau are marked with smaller symbols and a dashed line, while for the BP measurement a with larger symbols and a solid line was chosen. The right-hand side legends provide the fit parameter value, its standard deviation, and the R^2 for the fit. The 1σ standard deviation is included in the plots as a shaded area. BP, Bragg Peak; mD, microDiamond; UHDR, Ultra-High Dose Rate.

Consequently, reliable real-time beam monitoring with devices such as the fD is becoming increasingly important.²⁰ This capability allows precise instantaneous dose rate measurements when coupled to a digital oscilloscope, which is crucial for investigating the role of dose delivery structure in the FLASH effect during heavy ion therapy.

ACKNOWLEDGMENTS

This work was supported in part by the NIH-P01CA257904, German Research Council (DFG-Unite: SFB1389/2C05) and intramural funds from National Center for Tumor Diseases (NCT-PRO: 1030000042 and Biodose: 1030000043 programs). The authors would like to thank the whole accelerator team at HIT for helping with the synchrotron adjustments.

Open access funding enabled and organized by Projekt DEAL.

CONFLICT OF INTEREST STATEMENT

Rafael Kranzer is a PTW employee, while Marco Marinelli and Gianluca Verona-Rinati signed a contract with PTW-Freiburg involving financial interests derived from the PTW diamond detector's commercialization. The funding sources had no role in the study design, data collection, analysis, interpretation, or the decision to submit the results for publication. All other authors declare that there are no conflicts of interest regarding the publication of this paper.

DATA AVAILABILITY STATEMENT

Research data is stored in an institutional repository and will be shared upon request to the corresponding author.

REFERENCES

- Wilson JD, Hammond EM, Higgins GS, Petersson K. Ultra-high dose rate (FLASH) radiotherapy: silver bullet or fool's gold?. *Front Oncol.* 2020;9:1563.
- Friedl AA, Prise KM, Butterworth KT, Montay-Gruel P, Favaudon V. Radiobiology of the FLASH effect. *Med Phys.* 2021;49(3):1993-2013. doi:10.1002/mp.15184
- Tessonnier T, Mein S, Walsh DW, et al. FLASH dose rate helium ion beams: first in vitro investigations. *Inter J Radiation Oncol Biol Phys.* 2021;111(4):1011-1022.
- Favaudon V, Caplier L, Monceau V, et al. Ultrahigh dose-rate FLASH irradiation increases the differential response between normal and tumor tissue in mice. *Sci Transl Med.* 2014;6(245):245ra93-245ra93.
- Limoli CL, Vozenin MC. Reinventing radiobiology in the light of FLASH radiotherapy. *Ann Rev Cancer Biol.* 2023;7(1):1-21.
- Bourhis J, Sozzi WJ, Jorge PG, et al. Treatment of a first patient with FLASH-radiotherapy. *Radiother Oncol.* 2019;139:18-22. doi:10.1016/j.radonc.2019.06.019
- Mascia AE, Daugherty EC, Zhang Y, et al. Proton FLASH radiotherapy for the treatment of symptomatic bone metastases: the FAST-01 nonrandomized trial. *JAMA Oncol.* 2022.
- Durante M, Loeffler JS. Charged particles in radiation oncology. *Nat Rev Clin Oncol.* 2009;7(1):37-43. doi:10.1038/nrclinonc.2009.183
- Klein C, Dokic I, Mairani A, et al. Overcoming hypoxia-induced tumor radioresistance in non-small cell lung cancer by targeting DNA-dependent protein kinase in combination with carbon ion irradiation. *Radiat Oncol.* 2017;12(1):1-8.
- Bassler N, Toftegaard J, Lühr A, et al. LET-painting increases tumour control probability in hypoxic tumours. *Acta Oncol.* 2014;53(1):25-32.
- Tinganelli W, Sokol O, Quartieri M, et al. Ultra-high dose rate (FLASH) carbon ion irradiation: dosimetry and first cell experiments. *Int J Radiation Oncol Biol Phys.* 2022;112(4):1012-1022.
- Weber UA, Scifoni E, Durante M. FLASH radiotherapy with carbon ion beams. *Med Phys.* 2022;49(3):1974-1992.
- Tinganelli W, Weber U, Puspitasari A, et al. FLASH with carbon ions: tumor control, normal tissue sparing, and distal metastasis in a mouse osteosarcoma model. *Radiother Oncol.* 2022;175:185-190.
- Tinganelli W, Sokol O, Puspitasari A, et al. FLASH Bragg-peak irradiation with a therapeutic carbon ion beam: first in vivo results. *Biorxiv.* 2024:2024-2007.
- Jansen J, Beyreuther E, García-Calderón D, et al. Changes in radical levels as a cause for the FLASH effect: impact of beam structure parameters at ultra-high dose rates on oxygen depletion in water. *Radiother Oncol.* 2022;175:193-196.
- Ruan JL, Lee C, Wouters S, et al. Irradiation at ultra-high (FLASH) dose rates reduces acute normal tissue toxicity in the mouse gastrointestinal system. *International Journal of Radiation Oncology Biology Physics.* 2021;111(5):1250-1261.
- Karsch L, Pawelke J, Brand M, et al. Beam pulse structure and dose rate as determinants for the flash effect observed in zebrafish embryo. *Radiother Oncol.* 2022;173:49-54.
- Romano F, Bailat C, Jorge PG, Lerch MLF, Darafsheh A. Ultra-high dose rate dosimetry: challenges and opportunities for FLASH radiation therapy. *Med Phys.* 2022;49(7):4912-4932. doi:10.1002/mp.15649
- Böhlen T, Psoroulas S, Aylward JD, et al. Recording and reporting of ultra-high dose rate "FLASH" delivery for preclinical and clinical settings. *Radiother Oncol.* 2024;200:110507.
- Psoroulas S, Aylward JD, Beddar S, et al. Recording and reporting of ultra-high dose rate "FLASH" delivery for preclinical and clinical settings. *Radiother Oncol.* 2024;200:110507. doi:10.1016/j.radonc.2024.110507
- Rank L, Dogan O, Kopp B, et al. Development and benchmarking of a dose rate engine for raster-scanned FLASH helium ions. *Med Phys.* 2024;51(3):2251-2262.
- Karger CP, Jäkel O, Palmans H, Kanai T. Dosimetry for ion beam radiotherapy. *Phys Med Biol.* 2010;55(21):R193.
- Angelou C, Patallo IS, Doherty D, Romano F, Schettino G. A review of diamond dosimeters in advanced radiotherapy techniques. *Med Phys.* 2024;51(12):9230-9249. doi:10.1002/mp.17370
- Rossomme S, Delor A, Lorentini S, et al. Three-voltage linear method to determine ion recombination in proton and light-ion beams. *Phys Med Biol.* 2020;65(4).
- IAEA. Absorbed dose determination in external beam radiotherapy: an international code of practice for dosimetry based on standards of absorbed dose to water. Technical Reports Series No. 398. IAEA; 2000.
- Togno M, Nesteruk KP, Schäfer R, et al. Ultra-high dose rate dosimetry for pre-clinical experiments with mm-small proton fields. *Physica Med.* 2022;104:101-111.
- Di Martino F, Barca P, Barone S, et al. FLASH radiotherapy with electrons: issues related to the production, monitoring, and dosimetric characterization of the beam. *Front Phys.* 2020;8. doi:10.3389/fphy.2020.570697
- Looe HK, Poppinga D, Kranzer R, et al. The role of radiation-induced charge imbalance on the dose-response of a commercial synthetic diamond detector in small field dosimetry. *Med Phys.* 2019;46(6):2752-2759. doi:10.1002/mp.13542

29. Subiel A, Romano F. Recent developments in absolute dosimetry for FLASH radiotherapy. *Br J Radiol.* 2023;96(1148):20220560. [10.1259/bjr.20220560](https://doi.org/10.1259/bjr.20220560)
30. Baack L, Schuy C, Brons S, et al. Reduction of recombination effects in large plane parallel beam monitors for FLASH radiotherapy with scanned ion beams. *Physica Med.* 2022;104:136–144.
31. Gómez F, Gonzalez-Castaño DM, Fernández NG, et al. Development of an ultra-thin parallel plate ionization chamber for dosimetry in FLASH radiotherapy. *Med Phys.* 2022;49(7):4705–4714. [10.1002/mp.15668](https://doi.org/10.1002/mp.15668)
32. Ashraf MR, Rahman M, Zhang R, et al. Dosimetry for FLASH radiotherapy: a review of tools and the role of radioluminescence and cherenkov emission. *Front Phys.* 2020;8:328. [10.3389/fphy.2020.00328](https://doi.org/10.3389/fphy.2020.00328)
33. Birks JB. Scintillations from organic crystals: specific fluorescence and relative response to different radiations. *Proc Phys Soc A.* 1951;64(10):874. doi:[10.1088/0370-1298/64/10/303](https://doi.org/10.1088/0370-1298/64/10/303)
34. Tretyak VI. Semi-empirical calculation of quenching factors for ions in scintillators. *Astropart Phys.* 2010;33(1):40–53. [10.1016/j.astropartphys.2009.11.002](https://doi.org/10.1016/j.astropartphys.2009.11.002)
35. Wang LLW, Perles LA, Archambault L, Sahoo N, Mirkovic D, Beddar S. Determination of the quenching correction factors for plastic scintillation detectors in therapeutic high-energy proton beams. *Phys Med Biol.* 2012;57(23):7767. [10.1088/0031-9155/57/23/7767](https://doi.org/10.1088/0031-9155/57/23/7767)
36. Giguère C, Hart A, Bateman J, et al. Radiation damage and recovery of plastic scintillators under ultra-high dose rate 200 MeV electrons at CERN CLEAR facility. *arXiv preprint arXiv:241012535*.
37. Marinelli M, Prestopino G, Verona C, et al. Dosimetric characterization of a microDiamond detector in clinical scanned carbon ion beams. *Med Phys.* 2015;42(4):2085–2093.
38. Bucciolini M, Banci Buonamici F, Mazzocchi S, De Angelis C, Onori S, Cirrone GaP. Diamond detector versus silicon diode and ion chamber in photon beams of different energy and field size. *Med Phys.* 2003;30(8):2149–2154. doi:[10.1118/1.1591431](https://doi.org/10.1118/1.1591431)
39. Lempart M, Blad B, Adrian G, et al. Modifying a clinical linear accelerator for delivery of ultra-high dose rate irradiation. *Radiother Oncol.* 2019;139:40–45. doi:[10.1016/j.radonc.2019.01.031](https://doi.org/10.1016/j.radonc.2019.01.031)
40. Ciancaglion I, Marinelli M, Milani E, et al. Dosimetric characterization of a synthetic single crystal diamond detector in clinical radiation therapy small photon beams. *Med Phys.* 2012;39(7Part1):4493–4501. doi:[10.1118/1.4729739](https://doi.org/10.1118/1.4729739)
41. Lagomarsino S, Bellini M, Corsi C, et al. Radiation hardness of three-dimensional polycrystalline diamond detectors. *Appl Phys Lett.* 2015;106(19):193509. doi:[10.1063/1.4921116](https://doi.org/10.1063/1.4921116)
42. PTW. *microDiamond*. 2025. Accessed January 29, 2025. <https://www.ptwdosimetry.com/en/products/microdiamond>
43. PTW. *flashDiamond*. 2025. Accessed February 3, 2025. <https://www.ptwdosimetry.com/en/products/flashdiamond-detector>
44. Milluzzo G, De Napoli M, Di Martino F, et al. Comprehensive dosimetric characterization of novel silicon carbide detectors with UHDR electron beams for FLASH radiotherapy. *Med Phys.* 2024;51(9):6390–6401. doi:[10.1002/mp.17172](https://doi.org/10.1002/mp.17172)
45. Verona Rinati G, Felici G, Galante F, et al. Application of a novel diamond detector for commissioning of FLASH radiotherapy electron beams. *Med Phys.* 2022;49(8):5513–5522. doi:[10.1002/mp.15782](https://doi.org/10.1002/mp.15782)
46. Tessonnier T, Verona-Rinati G, Rank L, Kranzer R, Mairani A, Marinelli M. Diamond detectors for dose and instantaneous dose-rate measurements for ultra-high dose-rate scanned helium ion beams. *Med Phys.* 2024;51(2):1450–1459.
47. Rossomme S, Marinelli M, Verona-Rinati G, et al. Response of synthetic diamond detectors in proton, carbon, and oxygen ion beams. *Med Phys.* 2017;44(10):5445–5449.
48. Subiel A, Bourgouin A, Kranzer R, et al. Metrology for advanced radiotherapy using particle beams with ultra-high dose rates. *Phys Med Biol.* 2024;69(14):14TR01. doi:[10.1088/1361-6560/ad539d](https://doi.org/10.1088/1361-6560/ad539d)
49. Marinelli M, Felici G, Galante F, et al. Design, realization, and characterization of a novel diamond detector prototype for FLASH radiotherapy dosimetry. *Med Phys.* 2022;49(3):1902–1910. [10.1002/mp.15473](https://doi.org/10.1002/mp.15473)
50. Almaviva S, Marinelli M, Milani E, et al. Chemical vapor deposition diamond based multilayered radiation detector: physical analysis of detection properties. *J Appl Phys.* 2010;107(1):014511. [10.1063/1.3275501](https://doi.org/10.1063/1.3275501)
51. Tessonnier T, Marcelos T, Mairani A, Brons S, Parodi K. Phase space generation for proton and carbon ion beams for external users' applications at the Heidelberg Ion Therapy Center. *Front Oncol.* 2016;5:297.
52. Parodi K, Mairani A, Brons S, et al. Monte Carlo simulations to support start-up and treatment planning of scanned proton and carbon ion therapy at a synchrotron-based facility. *Phys Med Biol.* 2012;57(12):3759.
53. Ondreka D, Weinrich U, The Heidelberg Ion Therapy (HIT) accelerator coming into operation. In: *Proceedings of the European Particle Accelerator Conference (EPAC08)*. 2008:979–981.
54. Schömers C, Feldmeier E, Naumann J, Panse R, Peters A, Haberer T. The intensity feedback system at heidelberg ion-beam therapy centre. *Nucl Instrum Methods Phys Res A.* 2015;795:92–99.
55. Schömers C, Brons S, Cee R, Peters A, Scheloske S, Haberer T. Beam properties beyond the therapeutic range at hit. In: *Proceedings of IPAC 23*, 2023. Paper THPM064. Published online 2022.
56. Kurz C, Mairani A, Parodi K. First experimental-based characterization of oxygen ion beam depth dose distributions at the Heidelberg Ion-Beam Therapy Center. *Phys Med Biol.* 2012;57(15):5017.
57. Böhlen TT, Cerutti F, Dosanjh M, et al. Benchmarking nuclear models of FLUKA and GEANT4 for carbon ion therapy. *Phys Med Biol.* 2010;55(19):5833. [10.1088/0031-9155/55/19/014](https://doi.org/10.1088/0031-9155/55/19/014)
58. Kanouta E, Poulsen PR, Kertzscher G, Sitarz MK, Sørensen BS, Johansen JG. Time-resolved dose rate measurements in pencil beam scanning proton FLASH therapy with a fiber-coupled scintillator detector system. *Med Phys.* 2023;50(4):2450–2462. [10.1002/mp.16156](https://doi.org/10.1002/mp.16156)

How to cite this article: Karle C, Verona-Rinati G, Brons S, et al. Characterizing diamond detectors for various dose and dose rate measurements in scanned carbon and oxygen beams. *Med Phys.* 2025;52:e17893. <https://doi.org/10.1002/mp.17893>

6.2 “Oxygen Consumption Measurements at Ultra-High Dose Rate over a Wide LET Range”

Authors	<u>Celine Karle</u> , Hans Liew, Thomas Tessonnier, Stewart Mein, Kristoffer Petersson, Christian Schömers, Stefan Scheloske, Stephan Brons, Rainer Cee, Gerald Major, Thomas Haberer, Amir Abdollahi, Jürgen Debus, Ivana Dokic, Andrea Mairani
Publication Status	Published - 06 November 2024
Journal	Medical Physics
DOI	https://doi.org/10.1002/mp.17496
Contribution	<u>CK</u> , HL, and AM contributed to the conceptualization and methodology of the study. KP provided the OxyLite™ measurement device. TT, SB, RC, SS, and CS ensured the technical resources and requirements at the HIT facility, while GM contributed technical support and dosimetry at the Mobetron. <u>CK</u> was responsible for data acquisition, curation, and formal analysis. The interpretation of the results was performed by <u>CK</u> , HL, and AM. All visualizations were prepared by <u>CK</u> . The original draft was written by <u>CK</u> with the assistance of HL. The manuscript was reviewed and edited by <u>CK</u> , HL, TT, KP, CS, SS, SB, RC, GM, and AM. Supervision was provided by AM, SM, and ID, while TH, AA, and JD contributed to funding acquisition and clinical direction.

©2024 The Author(s). Medical Physics published by Wiley Periodicals LLC on behalf of American Association of Physicists in Medicine. This is an open access article under the terms of the Creative Commons Attribution License, which permits use, distribution and reproduction in any medium, provided the original work is properly cited.

RESEARCH ARTICLE

MEDICAL PHYSICS

Oxygen consumption measurements at ultra-high dose rate over a wide LET range

Celine Karle^{1,2} | Hans Liew^{1,3,4} | Thomas Tessonier^{5,6} | Stewart Mein^{1,3,4,7} |
 Kristoffer Petersson⁸ | Christian Schömers⁵ | Stefan Scheloske⁵ |
 Stephan Brons⁵ | Rainer Cee⁵ | Gerald Major⁹ | Thomas Haberer⁵ |
 Amir Abdollahi^{1,3,4} | Jürgen Debus^{3,4,5,9} | Ivana Dokic^{1,3,4} | Andrea Mairani^{1,5,9,10}

¹Clinical Cooperation Unit Translational Radiation Oncology, National Center for Tumor Diseases (NCT), Heidelberg University Hospital (UKHD) and German Cancer Research Center (DKFZ), Heidelberg, Germany

²Department of Physics and Astronomy, Heidelberg University, Heidelberg, Germany

³Division of Molecular and Translational Radiation Oncology, Heidelberg Faculty of Medicine (MFHD) and Heidelberg University Hospital (UKHD), Heidelberg Ion-Beam Therapy Center (HIT), Heidelberg, Germany

⁴Heidelberg Institute of Radiation Oncology (HIRO), National Center for Radiation Oncology (NCRO), Heidelberg University and German Cancer Research Center (DKFZ), Heidelberg, Germany

⁵Heidelberg Ion-Beam Therapy Center (HIT), Department of Radiation Oncology, Heidelberg University Hospital, Heidelberg, Germany

⁶Clinical Cooperation Unit Radiation Oncology, National Center for Tumor Diseases (NCT), Heidelberg University Hospital (UKHD) and German Cancer Research Center (DKFZ), Heidelberg, Germany

⁷Department of Radiation Oncology, University of Pennsylvania, Philadelphia, Pennsylvania, USA

⁸Oxford Institute for Radiation Oncology, Department of Oncology, Old Road Campus Research Building, University of Oxford, Oxford, UK

⁹Department of Radiation Oncology, Heidelberg University Hospital, Heidelberg Institute of Radiation Oncology (HIRO), University Hospital Heidelberg, National Center for Tumor Diseases (NCT), University Hospital Heidelberg, Heidelberg, Germany

¹⁰National Center for Oncological Hadrontherapy (CNAO), Medical Physics, Pavia, Italy

Correspondence

Andrea Mairani, Heidelberg Ion-beam Therapy Center (HIT), Im Neuenheimer Feld (INF) 450, Heidelberg, DE 69120, Germany.
 Email:
Andrea.Mairani@med.uni-heidelberg.de

Funding information

German Research Council, Grant/Award Number: SFB1389/2C05; National Center for Tumor Diseases, Grant/Award Numbers: NCT-PRO: 1030000042, Biodose: 1030000043; National Institutes of Health, Grant/Award Number: NIH-1P01CA257904-01A1

Abstract

Background: The role of radiolytic oxygen consumption for the in-vitro “Ultra-High Dose Rate” (UHDR) sparing and in-vivo FLASH effect is subject to active debate, but data on key dependencies such as the radiation quality are lacking.

Purpose: The influence of “dose-averaged Linear Energy Transfer” (LET_d) and dose rate on radiolytic oxygen consumption was investigated by monitoring the oxygen concentration during irradiation with electrons, protons, helium, carbon, and oxygen ions at UHDR and “Standard Dose Rates” (SDR).

Methods: Sealed “Bovine Serum Albumin” (BSA) 5% samples were exposed to 15 Gy of electrons and protons, and for the first time helium, carbon, and oxygen ions with LET_d values of 1, 5.4, 14.4, 65, and 100.3 keV/μm, respectively, delivered at mean dose rates of either 0.3–0.4 Gy/s for SDR or approximately 100 Gy/s for UHDR. The Oxylite (Oxford Optronics) system allowed measurements of the oxygen concentration before and after irradiation to calculate the oxygen consumption rate.

Results: The oxygen consumption rate was found to decrease with increasing LET_d from 0.351 mmHg/Gy for low LET electrons to 0.1796 mmHg/Gy for

This is an open access article under the terms of the [Creative Commons Attribution](https://creativecommons.org/licenses/by/4.0/) License, which permits use, distribution and reproduction in any medium, provided the original work is properly cited.

© 2024 The Author(s). *Medical Physics* published by Wiley Periodicals LLC on behalf of American Association of Physicists in Medicine.

high LET oxygen ions at SDR and for UHDR from 0.317 to 0.1556 mmHg/Gy, respectively. A higher consumption rate for SDR irradiation compared to the corresponding UHDR irradiation persisted for all particle types.

Conclusion: The measured consumption rates demonstrate a distinct LETd dependence. The obtained dataset, encompassing a wide range of LETd values, could serve as a benchmark for Monte Carlo simulations, which may aid in enhancing our comprehension of oxygen-related mechanisms after irradiations. Ultimately, they could help assess the viability of different hypotheses regarding UHDR sparing mechanisms and the FLASH effect. The found LETd dependence underscores the potential of heavy ion therapy, wherein elevated consumption rates in adjacent normal tissue offer protective benefits, while leaving tumor regions with generally higher “Linear Energy Transfer” (LET) vulnerable.

KEYWORDS

heavy ions, LET, oxygen consumption

1 | INTRODUCTION

Since the 1920s, the pivotal role of oxygen concentration in influencing cellular sensitivity to radiation and, consequently, radiotherapy outcomes has been recognized.¹ When incident radiation interacts with the water molecules, free radicals are produced, which are important contributors to the induction of DNA damage. Subsequent chemical reactions consume the present molecular oxygen.^{2,3} The radiolytic reaction cascades and oxygen concentration are linked to the physical beam parameters, specifically, dose rate, and “dose-averaged Linear Energy Transfer” (LETd).^{4–6}

The recent resurgence of interest in the oxygen effect emerged mainly by the first reports of the so-called FLASH effect in 2014.⁷ The FLASH effect describes the differential response of normal and tumor tissue in vivo to “Ultra-High Dose Rate” (UHDR) irradiation above 40 Gy/s, with the former being spared and the latter being treated iso-effectively compared to the same dose irradiated at “Standard Dose Rates” (SDR) approximately 0.001–0.5 Gy/s.⁸ However, the underlying mechanisms of the in vivo FLASH effect remain to be elucidated.

As early as 1959, in vitro experiments to investigate dose-rate-dependent mechanisms showed an increase in cell survival rates after UHDR irradiation.⁶ On this cellular level, the extent of UHDR sparing was generally found to be affected by the oxygen concentration within the system leading many to believe that oxygen and the oxygen consumption processes play a key role in the underlying sparing mechanism.^{9–12}

The “oxygen depletion hypothesis” postulates that the reactions induced by UHDR radiation could consume oxygen, resulting in a transient state of oxygen deprivation that could protect the cells.^{9,11} Since it takes about 50 ms to unload oxygen from oxyhemoglobin alone, re-oxygenation begins long after the free radical chem-

istry has started after the incident UHDR irradiation, and the cells remain in a state of oxygen depletion.¹³ Consequently, during prolonged SDR irradiation where the irradiation timescale could be in the same range or even longer than the reoxygenation timescale, reoxygenation could counteract the oxygen consumption during the irradiation time.¹² This explanation has been criticized since the radiation-induced decrease in oxygen concentration may not be sufficient to induce the hypoxic state that would explain the overall sparing effect.^{14,15}

Another contributing factor might be altered radical-radical interactions. After UHDR exposure, the reactions occur in closer spatiotemporal proximity, which promotes radical-radical interactions.

A common feature of the proposed mechanisms is that the dynamics of the chemical reactions differ between UHDR and SDR irradiation.¹⁶ Therefore, direct measurements of the outcome of these reactions, like the changes in oxygen concentration, are crucial for assessing the plausibility of these approaches and understanding irradiation-induced reactions with oxygen. Such measurements have already been conducted in deionized water^{15,17} and solutions closer to biological systems,¹⁷ such as “Bovine Serum Albumin” (BSA)¹⁴ or CELL,¹⁸ a solution mimicking the intracellular environment. The studies conducted in such surrogate media using electron or proton beams consistently found that the UHDR oxygen consumption rate is smaller than the corresponding SDR value. For UHDR irradiation with heavier ions, so far only in silico studies have explored the additional factor of LETd.^{19,20}

In this study, we conducted a comprehensive examination of oxygen consumption measurements at various LETds up to 100.3 keV/μm. Beyond electrons and protons, we, for the first time, irradiated BSA 5% samples additionally with helium, carbon, and oxygen ions at UHDR and SDR. We discuss the reasons behind observed oxygen consumption trends as well as the

potential implications for FLASH dose rates in heavy ion therapy and their contribution to understanding the underlying mechanisms of UHDR sparing.

2 | MATERIAL AND METHODS

2.1 | Sample preparation

Prior to each irradiation, a fresh BSA 5% stock was prepared with BSA from ROTH (Art.-Nr. 0163.3) dissolved in DPBS from Gibco (Kat.Nr. 14190250). The air-equilibrated stock was filled into 2 mL Eppendorf tubes. The electron irradiation field covered the entire sample, while for irradiations at the “Heidelberg Ion-Beam Therapy Center” (HIT), the Eppendorf tubes were cut off at 1 mL to fit into the 2 cm “Spread-Out Bragg Peak” (SOBP). The Eppendorf tubes were sealed with parafilm while maintaining a bubble-free environment to inhibit reoxygenation.

2.2 | Oxygen measurement

The oxygen measurements during irradiation were conducted with the OxyLite system (Oxford Optonix). The NX-BF/OT/E Oxygen/Temperature bare-fiber sensor attached to the OxyLite system measures the lifetime of fluorescence in ruthenium luminophore, located in the silicon rubber polymer of the probe tip. Since the presence of oxygen quenches the fluorescence lifetime, the latter is inversely proportional to the oxygen concentration. Using this method, the oxygen concentration in the liquid is determined.²¹ OxyLite was shown

to provide reliable oxygen concentration values²¹ with 10% accuracy in the range of 7–150 mmHg, and below 7 mmHg an accuracy of ± 0.7 mmHg. All used sensors were pre-calibrated and possess an internal temperature compensation.

2.3 | Irradiation setup and dosimetry

For electron irradiation, the Mobetron from IntraOp was utilized (Figure 1). The dose rate of the 9 MeV beam was modified by adjusting the pulse repetition frequency and pulse length (Table 1). The dosimetry mimicking the required setup was conducted with the “FLASH- μ Diamond” (PTW, SN:7602), which was cross-calibrated with an Advanced Marcus chamber (PTW, REF: TM34045, SN:0535).

The samples were horizontally positioned within a dedicated phantom and uniformly irradiated from above by a circular field with a diameter of 6 cm (Figure 1).

The active raster scanning delivery of protons (p), helium (^4He), carbon (^{12}C), and oxygen (^{16}O) ions was performed at the HIT experimental room (Figure 2 and Table 2). The LETd of the p, ^4He , ^{12}C , and ^{16}O beams were estimated using FLUKA “Monte Carlo” (MC) simulations^{23,24} to be approx. 5.4 (range in the region of interest 4.9–6.0 keV/ μm) keV/ μm , 14.4 (12–33) keV/ μm , 65 (56–153) keV/ μm , and 100.3 (88–235) keV/ μm , respectively. Daily dosimetric measurements were conducted with a PinPoint ionization chamber (PTW, REF: TM31015, SN:0903)²⁵ following clinical practice TRS398 to guarantee a correct dose application. Additionally, Gafchromic EBT3 films (8”X10” (x25), Ashland 828204) were irradiated to ensure the homogeneity of

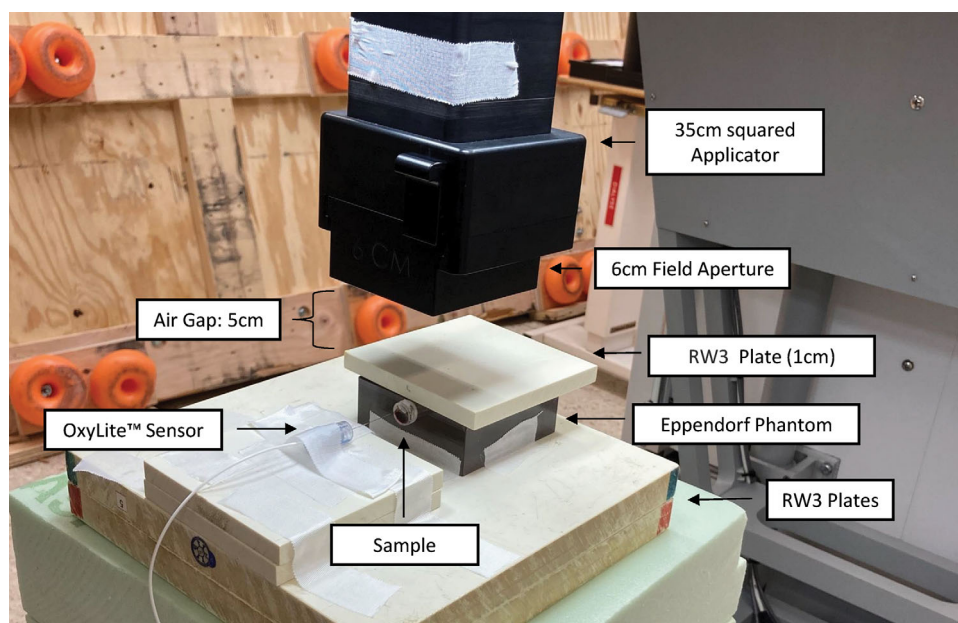


FIGURE 1 Experimental setup at the Mobetron for electron SDR and UHDR irradiation of the Eppendorf tubes.

TABLE 1 Dosimetry measurements and setting details for electron SDR and UHDR irradiation with the Mobetron (IntraOp) for the planned dose of 15 Gy. The dose values are averages of at least three values and standard deviations are given.

Field diameter (cm)	Source-surface distance (cm)	Extraction energy (MeV)	Mean LETd (keV/μm)	Mean dose rate (Gy/s)	Pulse repetition frequency (Hz)	Puls length (μs)	Radiation unit	Dose (Gy)
6	40	9	1	0.338 ± 0.003	30	1.2	707 Monitor Units	15.011 ± 0.005
				112.2 ± 0.9	45	4	6 Pulses	15.01 ± 0.18

The electrons LETd was estimated to be 1 keV/μm.²²

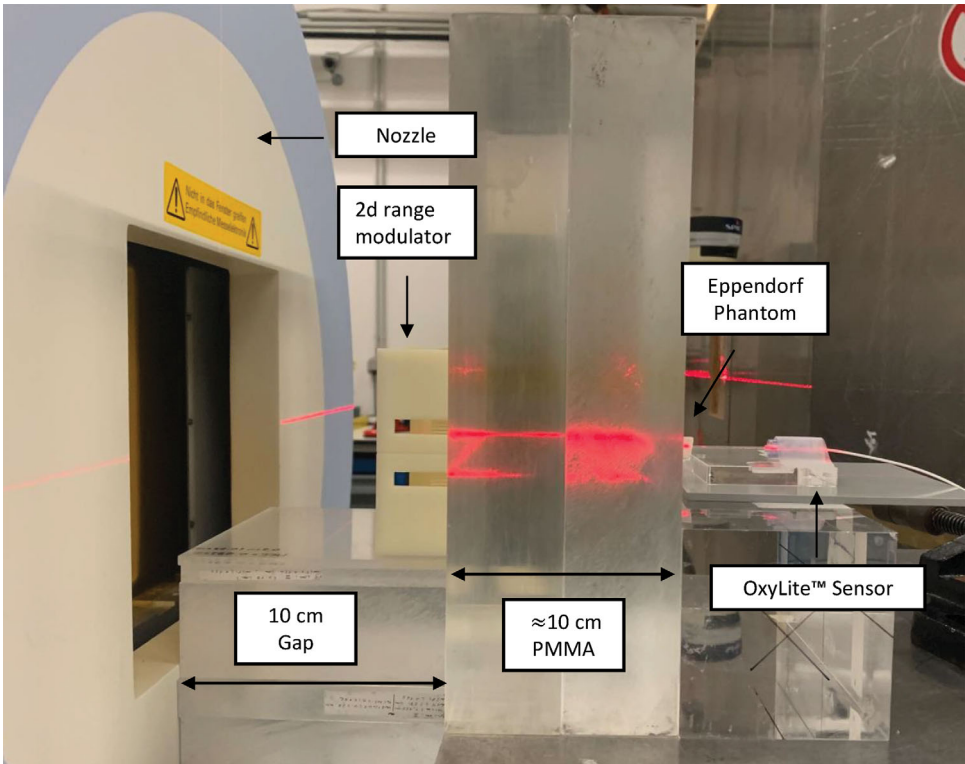


FIGURE 2 Experimental setup at the HIT beamline for SDR and UHDR irradiation of the Eppendorf tubes with protons, helium, carbon, and oxygen ions.

TABLE 2 Field and irradiation parameter details for SDR and UHDR irradiation at the HIT facility.

Particle	Field size (mm ²)	Spot spacing (mm)	Mean LETd (keV/μm)	Extraction energy (MeV/u)	Mean dose rate (Gy/s)	Delivery time (s)	Spill time (ms)	Interspill time (s)	Dose (Gy)
p	12	3	5.4 [range 4.9–6.0]	146.56	0.40 ± 0.03	38 ± 3	533 ± 67	3.46 ± 0.03	14.997 ± 0.026
					121 ± 8	0.125 ± 0.008	125 ± 8	–	15.08 ± 0.03
⁴ He	10	2	14.4 [range 12.0–33.0]	145.74	0.4074 ± 0.0015	36.82 ± 0.12	336.0 ± 1.7	3.654 ± 0.004	15.003 ± 0.015
					121 ± 6	0.125 ± 0.006	125 ± 6	–	15.07 ± 0.12
¹² C	10.5	1.5	65 [range 56–153]	275.98	0.341 ± 0.009	44.6 ± 1.2	696 ± 115	4.5 ± 0.8	15.21 ± 0.11
					113 ± 8	0.136 ± 0.009	136 ± 9	–	15.27 ± 0.12
¹⁶ O	9	1.5	100.3 [range 88.0–235.0]	325.98	0.309 ± 0.010	48.5 ± 1.6	876 ± 154	4.39 ± 0.05	15.02 ± 0.04
					108 ± 10	0.138 ± 0.012	137 ± 12	–	14.86 ± 0.16

All values are averaged from at least three samples and are given with their standard deviations. The “Delivery Time” describes the time span from the beginning of the first spill to the end of the last one, while the “Interspill Time” lasts from the end of one spill until the beginning of the following spill. The “Spill Time” refers to the temporal length of a single spill. The “Mean Dose Rate” is calculated by dividing the delivered dose by the delivery time.

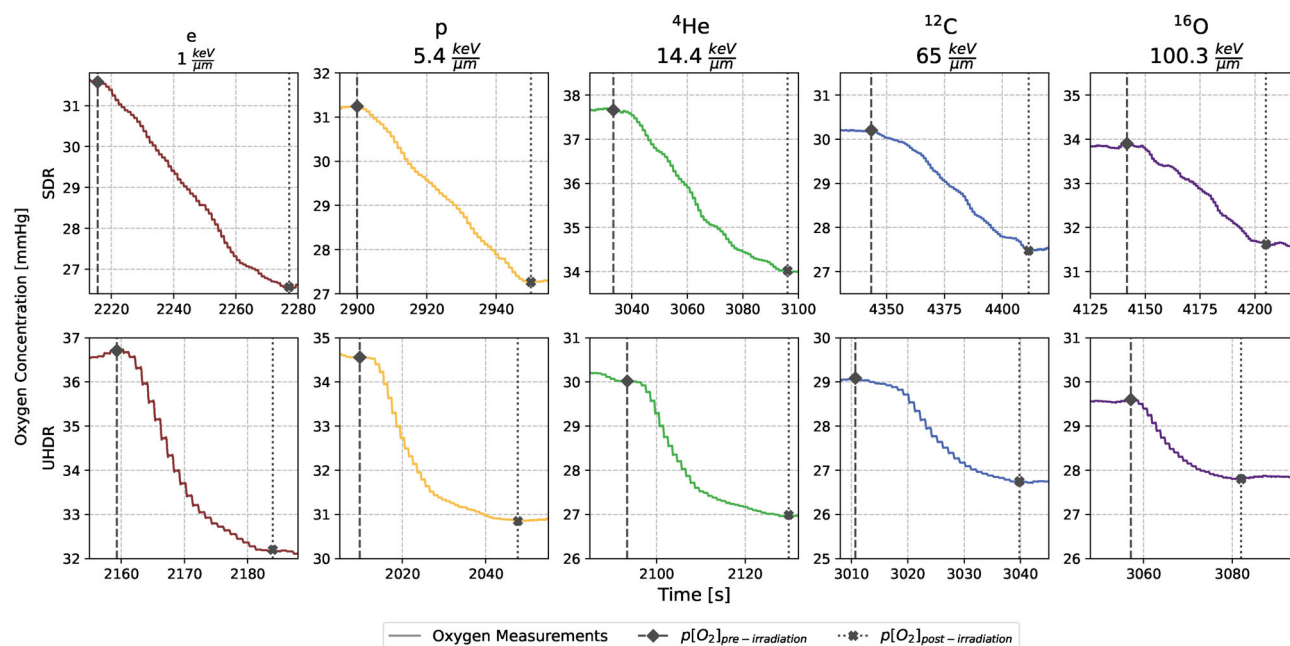


FIGURE 3 Examples for each particle and dose rate combination of the oxygen concentration over time during a single irradiation. The LETd values are given in the subtitles. $p[\text{O}_2]_{\text{pre-irradiation}}$ is the oxygen concentration marked with a black diamond and a dashed line before the radiation has started, while $p[\text{O}_2]_{\text{post-irradiation}}$ symbolized with a cross mark and a dotted line hints at the start concentration equilibrium after the dose application. The y-axis always shows a range of 5 mmHg for better comparability, while the time-axis is chosen to display the whole consumption process. Due to the 20 s response time of the OxyLite, the drop in oxygen concentration after UHDR irradiation is not instantaneous, but rather slowly decreases as the sensor equilibrates with the depleted medium.

the fields. The monitoring chamber in the beam nozzle was flushed with 96%/4% helium/ CO_2 gas mixture, to prevent saturation during UHDR irradiations.²⁶ Therewith, the spill length and its delivery could be monitored and evaluated (Table 2). All plans have a field size larger than $9 \times 9 \text{ mm}^2$ to ensure full coverage of the Eppendorf tubes. The spot spacings were adapted to the different lateral scattering properties of the particles. To ensure comparability between UHDR and SDR plans, the field size and spot spacing patterns were kept identical for each ion. Only two key parameters were changed between the two modes, namely the beam current and the number of spills. First, to bunch all particles into one single spill for the UHDR irradiation, the requested beam current was increased by a factor of approximately 100. This enables a faster particle extraction using a stronger radiofrequency-knockout exciter amplitude.²⁷ Second, the total amount of particles from the UHDR plan was split into 10 separate spills for the SDR. Therewith, a clinical SDR of about 0.3–0.4 Gy/s on average was achieved.²⁸

To employ the clinically established active raster beam scanning delivery technique, it is necessary to extend the pristine Bragg peak from the delivered monoenergetic beams to cover the entire sample during a single spill. For this purpose, a “2-Dimensional Range Modulator” (2DRM) was used.^{29,30} The $10 \times 10 \text{ cm}^2$ 2DRM contains 50×50 pins with a length of 20 mm to produce a 2 cm SOB. Depth dose curves were assessed for

each particle (Figure S1).²⁸ The samples were placed horizontally into a dedicated “Poly(methyl methacrylate)” (PMMA) phantom and slices of PMMA were positioned in front of the samples (Figure 2).²⁸

2.4 | Data evaluation and statistical analysis

At least three independent replicates were evaluated with the recordings from the OxyLite Software LabChart8 (v8.1.19). To assess the oxygen consumption rate g [mmHg/Gy], the stabilized oxygen concentration after irradiation $p[\text{O}_2]_{\text{post-irradiation}}$ [mmHg] was subtracted from the concentration before irradiation $p[\text{O}_2]_{\text{pre-irradiation}}$ [mmHg] (Figure 3). This value was divided by the actual applied doses D [Gy] given from dosimetric measurements:

$$g = \frac{p[\text{O}_2]_{\text{pre-irradiation}} - p[\text{O}_2]_{\text{post-irradiation}}}{D} \quad (1)$$

The start time of the irradiation was recorded in order to identify the beginning of oxygen consumption in the LabChart files, which corresponds to the point labelled $p[\text{O}_2]_{\text{pre-irradiation}}$ in Figure 3 and Equation (1). Subsequently, the first 20-second interval where the deviation from the mean oxygen concentration was less than or equal to $\pm 0.5 \text{ mmHg}$ was identified. The start of this

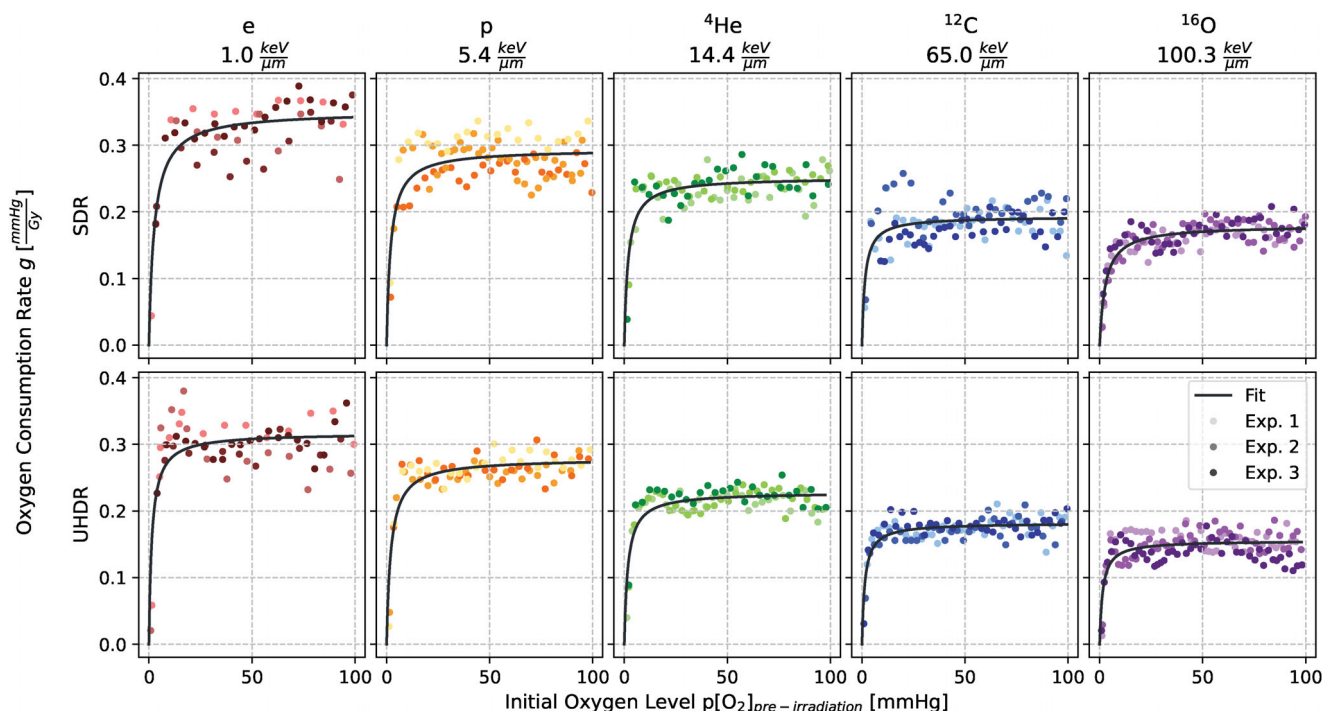


FIGURE 4 Oxygen consumption rate g in BSA 5% against the oxygen concentration prior to the application of 15 Gy for all the various particle and dose rate combinations. Each shade within a given color chosen for one particle represents an independent replicate and thus experiment (Exp.).

interval, which represents a period of stabilization, is labelled $p[O_2]_{\text{post-irradiation}}$ in Figure 3 and Equation (1). The different g -values from the three replicates were pooled and fitted with a Michaelis-Menten styled function to correlate the initial $p[O_2]_{\text{pre-irradiation}}$ with the g -value^{14,15,31}:

$$g(p[O_2]_{\text{pre-irradiation}}) = \frac{g_{\text{max}} \cdot p[O_2]_{\text{pre-irradiation}}}{k + p[O_2]_{\text{pre-irradiation}}} \quad (2)$$

Here, g_{max} and k correspond to the plateau g -value, which is reached for high initial oxygen values and to the concentration where half of the g_{max} is reached, respectively. Thus, k also indicates the steepness of the slope. In this context, the fit function describes the variation in oxygen concentration per unit dose. This may be conceptualized as a G -value, which is defined as the number of molecules consumed per 100 eV of energy deposited, and is employed to describe the rate of reaction.¹⁵ The fitting was performed with a least squares fit from scipy package optimize.curve_fit (Scipy Version 1.11.1).

3 | RESULTS

3.1 | Influence of initial oxygen levels on oxygen consumption rate

In Figure 4, the measured g -values calculated with Equation (1) are presented in relation to the initial oxy-

TABLE 3 Fit values of the Michaelis-Menten function for all conditions.

Particle	Dose rate mode	g_{max} (mmHg/Gy)	k (mmHg)
e	SDR	0.351 ± 0.007	2.6 ± 0.6
	UHDR	0.317 ± 0.007	1.5 ± 0.4
p	SDR	0.294 ± 0.005	2.0 ± 0.4
	UHDR	0.279 ± 0.004	2.1 ± 0.3
⁴ He	SDR	0.252 ± 0.004	1.9 ± 0.3
	UHDR	0.2282 ± 0.0027	1.74 ± 0.25
¹² C	SDR	0.193 ± 0.004	1.4 ± 0.4
	UHDR	0.1822 ± 0.0019	1.39 ± 0.20
¹⁶ O	SDR	0.1796 ± 0.0022	2.79 ± 0.29
	UHDR	0.1556 ± 0.0022	1.46 ± 0.27

The values are accompanied by their respective statistical uncertainty of the fit represented by the standard deviation.

gen levels with the fitted function (2). This fit function describes the saturating behavior of the depletion rate g for high initial oxygen concentrations and the corresponding fit values can be found in Table 3. While for the slope parameter k no trend is observable (Figure S2), g_{max} shows dose rate and LETd dependencies.

3.2 | LETd dependency of oxygen consumption

A decrease of g_{max} with increasing LETd of the particle species can be seen for both UHDR and SDR

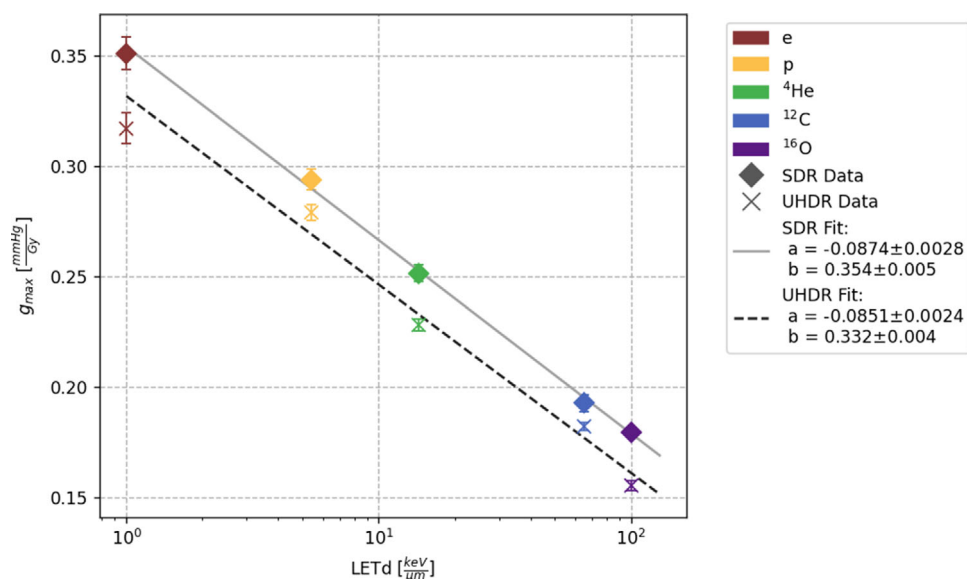


FIGURE 5 Fitted g_{max} values and their standard deviations for every particle type are plotted against their LETd values. The SDR values are marked with a diamond and fitted by the solid line while the UHDR are represented by a cross and fitted by the dashed line. The fit parameters for equation (III) are given with their statistical uncertainties.

irradiations (Figure 5). Specifically, electrons exhibit the highest consumption rate with values above 0.3 mmHg/Gy, while oxygen ions with a LETd of 100.3 keV/μm demonstrate the lowest consumption rates below 0.2 mmHg/Gy. A linear function with the logarithm of the LETd:

$$g_{max} = a \cdot \log_{10}(LETd) + b \quad (3)$$

was fitted to the UHDR and SDR data, respectively, and showed a good agreement with the data. The consumption rates of SDR and UHDR separately show a linearly descending trend when the LETd is graphed in logarithmic scale seen in Figure 5. The R-square values were for both SDR and UHDR fit above 0.98.

3.3 | Difference in oxygen consumption from SDR versus UHDR consistent with increasing LETd

For SDR irradiations, the g_{max} value for each particle is consistently greater compared to the corresponding UHDR value. Since the slopes in Figure 5 for SDR and UHDR are slightly different, we evaluated the evolution of the difference between the g_{max} values for SDR and UHDR (Δg_{max}) and the deviation between the SDR and UHDR fits for the g_{max} and LET correlation (Figure 6). The difference in Δg_{max} is slowly decreasing with increasing LETd.

4 | DISCUSSION

For the first time, we were able to include not only electrons and protons, but also helium, as well as the heavy ions carbon and oxygen for UHDR irradiations to enable a comprehensive study of oxygen consumption for SDR and UHDR over a large span of LETd values in BSA. This direct measurement method revealed that the maximum amount of oxygen consumption given by g_{max} in BSA decreases with increasing LETd. Furthermore, the amount of oxygen consumption was found to be smaller for UHDR in comparison to SDR, throughout the LETd range.

The differences in oxygen consumption associated with LETd may be due to altered radiochemical reactions occurring at the molecular level. This nanoscale interpretation presents a significant challenge, as these reactions are inherently difficult to measure directly due to their short-lived nature, typically occurring on timescales of less than 1 μs. Computational tools such as TRAX-CHEM,³² IONLYS-IRT,³³ or Geant4-DNA³⁴ have demonstrated the ability to model these intricate reaction patterns, although limited to pure water environments and single track simulations.^{32–34}

Our results agree qualitatively with previously conducted in silico studies performed with MC simulations in water, which also found that higher LET result in lower oxygen consumption rates. More specifically, Boscolo et al. demonstrated in silico that the overall yield of chemical species generated during high LET irradiation is reduced compared to low LET conditions.¹⁹

While inter-track interactions can be neglected for the investigated LET during SDR irradiation,³⁵ the elevated

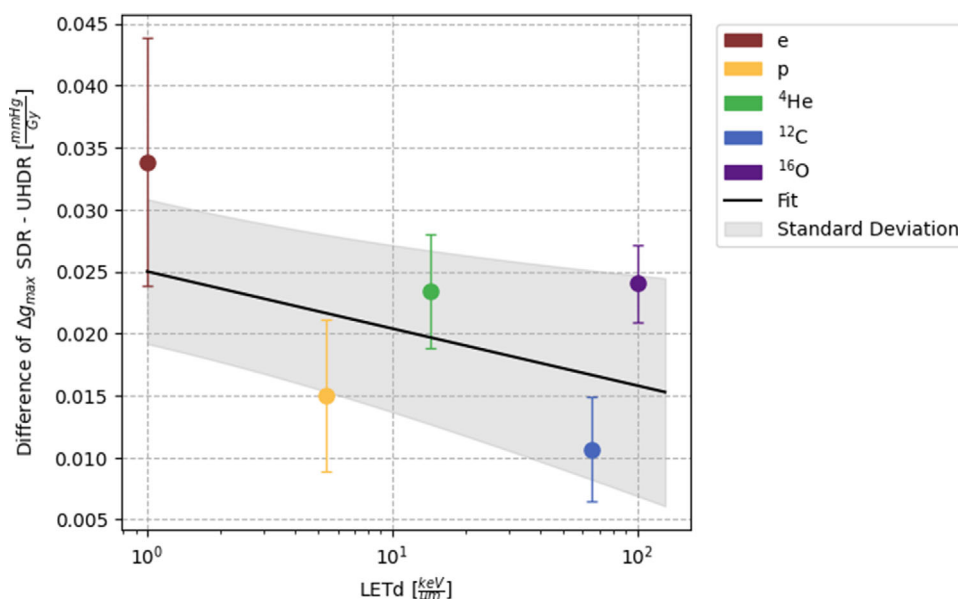


FIGURE 6 Difference of g_{\max} values of SDR and UHDR irradiation for the individual particle beams against their LETd. The values are given with their corresponding standard deviations. Additionally, the difference between the fits for the SDR and UHDR g_{\max} values in dependence with LET, as shown in Figure 5, is plotted with its standard deviation represented by the shaded grey area.

LET values may correspond to an increased density of chemical reactions within the track. This increase in spatiotemporal proximity of radicals for high LET and consequent acceleration of intra-track reaction kinetics enhances the likelihood of radical recombination and self-interaction between the primary chemical species. About 1 ps after the initial irradiation, the primary species are mainly $\text{HO}\cdot$, e^-_{aq} , $\text{H}\cdot$, and H_3O^+ .^{19,36} As the LET increases, the spatial distance between these radiation products decreases within the track, facilitating interaction between the radicals, like the self-interactions $\text{H}\cdot + \text{H}\cdot$ and $\text{HO}\cdot + \text{HO}\cdot$, which lead to more molecular species H_2 and H_2O_2 , respectively.¹⁹ Furthermore, the radical recombination, $\text{HO}\cdot + \text{e}^-_{\text{aq}}$, becomes the dominant reaction over $\text{HO}\cdot + \text{O}_2$ due to this increased density of the two radicals. The overall G-values of $\text{HO}\cdot$, e^-_{aq} , H_3O^+ , and peroxide radicals decrease with increasing LET due to radical interactions.^{32,33,36} These examples highlight how self-interaction and radical-radical recombination decrease the interaction rate with molecular oxygen, leading to reduced oxygen consumption during high LET irradiation.¹⁹ The effect of oxygen consumption may also be marginally minimized by the simultaneous generation of oxygen within high LET particle tracks. The “Oxygen in Track Hypothesis” describes the creation of an oxygen-enriched microenvironment around the high-dose track core of ions.³³ According to Meesungnoen et al., the oxygen produced during irradiation primarily affects the early stages of chemical reactions (around 1 μs post-irradiation).³³ In contrast, Boscolo et al. report that the yield of oxygen consumption is 500 times higher than the production of oxygen

at the same time point and LET value.¹⁹ Considering the difference in the simulation approaches, the difference in production and consumption yield would suggest that the oxygen produced has a minimal effect on the total oxygen concentration seconds after the irradiation. The measurements conducted in this study reflect the overall changes in oxygen concentration, suggesting that the reduced oxygen consumption at high LET may be due to the inherently lower reaction rate with molecular oxygen, primarily due to radical-radical and self-interaction, and to a lesser extent the oxygen production within the tracks.^{19,33}

The data obtained in this study, with its wide range of LETd values, might act as a valuable benchmarking resource for future developments in radio-chemical MC simulations, which could enable more accurate predictions of the oxygen-dependent reactions following ionizing radiation.

The rate of consumption is observed to be lower for UHDR irradiation compared to SDR irradiation. For lower LET irradiation, this behavior was already observed in several studies using water,¹⁵ different BSA concentrations,^{14,31} and solutions that mimicked the intracellular chemical milieu with higher fidelity (namely “CELL”).¹⁸

This difference between SDR and UHDR may be attributed to the accelerated temporal application of particles, which could promote inter-track interactions. Inter-track radical-radical reactions and self-scavenging of radicals would lead to a reduce the likelihood of interactions with oxygen molecules present in the sample.¹⁹ Nevertheless, some MC studies have indicated that

such inter-track interactions may not be the underlying mechanism responsible for the observed decrease in oxygen consumption rates,^{35,37,38} while other studies have suggested that, under specific conditions, such as the administration of large doses and the utilization of low-LET, inter-track interactions at UHDR may potentially contribute to the enhancement of radical interactions.^{20,39,40} Given the ongoing debate surrounding the fundamental parameters of these analyses, including the diffusion constant for radicals within cells, further research is required to elucidate the underlying mechanism behind the UHDR-mediated reduction in oxygen consumption.

In this work, we demonstrated that with increasing LETd, the discrepancy between UHDR and SDR consumption rate slightly declined. As LETd and UHDR increased gradually, the radical-scavenging effect may have reached a saturation point, resulting in a reduction in the difference between SDR and UHDR. This hypothesis may be supported by the slightly smaller decreasing slope of the UHDR consumption rate fit. To investigate this further, measurements with an even higher LETd would be required.

Hence, both high LET and UHDR individually may result in closer spatiotemporal proximity of radicals and lead to radical-scavenging and thus a reduced interaction rate with molecular oxygen in the sample.^{19,33,36}

This radical scavenging could be beneficial for cell survival by reducing oxidative damage to key cellular biomolecules.^{16,41} Normal cells possess an advantage over tumor cells due to their lower prooxidant burden and higher reserves of antioxidant enzymes and pathways.⁴² This enables normal cells to rapidly and efficiently eliminate remaining radicals, even before the initiation of further harmful Fenton-type reactions or peroxidation chains, providing superior protection against further damage in contrast to tumor cells, which lack these robust cellular defense mechanisms. Consequently, the differential antioxidant capacities of normal and tumor cells may contribute to their varied responses to UHDR, where the total amount of radicals might be reduced.¹³

Our analysis was based on the plateau parameter g_{max} obtained by fitting the g -values to a Michaelis-Menten curve. The second fit parameter k correlates with the oxygen concentration that yields half the maximum consumption rate and thus with the slope of the initial increase. The smaller this value, the faster the plateau value g_{max} is reached. No clear LETd trend or dose rate effect can be seen in the data (Figure S2). However, due to the inherent resolution limitations of the OxyLite, measurements at concentrations below 7 mmHg are more prone to error with a resolution of ± 0.7 mmHg. This resolution limit could theoretically be overcome by using phosphorescence measurement methods due to their longer lifetimes and correspondingly higher accuracy in low oxygen environ-

ments. Despite this, given the additional small number of data points in the low oxygen concentration region, the fit of the k parameter is associated with larger standard deviations (Table 3), which hinders sensible interpretation of the data. Furthermore, the response time of the OxyLite system is limited to 20 s, a characteristic common to detectors embedded in membranes, such as the TROXsP5.⁴³ However, the longer response time was considered sufficient for our purposes, as it enables the evaluation of the total oxygen changes caused by the applied beams (Figure 3).

While several studies of oxygen consumption for electrons and protons have been conducted,^{14,18,31,44} only one study in literature measured the consumption rate in deionized water after carbon ion irradiation. However, the LET reached in this experiment was relatively low at 19.47 keV/ μ m and so was the dose rate with a maximum of 1.8 Gy/s.⁴⁵ Since deionized water is not recommended as surrogate for cellular milieu,^{17,41} in this study, BSA was used as a surrogate for the extracellular environment.¹⁸ The simplicity, stability, and reproducibility of this solution allowed us to discern the slight differences in oxygen consumption between each radiation quality. However, in comparison to actual cells, no thiols, lipids, or scavengers are present in the BSA solution. Slyker et al. demonstrated that in the "CELL" solution, the consumption rates were higher than in BSA but still showed the same dose rate trend. While the applicability of BSA is surely limited, it gives a first hint on how the consumption rate changes with dose rate and LET in a medium with proteins and a high percentage of water.¹⁸ The tendency of a higher consumption for SDR compared to UHDR was already found in other experiments using BSA solutions.^{14,31,44} Our experiment is qualitatively consistent with their findings and provides an extrapolation to higher LETd. Differences in the quantitative values may be caused by deviations in the irradiation setups.

A recent study by Khatlib et al. directly measured intracellular oxygen consumption.⁴⁶ Notably, this study observed the disappearance of the disparity in oxygen consumption rates between SDR and UHDR irradiations against the expectancy that organic substances would enhance the oxygen consumption. This phenomenon could be explained by cellular antioxidant mechanisms, such as catalase and superoxide dismutase reactions, which convert radicals back to oxygen and potentially compensate for oxygen consumption.⁴⁶ Additionally, several reducing agents influence the consumption rate in different ways. For instance, glutathione enhances it, while ascorbate decreases it, as demonstrated by Koch et al.¹⁷ To decipher the complex radiochemistry behind the radiochemical oxygen consumption and whether the LETd effect on oxygen consumption also disappears intracellularly or even in actual tissue needs to be examined in further studies.

If oxygen consumption and the following transient hypoxia was one of the underlying mechanisms of UHDR sparing, our findings would suggest that sparing would decrease for higher LETd. While separate studies of in vitro UHDR-sparing effects after ion beam irradiations exist, namely for helium²⁸ and carbon²⁵ ions, comprehensive data sets ranging over a substantial LET-region are still lacking. In combination with the results of our investigations, such in vitro datasets could allow a test of biophysical models related to radiochemical oxygen change.

Regarding the in vivo FLASH effect, a number of low-LET electron and proton studies are available for consideration.^{47–49} Furthermore, Tinganelli et al. presented evidence of the benefits of lower LET (14.5–15.5 keV/μm)⁵⁰ and recently also for high LET (65–85 keV/μm)⁵¹ carbon ion irradiation at UHDR in vivo. Consequently, high LET data is also a crucial area of investigation in vivo and could lead to profound implications for FLASH treatments with heavy ions. In heavy ion radiotherapy, the target is usually exposed to elevated LET, while the normal tissue is predominantly receiving low LET radiation. Given the LET dependence of oxygen consumption observed in this study, in tumor cells subjected to high LET irradiation less oxygen would be consumed. This would be advantageous, as it reduces the likelihood of sparing tumor cells. Furthermore, biological efficacy of high LET irradiation in general is known to be less influenced by the oxygen environment, since the densely ionizing tracks induce a higher proportion of direct damage and rely less on the indirect processes.^{52,53} This could even further decrease the biological effect of the theoretically expected marginal oxygen consumption induced sparing. For the normal tissue exposed to low LET irradiation, increased oxygen consumption would refer to a beneficial larger sparing.

Although the oxygen consumption rate of UHDR is slightly lower than that of SDR irradiation, this rate only includes oxygen consumption, not the associated reoxygenation processes, which is substantially changed after irradiation of UHDR and SDR due to their time scale differences. The advantage of UHDR is that oxygen consumption happens so quickly that cells remain in a state of reduced oxygen until reoxygenation can compensate for the oxygen loss. Conversely, during SDR irradiation, oxygen consumption is directly compensated by reoxygenation due to the longer irradiation duration.^{11,12,54}

Consequently, this study indicates that heavy ion radiotherapy at UHDR may further expand the therapeutic window by ensuring higher consumption rates and thus sparing in normal tissue while providing increased radiobiological effectiveness in the target region.^{38,50,55} One may even consider enhancing this effect by employing strategies to maximize the LET in the target region, since higher LET corresponds to lower oxygen consumption.⁵⁶

5 | CONCLUSION

This study presents the first direct measurements of the oxygen consumption rates in BSA 5% samples with different particles over a wide range of LETd up to 100.3 keV/μm. Using the HIT synchrotron, we were able to perform UHDR irradiations with protons, helium, carbon ions and, for the first time, oxygen ions. The results show a systematic decrease of the oxygen consumption rate with increasing LETd. In addition, the UHDR consumption rate remains consistently lower than the corresponding SDR consumption rate.

Through its comprehensiveness, our dataset could be a valuable benchmark resource for radiochemical MC simulations and oxygen dynamics models. Comparison of the simulation results with our empirical findings could enhance the understanding of the combined effects of high-dose rates and increased LETd in relation to oxygen-dependent reactions after irradiation.

In combination with additional data on the trend of sparing effects over the LETd, our results may aid the appraisal of key candidates for the underlying mechanism of UHDR sparing and eventually the FLASH effect.

If the sparing phenomenon persists in higher-order biological samples and correlates with the oxygen consumption trends observed in this study, it suggests potential synergies between heavy ions and UHDR. In this scenario, high consumption rates may confer protection in normal tissues and organs at risk, while the high LET in the target would ensure reduced consumption and thus may avoid potential sparing of the tumor.

ACKNOWLEDGMENTS

This work was supported in part by the NIH-P01CA257904. The authors would like to thank the whole accelerator team at HIT for helping with the synchrotron adjustments and Uli Weber from GSI for providing the 2DRM.

This work was supported by German Research Council (DFG-Unite: SFB1389/2C05) and intramural funds from National Center for Tumor Diseases (NCT-PRO: 1030000042 and Biodose: 1030000043 programs). This work was supported in part by National Institutes of Health (NIH-1P01CA257904-01A1). The funders had no role in study design, data collection and analysis, decision to publish, or preparation of the manuscript.

Statistical analyses were performed by Celine Karle.

Open access funding enabled and organized by Projekt DEAL.

CONFLICT OF INTEREST STATEMENT

Jürgen Debus reports grants from CRI—The Clinical Research Institute GmbH grants from View Ray Inc., grants from Accuray International Sarl, grants from Accuray Incorporated, grants from RaySearch Laboratories AB, grants from Vision RT limited, grants from Merck

Serono GmbH, grants from Astellas Pharma GmbH, grants from AstraZeneca GmbH, grants from Siemens Healthcare GmbH, grants from Merck KGaA, grants from Solution Akademie GmbH, grants from Ergomed PLC Surrey Research Park, grants from Siemens Healthcare GmbH, grants from Quintiles GmbH, grants from Pharmaceutical Research Associates GmbH, grants from Boehringer Ingelheim Pharma GmbH Co, grants from PTW-Freiburg Dr. Pychlau GmbH, grants from Nanobiotix AA, outside the submitted work. Amir Abdollahi and report grants and other from Merck and EMD, grants and other from Fibrogen, other from BMS, other from BioMedX, other from Roche, outside the submitted work.

DATA AVAILABILITY STATEMENT

Research data is stored in an institutional repository and will be shared upon request to the corresponding author.

REFERENCES

- Holthusen H. Beiträge zur Biologie der Strahlenwirkung. Untersuchungen an Ascarideneieren. *Pflüger's Arch ges Physiol*. 1921;187:1.
- Hall E, Giaccia A. *Radiobiology for the Radiologist*. Lippincott Williams & Wilkins. 6th ed. Published online 2006.
- Thoday J, Read J. Effect of oxygen on the frequency of chromosome aberrations produced by X-rays. *Nature*. 1947;160(4070):608-608.
- Baverstock K, Burns W. Primary production of oxygen from irradiated water as an explanation for decreased radiobiological oxygen enhancement at high LET. *Nature*. 1976;260(5549):316-318.
- Anderson A, Hart EJ. Radiation chemistry of water with pulsed high intensity electron beams. *J Phys Chem*. 1962;66(1):70-75.
- Dewey D, Boag J. Modification of the oxygen effect when bacteria are given large pulses of radiation. *Nature*. 1959;183(4673):1450-1451.
- Favaudon V, Caplier L, Monceau V, et al. Ultrahigh dose-rate FLASH irradiation increases the differential response between normal and tumor tissue in mice. *Sci Transl Med*. 2014;6(245):245ra93-245ra93.
- Held KD, McNamara AL, Daartz J, Bhagwat MS, Rothwell B, Schuermann J. Dose rate effects from the 1950s through to the Era of FLASH. *Radiat Res*. Published online 2024.
- Adrian G, Konradsson E, Lempart M, Bäck S, Ceberg C, Petersson K. The FLASH effect depends on oxygen concentration. *Br J Radiol*. 2020;92(1106):20190702.
- Montay-Gruel P, Acharya MM, Petersson K, et al. Long-term neurocognitive benefits of FLASH radiotherapy driven by reduced reactive oxygen species. *Proc Natl Acad Sci*. 2019;116(22):10943-10951.
- Petersson K, Adrian G, Butterworth K, McMahon SJ. A quantitative analysis of the role of oxygen tension in FLASH radiation therapy. *Int J Radiat Oncol Biol Phys*. 2020;107(3):539-547.
- Taylor E, Létoirneau D. How quickly does FLASH need to be delivered? A theoretical study of radiolytic oxygen depletion kinetics in tissues. *Phys Med Biol*. 2024;69(11):115008.
- Spitz DR, Buettner GR, Petronek MS, et al. An integrated physico-chemical approach for explaining the differential impact of FLASH versus conventional dose rate irradiation on cancer and normal tissue responses. *Radiother Oncol*. 2019;139:23-27.
- Cao X, Zhang R, Esipova TV, et al. Quantification of oxygen depletion during FLASH irradiation in vitro and in vivo. *Int J Radiat Oncol Biol Phys*. 2021;111(1):240-248.
- Jansen J, Beyreuther E, García-Calderón D, et al. Changes in radical levels as a cause for the FLASH effect: impact of beam structure parameters at ultra-high dose rates on oxygen depletion in water. *Radiother Oncol*. 2022;175:193-196.
- Favaudon V, Labarbe R, Limoli CL. Model studies of the role of oxygen in the FLASH effect. *Med Phys*. 2022;49(3):2068-2081.
- Koch CJ, Kim MM, Wiersma RD. Radiation-chemical oxygen depletion depends on chemical environment and dose rate: implications for the FLASH effect. *Int J Radiat Oncol Biol Phys*. 2023;117(1):214-222.
- Van Slyke AL, El Khatib M, Velalopoulou A, et al. Oxygen monitoring in model solutions and in vivo in mice during proton irradiation at conventional and flash dose rates. *Radiat Res*. 2022;198(2):181-189.
- Boscolo D, Krämer M, Fuss MC, Durante M, Scifoni E. Impact of target oxygenation on the chemical track evolution of ion and electron radiation. *Int J Mol Sci*. 2020;21(2):424.
- Baikalov A, Abolfath R, Mohan R, Schüler E, Wilkens JJ, Bartsch S. Modeling interspur interactions as a potential mechanism of the FLASH effect. *arXiv preprint arXiv:220712287*. Published online 2022.
- Griffiths J, Robinson S. The OxyLite: a fibre-optic oxygen sensor. *Br J Radiol*. 1999;72(859):627-630.
- Kassis AI. Molecular and cellular radiobiological effects of Auger emitting radionuclides. *Radiat Prot Dosim*. 2011;143(2-4):241-247.
- Ferrari A, Ranft J, Sala PR, Fassò A. FLUKA: A Multi-Particle Transport Code (Program Version 2005). Cern; 2005.
- Battistoni G, Bauer J, Boehlen TT, et al. The FLUKA code: an accurate simulation tool for particle therapy. *Front Oncol*. 2016;6:116.
- Tinganelli W, Sokol O, Quartieri M, et al. Ultra-high dose rate (FLASH) carbon ion irradiation: dosimetry and first cell experiments. *Int J Radiat Oncol Biol Phys*. 2022;112(4):1012-1022.
- Baack L, Schuy C, Brons S, et al. Reduction of recombination effects in large plane parallel beam monitors for FLASH radiotherapy with scanned ion beams. *Physica Med*. 2022;104:136-144.
- Schömers C, Brons S, Cee R, Peters A, Scheloske S, Haberer T. Beam properties beyond the therapeutic range at HIT. In Proceedings of IPAC 23, Venice, Italy, May 2023, Paper THPM064. Published online 2022.
- Tessonnier T, Mein S, Walsh DW, et al. FLASH dose rate helium ion beams: first in vitro investigations. *Int J Radiat Oncol Biol Phys*. 2021;111(4):1011-1022.
- Holm KM, Weber U, Simeonov Y, Krauss A, Jäkel O, Greilich S. 2D range modulator for high-precision water calorimetry in scanned carbon-ion beams. *Phys Med Biol*. 2020;65(21):215003.
- Simeonov Y, Weber U, Schuy C, et al. Monte Carlo simulations and dose measurements of 2D range-modulators for scanned particle therapy. *Zeitschrift für Medizinische Physik*. 2021;31(2):203-214.
- El Khatib M, Van Slyke AL, Velalopoulou A, et al. Ultrafast tracking of oxygen dynamics during proton FLASH. *Int J Radiat Oncol Biol Phys*. 2022;113(3):624-634.
- Boscolo D, Krämer M, Durante M, Fuss M, Scifoni E, TRAX-CHEM. A pre-chemical and chemical stage extension of the particle track structure code TRAX in water targets. *Chem Phys Lett*. 2018;698:11-18.
- Meesungnoen J, Jay-Gerin JP. High-LET ion radiolysis of water: oxygen production in tracks. *Radiat Res*. 2009;171(3):379-386.
- Chappuis F, Tran HN, Zein SA, et al. The general-purpose Geant4 Monte Carlo toolkit and its Geant4-DNA extension to investigate mechanisms underlying the FLASH effect in radiotherapy: current status and challenges. *Physica Med*. 2023;110:102601.
- Thompson SJ, Prise KM, McMahon SJ. Investigating the potential contribution of inter-track interactions within ultra-high dose-rate proton therapy. *Phys Med Biol*. 2023;68(5):055006.

36. Coliaux A, Gervais B, Rodriguez-Lafrasse C, Beuve M. Simulation of ion-induced water radiolysis in different conditions of oxygenation. *Nucl Instrum Methods Phys Res Sect B*. 2015;365:596-605.
37. Kreipl MS, Friedland W, Paretzke HG. Interaction of ion tracks in spatial and temporal proximity. *Radiat Environ Biophys*. 2009;48(4):349-359.
38. Weber UA, Scifoni E, Durante M. FLASH radiotherapy with carbon ion beams. *Med Phys*. 2022;49(3):1974-1992.
39. Abolfath R, Baikalov A, Bartzsch S, Afshordi N, Mohan R. The effect of non-ionizing excitations on the diffusion of ion species and inter-track correlations in FLASH ultra-high dose rate radiotherapy. *Phys Med Biol*. 2022;67(10):105005.
40. Ramos-Méndez J, Domínguez-Kondo N, Schuemann J, McNamara A, Moreno-Barbosa E, Faddegon B. LET-dependent intertrack yields in proton irradiation at ultra-high dose rates relevant for FLASH therapy. *Radiat Res*. 2020;194(4). doi:10.1667/rade-20-00084.1
41. Wardman P. Mechanisms of the 'FLASH' effect: radiation chemistry should not be ignored in developing models. *Radiother Oncol*. 2023;184.
42. Hayes JD, Dinkova-Kostova AT, Tew KD. Oxidative stress in cancer. *Cancer Cell*. 2020;38(2):167-197.
43. Technology P sensor. Specifications TRACE Oxygen Sensors—Document Version V1.28. Pyroscience sensor technology. Published online May 2015. <https://www.pyroscience.com/en/products/all-sensors/troxsp5#Downloads>
44. Sunnerberg JP, Zhang R, Gladstone DJ, Swartz HM, Gui J, Pogue BW. Mean dose rate in ultra-high dose rate electron irradiation is a significant predictor for O₂ consumption and H₂O₂ yield. *Phys Med Biol*. 2023;68(16):165014.
45. Jansen J, Knoll J, Beyreuther E, et al. Does FLASH deplete oxygen? Experimental evaluation for photons, protons, and carbon ions. *Med Phys*. 2021;48(7):3982-3990.
46. El Khatib M, Motlagh AO, Beyer JN, et al. Direct measurements of FLASH-induced changes in intracellular oxygenation. *Int J Radiat Oncol Biol Phys*. 2024;118(3):781-789.
47. Wilson JD, Hammond EM, Higgins GS, Petersson K. Ultra-high dose rate (FLASH) radiotherapy: silver bullet or fool's gold? *Front Oncol*. 2020;9:1563.
48. Gao Y, Liu R, Chang CW, et al. A potential revolution in cancer treatment: a topical review of FLASH radiotherapy. *J Appl Clin Med Phys*. 2022;23(10):e13790.
49. Almeida A, Togno M, Ballesteros-Zebadua P, et al. Dosimetric and biologic intercomparison between electron and proton FLASH beams. *Radiother Oncol*. 2024;190:109953.
50. Tinganelli W, Weber U, Puspitasari A, et al. FLASH with carbon ions: tumor control, normal tissue sparing, and distal metastasis in a mouse osteosarcoma model. *Radiother Oncol*. 2022;175:185-190.
51. Tinganelli W, Sokol O, Puspitasari A, et al. FLASH Bragg-peak irradiation with a therapeutic carbon ion beam: first in vivo results. *bioRxiv* 2024.07.12.603197; doi:10.1101/2024.07.12.603197
52. Klein C, Dokic I, Mairani A, et al. Overcoming hypoxia-induced tumor radioresistance in non-small cell lung cancer by targeting DNA-dependent protein kinase in combination with carbon ion irradiation. *Radiat Oncol*. 2017;12(1):1-8.
53. Moon EJ, Petersson K, Olcina MM. The importance of hypoxia in radiotherapy for the immune response, metastatic potential and FLASH-RT. *Int J Radiat Biol*. 2022;98(3):439-451.
54. Liew H, Mein S, Dokic I, et al. Deciphering time-dependent DNA damage complexity, repair, and oxygen tension: a mechanistic model for FLASH-dose-rate radiation therapy. *Int J Radiat Oncol Biol Phys*. 2021;110(2):574-586.
55. Zakaria AM, Colangelo NW, Meesungnoen J, Azzam EI, Plourde ME, Jay-Gerin JP. Ultra-high dose-rate, pulsed (FLASH) radiotherapy with carbon ions: generation of early, transient, highly oxygenated conditions in the tumor environment. *Radiat Res*. 2020;194(6):587-593.
56. Fredriksson A, Glimelius L, Bokrantz R. The LET trilemma: conflicts between robust target coverage, uniform dose, and dose-averaged LET in carbon therapy. *Med Phys*. 2023;50(12):7338-7348.

SUPPORTING INFORMATION

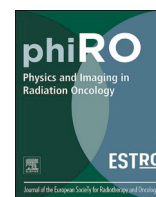
Additional supporting information can be found online in the Supporting Information section at the end of this article.

How to cite this article: Karle C, Liew H, Tessonnier T, et al. Oxygen consumption measurements at ultra-high dose rate over a wide LET range. *Med Phys*. 2025;52:1323–1334. <https://doi.org/10.1002/mp.17496>

6.3 “First In Vitro and In Vivo Experiments with Ultra High-Dose Rate Oxygen Ion Radiotherapy”

Authors	<u>Celine Karle</u> , Domenico I. Filosa, Mahdi Akbarpour, Nora Schuhmacher, Stephan Brons, Rainer Cee, Christian Schömers, Stefan Scheloske, Kristoffer Petersson, Thomas Haberer, Amir Abdollahi, Jürgen Debus, Thomas Tessonier, Mahmoud Moustafa, Andrea Mairani, Ivana Dokic
Publication Status	Published - 03 July 2025
Journal	Physics and Imaging in Radiation Oncology
DOI	https://doi.org/10.1016/j.phro.2025.100803
Contribution	<u>CK</u> , ID, and AM were responsible for the conceptualization and methodology. KP provided the OxyLite™ measurement device, while TT, SB, RC, SS, and CS ensured the technical resources at the HIT facility. <u>CK</u> performed the dosimetry, and supervised and coordinated all experiments. The oxygen consumption experiments were carried out, analyzed, and visualized by <u>CK</u> . In vitro data were acquired by <u>CK</u> , DIF, and NS, and were analyzed and interpreted by <u>CK</u> and ID. The in vivo mouse irradiation was conducted by <u>CK</u> and MA, with mice measurements from MA and data analysis performed by ID and MM. The overall interpretation was performed by <u>CK</u> , ID, and AM. The original draft and the visualizations were prepared by <u>CK</u> with assistance from ID. The final manuscript was reviewed and edited by <u>CK</u> , NS, SB, CS, KP, TT, MM, AM, and ID. Supervision was provided by AM and ID, while TH, AA, and JD contributed to funding acquisition and clinical direction.

©2025 The Author(s). Published by Elsevier B.V. on behalf of European Society of Radiotherapy & Oncology.



Short Communication

First in vitro and in vivo experiments with ultra high-dose rate oxygen ion radiotherapy



Celine Karle^{a,b}, Domenico I. Filosa^{a,j}, Mahdi Akbarpour^{a,c,d,e,f}, Nora Schuhmacher^{a,c,d,f},
Stephan Brons^f, Rainer Cee^f, Christian Schömers^f, Stefan Scheloske^f, Kristoffer Petersson^g,
Thomas Haberer^f, Amir Abdollahi^{a,c,d,e,f}, Jürgen Debus^{a,c,d,e,f},
Thomas Tessonier^{a,f}, Mahmoud Moustafa^{a,c,d,e,f,h}, Andrea Mairani^{a,f,i,j,*},
Ivana Dokic^{a,c,d,e,f,*}

^a Clinical Cooperation Unit Translational Radiation Oncology, National Center for Tumor Diseases (NCT), Heidelberg University Hospital (UKHD) and German Cancer Research Center (DKFZ), Im Neuenheimer Feld 460, Heidelberg, Germany

^b Department of Physics and Astronomy, Heidelberg University, Im Neuenheimer Feld 226, 69120 Heidelberg, Germany

^c Division of Molecular and Translational Radiation Oncology, Department of Radiation Oncology, Heidelberg Faculty of Medicine (MFHD) and Heidelberg University Hospital (UKHD), Heidelberg Ion-Beam Therapy Center (HIT), Im Neuenheimer Feld 450, 69120 Heidelberg, Germany

^d German Cancer Consortium (DKTK) Core-Center Heidelberg, German Cancer Research Center (DKFZ), Im Neuenheimer Feld 280, 69120 Heidelberg, Germany

^e Heidelberg Institute of Radiation Oncology (HIRO), National Center for Radiation Oncology (NCRO), Heidelberg University and German Cancer Research Center (DKFZ), Im Neuenheimer Feld 222, 69120 Heidelberg, Germany

^f Heidelberg Ion-Beam Therapy Center (HIT), Department of Radiation Oncology, Heidelberg University Hospital (UKHD), Im Neuenheimer Feld 450, 69120 Heidelberg, Germany

^g Oxford Institute for Radiation Oncology, Department of Oncology, University of Oxford, Old Road Campus Research Building, Oxford OX3 7DQ, UK

^h Department of Clinical Pathology, Suez Canal University, Ismailia, Egypt

ⁱ National Center for Oncological Hadrontherapy (CNAO), Str. Campeggi 53, Pavia, Italy

^j Medical Faculty, Heidelberg University, Im Neuenheimer Feld 672, 69120 Heidelberg, Germany

ARTICLE INFO

Keywords:

High LET
Ultra-high dose rates
Oxygen ions
In vitro experiments
In vivo experiments
PDAC

ABSTRACT

Within this study, we demonstrated the feasibility of ultra-high dose rate (UHDR) oxygen ion irradiation at three different levels of biological complexity. The difference in oxygen consumption between UHDR and standard dose rates (SDR) was negligible in a protein-enriched saline solution. For the studied conditions of dose, dose rate and linear energy transfer (LET), UHDR irradiation showed comparable efficacy to SDR in pancreatic cancer cell killing in vitro, along with inducing a similar tumor growth delay in vivo. These findings emphasize the potential of high-LET UHDR irradiation and support further investigation of oxygen ions at UHDR.

1. Introduction

Patients diagnosed with pancreatic cancer have the lowest 5-year survival rate of all cancers at around 13 %, ranking it as the third most common cause of cancer death [1]. The high mortality rate is attributed to late diagnosis, resulting in advanced tumors growth with unresectable metastases [2]. When surgical intervention is not feasible, chemotherapy and external beam radiotherapy often represent the only viable treatment option [3,4].

Three major challenges limit the effectiveness of standard radiotherapy in treating pancreatic cancer: proximity to radiosensitive organs

at risk (OAR), a hypoxic microenvironment and tumor motion i.e. bowel activity [5,6]. Particle irradiation offers precise dose distributions compared to photon irradiation, allowing superior tumor coverage with minimal exposure to surrounding OAR. In particular, irradiation with carbon ions [7,8] has demonstrated promising results due to their highly conformal dose distribution [8] combined with high linear energy transfer (LET) [9,10]. Indeed, studies have shown that high dose-averaged LET (LET_d) irradiation may be effective in treating pancreatic tumors [11], primarily attributed to its capacity to overcome hypoxia-induced radioresistance by directly inducing lethal DNA damage [9,12].

* Corresponding authors.

E-mail addresses: Andrea.Mairani@med.uni-heidelberg.de (A. Mairani), i.dokic@nct-heidelberg.de (I. Dokic).

<https://doi.org/10.1016/j.phro.2025.100803>

Received 24 January 2025; Received in revised form 29 June 2025; Accepted 29 June 2025

Available online 3 July 2025

2405-6316/© 2025 The Author(s). Published by Elsevier B.V. on behalf of European Society of Radiotherapy & Oncology. This is an open access article under the CC BY-NC-ND license (<http://creativecommons.org/licenses/by-nc-nd/4.0/>).

To address tumor motion, techniques such as abdominal compression have demonstrated promising results [13]. Ultra-high dose rate (UHDR) irradiation could additionally mitigate intra-fractional motion and minimize motion-related uncertainties by delivering doses 100 times faster than conventional radiotherapy. Moreover, the FLASH effect observed at UHDR enables the protection of healthy tissue while preserving effective tumor control, thereby broadening the therapeutic window [14–16]. However, preclinical studies focusing on radiotherapy for pancreatic cancer are limited [17], particularly those involving high LET radiotherapy.

Building on the potential of high LET particle therapy at UHDR to address the challenges of pancreatic cancer radiotherapy, this study explored for the first time the effects of oxygen ion UHDR irradiation on three levels of biological complexity: as an initial feasibility study, molecular oxygen consumption in a simplified plasma model was evaluated. Subsequently, in vitro survival of pancreatic cancer cells under hypoxic and normoxic conditions was assessed. Lastly, the effects on tumor growth delay and survival of UHDR irradiation were investigated in vivo using a resistant KPC mouse model, a clinically relevant analogue of human pancreatic ductal adenocarcinoma (PDAC).

2. Material and Methods

2.1. Dosimetry

For all experiments conducted at UHDR and standard dose rates (SDR) a monoenergetic oxygen ion beam of 326 MeV/u was used, incorporating a 3 mm ripple filter at the nozzle to widen the pristine Bragg Peak (BP). Further details about the Heidelberg Ion Beam Therapy Centre irradiation facility and the temporal beam structure can be found in the [supplementary material](#). Given this default, the experiments were conducted with the setups shown in [Fig. 1](#).

Daily dosimetric measurements were conducted with a PinPoint ionization chamber (PTW, REF: TM31015, SN:0903) following clinical practice TRS398 [20]. At least three dose measurements per experiment were conducted. To calculate the mean dose rate, the recordings from the beam application and monitoring system in the nozzle were used to extract the length of the spills ([Tab. S1](#)). Additionally, Gafchromic EBT3 films (8'X10' (x25), Ashland 828204) were irradiated to ensure homogeneity within the fields. Details about the irradiated films evaluation can be found in the [supplementary material](#) ([Fig. S1](#)).

2.2. Oxygen Consumption Measurements

The effect of oxygen ion UHDR and SDR irradiation on the inherent oxygen concentration in sealed samples containing 5 % bovine serum albumin (BSA) was examined ([Fig. 1 A](#)). The oxygen concentration was monitored with the OxyLite™ system (Oxford Optronix) [21]. As reported in [21], the oxygen consumption per dose g was calculated for each irradiation, investigating higher initial oxygen concentrations up to 20 % in this study. The resulting g -values were fitted using the following equation:

$$g(p[O_2]_{pre-irradiation}) = \frac{g_{max} \cdot p[O_2]_{pre-irradiation}}{k + p[O_2]_{pre-irradiation}} \quad (1)$$

Here, $p[O_2]_{pre-irradiation}$ is the oxygen concentration pre-irradiation, while the fit parameters g_{max} and k correspond to the saturating g -value and to the concentration where half of the g_{max} is reached, respectively [21]. For each dose rate, three different samples were irradiated, the g -values calculated, and the data fitted with [Eq. \(1\)](#). The difference between the fit of the SDR and the UHDR data was analyzed.

2.3. Cell Culture and Colony Formation Assay

Pancreatic cancer cells derived from the autochthonous PDAC KPC mouse model (KPC; 6419c5 Kerafast) [22,23] were cultured in Dulbecco modified Eagle medium (DMEM, ATCC) supplemented with 10 % heat-inactivated fetal bovine serum (FBS; Gibco) and 1 % penicillin/streptomycin at 37 °C in a humidified atmosphere of 5 % CO₂.

For the irradiation cells were prepared as described in Tessonnier et al. [24]. The cells were placed in a hypoxia chamber (Biospherix) at ~1 % O₂ 5 h pre-irradiation and maintained in hypoxic conditions within the chamber during irradiation or at 20 % O₂ outside of the chamber. During the irradiation, 8 Gy were applied at SDR and UHDR with an average LETd of 100.3 keV/μm ([Fig. 1 B](#)).

Colony formation assay has been performed as described previously [24]. Briefly, after colony formation (7 days), cells were fixed with 75 % methanol and 25 % acetic acid for 10 min at room temperature and stained with 0.1 % crystal violet for 10 min. Three independent biological experiments for hypoxia and two for normoxia were conducted, resulting in at least two to five replicates.

The significance of the difference in clonogenic cell survival between UHDR and SDR irradiation was evaluated with a Mann-Whitney-U-Test using the GraphPad Prism software.

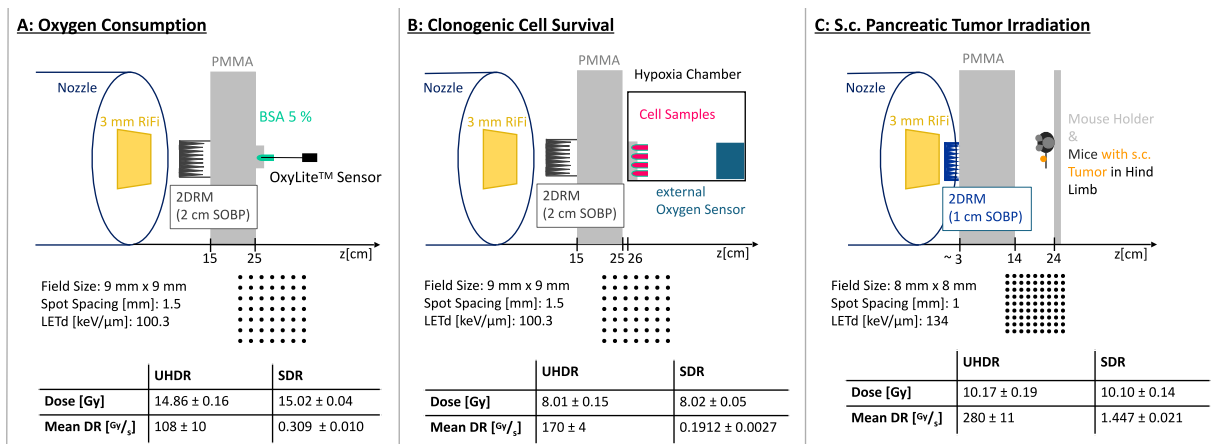


Fig. 1. The experimental setups: A: Oxygen Consumption Measurements, B: Clonogenic Cell Survival and C: Pancreatic Tumor Irradiation In Vivo. The “Setup” illustrations contain the experimental components and the spatial information. The “Irradiation Parameters” include details about the field sizes with the corresponding spot spacing, average LETd, dose and mean dose rate (“Mean DR”). The dosimetric quantities are given with their standard deviation. The “3 mm RiFi” abbreviates the ripple filter installed in the nozzle. 2D range modulators (2DRM) producing a 1 cm or 2 cm spread out BP (SOBP) were used for the in vivo or oxygen consumption and in vitro experiment respectively [18,19]. PMMA refers to Polymethylmethacrylate.

2.4. Animal Model

Subcutaneous (s.c) KPC mouse model was established by injecting 5×10^5 KPC cells resuspended in 100 μ l PBS s.c. into the hind limb of 6–8 weeks-old female C57BL/6 mice (Janvier Labs). When the tumor size

reached $80 \pm 20 \text{ mm}^3$, the mice were randomized for irradiation ($n = 6$ per condition) and irradiated with 10 Gy SDR or UHDR oxygen ion beams at an average LETd of 134 $\text{keV}/\mu\text{m}$. Mice were anesthetized with isoflurane for irradiation and fixed in a custom-made holder during irradiation. The s.c. tumors were irradiated assuring complete tumor

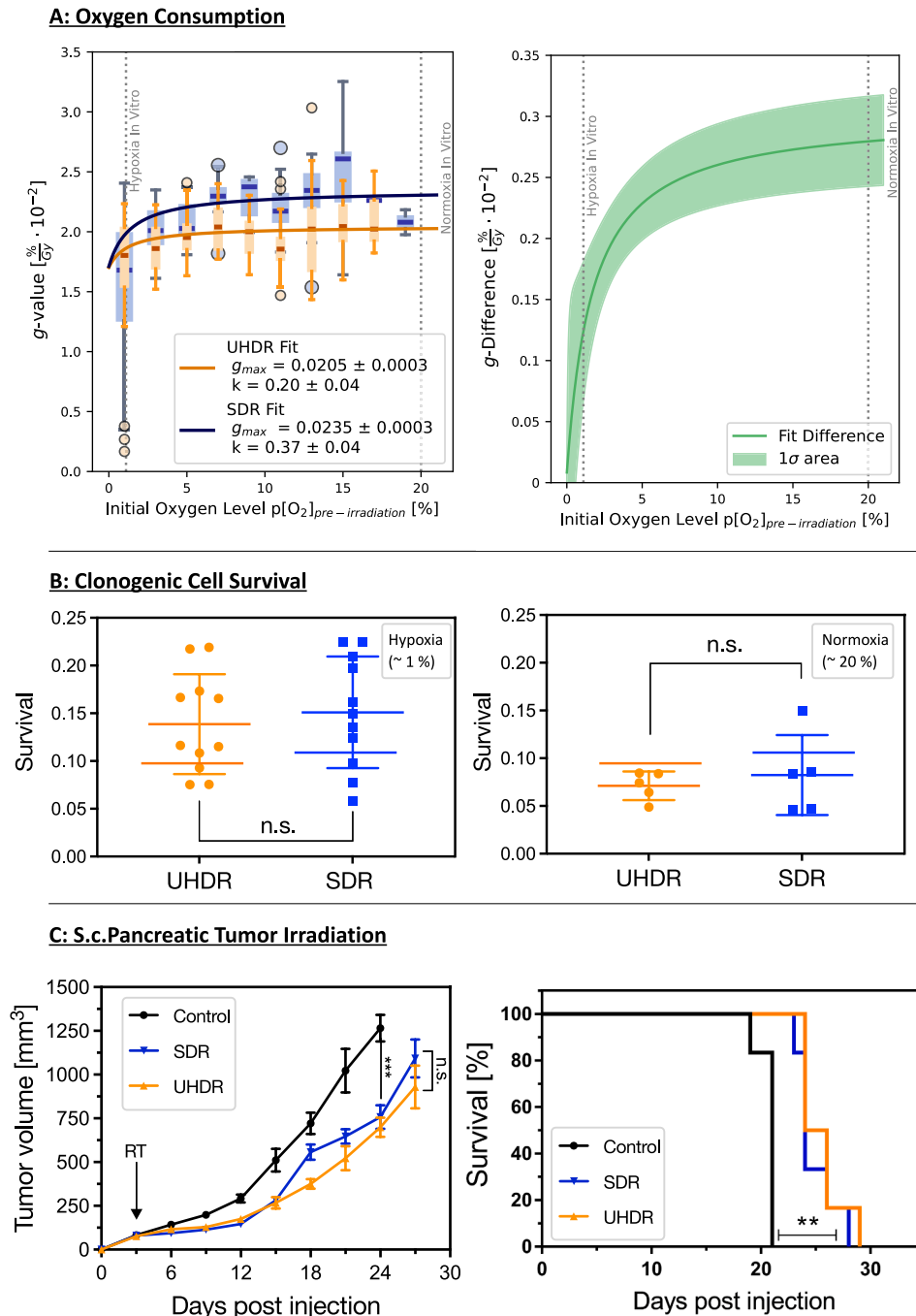


Fig. 2. Oxygen Ion UHDR Experimental Results – Panel A – Oxygen Consumption Results: On the left are the individual g -values plotted as box plots with 2 % bin intervals, displaying medians, quartiles (boxes), whiskers (extremes), and outliers. The fit functions from equation I are displayed as solid lines (orange for UHDR and blue for SDR) with the parameters and their standard deviations given in the legend. The difference between UHDR and SDR g -value fits is shown as a function of initial oxygen levels with the standard deviation area shaded on the right side. In both graphs, the vertical lines mark the oxygen concentrations used in the in vitro experiments. Panel B – Clonogenic Cell Survival: Hypoxia data on the left and normoxia data on the right are presented as box plots representing means (horizontal lines) and whiskers, with p-value results (n.s. = non-significant). Each dot represents a single value. $N_{\text{hypoxia}} = 3$ independent experiments, each $n \geq 3$ replicates; $N_{\text{normoxia}} = 2$, each $n \geq 2$ replicates). Panel C – Pancreatic Tumor Irradiation: Tumor volume progression and Kaplan-Meier survival curves for the left and right sides, respectively. Tumor volumes are presented as mean \pm standard error of mean ($N = 6$), with n.s. = non-significant; *** significant p-values. The arrow marks the day of the irradiation. Kaplan-Meier survival curves (Log-Rank test: Ctrl vs. SDR ** significant; Ctrl vs. UHDR ** significant; SDR vs. UHDR n.s.; $N = 6$). (For interpretation of the references to colour in this figure legend, the reader is referred to the web version of this article.)

target coverage (Fig. 1 C). The tumor sizes were measured 3 times per week using a calliper. The volumes were calculated with the following formula: Tumor Volume [mm^3] = length \times width $\times \frac{\text{width}}{2}$.

Animal work was carried out in accordance with the rules approved by the local and governmental animal care committee established by the German government (Regierungspraesidium, Karlsruhe).

Tumor volumes were compared at given time points using one-way analysis of variance (ANOVA) with Tukey's multiple comparison test in GraphPad Prism Software. Kaplan-Meier survival curves were compared using the Log-Rank test (GraphPad Prism).

3. Results

In a simplified BSA solution, the oxygen consumption saturated for high initial oxygen concentrations after UHDR irradiation at $0.0205 \pm 0.0003 \text{ \%}/\text{Gy}$ and for SDR at $0.0235 \pm 0.0003 \text{ \%}/\text{Gy}$ (Fig. 2 A). The difference in oxygen consumption between the SDR and UHDR irradiated samples was negligible, with less than $0.003 \text{ \%}/\text{Gy}$.

In vitro, our findings suggested a similar cytotoxic efficacy of SDR and UHDR in normoxic and hypoxic conditions when irradiated with 8 Gy (Fig. 2 B). In vivo, both SDR and UHDR irradiations at a single 10 Gy fraction with an LETd of $134 \text{ keV}/\mu\text{m}$ indicated potential efficacy in treating resistant KPC tumors, with both modalities showing modest but significant tumor volume growth delay compared to control. Median survival for SDR and UHDR treated animals was 24 and 25 days, respectively, compared to 21 days for the controls (Fig. 2 C). Given the highly resistant and hypoxic nature of KPC tumor model, this extended survival is a valuable starting point for further preclinical high LET investigations aimed at PDAC tumor treatment.

4. Discussion

Pancreatic cancer is highly therapy-resistant, with a median survival of 3–5 months. Its proximity to vital organs further complicates precise targeting. In this study, we have demonstrated the first application of oxygen ion UHDR irradiation offering a promising therapeutic option for pancreatic cancer. Marginal differences in oxygen consumption between UHDR and SDR were observed in protein-enriched saline solutions. According to the oxygen depletion hypothesis, this minimal difference suggested that the oxygen consumption mechanism plays a lesser role at higher LETs. In vitro experiments revealed comparable PDAC cell survival after UHDR and SDR regardless of normoxic or hypoxic (1 % O_2) conditions in the studied settings (8 Gy, $100.3 \text{ keV}/\mu\text{m}$).

Contrasting findings have been reported in previous studies examining lower-LET irradiation. Although an UHDR sparing under hypoxia (1 % O_2) was demonstrated for several cell lines below $20 \text{ keV}/\mu\text{m}$ at $\sim 8 \text{ Gy}$ [24–27], a study with pancreatic tumor cells reported a cell over-killing after UHDR electron irradiation in normoxia [28]. The absence of sparing with higher LET oxygen ions may originate from their reduced reliance on O_2 for inducing cell killing [29,30]. Higher LET beams exhibit a reduced dependence on indirect DNA damage mechanisms [31,32], thereby minimizing the impact of O_2 consumption and potentially reducing differential sparing effects between SDR and UHDR. However, future experiments under varied O_2 , dose and LET conditions are required to validate these findings.

A fundamental question concerning UHDR radiation pertains to its comparative efficacy in controlling tumors when compared with that of SDR. To date, UHDR effects, especially at high LET, have been predominantly investigated in healthy tissues [15]. In this work, we address tumor-specific impacts of high LET UHDR using the highly resistant KPC PDAC tumor model, which closely mirrors human disease [22,23]. Both SDR and UHDR showed a moderate impact on tumor progression and Kaplan-Meier survival rates. However, a notable 20 % improvement in survival highlighted the potential therapeutic benefits of high LET oxygen ions. These results underscore the need for preclinical studies

employing oxygen ions in pancreatic cancer to extend patient life expectancy and refine treatment approaches. Investigations utilizing normal tissue readouts are crucial to determine the potential existence of a FLASH effect with oxygen ion beams. The presented setup offers a versatile platform for high-LET UHDR experiments and lays the groundwork for future studies.

CRedit authorship contribution statement

Celine Karle: Conceptualization, Data curation, Formal analysis, Investigation, Methodology, Software, Validation, Visualization. **Domenico I. Filosa:** Investigation, Writing – review & editing. **Mahdi Akbarpour:** Investigation, Formal analysis, Data curation, Writing – review & editing. **Nora Schuhmacher:** Investigation, Writing – review & editing. **Stephan Brons:** Investigation, Resources, Writing – review & editing. **Rainer Cee:** Resources, Writing – review & editing. **Christian Schömers:** Resources, Writing – review & editing. **Stefan Scheloske:** Resources, Writing – review & editing. **Kristoffer Petersson:** Resources, Writing – review & editing. **Thomas Haberer:** Funding acquisition, Resources, Supervision, Writing – review & editing. **Amir Abdollahi:** Funding acquisition, Resources, Supervision, Writing – review & editing. **Jürgen Debus:** Funding acquisition, Resources, Supervision, Writing – review & editing. **Thomas Tessonnier:** Conceptualization, Methodology, Writing – review & editing. **Mahmoud Moustafa:** Investigation, Formal analysis, Data curation, Writing – review & editing. **Andrea Mairani:** Conceptualization, Funding acquisition, Methodology, Project administration, Resources, Supervision, Writing – review & editing. **Ivana Dokic:** Conceptualization, Formal analysis, Methodology, Project administration, Resources, Supervision, Writing – review & editing.

Declaration of competing interest

The authors declare the following financial interests/personal relationships which may be considered as potential competing interests: This work was supported by intramural funds from the National Center for Tumor Diseases (NCT-PRO: 1030000042 and Biodose: 1030000043 programs). This work was supported in part by the National Institutes of Health (NIH-1P01CA257904-01A1). The funders had no role in study design, data collection and analysis, decision to publish or preparation of the manuscript.

J. Debus reports grants from CRI – The Clinical Research Institute GmbH grants from View Ray Inc., grants from Accuray International Sarl, grants from Accuray Incorporated, grants from RaySearch Laboratories AB, grants from Vision RT limited, grants from Merck Serono GmbH, grants from Astellas Pharma GmbH, grants from Astra Zeneca GmbH, grants from Siemens Healthcare GmbH, grants from Merck KGaA Accounts Payable, grants from Solution Akademie GmbH, grants from Ergomed PLC Surrey Research Park, grants from Siemens Healthcare GmbH, grants from Quintiles GmbH, grants from Pharmaceutical Research Associates GmbH, grants from Boehringer Ingelheim Pharma GmbH Co, grants from PTW-Freiburg Dr. Pynchlau GmbH. A. Abdollahi reports grants and other support from Merck KGaA, FibroGen Inc., Bayer, Roche, and Merck Serono and other support from BMS and BioMedX outside the submitted work. Other authors: none.

Acknowledgement

The authors would like to thank the whole accelerator team at HIT for helping with the synchrotron adjustments and Uli Weber from GSI for providing the 2DRMs.

Appendix A. Supplementary data

Supplementary data to this article can be found online at <https://doi.org/10.1016/j.phro.2025.100803>.

References

- [1] Siegel RL, Giaquinto AN, Jemal A. Cancer statistics, 2024. *CA Cancer J. Clin.* 2024; 74:12–49. <https://doi.org/10.3322/caac.21820>.
- [2] Kobeissi JM, Simone CB, Lin H, Hilal L, Hajj C. Proton Therapy in the Management of Pancreatic Cancer. *Cancers* 2022;14:2789. <https://doi.org/10.3390/cancers14112789>.
- [3] Comito T, Cozzi L, Zerbi A, Franzese C, Clerici E, Tozzi A, et al. Clinical results of stereotactic body radiotherapy (SBRT) in the treatment of isolated local recurrence of pancreatic cancer after R0 surgery: a retrospective study. *Eur. J. Surg. Oncol.* 2017;43:735–42. <https://doi.org/10.1016/j.ejso.2016.12.012>.
- [4] Kolbeinsdóttir HM, Chandana S, Wright GP, Chung M. Pancreatic cancer: a review of current treatment and novel therapies. *J. Invest. Surg.* 2023;36:2129884. <https://doi.org/10.1080/08941939.2022.2129884>.
- [5] Koong AC, Mehta VK, Le QT, Fisher GA, Terris DJ, Brown JM, et al. Pancreatic tumors show high levels of hypoxia. *Int. J. Radiat. Oncol. Biol. Phys.* 2000;48: 919–22. [https://doi.org/10.1016/S0360-3016\(00\)00803-8](https://doi.org/10.1016/S0360-3016(00)00803-8).
- [6] McKeown S. Defining normoxia, physoxia and hypoxia in tumours—implications for treatment response. *Br. J. Radiol.* 2014;87:20130676. <https://doi.org/10.1259/bjr.20130676>.
- [7] Shinoto M, Yamada S, Terashima K, Yasuda S, Shioyama Y, Honda H, et al. Carbon ion radiation therapy with concurrent gemcitabine for patients with locally advanced pancreatic cancer. *Int. J. Radiat. Oncol. Biol. Phys.* 2016;95:498–504. <https://doi.org/10.1016/j.ijrobp.2015.12.362>.
- [8] Baltazar F, Tessonnier T, Haberer T, Debus J, Herfarth K, Tawak B, et al. Carbon-ion radiotherapy (CIRT) as treatment of pancreatic cancer at HIT: initial radiation plan analysis of the prospective phase II PACK-study. *Radiother. Oncol.* 2023;188: 109872. <https://doi.org/10.1016/j.radonc.2023.109872>.
- [9] Durante M, Loeffler JS. Charged particles in radiation oncology. *Nat. Rev. Clin. Oncol.* 2009;7:37–43. <https://doi.org/10.1038/nrclinonc.2009.183>.
- [10] Jäkel O, Karger CP, Debus J. The future of heavy ion radiotherapy. *Med. Phys.* 2008;35:5653–63. <https://doi.org/10.1118/1.3002307>.
- [11] Hagiwara Y, Bhattacharyya T, Matsufuji N, Isozaki Y, Takiyama H, Nemoto K, et al. Influence of dose-averaged linear energy transfer on tumour control after carbon-ion radiation therapy for pancreatic cancer. *Clin. Transl. Radiat. Oncol.* 2020;21: 19–24. <https://doi.org/10.1016/j.ctro.2019.11.002>.
- [12] Sokol O, Durante M. Carbon ions for hypoxic tumors: are we making the most of them? *Cancers* 2023;15:4494. <https://doi.org/10.3390/cancers15184494>.
- [13] Webster A, Mundora Y, Clark CH, Hawkins MA. To compress or to breath-hold? a systematic review of the impact of motion mitigation techniques on motion, interfraction set-up errors, and intrafraction errors in patients with hepatobiliary and pancreatic malignancies. *Radiother. Oncol.* 2024;201:110581. <https://doi.org/10.1016/j.radonc.2024.110581>.
- [14] Weber UA, Scifoni E, Durante M. FLASH radiotherapy with carbon ion beams. *Med. Phys.* 2022;49:1974–92. <https://doi.org/10.1002/mp.15135>.
- [15] Tinganelli W, Sokol O, Puspitasari A, Helm A, Simoniello P, Schuy C, et al. FLASH Bragg-peak irradiation with a therapeutic carbon ion beam: first in vivo results. *Int. J. Radiat. Oncol. Biol. Phys.* 2024;121:1282–92. <https://doi.org/10.1016/j.ijrobp.2024.11.089>.
- [16] Montay-Gruel P, Acharya MM, Petersson K, Alikhani L, Yakkala C, Allen BD, et al. Long-term neurocognitive benefits of FLASH radiotherapy driven by reduced reactive oxygen species. *PNAS* 2019;116:10943–51. <https://doi.org/10.1073/pnas.1901777116>.
- [17] Tesson M, Morton JP. The preclinical gap in pancreatic cancer and radiotherapy. *Dis. Model. Mech.* 2024;17:dmm050703. <https://doi.org/10.1242/dmm.050703>.
- [18] Holm KM, Weber U, Simeonov Y, Krauss A, Jäkel O, Greilich S. 2D range modulator for high-precision water calorimetry in scanned carbon-ion beams. *Phys. Med. Biol.* 2020;65:215003. <https://doi.org/10.1088/1361-6560/aba6d5>.
- [19] Simeonov Y, Weber U, Schuy C, Engenhardt-Cabillie R, Penchev P, Durante M, et al. Monte Carlo simulations and dose measurements of 2D range-modulators for scanned particle therapy. *Z. Med. Phys.* 2021;31:203–14. <https://doi.org/10.1016/j.zemedi.2020.06.008>.
- [20] Iaea. Absorbed Dose Determination in External Beam Radiotherapy. Vienna: INTERNATIONAL ATOMIC ENERGY AGENCY 2001.
- [21] Karle C, Liew H, Tessonnier T, Mein S, Petersson K, Schömers C, et al. Oxygen consumption measurements at ultra-high dose rate over a wide LET range. *Med. Phys.* 2024;52:1323–34. <https://doi.org/10.1002/mp.17496>.
- [22] Hingorani SR, Wang L, Multani AS, Combs C, Deramaut TB, Hruban RH, et al. Trp53R172H and KrasG12D cooperate to promote chromosomal instability and widely metastatic pancreatic ductal adenocarcinoma in mice. *Cancer Cell* 2005;7: 469–83. <https://doi.org/10.1016/j.ccr.2005.04.023>.
- [23] Li J, Byrne KT, Yan F, Yamazoe T, Chen Z, Baslan T, et al. Tumor cell-intrinsic factors underlie heterogeneity of immune cell infiltration and response to immunotherapy. *Immunity* 2018;49:178–93. <https://doi.org/10.1016/j.ccr.2005.04.023>.
- [24] Tessonnier T, Mein S, Walsh DW, Schuhmacher N, Liew H, Cee R, et al. FLASH dose rate helium ion beams: first in vitro investigations. *Int. J. Radiat. Oncol. Biol. Phys.* 2021;111:1011–22. <https://doi.org/10.1016/j.ijrobp.2021.07.1703>.
- [25] Adrian G, Konradsson E, Lempert M, Bäck S, Ceberg C, Petersson K. The FLASH effect depends on oxygen concentration. *Br. J. Radiol.* 2020;92:20190702. <https://doi.org/10.1259/bjr.20190702>.
- [26] Tinganelli W, Sokol O, Quartieri M, Puspitasari A, Dokic I, Abdollahi A, et al. Ultra-High Dose Rate (FLASH) Carbon Ion Irradiation: Dosimetry and first Cell Experiments. *Int. J. Radiat. Oncol. Biol. Phys.* 2022;112:1012–22. <https://doi.org/10.1016/j.ijrobp.2021.11.020>.
- [27] Adrian G, Ruan J-L, Paillas S, Cooper CR, Petersson K. In vitro assays for investigating the FLASH effect. *Expert Rev. Mol. Med.* 2022;24:e10.
- [28] Venkatesulu BP, Sharma A, Pollard-Larkin JM, Sadagopan R, Symons J, Neri S, et al. Ultra high dose rate (35 Gy/sec) radiation does not spare the normal tissue in cardiac and splenic models of lymphopenia and gastrointestinal syndrome. *Sci. Rep.* 2019;9:17180. <https://doi.org/10.1038/s41598-019-53562-y>.
- [29] Chatterjee A, Holley WR. Biochemical mechanisms and clusters of damage for high-let radiation. *Adv. Space Res.* 1992;12:33–43. [https://doi.org/10.1016/0273-1177\(92\)90087-E](https://doi.org/10.1016/0273-1177(92)90087-E).
- [30] Furusawa Y, Fukutsu K, Aoki M, Itsukaichi H, Eguchi-Kasai K, Ohara H, et al. Inactivation of Aerobic and Hypoxic Cells from three Different Cell Lines by Accelerated 3He-, 12C- and 20Ne-Ion Beams. *Radiat. Res.* 2000;154:485–96. [https://doi.org/10.1667/0033-7587\(2000\)154\[0485:IOAAHC\]2.0.CO;2](https://doi.org/10.1667/0033-7587(2000)154[0485:IOAAHC]2.0.CO;2).
- [31] Alper T, Bryant PE. Reduction in Oxygen Enhancement Ratio with increase in LET: Tests of two Hypotheses. *Int. J. Radiat. Biol.* 1974;26:203–18. <https://doi.org/10.1080/09553007414551171>.
- [32] Hirayama R, Ito A, Tomita M, Tsukada T, Yatagai F, Noguchi M, et al. Contributions of Direct and indirect Actions in Cell Killing by High-LET Radiations. *Radiat. Res.* 2009;171:212–8. <https://doi.org/10.1667/RR1490.1>.

HEAVY ION UHDR TOWARDS CLINICAL IMPLEMENTATION

The systematic investigations established three key findings: First, the technical feasibility of Ultra-High Dose Rate (UHDR) heavy ion at the Heidelberg Ion Beam Therapy Center (HIT) was validated through comprehensive dosimetric characterization. The flashDiamond (fD) detector showed a response independent of both UHDR and dose-averaged LET (LET_d). Second, mechanistic studies revealed an inverse relationship between oxygen consumption rates and LET_d, with consistently lower consumption under UHDR conditions across all particle types. Finally, biological investigations spanning in vitro to in vivo experiments demonstrated a comparable therapeutic efficacy between UHDR and Standard Dose Rate (SDR) oxygen ion treatments in Pancreatic Ductal Adenocarcinoma (PDAC) cell killing and tumor growth delay. These findings not only validate the technical implementation but also provide insights into potential mechanisms and therapeutic applications of UHDR heavy ion therapy.

Together, these results lay the foundation for potential integration of UHDR oxygen ion therapy into clinical practice, particularly for PDAC treatment. Consequently, the following sections will discuss the implications of these findings for future clinical applications, as well as the necessary requirements for subsequent steps.

7.1 Technical Implementation of Heavy Ion UHDR Therapy at HIT

The successful demonstration of UHDR heavy ion delivery at HIT with small targets represents an important technical milestone. However, clinical translation will require further advancements, particularly in scaling up particle numbers for larger fields and achieving conformal coverage of complex tumor geometries.

A key challenge is the limited **number of particles**. While the Electron Cyclotron Resonance Ion Source (ECRIS) and synchrotron can, in principle, support higher particle numbers, the current bottleneck lies in the limited transmission efficiency of the Radio Frequency Quadrupole (RFQ) at the Linear Accelerator (LINAC) (Fig. 2.1). Merely half of the ions generated in the ECRIS fit into the RFQ phase space.

Current investigations of the accelerator team are focused on enhancing the RFQ transmission, with the ultimate objective of facilitating higher currents and, consequently, larger doses and wider fields for UHDR irradiations. [210]

Equally important is the ability to conform the monoenergetic UHDR beam to the complex three-dimensional shape of tumor targets. In conventional irradiation, active Pencil Beam Scanning (PBS) provide **conformal coverage** of the target volume in both lateral and longitudinal direction (Sec. 2.1.3). At UHDR, lateral coverage is still achieved through conventional PBS, with the flexibility to adjust the beam pattern to match the anatomy of the targets. In contrast, the longitudinal coverage typically requires Iso-Energy Layer (IEL) switching with a new synchrotron cycle, which takes up too much time for UHDR delivery (Sec. 5.2.1). To overcome this limitation at HIT, 2D Range Modulator (2DRM) are employed to achieve full longitudinal coverage in a single spill, enabling homogeneous Spread-Out Bragg Peak (SOBP) delivery for preclinical experiments (Fig. 5.2). For clinical application, more sophisticated 3D Range Modulators (3DRMs) with patient-specific, non-homogeneous pin geometries would be required to achieve optimal target conformity (Fig. 7.1). [211]

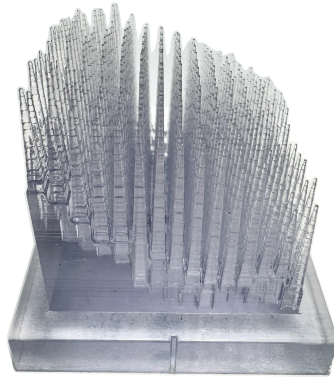


Figure 7.1.: 3DRM Design: The heterogeneous pin structure is chosen to conformally irradiate a specific target volume in one spill. This is a picture of a prototype kindly provided by Sae Hyun Ahn.

The clinical use of 3DRM requires an additional optimization step after the dose planning to generate the corresponding ideal 3DRM geometry. This optimization step must take into account for technical constraints from the design and production processes of such range modulators. Several production processes have been trialed and are available for the fabricating 3DRMs, such as 3D printing with a polymer resin or laser melting techniques to produce 3DRM out of aluminum.

The additional materials introduced into the beam line alter the beam quality due to increased fragmentation and induced scattering. The extent of the alterations mainly depends on the geometry and materials of the 3DRM: One study showed that, when aluminum is used as 3DRM material, fewer neutrons and fragments are produced compared to 3DRM made from polymer resins. At the same time, the scattering contribution would increase if aluminum were in the beam line. [212] These beam modifications must be accurately characterized through measurements and simulations to ensure proper integration into the Treatment Planning System (TPS).

Exactly these beam alterations and contaminations caused by passive degrader systems were the initial reasons to use active PBS at HIT to achieve a more conformal dose application on the distal and proximal edges of the target. [29] Although passive energy degraders are not standard at HIT, this is well-established in clinical practice in Japan (e.g., at HIMAC).

There, passive energy degraders are utilized for beam shaping, such as patient-specific brass collimators for lateral shaping and polyethylene range compensators for longitudinal modulation. [213] While the full potential of the active PBS cannot yet be realized at UHDR due to energy switching limitations, the expertise and infrastructure for 3DRM optimization and production at HIT in combination with existing clinical protocols, provide a solid foundation for implementation of UHDR heavy ion irradiation into the clinical workflow.

7.2 Dosimetric Protocol for Heavy Ion UHDR at HIT

A robust dosimetric protocol for Quality Assurance (QA) is fundamental for safe and effective UHDR heavy ion therapy. Given the absence of standardized guidelines for high-Linear Energy Transfer (LET) UHDR irradiation (Sec. 5.3.1), we implemented a comprehensive protocol following established code-of-practice principles, ensuring reliable and accurate dose measurement across the entire field, and while also monitoring the temporal dose delivery structure needed for UHDR characterization (Sec. 4.2).

Daily **absolute dose measurements** were performed with the PinPoint chamber (PTW, REF: TM31015, SN:0903) [186].¹ The PinPoint chamber is recommended for high LET and for small field dosimetry. [180] Additionally, for the purpose of heavy ion UHDR applications, it has been validated for UHDR helium [200] and carbon ion SDR irradiation. [214] Specifically for carbon ions, Hamatani et al. demonstrated a low saturation and recombination correction factor (max 6.15 %) and acceptable measurement precision (1.5 %) at the operating voltage of 400 V. [214]

The **field homogeneity** was verified using passive radiochromic EBT3 films (Gafchromic™ EBT3, 8×10), which provide a high spatial resolution. While EBT3 films have been shown to be reliable for UHDR proton irradiation [187], EBT3 films have underresponded to high-LET carbon ions due to LET-dependent quenching. [215, 216] Thus, EBT3 films were used solely for homogeneity checks rather than absolute dose measurements. [206] To overcome this limitation in the future, advanced 2D detector arrays, such as the Octavius Detector 1500XDR [217], may offer simultaneous assessment of absolute dose and field uniformity at high-LET UHDR. [218]

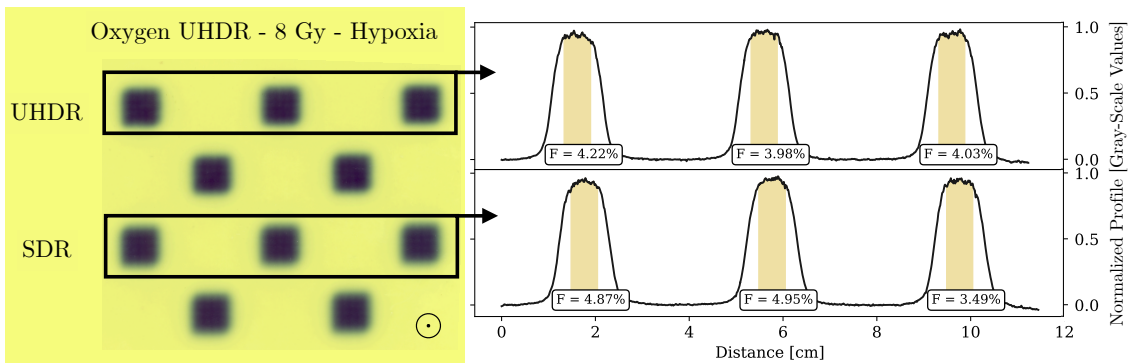


Figure 7.2.: Evaluation of EBT3 Gafchromic Films: The films on the left side of the image were used during the in vitro experiments described in Sec. 6.3.[207] On the right side, representative line profiles obtained from the marked rows are displayed. Profile extraction and analysis were performed as outlined in the 1st Paper in Sec. 6.1. [206] The flatness index was calculated within the central region encompassing 50 % of the total area under the curve. A flatness index below 5 % is generally regarded as indicative of a homogeneous profile. [206]

¹The diamond detectors used in the characterization study (Sec. 6.1 [206]) were provided temporarily by our collaborators at the University of Rome “Tor Vergata” and therefore not used daily.

A critical aspect of UHDR dosimetry is the monitoring of the dose delivery **temporal structure**. As neither the PinPoint chamber nor EBT3 films record temporal information, the UHDR-optimized Beam Application Monitoring System (BAMS) system, specifically the second Ionization Chamber (IC) (Sec. 2.1.3), was utilized to record the total irradiation time. Examples of such recordings are shown in Fig. 5.1 and Fig. 7.4. Combined with the absolute dose measured by the PinPoint chamber, the acquired data allowed the calculation of the averaged Dose Rate (\bar{D}) for each irradiation. In UHDR experiments, the \bar{D} defines the baseline requirement for temporal dose assessment (Sec. 4.2).

The daily dosimetric protocol was established by combining PinPoint chamber measurements for absolute dose and EBT3 films for field homogeneity assessment, supplemented with BAMS temporal recordings, which enable extraction of irradiation time and the subsequent calculation of \bar{D} . Together, this integrated approach forms the backbone of our dosimetric strategy, sufficient for daily experimental utilization and possible QA protocols.

7.2.1 Advanced Temporal Dosimetry with Diamond Detectors

To further advance the dosimetric protocol of the temporal characterization, diamond detectors present a valuable addition. Their potential for straightforward integration into clinical workflows at HIT, compatibility with existing electrometers, and commercial availability make them attractive for QA-use. [195, 196] Most importantly, diamond detectors enable measurements of the local instantaneous Dose Rate (\dot{D}_{inst}) within one pulse (Sec. 5.3.1), providing detailed insight into the spatio-temporal dose distribution, which is essential for understanding and optimizing UHDR effects (Sec. 4.2).

To demonstrate this, the temporal structure of various PBS patterns was measured to assess their effect on the \dot{D}_{inst} . For this purpose, the diamond detectors were connected to a transimpedance amplifier with adjustable gain (Model DLPCA-200, FEMTO, Germany) and subsequently to a 12-bit 200 MHz digital oscilloscope (PicoScope 5444A, PicoScope Version 7, Pico Technology, UK). For the microDiamond (mD), a gain and bandwidth combination of 10^6 V/A with 200 kHz was used. For the fD, a combination of 10^7 V/A with 50 kHz would have been required to obtain a measurable signal; however, such high amplification rendered the measurement chain highly sensitive to electromagnetic interference and noise. Consequently, the mD was preferred for its stability, despite the slight LET dependence. The latter effect and mitigation strategies are discussed in the next section.

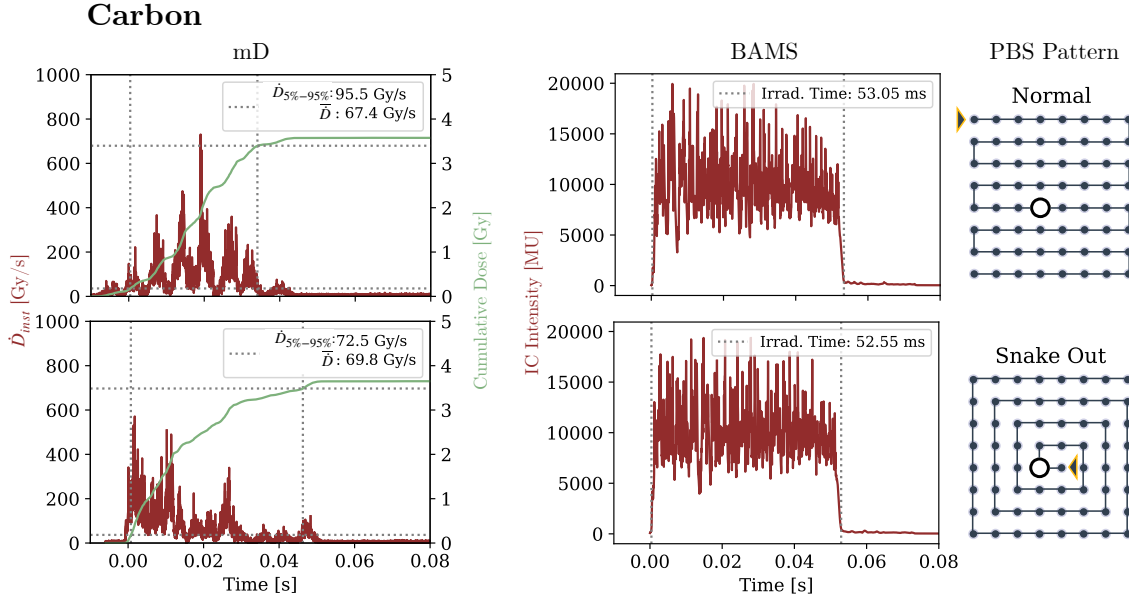


Figure 7.3.: Various Dose Rate Measures and Cumulative Dose Assessment for Carbon Ion Irradiations: The first column shows the \dot{D}_{inst} and the corresponding cumulative dose (green) measured with the mD. The calculation of $\dot{D}_{5\%-95\%}$ is illustrated, with grey dotted lines marking the 5% and 95% dose thresholds and their corresponding time points. The $\dot{D}_{5\%-95\%}$ and \bar{D} are given in the legend, while the latter was determined from the total cumulative dose of the mD measurement and irradiation time measured by the BAMS. The corresponding BAMS signal and the total irradiation time, indicated by grey dotted lines, are presented in the middle column. The right column shows the PBS spot pattern, with the estimated mD position marked by a white circle. The starting point of the raster scan is indicated by a yellow outlined arrowhead. The beam then follows the blue line to cover the full PBS pattern.

The signal-based, uncorrected \dot{D}_{inst} was calculated by dividing the background-corrected signal [V] by the amplifier gain to obtain values in [C/s] and normalizing by the dose linearity factor [C/Gy] for the respective detector and particle type (Sec. 6.1 [206], Fig. 6). The cumulative dose was obtained by integrating the \dot{D}_{inst} . The results for carbon and oxygen ions are illustrated in Fig. 7.3 and Fig. 7.4, respectively. These visualizations emphasize how the temporal and spatial delivery pattern directly affect the local dose rate experienced by the sample.

Two PBS patterns were compared: the standard UHDR “Normal” pattern with conventional sequential scanning of the lines, and the “Snake Out” pattern, where spots are irradiated from the center outward. For both carbon and oxygen, the number of particles per spot and the synchrotron settings were identical; the sole variable was the sequence of spot delivery. The influence of the irradiation pattern is evident in the resulting \bar{D} , \dot{D}_{inst} , and $\dot{D}_{5\%-95\%}$.

The \bar{D} depends solely on the total dose and overall irradiation time and is therefore expected to remain constant across the irradiated patterns, since the same number of particles were applied to each spot. Indeed, BAMS records confirmed that the total irradiation time² varied by less than 7 ms. With uncorrected cumulative doses of approximately 2 Gy for oxygen and 3.6 Gy for carbon, the resulting \bar{D} differs only marginally and maintains values of ≈ 68 Gy/s for carbon and ≈ 23 Gy/s for oxygen. Small variations could be attributed to the inherent instability of synchrotron extraction at UHDR settings (Sec. 5.2.1).

In contrast, the \dot{D}_{inst} is highly sensitive to the delivery sequence: it exhibited sharp peaks when the detector was traversed by the beam, reaching values of up to 800 Gy/s for both ions.

²Determined from the point at which the BAMS intensity exceeds a threshold of 400 MU and decreased below this value again.

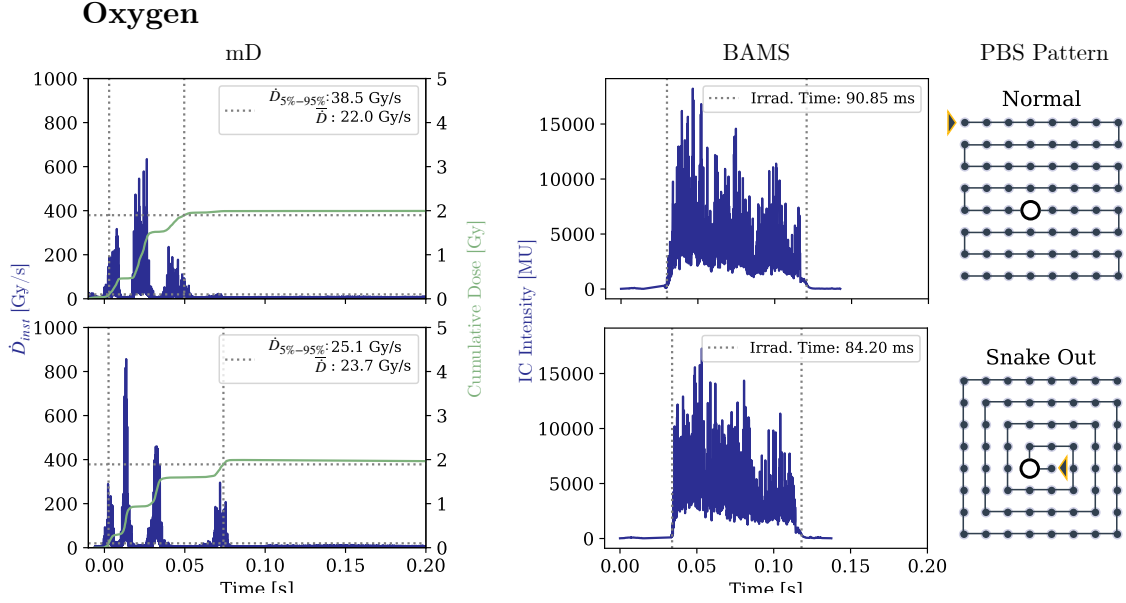


Figure 7.4.: Various Dose Rate Assessment and Cumulative Dose Assessment for Oxygen Ion Irradiations: Dose rate and cumulative dose assessment for oxygen ion irradiations, following the same structure as described for carbon ions (see Fig. 7.3). The first column shows the \dot{D}_{inst} and cumulative dose (green) measured with the mD, including the $\dot{D}_{5\%-95\%}$ interval determined from the 5 % and 95 % dose thresholds (grey dotted lines). The middle column presents the corresponding BAMS signal, with grey dotted lines indicating the total irradiation time. The rightmost column shows the PBS spot pattern, with the estimated mD position marked by a white circle and the raster scanning path beginning at the yellow arrowhead.

The number and timing of these peaks depended on the spot pattern and the beam’s Full Width Half Maximum (FWHM), e.g., the “Normal” pattern irradiation produced eight distinct peaks corresponding to the eight scanned lines (Fig. 7.3), whereas for oxygen, owing to its smaller FWHM, only five peaks were observed (Fig. 7.4), corresponding to two neighboring PBS lines.

The $\dot{D}_{5\%-95\%}$ metric focuses on the time interval during which the dose rises from 5 % to 95 % of the total and provides a more representative measure of the effective dose rate experienced locally: For the “Normal” pattern, the $\dot{D}_{5\%-95\%}$ is considerably higher than the \bar{D} , as the first signal peaks for carbon and oxygen did not contribute more than 5 % of the dose, so these were not included in the dose rate metric. The time span of this metric was reduced, so the $\dot{D}_{5\%-95\%}$ was higher than the \bar{D} . In the “Snake Out” pattern, the detector remained exposed to the beam for a longer duration due to the outgoing sequential pattern, making the time span for the $\dot{D}_{5\%-95\%}$ and total irradiation time nearly identical. Also for oxygen with the narrower FWHM (Fig. 7.5), this behavior was evident (Fig. 7.4).

This demonstrates that $\dot{D}_{5\%-95\%}$ is sensitive to both the temporal and spatial characteristics of the delivery plan, and thus distinguishes between patterns that would appear similar in the \bar{D} metric.

The figures in this section illustrate the importance of employing multiple dose rate metrics to comprehensively characterize UHDR delivery. While \bar{D} provides a general summary, the $\dot{D}_{5\%-95\%}$ captures the local, time-resolved dose rate. Ideally, the \dot{D}_{inst} provides all the necessary information to calculate the metrics given the total irradiation time. These observations highlight the importance of detailed temporal characterization in both research and potential clinical UHDR protocols (Sec. 4.2).

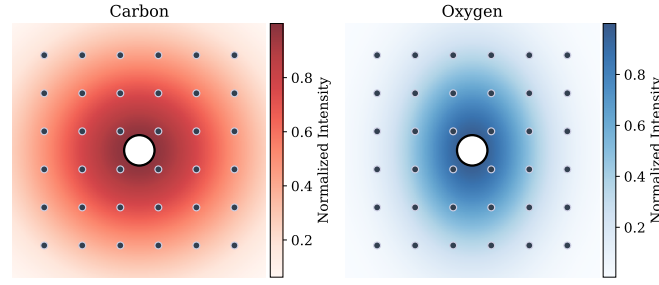


Figure 7.5.: Beam FWHM for Carbon and Oxygen Ions: Single spot beams are illustrated with their measured FWHM in x and y directions^a for both carbon and oxygen ion beams. The irradiated field with a size of $10.5\text{ mm} \times 10.5\text{ mm}$ and a spot spacing of 1.5 mm is shown for reference. (Tab. 5.1). Due to scattering, the FWHM of one carbon spot is larger compared to oxygen ions (Eq. 2.10). The FWHM in x and y direction varies for the oxygen ion beam and produces an ellipsoidal shape. This does not pose a limitation since this behavior can be accurately modeled in treatment planning to ensure correct dose rate calculations. For comparison, the sensitive area of the detector is indicated with a circle.

^aThe FWHM is measured with the MWPC in the BAMS. The beam is displayed as a Gaussian function with different FWHM in x and y directions.

7.2.2 Detector Response and Correction Strategies

The amplified noise was the reason to conduct this first signal investigation with the mD. However, it should be noted that the mD detectors exhibited a slight LET-dependent deviation, with an increasing overestimation of the dose at SDR and a constant 5 % overestimation at UHDR. [206] Firstly, such tiny deviations often result from **setup** or **positioning uncertainties**, as detailed in Sec. 6.1. [206]

Secondly, for future mD applications, linear deviations can be corrected, maintaining the detector suitability for absolute dosimetry. Similar to ionization chambers, which are routinely corrected for temperature, pressure, [179] or recombination for UHDR application [190], appropriate **correction factors** could be derived for mD detectors to account for their signal overestimation.

However, the literature presents an inconsistent picture on the signal trend of the mD from PTW Type 60019, used at HIT. While no LET-dependence was reported in the lower-LET proton regime [219], multiple studies identified systematic deviations at higher LET. In helium-ion UHDR experiments, the mD detector exhibited a dose overestimation of up to 4 %. [200] Whereas for monoenergetic carbon ions at 62 MeV/u in the distal Bragg peak, Rossomme et al. reported under-responses of up to 20 % relative to Advanced Markus Chamber (AMC) measurements with increasing LET. [220] Conversely, Marinelli et al. observed no LET or dose-rate dependence for scanned clinical carbon beams up to 380 MeV/u . [197] Subsequent studies refuted the hypothesis that such discrepancies arose from inconsistent mD fabrication, demonstrating high reproducibility across different production batches. [221]

Part of these discrepancies may stem from differences in beam characteristics: for instance, the strong under-response was observed in a purely monoenergetic carbon beam without range modulation, whereas studies using modulated beams with broader LET distributions did not show this effect. [220]

Physical mechanisms to explain the over- and under-response have also been proposed. Under-response at high LET was attributed to enhanced recombination of electron-hole pairs within the thin diamond layers. [219]

Over-response, though less intuitive, has been linked to radiation-induced charge imbalances in detector contacts and cables, a mechanism demonstrated in small-field electron beams, where reducing exposed electronics mitigated this effect. [188]

Overall, the small deviations observed with mD detectors are more likely attributable to experimental uncertainties or setup effects than intrinsic detector physics, especially given inconsistent literature trends. For absolute dosimetry, detector-specific characterization and correction factors remain necessary, as is standard for other detector types. Since this study focused on the combined challenges of high-LET and UHDR irradiation, a systematic characterization of mD detectors should be pursued in future work.

7.3 Mechanistic Insights into UHDR Effects

Echoing Max Planck’s quote on the importance of understanding the mechanisms (Chap. 1), unraveling the basis of UHDR effects is essential for advancing this modality. While it is established that the temporal irradiation structure strongly influences UHDR effects – an aspect that can be precisely characterized with diamond detectors – the pathways by which it modulates the radiochemical cascade and biological outcomes remain incompletely understood (Sec. 4.3). The identification of these pathways is therefore a critical next step.

7.3.1 Impact of Solution Composition

Systematic solution studies are essential for dissecting the molecular contributions within the radiochemical cascade (Sec. 4.3). By isolating and examining each stage and component, these studies provide insight into the role of specific molecules, for example oxygen, in modulating UHDR effects. Such understanding is fundamental for both the mechanistic elucidation of the UHDR effects and for the accurate benchmarking and validation of radiochemical Monte Carlo Simulations (MCs).

The composition of the solution critically determines the dynamics of the radiochemical cascade, as demonstrated for organic molecules, highlighted in red in Fig. 2.6. Consequently, experiments conducted in pure water are insufficient to capture the complexity of radiochemical processes. [57, 222]

Therefore, in this work, **Bovine Serum Albumin (BSA)**, a protein-enriched saline solution, was selected to model the extracellular environment. [144] This model provides a simple, stable, and reproducible solution well suited for sensitive detection of oxygen consumption differences. [67]

To approximate intracellular conditions, additional components such as thiols and scavengers must be considered, as they further affect the cascade (Sec. 2.3). [54, 61] Model solutions containing these components, such as “CELL”, have shown similar trends in oxygen consumption under UHDR exposure as observed for BSA. [144] However, one recent study using cell lysate reported no difference in oxygen consumption between UHDR and SDR irradiation [223], underscoring the complexity of the cascade in heterogeneous cellular environments. While BSA is suitable for initial investigations, more complex solutions are ultimately required to fully elucidate oxygen consumption dynamics.

Current MCs for radiochemical interaction cascades are limited by the use of oversimplified solution models (Sec. 5.3.2). For elevating the complexity and an accurate representation of the chemical stage, detailed information about reaction rates for relevant molecules is needed, accounting for variables such as pH and oxygen concentration.

These rates and parameters, such as the g-value for oxygen depletion [67], are essential for creating accurate MC models of the chemical cascade but are also used for robust benchmarking. [204, 206]

7.3.2 Hypothetical ODH Mechanism

The **Oxygen Depletion Hypothesis (ODH)** remains debated and largely hypothetical (Sec. 4.3.1). Data from Sec. 6.2 suggest that high-LET UHDR irradiation may provide a unique advantage when following the ODH. Heavy ion therapy produces an inhomogeneous LET distribution, with Tumor Tissue (TT) receiving high LET and Normal Tissue (NT) exposed to lower LET (Fig. 3.2). According to the ODH hypothesis and the experimental evidence from the oxygen consumption study [67], increased oxygen consumption in low-LET regions could induce a transient oxygen-depleted state, potentially sparing NT. In contrast, TT exposed to high LET would exhibit lower oxygen consumption and thus reduced sparing.

In tissue, the oxygen concentration itself is an additional determinant that could amplify the FLASH sparing: Compared with **NT**, **TT** is often hypoxic [108, 224], so further oxygen consumption may have little impact on its radiosensitivity, whereas physiologically oxygenated NT could transiently become more radioresistant under UHDR conditions and the additionally higher consumption rate may amplify this.

However, **absolute oxygen consumption** values are quantitatively small. [67] Nevertheless, even minor shifts in oxygen levels can strongly modulate radiosensitivity, particularly under low-LET irradiation. [225] Whether such shifts are sufficient to account for radioprotection remains unresolved.

When accounting for oxygen consumption, the process of **reoxygenation** adds an additional layer of complexity (Sec. 4.3.1). For example, in vivo measurements during SDR irradiation showed no net oxygen consumption, as reoxygenation compensated for the radiation-induced oxygen consumption. [146] The oxygen perfusion and distribution within tissue was demonstrated to influence the effect of the UHDR irradiation. [141] Thus, a comprehensive description of the oxygen kinetics is essential when the dependence of the UHDR effects on oxygen is investigated. [140]

In summary, oxygen dynamics are likely to play a role in UHDR effects, though their extent remains unresolved. Given the conflicting evidence both supporting [141, 151] and challenging [60, 146] on the importance of oxygen consumption, further research is required. Systematic investigation of the radiochemical cascade as a whole will be critical for elucidating UHDR effects and predicting their clinical relevance.

7.3.3 Dose Rate Effects in Pancreatic Cancer Models

The variability of UHDR experimental results across cell types is discussed in Sec. 4.1. For PDAC in particular, data remains limited. Katsuki et al. irradiated two pancreatic cancer cell lines (PANC01 and B16F10) with high-LET (55 keV/ μm) carbon ions at UHDR (380 Gy/s) and SDR (1.1 Gy/s). Clonogenic assays revealed **no UHDR sparing effect**, although differences in Double-Strand Breaks (DSB) repair pathways were observed in Western blots and flow cytometry. [175] In our study, survival outcomes likewise showed no sparing effect; still, the influence of 100 keV/ μm oxygen ions on DSB repair mechanisms remains to be determined.

The importance of mechanistic investigations is underscored by an “**anti-UHDR sparing effect**” reported by Venkatesulu et al.: Using PANC01 and KPC cells (the latter also applied in the oxygen UHDR study [207]), electron irradiation under normoxic conditions at higher dose rates (35 Gy/s)³ resulted in greater cell killing than at SDR (0.1 Gy/s). [226] While sparing effects under normoxia have been observed in other cell lines [139], an inverse dose-rate effect has only been described at extremely low dose rates (0.37 Gy/h) used in brachytherapy, where enhanced killing is attributed to low-dose hypersensitivity and cell cycle effects. [116, 227] However, the dose rate in Venkatesulu et al. was in the higher range, making these mechanisms unlikely explanations. This single study needs inter-institutional validation to confirm its findings.

Overall, these results highlight the need for further mechanistic and inter-institutional studies to unravel cell-type-specific responses to dose rate in pancreatic cancer.

7.4 Future Directions for Biological Investigations

Having established robust dosimetric protocols and identified mechanistic differences at high-LET UHDR, the next step is to expand biological investigations, since the presented findings suggest that future clinical applications of UHDR irradiation merit further exploration. [207]

The initial biological experiments were designed to minimize biological samples in accordance with ethical guidelines. Consequently, one dose of 8 Gy was employed based on prior carbon ion experiments showing sparing effects at 7.5 Gy, and technical constraints of the synchrotron. [207] Moving forward with oxygen ion UHDR, comprehensive **dose-response curves** for cell survival are required, particularly at higher doses, to determine whether combined high LET and UHDR effects become more pronounced with increased oxygen consumption or radical-radical interactions. Under hypoxic conditions, the observed Oxygen Enhancement Ratio (OER) of approximately 1.8 at 100 keV/μm [207] was consistent with expectations (Fig. 3.5). Extending dose-response studies also in hypoxia may reveal whether UHDR modifies **the oxygen-dependent radiosensitivity** and, if so, at which dose level.

The KPC cell line used is a well-established murine model for PDAC. [208, 209] Complementary studies in **human pancreatic cancer cell lines** are warranted to identify cell-type and species-specific differences in the UHDR response. Given the ongoing debate regarding the biological mechanisms underlying FLASH (Sec. 4.3.3), future investigations should also address Desoxyribonucleic Acid (DNA) damage, repair dynamics, and associated **signaling pathways**, using assays such as Western blotting, flow cytometry, or advanced microscopy.

In summary, further in vitro experiments are required, incorporating a broader range of doses and oxygen concentrations across multiple cell lines.

Beyond in vitro investigations, in vivo data are essential for clinical translation. Our preliminary in vivo experiments, though limited in sample size, established iso-efficacy between UHDR and SDR irradiation and showed a survival benefit. Although modest, the survival extension is especially valuable for PDAC with its poor prognosis in general (Sec. 3.3.1). These findings serve as a necessary foundation for subsequent studies of the oxygen ion **FLASH effect** in NT.

³The dose rate of 35 Gy/s used in this study is technically below the commonly cited threshold for UHDR irradiation. While there are no strict physical boundaries defining UHDR, most experimental and theoretical studies classify dose rates above approximately 40 Gy/s as UHDR. [136] Higher dose rates are typically applied in FLASH experiments to ensure the characteristic biological effects.

Inter-institutional comparison for in vitro and in vivo experiments will be critical, as reported UHDR results remain variable across centers. Collaborative efforts are needed to provide independent validation, especially in the context of clinical translation.

Finally, beyond potential sparing effects, UHDR irradiation offers a technical advantage for pancreatic cancer by mitigating motion-related uncertainties (Sec. 5.4). With the demonstrated feasibility of oxygen-ion UHDR, the tumor iso-effectiveness and the modest survival extension further suggest a clinical potential.

7.4.1 Pathway to Clinical Translation

For clinical translation, it is essential to quantitatively characterize the effects of oxygen ion UHDR irradiation and implement **dependencies on key variables** into the TPS.

The TPS workflow begins with patient imaging with a Computer Tomography (CT), followed by delineation of the tumor and Organ At Risk (OAR). Physicians then prescribe the tumor dose, the treatment scheme, and dose constraints for the OAR. Based on this ideal plan, the TPS inversely optimizes particle irradiation parameters to achieve the prescribed dose distribution, accounting for accelerator, beamline specifics, and possible 3DRMs. Therefore, the TPS requires physical models to accurately predict the physical dose in the patient anatomy.

At present, no clinically approved TPS exists for high-LET oxygen ion irradiation. However, protocols are established for other particle irradiation modalities, such as helium and carbon ions. In this context, the physical dose is weighted by the biological effectiveness to predict the biological outcome in the patient, necessitating robust Relative Biologic Effectiveness (RBE) models (Sec. 3.1.3). [10, 228]

Starting with the **physical dose prediction**, MCs are the most advanced tool for predicting Depth Dose Distribution (DDD) in patient geometries. However, their clinical application is challenged by high computational demands and incomplete hadronic physics models (Sec. 3.2). The latter is particularly relevant for heavy ions such as oxygen, since inelastic nuclear interactions generate numerous secondary fragments, which contribute to the dose and the LET distribution in the distal part of the Bragg Peak (BP) and the tail region. [204, 206] Nevertheless, MC studies using FLUKA have demonstrated a large agreement with experimental dose measurements for oxygen ions. [77, 229]

Beyond the physical dose, a TPS must also predict the resulting biological effect of the radiation quality. Since RBE depends strongly on LET (Sec. 3.1, Eq. 3.2), accurate LET distributions are essential. However, the LET is sensitive to the spectrum of secondary particles. The potential deviations in LET prediction may translate to deviations in biological dose estimation. [204]

Thus, high-precision cross-section data for clinically relevant ions and energies are crucial for further improving both dose and LET predictions, and, consequently, the biological effect estimation.

Additionally, RBE and biological outcome prediction further depend on tissue type and fractionation scheme, aside from other biological factors (Sec. 3.1.3), necessitating sophisticated models. Current models, like Local Effect Model (LEM) and the Microdosimetric Kinetic Model (MKM), are available for carbon ion biological outcome prediction. [10]

Despite their utility, these models do not account for all relevant variables that would be needed for oxygen-ion UHDR outcome predictions. Given a proper RBE and biological dose prediction, neither **OER** nor **local oxygen concentration** is included in existing clinical TPSs.

Incorporating these factors will be essential for UHDR-TPS, since oxygen dynamics are expected to play a decisive role in biological effects.

Extending the biological prediction to UHDR irradiation, analogous to RBE and OER, the **FLASH Modifying Factor (FMF)** is defined as the ratio of the SDR dose to the UHDR dose required to achieve a specific biological endpoint. [230] This factor could be used to implement an UHDR effect prediction in the TPS. Therefore, the FMF depends on dose, LET, oxygen tension, and biological endpoint and thus can be expressed as a function of multiple parameters:

$$\text{FMF}(\text{Dose, LET, O}_2, \text{RBE, Biological endpoint}) \quad (7.1)$$

Quantitative characterization of these dependencies is required for accurate modeling and clinical implementation of the UHDR effect in TPS.

In the presented data set in Sec. 6.3 [207], the FMF is unity. However, this may change at higher doses or altered experimental conditions, highlighting the need for further biological investigation.

Integrating the various dependencies of FMF, RBE, and OER into the TPS is essential for clinical implementation of oxygen-ion high-LET UHDR irradiation. Achieving this requires comprehensive mechanistic insight and quantitative modeling of the effects of these modalities.

A FLASH-DEBATE: IS HEAVY-ION UHDR NEEDED?

The preceding chapters have outlined the technical, dosimetric, and biological groundwork for heavy ion Ultra-High Dose Rate (UHDR) irradiation. Radiation is no longer a trivial tool for shoe fitting, but a central pillar of modern cancer therapy. Yet, a critical question arises: is heavy ion UHDR truly needed in clinical practice?

Skeptics may highlight the current absence of a clear UHDR sparing effect in high-Linear Energy Transfer (LET) regimes, the technical complexity of implementation, and the substantial therapeutic gains already achieved with conventional heavy ion therapy.

However, the absence of in vitro tumor cell sparing for oxygen UHDR does not necessarily preclude the possibility of FLASH sparing effects for in vivo Normal Tissue (NT).¹ Moreover, the technical barriers and subsequent solutions have been systematically addressed in this work, by showing the feasibility of precise dose delivery at the Heidelberg Ion Beam Therapy Center (HIT) synchrotron. A detailed dosimetric protocol with possible advanced temporal monitoring with characterized diamond detectors was provided. With the ongoing developments in beam delivery with 3D Range Modulators (3DRMs) for conformal UHDR at HIT – from a technical point of view – clinical translation may be within reach.

Importantly, high-LET ions could offer unique advantages for treating hypoxic and radioresistant tumors. Particularly, the focus of this thesis on biological experiments was oxygen ions. While potential risks must be weighed carefully, even incremental survival gains, as observed here for oxygen ions in preclinical Pancreatic Ductal Adenocarcinoma (PDAC) models, may translate into meaningful clinical benefits for patients with poor prognosis and limited options. Due to the iso-efficacy between UHDR and Standard Dose Rate (SDR), the demonstrated therapeutic potential of oxygen ion irradiation in general may already justify exploration of this modality. The add-on in favor of UHDR is the mitigation of intra-fractional motions, which could not be investigated in the mouse model. This could provide additional benefit for motion-influenced indications such as PDAC. Notably, even in the absence of a measurable normal tissue sparing FLASH effect, the iso-effectiveness of oxygen ion treatments at UHDR, combined with possible motion mitigation, could support clinical adoption.

¹As discussed in Sec. 5.1, in vivo FLASH sparing has been reported by Tinganelli et al. for high-LET carbon ion irradiation, although other studies have shown no in vitro UHDR sparing.

Perhaps rather the debate is not whether heavy ion UHDR is universally “needed”, rather the question should be: “Is heavy ion UHDR a new therapeutic avenue for selected patient populations where current treatment options remain inadequate?”. Innovation in oncology has often emerged from addressing such unmet needs. The clinical evaluation of this very “*fast and furious*” modality remains to be answered.²

In conclusion, the central focus of this thesis was to establish the physical and methodological foundations for heavy ion UHDR. A comprehensive dosimetric protocol was developed, and diamond detectors were thoroughly characterized for carbon and oxygen ion UHDR, thereby demonstrating their suitability for this modality. [206] The functionality of these diamond detectors facilitates the measurement of instantaneous Dose Rate (\dot{D}_{inst}), which has the potential to serve as a powerful tool for unravelling the temporal dependencies underlying UHDR effects.

At the mechanistic level, it has been demonstrated that the oxygen consumption – a potential contributor to the UHDR effect – decreases with increasing LET. This finding not only suggests a plausible mechanism but also delivers valuable reference data for benchmarking Monte Carlo Simulations (MCs), thereby advancing the search for the underlying processes of UHDR. [67]

The final demonstration confirmed the feasibility of conducting biological experiments. The initial results indicate that oxygen ion UHDR is iso-effective compared to SDR in terms of in vitro cell killing and in vivo tumor growth delay. The modest survival benefits in the PDAC model observed with oxygen ion irradiation may serve as a foundation for further preclinical experiments.

While definitive clinical conclusions await further biological and clinical studies, the technical and physical basis has now been established. The subsequent pivotal stage is to undertake a thorough investigation of the biological mechanisms – following Max Planck – to determine which patients and tumor types might benefit from this modality in terms of enhanced therapeutic efficacy.

²The response to this question is more likely to be provided within the context of a biological rather than physical thesis.

APPENDIX



LIST OF SCIENTIFIC CONTRIBUTIONS

A.1 Peer-Reviewed Publications

- Thomas Tessonnier, Domenico I. Filosa, Celine Karle, Filipa Baltazar, Lorenzo Manti, Lars Glimelius, Thomas Haberer, Amir Abdollahi, Juergen Debus, Stewart Mein, Ivana Dokic, Andrea Mairani. **“First Dosimetric and Biological Verification for Spot-Scanning Hadron Arc Radiation Therapy With Carbon Ions”**. *Advances in Radiation Oncology* (2024); DOI: <https://doi.org/10.1016/j.adro.2024.101611>.
- Celine Karle, Hans Liew, Thomas Tessonnier, Stewart Mein, Kristoffer Petersson, Christian Schömers, Stefan Scheloske, Stephan Brons, Rainer Cee, Gerald Major, Thomas Haberer, Amir Abdollahi, Jürgen Debus, Ivana Dokic, Andrea Mairani. **“Oxygen consumption measurements at ultra-high dose rate over a wide LET range”**. *Medical Physics* (2024); DOI: <https://doi.org/10.1002/mp.17496>.
- Celine Karle, Gianluca Verona-Rinati, Stephan Brons, Rainer Cee, Stefan Scheloske, Christian Schömers, Rafael Kranzer, Thomas Haberer, Marco Marinelli, Andrea Mairani, Thomas Tessonnier. **“Characterizing diamond detectors for various dose and dose rate measurements in scanned carbon and oxygen beams”**. *Medical Physics* (2025); DOI: <https://doi.org/10.1002/mp.17893>.
- Celine Karle, Domenico I. Filosa, Mahdi Akbarpour, Nora Schuhmacher, Stephan Brons, Rainer Cee, Christian Schömers, Stefan Scheloske, Kristoffer Petersson, Thomas Haberer, Amir Abdollahi, Jürgen Debus, Thomas Tessonnier, Mahmoud Moustafa, Andrea Mairani, Ivana Dokic. **“First in vitro and in vivo experiments with ultra high-dose rate oxygen ion radiotherapy”**. *Physics and Imaging in Radiation Oncology* (2025); DOI: <https://doi.org/10.1016/j.phro.2025.100803>.

A.2 Conference Contributions

- Celine Karle, Hans Liew, Thomas Tessonnier, Stewart Mein, Kristoffer Petersson, Amir Abdollahi, Ivana Dokic, Jürgen Debus, Andrea Mairani. **LET-DEPENDENCE OF OXYGEN DEPLETION AFTER UHDR IRRADIATION**. Oral Poster Presentation at *FLASH RADIOTHERAPY AND PARTICLE THERAPY* (2023 - Toronto).
- Celine Karle, Hans Liew, Thomas Tessonnier, Stewart Mein, Kristoffer Petersson, Amir Abdollahi, Ivana Dokic, Jürgen Debus, Andrea Mairani. **MODELLING CRYPS SURVIVAL AFTER UHDR IRRADIATION WITH UNIVERSE**. Oral Poster Presentation by Hans Liew at *FLASH RADIOTHERAPY AND PARTICLE THERAPY* (2023 - Toronto).
- Celine Karle, Hans Liew, Thomas Tessonnier, Nora Schuhmacher, Christian Schömers, Stefan Scheloske, Stephan Brons, Stewart Mein, Amir Abdollahi, Ivana Dokic, Jürgen Debus, Andrea Mairani. **EXPLORING ULTRA-HIGH DOSE RATE SPARING FOR HEAVY ION IRRADIATION**. Oral Presentation at *62st Annual Meeting of the Particle Therapy Co-Operative Group (PTCOG)* (2024 - Singapore).
- Celine Karle, Thomas Tessonnier, Gianluca Verona-Rinati, Luisa Rank, Rafael Kranzer, Andrea Mairani, Marco Marinelli. **CHARACTERIZATION OF DIAMOND DETECTORS RESPONSE IN ULTRA-HIGH DOSE-RATE CHARGED PARTICLE RADIOTHERAPY**. Oral Poster Presentation (presentation prize) at *FLASH RADIOTHERAPY AND PARTICLE THERAPY* (2024 - Rome).
- Celine Karle, Domenico Ivan Filosa, Nora Schuhmacher, Mahdi Akbarpour, Mahmoud Moustafa, Stephan Brons, Rainer Cee, Christian Schömers, Stefan Scheloske, Kristoffer Petersson, Thomas Haberer, Amir Abdollahi, Jürgen Debus, Thomas Tessonnier, Ivana Dokic, Andrea Mairani. **HIGH LET OXYGEN ION FLASH RADIATION: A POTENTIAL TO OVERCOME PANCREATIC TUMOR RADIORESISTANCE?**. Oral Presentation at *63st Annual Meeting of the Particle Therapy Co-Operative Group (PTCOG)* (2025 - Buenos Aires).

B

LIST OF FIGURES

1.1. “The Night” by Michele di Rodolfo del Ghirlandaio (1550s)	1
1.2. Certificate for a Shoe Fitting Test	2
1.3. Depth Dose Distributions of Photons, Protons, Helium and Carbon Ions and a Photon and Proton Treatment Plan for a Medulloblastoma	3
2.1. HIT Accelerator Complex	8
2.2. Beam Exit Nozzle at HIT with the BAMS	10
2.3. Active Raster Scanning Beam Application	10
2.4. Particle Interactions in Matter	12
2.5. DNA Model	16
2.6. Schematic Radiochemical Cascade	17
3.1. DDD and Lateral Scattering for Different Ions	22
3.2. LETd Distribution of 2 Gy Spread-Out Bragg Peak (SOBP) Plan with Various Par- ticles	23
3.3. Trackstructure of a Proton and Carbon Ion	23
3.4. OER and RBE Calculation	25
3.5. OER and RBE over LET	25
3.6. Fluence and LET Dependence	26
3.7. RBE over LET for Various Ions	27
3.8. Anatomical Location of the Pancreas	30
4.1. Summary of In Vivo FLASH Effect Results	32
4.2. Temporal Beam Structure Characterization	33
5.1. Carbon-Ion UHDR Spill at HIT	41

5.2. 2DRM Example for SOBP Production	41
5.3. Exemplary PBS Spot Pattern	42
5.4. Chemical Track MC	45
6.1. Structure of This Research Project	47
6.2. Experimental Setup for Dosimetric Validation of the Diamond Detectors	48
6.3. Experimental Setup for Oxygen Consumption Measurements	49
6.4. Experimental Setup for In Vitro and In Vivo Oxygen UHDR Experiments	51
7.1. 3DRM Design	88
7.2. EBT3 Film Evaluation Example	89
7.3. Dose Rate and Dose Assessment for Carbon Ions UHDR	91
7.4. Dose Rate and Dose Assessment for Oxygen Ions UHDR	92
7.5. Beam FWHM for Carbon and Oxygen Ions	93



LIST OF TABLES

5.1. UHDR Settings at HIT	40
5.2. Detector Performance Comparison	43



BIBLIOGRAPHY

- [1] M. M. Zarshenas and A. Mohammadi-Bardbori, “A medieval description of metastatic breast cancer; from avicenna’s view point,” *The Breast*, vol. 31, pp. 20–21, Feb. 2017. DOI: 10.1016/j.breast.2016.10.019.
- [2] R. Bianucci, A. Perciaccante, P. Charlier, O. Appenzeller, and D. Lippi, “Earliest evidence of malignant breast cancer in renaissance paintings,” *The Lancet Oncology*, vol. 19, no. 2, pp. 166–167, Feb. 2018. DOI: 10.1016/s1470-2045(18)30035-4.
- [3] G. Colonna. “La notte - michele ridolfo del ghirlandaio,” Accessed: Jul. 25, 2025. [Online]. Available: <https://www.galleriacolonna.it/de/la-notte-michele-ridolfo-del-ghirlandaio-prestito-dal-21-settembre-2017-al-21-gennaio-2018/>.
- [4] H. Leutz, G. Schulz, and H. Wenninger, “The decay of potassium-40,” *Zeitschrift für Physik*, vol. 187, no. 2, pp. 151–164, Apr. 1965. DOI: 10.1007/bf01387190.
- [5] W. C. Röntgen, “On a new kind of rays,” *Science*, vol. 3, no. 59, pp. 227–231, Feb. 1896. DOI: 10.1126/science.3.59.22.
- [6] E. D. Dyson, “Shoe-fitting x-ray fluoroscopes,” *British Medical Journal*, vol. 2, no. 4987, pp. 269–272, Aug. 1956. DOI: 10.1136/bmj.2.4987.269.
- [7] Oak Ridge Associated Universities, Museum of Radiation and Radioactivity. “Shoe-fitting fluoroscope (ca. 1930–1940),” Accessed: Jul. 31, 2025. [Online]. Available: <https://www.orau.org/health-physics-museum/collection/shoe-fitting-fluoroscope/index.html>.
- [8] E. H. Grubbé, “Priority in the therapeutic use of x-rays,” *Radiology*, vol. 21, no. 2, pp. 156–162, Aug. 1933. DOI: 10.1148/21.2.156.
- [9] E. Hall and A. Giaccia, “Radiobiology for the Radiologist,” 7th ed. Philadelphia, PA: Lipincott Williams and Wilkins, Jun. 2011, ISBN: 978-1-60831-193-4.
- [10] W. Schlegel, C. Karger, O. Jäkel, and P. Bachert, “Medizinische Physik.” Berlin: Springer Spektrum, 2018, ISBN: 978-3-662-54800-4.
- [11] M. Hoogeman, J.-B. Prévost, J. Nuytens, J. Pöll, P. Levendag, and B. Heijmen, “Clinical accuracy of the respiratory tumor tracking system of the cyberknife: Assessment by analysis of log files,” *International Journal of Radiation Oncology, Biology, Physics*, vol. 74, no. 1, pp. 297–303, May 2009. DOI: 10.1016/j.ijrobp.2008.12.041.

- [12] W. H. Bragg, “LXXIII. on the absorption of α rays, and on the classification of the α rays from radium,” *The London, Edinburgh, and Dublin Philosophical Magazine and Journal of Science*, vol. 8, no. 48, pp. 719–725, Dec. 1904. DOI: [10.1080/14786440409463245](https://doi.org/10.1080/14786440409463245).
- [13] C. Tobias et al., “Pituitary irradiation with high-energy proton beams a preliminary report,” *Cancer Research*, vol. 18, no. 2, pp. 121–134, 1958.
- [14] C. H. Stokkevåg et al., “Estimated risk of radiation-induced cancer following paediatric cranio-spinal irradiation with electron, photon and proton therapy,” *Acta Oncologica*, vol. 53, no. 8, pp. 1048–1057, Jul. 2014. DOI: [10.3109/0284186X.2014.928420](https://doi.org/10.3109/0284186X.2014.928420).
- [15] M. Durante, J. Debus, and J. S. Loeffler, “Physics and biomedical challenges of cancer therapy with accelerated heavy ions,” *Nature Reviews Physics*, vol. 3, no. 12, pp. 777–790, Sep. 2021. DOI: [10.1038/s42254-021-00368-5](https://doi.org/10.1038/s42254-021-00368-5).
- [16] D. Schardt, T. Elsässer, and D. Schulz-Ertner, “Heavy-ion tumor therapy: Physical and radiobiological benefits,” *Reviews of Modern Physics*, vol. 82, no. 1, pp. 383–425, Feb. 2010. DOI: [10.1103/revmodphys.82.383](https://doi.org/10.1103/revmodphys.82.383).
- [17] International Astronomical Union Office of Astronomy for Education. “Glossary term: Metal,” IAU OAE, Accessed: Jul. 30, 2025. [Online]. Available: <https://www.astro4edu.org/resources/glossary/term/457/>.
- [18] G. T. Y. Chen, J. R. Castro, J. M. Collier, and W. M. Saunders, “Heavy ion radiotherapy at the lawrence berkeley laboratory,” *IEEE Transactions on Nuclear Science*, vol. 30, no. 2, pp. 1813–1815, 1983. DOI: [10.1109/TNS.1983.4332649](https://doi.org/10.1109/TNS.1983.4332649).
- [19] C. A. Tobias et al., “Molecular and cellular radiobiology of heavy ions,” en, *International Journal of Radiation Oncology, Biology, Physics*, vol. 8, no. 12, pp. 2109–2120, Dec. 1982. DOI: [10.1016/0360-3016\(82\)90554-5](https://doi.org/10.1016/0360-3016(82)90554-5).
- [20] J. R. Castro and M. M. Reimers, “Charged particle radiotherapy of selected tumors in the head and neck,” en, *International Journal of Radiation Oncology, Biology, Physics*, vol. 14, no. 4, pp. 711–720, Apr. 1988. DOI: [10.1016/0360-3016\(88\)90093-4](https://doi.org/10.1016/0360-3016(88)90093-4).
- [21] J. R. Castro, “Results of heavy ion radiotherapy,” en, *Radiation and Environmental Biophysics*, vol. 34, no. 1, pp. 45–48, Mar. 1995. DOI: [10.1007/BF01210545](https://doi.org/10.1007/BF01210545).
- [22] D. E. Linstadt, J. R. Castro, and T. L. Phillips, “Neon ion radiotherapy: Results of the phase I/II clinical trial,” *International Journal of Radiation Oncology, Biology, Physics*, vol. 20, no. 4, pp. 761–769, Apr. 1991. DOI: [10.1016/0360-3016\(91\)90020-5](https://doi.org/10.1016/0360-3016(91)90020-5).
- [23] D. Schardt et al., “Nuclear fragmentation of high-energy heavy-ion beams in water,” *Advances in Space Research*, vol. 17, no. 2, pp. 87–94, Jan. 1996. DOI: [10.1016/0273-1177\(95\)00516-h](https://doi.org/10.1016/0273-1177(95)00516-h).
- [24] M. Durante and H. Paganetti, “Nuclear physics in particle therapy: A review,” *Reports on Progress in Physics*, vol. 79, no. 9, p. 096 702, Aug. 2016. DOI: [10.1088/0034-4885/79/9/096702](https://doi.org/10.1088/0034-4885/79/9/096702).
- [25] Y. Hirao et al., “Heavy ion synchrotron for medical use himac project at nirs-japan,” *Nuclear Physics A*, vol. 538, pp. 541–550, 1992. DOI: [10.1016/0375-9474\(92\)90803-R](https://doi.org/10.1016/0375-9474(92)90803-R).
- [26] T. Haberer, W. Becher, D. Schardt, and G. Kraft, “Magnetic scanning system for heavy ion therapy,” *Nuclear Instruments and Methods in Physics Research Section A: Accelerators, Spectrometers, Detectors and Associated Equipment*, vol. 330, no. 1-2, pp. 296–305, 1993. DOI: [10.1016/0168-9002\(93\)91335-K](https://doi.org/10.1016/0168-9002(93)91335-K).

-
- [27] P. T. C.-O. G. (PTCOG). “Facilities in operation (public),” Accessed: Sep. 12, 2025. [Online]. Available: <https://www.ptcog.site/index.php/facilities-in-operation-public>.
 - [28] M.-C. Vozenin, J. Bourhis, and M. Durante, “Towards clinical translation of flash radiotherapy,” *Nature Reviews Clinical Oncology*, vol. 19, no. 12, pp. 791–803, Oct. 2022. DOI: 10.1038/s41571-022-00697-z.
 - [29] O. Jäkel, G. Kraft, and C. P. Karger, “The history of ion beam therapy in germany,” *Zeitschrift für Medizinische Physik*, vol. 32, no. 1, pp. 6–22, 2022, Special Issue: Ion Beam Therapy, Part II. DOI: 10.1016/j.zemedi.2021.11.003.
 - [30] Max-Planck-Gesellschaft. “Kurzportrait der max-planck-gesellschaft,” Accessed: Jul. 28, 2025. [Online]. Available: <https://www.mpg.de/kurzportrait>.
 - [31] H. Eickhoff et al., “Hicat-the german hospital-based light ion cancer therapy project,” in *Proceedings of the 2003 Particle Accelerator Conference*, IEEE, vol. 1, 2003, pp. 694–698.
 - [32] A. Dolinskii, H. Eickhoff, and B. Franczak, “The synchrotron of the dedicated ion beam facility for cancer therapy, proposed for the clinic in heidelberg,” *Proceedings of 7th European Particle Accelerator Conference (EPAC00)*, 2000.
 - [33] Heidelberg University Hospital. “Heidelberg Ion Beam Therapy Center (HIT): Technical and Medical Status,” Accessed: Jul. 23, 2025. [Online]. Available: https://www.klinikum.uni-heidelberg.de/fileadmin/hit/dokumente/121019KV_SS_HITImage_engl_web_ID17763.pdf.
 - [34] R. Geller, “Electron Cyclotron Resonance Ion Sources and ECR Plasmas.” Routledge, Dec. 2018. DOI: 10.1201/9780203758663.
 - [35] T. Winkelmann et al., “Electron cyclotron resonance ion source experience at the heidelberg ion beam therapy center,” *Review of Scientific Instruments*, vol. 79, no. 2, 2008. DOI: 10.1063/1.2823952.
 - [36] B. Schlitt and U. Ratzinger, “Design of a carbon injector for a medical accelerator complex,” in *Proceedings of the 6th European Particle Accelerator Conference (EPAC98)*, vol. 2377, 1998.
 - [37] B. Schlitt, A. Bechtold, U. Ratzinger, and A. Schempp, “Design of the 7 mev/u, 217 mhz injector linac for the proposed ion beam facility for cancer therapy at the clinic in heidelberg,” in *Proceedings of the LINAC2000*, vol. 2377, 2000. DOI: 10.48550/arXiv.physics/0008148.
 - [38] T. Winkelmann, R. Cee, T. Haberer, B. Naas, and A. Peters, “Test bench to commission a third ion source beam line and a newly designed extraction system,” *Review of Scientific Instruments*, vol. 83, no. 2, 02B904, Feb. 2012. DOI: 10.1063/1.3666186.
 - [39] C. Schömers, E. Feldmeier, J. Naumann, R. Panse, A. Peters, and T. Haberer, “The intensity feedback system at heidelberg ion-beam therapy centre,” *Nuclear Instruments and Methods in Physics Research Section A: Accelerators, Spectrometers, Detectors and Associated Equipment*, vol. 795, pp. 92–99, 2015. DOI: 10.1016/j.nima.2015.05.054.
 - [40] S. Gilardoni, M. Giovannozzi, and C. Hernalsteens, “First observations of intensity-dependent effects for transversely split beams during multiturn extraction studies at the cern proton synchrotron,” *Physical Review Special Topics - Accelerators and Beams*, vol. 16, no. 5, May 2013. DOI: 10.1103/physrevstab.16.051001.

- [41] C. Schömers, S. Brons, R. Cee, A. Peters, S. Scheloske, and T. Haberer, “Beam properties beyond the therapeutic range at hit,” in *in Proceedings of IPAC 23, Venice, Italy, May 2023, Paper THPM064*, 2022. DOI: 10.18429/JACoW-IPAC2023-THPM064.
- [42] L. Baack et al., “Reduction of recombination effects in large plane parallel beam monitors for flash radiotherapy with scanned ion beams,” *Physica Medica*, vol. 104, pp. 136–144, 2022. DOI: 10.1016/j.ejmp.2022.10.029.
- [43] P. Lysakovski, “MonteRay, a fast Monte Carlo dose engine for protons, helium ions and carbon ions.” Heidelberg, 2024. DOI: 10.11588/heidok.00034938.
- [44] S. M. Seltzer et al., “Report 85,” *Journal of the ICRU*, vol. 11, no. 1, Apr. 2011. DOI: 10.1093/jicru/ndr012.
- [45] E. B. Podgorsak, “Radiation Physics for Medical Physicists.” Springer International Publishing, 2016, ISBN: 9783319253824. DOI: 10.1007/978-3-319-25382-4.
- [46] V. Patera and I. Mattei, “Nuclear interactions and medicine,” *The European Physical Journal Plus*, vol. 134, no. 1, Jan. 2019. DOI: 10.1140/epjp/i2019-12484-6.
- [47] R. Serber, “Nuclear reactions at high energies,” *Physical Review*, vol. 72, no. 11, pp. 1114–1115, Dec. 1947. DOI: 10.1103/physrev.72.1114.
- [48] Particle Data Group, S. Navas et al., “Review of particle physics,” *Physical Review D*, vol. 110, no. 3, p. 030001, 2024. DOI: 10.1103/PhysRevD.110.030001.
- [49] H. Kolanoski and N. Wermes, “Particle Detectors: Fundamentals and Applications.” Jun. 2020. DOI: 10.1093/oso/9780198858362.001.0001.
- [50] S. Seltzer et al., “Key data for ionizing-radiation dosimetry: Measurement standards and applications, icru report 90,” 2016. DOI: 10.1093/jicru/ndw034.
- [51] C. Sonntag, “Free-Radical-Induced DNA Damage and Its Repair.” Berlin, Germany: Springer, Dec. 2006, ISBN: 3-540-26120-6.
- [52] P. Bernhardt, W. Friedland, P. Jacob, and H. Paretzke, “Modeling of ultrasoft x-ray induced dna damage using structured higher order dna targets,” *International Journal of Mass Spectrometry*, vol. 223224, pp. 579–597, Jan. 2003. DOI: 10.1016/s1387-3806(02)00879-5.
- [53] National Human Genome Research Institute. “Deoxyribonucleic acid (dna) genetics glossary,” Accessed: Jul. 23, 2025. [Online]. Available: <https://www.genome.gov/genetics-glossary/Deoxyribonucleic-Acid-DNA>.
- [54] P. Wardman, “Radiotherapy using high-intensity pulsed radiation beams (flash): A radiation-chemical perspective,” *Radiation Research*, vol. 194, no. 6, May 2020. DOI: 10.1667/rade-19-00016.
- [55] D. R. Spitz et al., “An integrated physico-chemical approach for explaining the differential impact of flash versus conventional dose rate irradiation on cancer and normal tissue responses,” *Radiotherapy and Oncology*, vol. 139, pp. 23–27, 2019. DOI: 10.1016/j.radonc.2019.03.028.
- [56] J. M. Herbert and M. P. Coons, “The hydrated electron,” *Annual Review of Physical Chemistry*, vol. 68, no. Volume 68, 2017, pp. 447–472, 2017. DOI: 10.1146/annurev-physchem-052516-050816.

-
- [57] M. El Khatib et al., “Ultrafast tracking of oxygen dynamics during proton flash,” *International Journal of Radiation Oncology Biology Physics*, vol. 113, no. 3, pp. 624–634, Jul. 2022. DOI: 10.1016/j.ijrobp.2022.03.016.
 - [58] J. Meesungnoen and J.-P. Jay-Gerin, “High-let radiolysis of liquid water with 1h^+ , 4he^{2+} , 12c^{6+} , and 20ne^{9+} ions: effects of multiple ionization,” *The Journal of Physical Chemistry A*, vol. 109, no. 29, pp. 6406–6419, Jul. 2005. DOI: 10.1021/jp058037z.
 - [59] J. F. Ward, “Dna damage as the cause of ionizing radiation-induced gene activation,” *Radiation Research*, vol. 138, no. 1, S85, Apr. 1994. DOI: 10.2307/3578769.
 - [60] V. Favaudon, R. Labarbe, and C. L. Limoli, “Model studies of the role of oxygen in the flash effect,” *Medical Physics*, vol. 49, no. 3, pp. 2068–2081, Aug. 2021. DOI: 10.1002/mp.15129.
 - [61] P. Wardman, “Radiation-chemical perspective of the radiobiology of pulsed (high dose-rate) radiation (flash): A postscript,” *Radiation Research*, vol. 201, no. 1, Dec. 2023. DOI: 10.1667/rade-23-00212.1.
 - [62] F. Chappuis et al., “Modeling of scavenging systems in water radiolysis with geant4-dna,” *Physica Medica*, vol. 108, p. 102549, Apr. 2023. DOI: 10.1016/j.ejmp.2023.102549.
 - [63] R. A. Weinberg, “The Biology of Cancer.” W.W. Norton and Company, Jun. 2006, ISBN: 9781136977381. DOI: 10.1201/9780203852569.
 - [64] A. A. Friedl, K. M. Prise, K. T. Butterworth, P. Montay-Gruel, and V. Favaudon, “Radiobiology of the FLASH effect,” *Medical Physics*, vol. 49, no. 3, pp. 1993–2013, Sep. 2021. DOI: 10.1002/mp.15184.
 - [65] L. Apetoh et al., “Toll-like receptor 4dependent contribution of the immune system to anticancer chemotherapy and radiotherapy,” *Nature Medicine*, vol. 13, no. 9, pp. 1050–1059, Aug. 2007. DOI: 10.1038/nm1622.
 - [66] T. A. van Schaik, K.-S. Chen, and K. Shah, “Therapy-induced tumor cell death: Friend or foe of immunotherapy?” *Frontiers in Oncology*, vol. 11, Jun. 2021. DOI: 10.3389/fonc.2021.678562.
 - [67] C. Karle et al., “Oxygen consumption measurements at ultra-high dose rate over a wide let range,” *Medical Physics*, vol. 52, no. 2, pp. 1323–1334, 2024. DOI: 10.1002/mp.17496.
 - [68] F. Tommasino, E. Scifoni, and M. Durante, “New ions for therapy,” *International Journal of Particle Therapy*, vol. 2, no. 3, pp. 428–438, Dec. 2015. DOI: 10.14338/ijpt-15-00027.1.
 - [69] M. Durante and J. Debus, “Heavy charged particles: Does improved precision and higher biological effectiveness translate to better outcome in patients?” *Seminars in Radiation Oncology*, vol. 28, no. 2, pp. 160–167, 2018. DOI: 10.1016/j.semradonc.2017.11.004.
 - [70] S. J. McMahon and K. M. Prise, “Mechanistic modelling of radiation responses,” *Cancers*, vol. 11, no. 2, p. 205, Feb. 2019. DOI: 10.3390/cancers11020205.
 - [71] R. Hirayama et al., “Contributions of direct and indirect actions in cell killing by high-let radiations,” *Radiation Research*, vol. 171, no. 2, pp. 212–218, Feb. 2009. DOI: 10.1667/rr1490.1.
 - [72] S. J. Thompson, K. M. Prise, and S. J. McMahon, “Investigating the potential contribution of inter-track interactions within ultra-high dose-rate proton therapy,” *Physics in Medicine & Biology*, vol. 68, no. 5, p. 055006, 2023. DOI: 10.1088/1361-6560/acb88a.

- [73] D. Boscolo, M. Krämer, M. Durante, M. Fuss, and E. Scifoni, “Trax-chem: A pre-chemical and chemical stage extension of the particle track structure code trax in water targets,” *Chemical Physics Letters*, vol. 698, pp. 11–18, 2018. DOI: 10.1016/j.cplett.2018.02.051.
- [74] J. Meesungnoen and J.-P. Jay-Gerin, “High-let ion radiolysis of water: Oxygen production in tracks,” *Radiation Research*, vol. 171, no. 3, pp. 379–386, 2009. DOI: 10.1667/RR1468.1.
- [75] A. Colliaux, B. Gervais, C. Rodriguez-Lafrasse, and M. Beuve, “Simulation of ion-induced water radiolysis in different conditions of oxygenation,” *Nuclear Instruments and Methods in Physics Research Section B: Beam Interactions with Materials and Atoms*, vol. 365, pp. 596–605, 2015. DOI: 10.1016/j.nimb.2015.08.057.
- [76] D. Goodhead, “Initial events in the cellular effects of ionizing radiations: Clustered damage in dna,” *International Journal of Radiation Biology*, vol. 65, no. 1, pp. 7–17, Jan. 1994. DOI: 10.1080/09553009414550021.
- [77] I. Dokic et al., “Next generation multi-scale biophysical characterization of high precision cancer particle radiotherapy using clinical proton, helium-, carbon- and oxygen ion beams,” *Oncotarget*, vol. 7, no. 35, pp. 56 676–56 689, Aug. 2016. DOI: 10.18632/oncotarget.10996.
- [78] M. Durante et al., “X-rays vs. carbon-ion tumor therapy: Cytogenetic damage in lymphocytes,” *International Journal of Radiation Oncology, Biology, Physics*, vol. 47, no. 3, pp. 793–798, Jun. 2000. DOI: 10.1016/s0360-3016(00)00455-7.
- [79] A. Schipler and G. Iliakis, “Dna double-strand-break complexity levels and their possible contributions to the probability for error-prone processing and repair pathway choice,” *Nucleic Acids Research*, vol. 41, no. 16, pp. 7589–7605, Jun. 2013. DOI: 10.1093/nar/gkt556.
- [80] A. Helm and C. Fournier, “High-let charged particles: Radiobiology and application for new approaches in radiotherapy,” *Strahlentherapie und Onkologie*, vol. 199, no. 12, pp. 1225–1241, Oct. 2023. DOI: 10.1007/s00066-023-02158-7.
- [81] B. Bell et al., “Immunological effectiveness of carbon ion radiotherapy in pancreatic cancer,” *International Journal of Radiation Oncology, Biology, Physics*, vol. 120, no. 2, S220, Oct. 2024. DOI: 10.1016/j.ijrobp.2024.07.2303.
- [82] T. Ogata et al., “Particle irradiation suppresses metastatic potential of cancer cells,” *Cancer Research*, vol. 65, no. 1, pp. 113–120, Jan. 2005. DOI: 10.1158/0008-5472.113.65.1.
- [83] C. Fournier and G. Taucher-Scholz, “Radiation induced cell cycle arrest: An overview of specific effects following high-let exposure,” *Radiotherapy and Oncology*, vol. 73, S119–S122, Dec. 2004. DOI: 10.1016/s0167-8140(04)80031-8.
- [84] Y. Furusawa et al., “Inactivation of aerobic and hypoxic cells from three different cell lines by accelerated ^3He -, ^{12}C - and ^{20}Ne -ion beams,” *Radiation Research*, vol. 154, no. 5, pp. 485–496, Nov. 2000. DOI: 10.1667/0033-7587(2000)154[0485:ioaahc]2.0.co;2.
- [85] B. J. McParland, “Biological Effects of Ionizing Radiation.” London: Springer London, 2010, pp. 401–453. DOI: 10.1007/978-1-84882-126-2_10.
- [86] R. Hirayama et al., “Determination of the relative biological effectiveness and oxygen enhancement ratio for micronuclei formation using high-let radiation in solid tumor cells: An in vitro and in vivo study,” *Mutation Research/Genetic Toxicology and Environmental Mutagenesis*, vol. 793, pp. 41–47, Nov. 2015. DOI: 10.1016/j.mrgentox.2015.08.003.

-
- [87] K. Baverstock and W. Burns, "Primary production of oxygen from irradiated water as an explanation for decreased radiobiological oxygen enhancement at high let," *Nature*, vol. 260, no. 5549, pp. 316–318, 1976. DOI: 10.1038/260316a0.
- [88] T. Alper and P. Bryant, "Reduction in oxygen enhancement ratio with increase in let: Tests of two hypotheses," *International Journal of Radiation Biology and Related Studies in Physics, Chemistry and Medicine*, vol. 26, no. 3, pp. 203–218, 1974. DOI: 10.1080/09553007414551171.
- [89] C. Klein et al., "Overcoming hypoxia-induced tumor radioresistance in non-small cell lung cancer by targeting dna-dependent protein kinase in combination with carbon ion irradiation," *Radiation Oncology*, vol. 12, no. 1, Dec. 2017. DOI: 10.1186/s13014-017-0939-0.
- [90] G. Kraft, W. Kraft-Weyrather, S. Ritter, M. Scholz, and J. Stanton, "Cellular and subcellular effect of heavy ions: A comparison of the induction of strand breaks and chromosomal aberration with the incidence of inactivation and mutation," *Advances in Space Research*, vol. 9, no. 10, pp. 59–72, 1989. DOI: 10.1016/0273-1177(89)90423-7.
- [91] M. Suzuki, Y. Kase, H. Yamaguchi, T. Kanai, and K. Ando, "Relative biological effectiveness for cell-killing effect on various human cell lines irradiated with heavy-ion medical accelerator in chiba (himac) carbon-ion beams," *International Journal of Radiation Oncology, Biology, Physics*, vol. 48, no. 1, pp. 241–250, 2000. DOI: 10.1016/S0360-3016(00)00568-X.
- [92] K. Weyrather, S. Ritter, M. Scholz, and G. Kraft, "Rbe for carbon track-segment irradiation in cell lines of differing repair capacity," *International Journal of Radiation Biology*, vol. 75, no. 11, pp. 1357–1364, 1999. DOI: 10.1080/095530099139232.
- [93] C. Glowa et al., "Relative biological effectiveness of oxygen ion beams in the rat spinal cord: Dependence on linear energy transfer and dose and comparison with model predictions," *Physics and Imaging in Radiation Oncology*, vol. 30, p. 100581, Apr. 2024. DOI: 10.1016/j.phro.2024.100581.
- [94] A. C. Kraan and A. Del Guerra, "Technological developments and future perspectives in particle therapy: A topical review," *IEEE Transactions on Radiation and Plasma Medical Sciences*, vol. 8, no. 5, pp. 453–481, 2024. DOI: 10.1109/TRPMS.2024.3372189.
- [95] R. Pestana, K. Seidensaal, C. Beyer, J. Debus, S. Klüter, and J. Bauer, "Evaluation of pelvic mri-to-ct deformable registration for adaptive mr-guided particle therapy," *International Journal of Particle Therapy*, vol. 14, p. 100636, Dec. 2024. DOI: 10.1016/j.ijpt.2024.100636.
- [96] J. M. Pakela, A. Knopf, L. Dong, A. Rucinski, and W. Zou, "Management of motion and anatomical variations in charged particle therapy: Past, present, and into the future," *Frontiers in Oncology*, vol. 12, Mar. 2022. DOI: 10.3389/fonc.2022.806153.
- [97] Particle Therapy Co-Operative Group (PTCOG). "Patient statistics," Accessed: Jul. 8, 2025. [Online]. Available: <https://www.ptcog.site/index.php/patient-statistics>.
- [98] American Society for Radiation Oncology (ASTRO). "Proton beam therapy model policy." Chicago, IL: American Medical Association, Accessed: Jul. 8, 2025. [Online]. Available: <https://www.astro.org/practice-support/reimbursement/model-policies>.
- [99] H. Paganetti et al., "Relative biological effectiveness (rbe) values for proton beam therapy," *International Journal of Radiation Oncology, Biology, Physics*, vol. 53, no. 2, pp. 407–421, Jun. 2002. DOI: 10.1016/s0360-3016(02)02754-2.

- [100] J. R. Castro et al., “Treatment of cancer with heavy charged particles,” *International Journal of Radiation Oncology, Biology, Physics*, vol. 8, no. 12, pp. 2191–2198, Dec. 1982. DOI: 10.1016/0360-3016(82)90569-7.
- [101] S. B. Harrabi, “Current standards and the future role of hadrontherapy in the treatment of central nervous system tumors,” *Health and Technology*, vol. 14, no. 5, pp. 853–858, Jul. 2024. DOI: 10.1007/s12553-024-00893-0.
- [102] A. Mairani et al., “Roadmap: Helium ion therapy,” *Physics in Medicine & Biology*, vol. 67, no. 15, 15TR02, Aug. 2022. DOI: 10.1088/1361-6560/ac65d3.
- [103] B. Vischioni et al., “Radioresistant, rare, recurrent, and radioinduced: 4rs of hadrontherapy for patients selections,” *International Journal of Particle Therapy*, vol. 15, p. 100737, Mar. 2025. DOI: 10.1016/j.ijpt.2024.100737.
- [104] T. Rackwitz and J. Debus, “Clinical applications of proton and carbon ion therapy,” *Seminars in Oncology*, vol. 46, no. 3, pp. 226–232, 2019. DOI: 10.1053/j.seminoncol.2019.07.005.
- [105] J. E. Yun, S. Kim, K. Y. Park, and W. Lee, “Effectiveness and safety of carbon ion radiotherapy in solid tumors: A systematic review and meta-analysis,” *Yonsei Medical Journal*, vol. 65, no. 6, p. 332, 2024. DOI: 10.3349/ymj.2023.0439.
- [106] American Cancer Society. “Cancer facts & figures 2025,” Accessed: Jul. 8, 2025. [Online]. Available: <https://www.cancer.org/research/cancer-facts-statistics/all-cancer-facts-figures/2025-cancer-facts-figures.html>.
- [107] B. D. Kavanagh et al., “Radiation dose-volume effects in the stomach and small bowel,” *International Journal of Radiation Oncology, Biology, Physics*, vol. 76, no. 3, S101–S107, Mar. 2010. DOI: 10.1016/j.ijrobp.2009.05.071.
- [108] A. C. Koong et al., “Pancreatic tumors show high levels of hypoxia,” *International Journal of Radiation Oncology, Biology, Physics*, vol. 48, no. 4, pp. 919–922, Nov. 2000. DOI: 10.1016/S0360-3016(00)00803-8.
- [109] F. Baltazar et al., “Carbon-ion radiotherapy (cirt) as treatment of pancreatic cancer at hit: Initial radiation plan analysis of the prospective phase ii pack-study,” *Radiotherapy and Oncology*, vol. 188, p. 109872, Nov. 2023. DOI: 10.1016/j.radonc.2023.109872.
- [110] Healthgrades Editorial Staff. “What does the pancreas do?” Healthgrades, Accessed: Jul. 18, 2025. [Online]. Available: <https://resources.healthgrades.com/right-care/digestive-health/what-does-the-pancreas-do>.
- [111] O. Sokol and M. Durante, “Carbon ions for hypoxic tumors: Are we making the most of them?” *Cancers*, vol. 15, no. 18, p. 4494, Sep. 2023. DOI: 10.3390/cancers15184494.
- [112] H. Tsujii et al., “Clinical results of carbon ion radiotherapy at nirs,” *Journal of Radiation Research*, vol. 48, A1–A13, 2007. DOI: 10.1269/jrr.48.A1.
- [113] M. Shinoto et al., “Carbon ion radiation therapy with concurrent gemcitabine for patients with locally advanced pancreatic cancer,” *International Journal of Radiation Oncology, Biology, Physics*, vol. 95, no. 1, pp. 498–504, May 2016. DOI: 10.1016/j.ijrobp.2015.12.362.
- [114] M. Shinoto et al., “Phase 1 trial of preoperative, shortcourse carbonion radiotherapy for patients with resectable pancreatic cancer,” *Cancer*, vol. 119, no. 1, pp. 45–51, Jun. 2012. DOI: 10.1002/cncr.27723.

-
- [115] J. Liermann et al., “Carbon ion radiotherapy as definitive treatment in non-metastasized pancreatic cancer: Study protocol of the prospective phase ii pack-study,” *BMC Cancer*, vol. 20, no. 1, Oct. 2020. DOI: [10.1186/s12885-020-07434-8](https://doi.org/10.1186/s12885-020-07434-8).
- [116] K. D. Held, A. L. McNamara, J. Daartz, M. S. Bhagwat, B. Rothwell, and J. Schuemann, “Dose rate effects from the 1950s through to the era of flash,” *Radiation Research*, vol. 202, no. 2, Jul. 2024. DOI: [10.1667/rade-24-00024.1](https://doi.org/10.1667/rade-24-00024.1).
- [117] D. Dewey and J. Boag, “Modification of the oxygen effect when bacteria are given large pulses of radiation,” *Nature*, vol. 183, no. 4673, pp. 1450–1451, 1959. DOI: [10.1038/1831450a0](https://doi.org/10.1038/1831450a0).
- [118] E. R. Epp, H. Weiss, and A. Santomaso, “The oxygen effect in bacterial cells irradiated with high-intensity pulsed electrons,” *Radiation Research*, vol. 34, no. 2, p. 320, May 1968. DOI: [10.2307/3572557](https://doi.org/10.2307/3572557).
- [119] H. Weiss, E. Epp, J. Heslin, C. Ling, and A. Santomaso, “Oxygen depletion in cells irradiated at ultra-high dose-rates and at conventional dose-rates,” *International Journal of Radiation Biology and Related Studies in Physics, Chemistry and Medicine*, vol. 26, no. 1, pp. 17–29, Jan. 1974. DOI: [10.1080/09553007414550901](https://doi.org/10.1080/09553007414550901).
- [120] V. Favaudon et al., “Ultrahigh dose-rate flash irradiation increases the differential response between normal and tumor tissue in mice,” *Science Translational Medicine*, vol. 6, no. 245, 245ra93–245ra93, 2014. DOI: [10.1126/scitranslmed.3008973](https://doi.org/10.1126/scitranslmed.3008973).
- [121] P. Montay-Gruel et al., “Irradiation in a flash: Unique sparing of memory in mice after whole brain irradiation with dose rates above 100 gy/s,” *Radiotherapy and Oncology*, vol. 124, no. 3, pp. 365–369, Sep. 2017. DOI: [10.1016/j.radonc.2017.05.003](https://doi.org/10.1016/j.radonc.2017.05.003).
- [122] E. Hageman, P.-P. Che, M. Dahele, B. J. Slotman, and P. Sminia, “Radiobiological aspects of flash radiotherapy,” *Biomolecules*, vol. 12, no. 10, p. 1376, 2022. DOI: [10.3390/biom12101376](https://doi.org/10.3390/biom12101376).
- [123] A. Borghini, L. Labate, S. Piccinini, C. M. V. Panaino, M. G. Andreassi, and L. A. Gizzi, “Flash radiotherapy: Expectations, challenges, and current knowledge,” *International Journal of Molecular Sciences*, vol. 25, no. 5, p. 2546, Feb. 2024. DOI: [10.3390/ijms25052546](https://doi.org/10.3390/ijms25052546).
- [124] Y. Ghannam et al., “First evidence of in vivo effect of flash radiotherapy with helium ions in zebrafish embryos,” *Radiotherapy and Oncology*, vol. 187, p. 109 820, Oct. 2023. DOI: [10.1016/j.radonc.2023.109820](https://doi.org/10.1016/j.radonc.2023.109820).
- [125] I. Dokic et al., “Neuroprotective effects of ultra-high dose rate flash bragg peak proton irradiation,” *International Journal of Radiation Oncology, Biology, Physics*, vol. 113, no. 3, pp. 614–623, Jul. 2022. DOI: [10.1016/j.ijrobp.2022.02.020](https://doi.org/10.1016/j.ijrobp.2022.02.020).
- [126] I. Dokic et al., “Ultrahigh dose rate helium ion beams: Minimizing brain tissue damage while preserving tumor control,” *Molecular Cancer Therapeutics*, vol. 24, no. 5, pp. 763–771, Dec. 2024. DOI: [10.1158/1535-7163.mct-24-0536](https://doi.org/10.1158/1535-7163.mct-24-0536).
- [127] W. Tinganelli et al., “Flash with carbon ions: Tumor control, normal tissue sparing, and distal metastasis in a mouse osteosarcoma model,” *Radiotherapy and Oncology*, vol. 175, pp. 185–190, Oct. 2022. DOI: [10.1016/j.radonc.2022.05.003](https://doi.org/10.1016/j.radonc.2022.05.003).
- [128] W. Tinganelli et al., “Flash bragg-peak irradiation with a therapeutic carbon ion beam: First in vivo results,” *International Journal of Radiation Oncology, Biology, Physics*, vol. 121, no. 5, pp. 1282–1292, Apr. 2025. DOI: [10.1016/j.ijrobp.2024.11.089](https://doi.org/10.1016/j.ijrobp.2024.11.089).

- [129] J. Bourhis et al., “Treatment of a first patient with FLASH-radiotherapy,” *Radiotherapy and Oncology*, vol. 139, pp. 18–22, Oct. 2019. DOI: 10.1016/j.radonc.2019.06.019.
- [130] A. E. Mascia et al., “Proton flash radiotherapy for the treatment of symptomatic bone metastases: The fast-01 nonrandomized trial,” *JAMA oncology*, 2022. DOI: 10.1001/jamaoncol.2022.5843.
- [131] E. Daugherty et al., “Flash radiotherapy for the treatment of symptomatic bone metastases in the thorax (fast-02): Protocol for a prospective study of a novel radiotherapy approach,” *Radiation Oncology*, vol. 19, no. 1, Mar. 2024. DOI: 10.1186/s13014-024-02419-4.
- [132] G. Adrian, J.-L. Ruan, S. Paillas, C. R. Cooper, and K. Petersson, “In vitro assays for investigating the flash effect,” *Expert Reviews in Molecular Medicine*, vol. 24, 2022. DOI: 10.1017/erm.2022.5.
- [133] T. T. Böhlen et al., “Effect of conventional and ultra-high dose rate irradiations on preclinical tumour models: A systematic analysis,” *International Journal of Radiation Oncology, Biology, Physics*, Jun. 2023. DOI: 10.1016/j.ijrobp.2023.05.045.
- [134] J.-L. Ruan et al., “Irradiation at ultra-high (flash) dose rates reduces acute normal tissue toxicity in the mouse gastrointestinal system,” *International Journal of Radiation Oncology, Biology, Physics*, vol. 111, no. 5, pp. 1250–1261, 2021. DOI: 10.1016/j.ijrobp.2021.08.004.
- [135] L. Karsch et al., “Beam pulse structure and dose rate as determinants for the flash effect observed in zebrafish embryo,” *Radiotherapy and Oncology*, vol. 173, pp. 49–54, Aug. 2022. DOI: 10.1016/j.radonc.2022.05.025.
- [136] T. T. Böhlen et al., “Recording and reporting of ultra-high dose rate flash delivery for preclinical and clinical settings,” *Radiotherapy and Oncology*, vol. 200, p. 110507, Nov. 2024. DOI: 10.1016/j.radonc.2024.110507.
- [137] V. Grilj et al., “Average dose rate is the major temporal beam structure parameter for preserving murine intestines with pulsed electron flash-rt,” *International Journal of Radiation Oncology, Biology, Physics*, May 2025. DOI: 10.1016/j.ijrobp.2025.04.021.
- [138] L. Rank et al., “Development and benchmarking of a dose rate engine for raster-scanned flash helium ions,” *Medical Physics*, 2023. DOI: 10.1002/mp.16793.
- [139] G. Adrian, E. Konradsson, M. Lempart, S. Bäck, C. Ceberg, and K. Petersson, “The flash effect depends on oxygen concentration,” *The British journal of radiology*, vol. 92, no. 1106, p. 20190702, 2020. DOI: 10.1259/bjr.20190702.
- [140] K. Petersson, G. Adrian, K. Butterworth, and S. J. McMahon, “A quantitative analysis of the role of oxygen tension in FLASH radiation therapy,” *International Journal of Radiation Oncology, Biology, Physics*, vol. 107, no. 3, pp. 539–547, Jul. 2020. DOI: 10.1016/j.ijrobp.2020.02.634.
- [141] E. Taylor and D. Létourneau, “How quickly does flash need to be delivered? a theoretical study of radiolytic oxygen depletion kinetics in tissues,” *Physics in Medicine and Biology*, 2024. DOI: 10.1088/1361-6560/ad3e5e.
- [142] P. Montay-Gruel et al., “Long-term neurocognitive benefits of flash radiotherapy driven by reduced reactive oxygen species,” *Proceedings of the National Academy of Sciences*, vol. 116, no. 22, pp. 10943–10951, 2019. DOI: 10.1073/pnas.190177711.

-
- [143] R. J. Berry, E. J. Hall, D. W. Forster, T. H. Storr, and M. J. Goodman, "Survival of mammalian cells exposed to x rays at ultra-high dose-rates," *The British Journal of Radiology*, vol. 42, no. 494, pp. 102–107, Feb. 1969. DOI: [10.1259/0007-1285-42-494-102](https://doi.org/10.1259/0007-1285-42-494-102).
- [144] A. L. Van Slyke et al., "Oxygen monitoring in model solutions and in vivo in mice during proton irradiation at conventional and flash dose rates," *Radiation Research*, vol. 198, no. 2, pp. 181–189, 2022. DOI: [10.1667/RADE-21-00232.1](https://doi.org/10.1667/RADE-21-00232.1).
- [145] V. Grilj et al., "In vivo measurements of change in tissue oxygen level during irradiation reveal novel dose rate dependence," *Radiotherapy and Oncology*, p. 110 539, Sep. 2024. DOI: [10.1016/j.radonc.2024.110539](https://doi.org/10.1016/j.radonc.2024.110539).
- [146] X. Cao et al., "Quantification of oxygen depletion during flash irradiation in vitro and in vivo," *International Journal of Radiation Oncology, Biology, Physics*, vol. 111, no. 1, pp. 240–248, 2021. DOI: [10.1016/j.ijrobp.2021.03.056](https://doi.org/10.1016/j.ijrobp.2021.03.056).
- [147] D. Boscolo, M. Krämer, M. C. Fuss, M. Durante, and E. Scifoni, "Impact of target oxygenation on the chemical track evolution of ion and electron radiation," *International Journal of Molecular Sciences*, vol. 21, no. 2, p. 424, 2020. DOI: [10.3390/ijms21020424](https://doi.org/10.3390/ijms21020424).
- [148] D. J. Carlson, P. J. Keall, B. W. Loo, Z. J. Chen, and J. M. Brown, "Hypofractionation results in reduced tumor cell kill compared to conventional fractionation for tumors with regions of hypoxia," *International Journal of Radiation Oncology, Biology, Physics*, vol. 79, no. 4, pp. 1188–1195, Mar. 2011. DOI: [10.1016/j.ijrobp.2010.10.007](https://doi.org/10.1016/j.ijrobp.2010.10.007).
- [149] S. R. McKeown, "Defining normoxia, physoxia and hypoxia in tumoursimplications for treatment response," *The British Journal of Radiology*, vol. 87, no. 1035, p. 20 130 676, Mar. 2014. DOI: [10.1259/bjr.20130676](https://doi.org/10.1259/bjr.20130676).
- [150] P. Wilson, B. Jones, T. Yokoi, M. Hill, and B. Vojnovic, "Revisiting the ultra-high dose rate effect: Implications for charged particle radiotherapy using protons and light ions," *The British journal of radiology*, vol. 85, no. 1018, e933–e939, 2012. DOI: [10.1259/bjr/17827549](https://doi.org/10.1259/bjr/17827549).
- [151] B. Rothwell et al., "Flash-induced dna damage reduction measured in vitro correlates with effective oxygen depletion determined in silico: Further support for oxygen depletion contributing to flashes reduced damage burden in vitro," *British Journal of Radiology*, vol. 98, no. 1171, pp. 1032–1037, May 2025. DOI: [10.1093/bjr/tqaf097](https://doi.org/10.1093/bjr/tqaf097).
- [152] R. Abolfath, A. Baikalov, S. Bartzsch, N. Afshordi, and R. Mohan, "The effect of non-ionizing excitations on the diffusion of ion species and inter-track correlations in flash ultra-high dose rate radiotherapy," *Physics in Medicine & Biology*, vol. 67, no. 10, p. 105 005, 2022. DOI: [10.1088/1361-6560/ac69a6](https://doi.org/10.1088/1361-6560/ac69a6).
- [153] J. Ramos-Méndez, N. Domínguez-Kondo, J. Schuemann, A. McNamara, E. Moreno-Barbosa, and B. Faddegon, "LET-dependent intertrack yields in proton irradiation at ultra-high dose rates relevant for FLASH therapy," *Radiation Research*, vol. 194, no. 4, Aug. 2020, Publisher: Radiation Research Society. DOI: [10.1667/rade-20-00084.1](https://doi.org/10.1667/rade-20-00084.1).
- [154] A. Anderson and E. J. Hart, "Radiation chemistry of water with pulsed high intensity electron beams," *The Journal of Physical Chemistry*, vol. 66, no. 1, pp. 70–75, 1962. DOI: [10.1021/j100807a014](https://doi.org/10.1021/j100807a014).
- [155] S. Rossomme et al., "Three-voltage linear method to determine ion recombination in proton and light-ion beams," *Physics in Medicine & Biology*, vol. 65, no. 4, p. 045 015, Feb. 2020. DOI: [10.1088/1361-6560/ab3779](https://doi.org/10.1088/1361-6560/ab3779).

- [156] M. S. Kreipl, W. Friedland, and H. G. Paretzke, “Interaction of ion tracks in spatial and temporal proximity,” *Radiation and Environmental Biophysics*, vol. 48, no. 4, pp. 349–359, 2009. DOI: [10.1007/s00411-009-0234-z](https://doi.org/10.1007/s00411-009-0234-z).
- [157] U. A. Weber, E. Scifoni, and M. Durante, “Flash radiotherapy with carbon ion beams,” *Medical Physics*, vol. 49, no. 3, pp. 1974–1992, 2022. DOI: [10.1002/mp.15135](https://doi.org/10.1002/mp.15135).
- [158] J. P. Sunnerberg, R. Zhang, D. J. Gladstone, H. M. Swartz, J. Gui, and B. W. Pogue, “Mean dose rate in ultra-high dose rate electron irradiation is a significant predictor for o2 consumption and h2o2 yield,” *Physics in Medicine & Biology*, vol. 68, no. 16, p. 165014, Aug. 2023. DOI: [10.1088/1361-6560/ace877](https://doi.org/10.1088/1361-6560/ace877).
- [159] G. Adrian et al., “Cancer cells can exhibit a sparing flash effect at low doses under normoxic in vitro-conditions,” *Frontiers in Oncology*, p. 2890, 2021. DOI: [10.3389/fonc.2021.686142](https://doi.org/10.3389/fonc.2021.686142).
- [160] M. Buonanno, V. Grilj, and D. J. Brenner, “Biological effects in normal cells exposed to flash dose rate protons,” *Radiotherapy and Oncology*, vol. 139, pp. 51–55, Oct. 2019. DOI: [10.1016/j.radonc.2019.02.009](https://doi.org/10.1016/j.radonc.2019.02.009).
- [161] T. Tessonier et al., “FLASH dose rate helium ion beams: First in vitro investigations,” *International Journal of Radiation Oncology, Biology, Physics*, vol. 111, no. 4, pp. 1011–1022, Nov. 2021. DOI: [10.1016/j.ijrobp.2021.07.1703](https://doi.org/10.1016/j.ijrobp.2021.07.1703).
- [162] C. Fouillade et al., “Flash irradiation spares lung progenitor cells and limits the incidence of radio-induced senescence,” *Clinical Cancer Research*, vol. 26, no. 6, pp. 1497–1506, Mar. 2020. DOI: [10.1158/1078-0432.ccr-19-1440](https://doi.org/10.1158/1078-0432.ccr-19-1440).
- [163] A. Perstin, Y. Poirier, A. Sawant, and M. Tambasco, “Quantifying the dna-damaging effects of flash irradiation with plasmid dna,” *International Journal of Radiation Oncology, Biology, Physics*, vol. 113, no. 2, pp. 437–447, Jun. 2022. DOI: [10.1016/j.ijrobp.2022.01.049](https://doi.org/10.1016/j.ijrobp.2022.01.049).
- [164] T. E. Schmid et al., “The effectiveness of 20 mev protons at nanosecond pulse lengths in producing chromosome aberrations in human-hamster hybrid cells,” *Radiation Research*, vol. 175, no. 6, pp. 719–727, Jun. 2011. DOI: [10.1667/rr2465.1](https://doi.org/10.1667/rr2465.1).
- [165] S. Acharya, N. N. Bhat, P. Joseph, G. Sanjeev, B. Sreedevi, and Y. Narayana, “Dose rate effect on micronuclei induction in human blood lymphocytes exposed to single pulse and multiple pulses of electrons,” *Radiation and Environmental Biophysics*, vol. 50, no. 2, pp. 253–263, Jan. 2011. DOI: [10.1007/s00411-011-0353-1](https://doi.org/10.1007/s00411-011-0353-1).
- [166] E. S. Diffenderfer, B. S. Sørensen, A. Mazal, and D. J. Carlson, “The current status of preclinical proton flash radiation and future directions,” *Medical Physics*, vol. 49, no. 3, pp. 2039–2054, Oct. 2021. DOI: [10.1002/mp.15276](https://doi.org/10.1002/mp.15276).
- [167] N. Aykin-Burns, I. M. Ahmad, Y. Zhu, L. W. Oberley, and D. R. Spitz, “Increased levels of superoxide and h2o2 mediate the differential susceptibility of cancer cells versus normal cells to glucose deprivation,” *Biochemical Journal*, vol. 418, no. 1, pp. 29–37, Jan. 2009. DOI: [10.1042/bj20081258](https://doi.org/10.1042/bj20081258).
- [168] J. D. Schoenfeld et al., “ $O_2 \cdot^-$ and H_2O_2 -mediated disruption of fe metabolism causes the differential susceptibility of nsclc and gbm cancer cells to pharmacological ascorbate,” *Cancer Cell*, vol. 31, no. 4, pp. 487–500.e8, Apr. 2017. DOI: [10.1016/j.ccell.2017.02.018](https://doi.org/10.1016/j.ccell.2017.02.018).
- [169] N. Vilaplana-Lopera, A. Abu-Halawa, E. Walker, J. Kim, and E. J. Moon, “Ferroptosis, a key to unravel the enigma of the flash effect?” *The British Journal of Radiology*, p. 20220825, 2022. DOI: [10.1259/bjr.20220825](https://doi.org/10.1259/bjr.20220825).

-
- [170] E. Konradsson et al., “Comparable long-term tumor control for hypofractionated flash vs. conventional radiation therapy in an immunocompetent rat glioma model,” *Advances in Radiation Oncology*, p. 101 011, 2022. DOI: 10.1016/j.adro.2022.101011.
- [171] N. Rama et al., “Improved tumor control through t-cell infiltration modulated by ultra-high dose rate proton flash using a clinical pencil beam scanning proton system,” *International Journal of Radiation Oncology, Biology, Physics*, vol. 105, no. 1, S164–S165, Sep. 2019. DOI: 10.1016/j.ijrobp.2019.06.187.
- [172] J. Bourhis et al., “Clinical translation of FLASH radiotherapy: Why and how?” *Radiotherapy and Oncology*, vol. 139, pp. 11–17, Oct. 2019. DOI: 10.1016/j.radonc.2019.04.008.
- [173] W. Tinganelli et al., “Ultra-high dose rate (flash) carbon ion irradiation: Dosimetry and first cell experiments,” *International Journal of Radiation Oncology, Biology, Physics*, vol. 112, no. 4, pp. 1012–1022, Mar. 2022. DOI: 10.1016/j.ijrobp.2021.11.020.
- [174] M. Tashiro et al., “First human cell experiments with flash carbon ions,” *Anticancer Research*, vol. 42, no. 5, pp. 2469–2477, Apr. 2022. DOI: 10.21873/anticancer.15725.
- [175] S. Katsuki et al., “Ultra-high dose rate (flash) carbon ion irradiation inhibited immune suppressive protein expression on pan02 cell line,” *Journal of Radiation Research*, vol. 66, no. 1, pp. 97–102, Dec. 2024. DOI: 10.1093/jrr/rrae091.
- [176] K. Minami et al., “The appropriate conditions for the cell sparing (flash) effect exist in ultra-high dose rate carbon ion irradiation,” *Anticancer Research*, vol. 45, no. 3, pp. 955–963, Mar. 2025. DOI: 10.21873/anticancer.17483.
- [177] R. Steinbrügge, C. Schömers, A. Peters, and T. Haberer, “Towards multiple energy extraction operation in ion beam therapy,” in *Proceedings of the 14th International Particle Accelerator Conference*, JACoW Publishing, 2023. DOI: 10.18429/JACOW-IPAC2023-THPM063.
- [178] W. Newhauser, “International commission on radiation units and measurements report 78: Prescribing, recording, and reporting proton-beam therapy,” *Radiation Protection Dosimetry*, vol. 133, pp. 60–62, 2009. DOI: 10.1093/rpd/ncp005.
- [179] C. P. Karger, O. Jäkel, H. Palmans, and T. Kanai, “Dosimetry for ion beam radiotherapy,” *Physics in Medicine & Biology*, vol. 55, no. 21, R193–234, Nov. 2010. DOI: 10.1088/0031-9155/55/21/R01.
- [180] International Atomic Energy Agency, “Absorbed dose determination in external beam radiotherapy: An international code of practice for dosimetry based on standards of absorbed dose to water; technical reports series no. 398 (rev. 1),” 2024. DOI: 10.61092/iaea.ve7q-y94k.
- [181] F. Romano, C. Bailat, P. G. Jorge, M. L. F. Lerch, and A. Darafsheh, “Ultra-high dose rate dosimetry: Challenges and opportunities for flash radiation therapy,” *Medical Physics*, vol. 49, no. 7, pp. 4912–4932, May 2022. DOI: 10.1002/mp.15649.
- [182] A. Subiel et al., “Metrology for advanced radiotherapy using particle beams with ultra-high dose rates,” *Physics in Medicine & Biology*, vol. 69, no. 14, 14TR01, Jul. 2024. DOI: 10.1088/1361-6560/ad539d.
- [183] M. R. Ashraf et al., “Dosimetry for flash radiotherapy: A review of tools and the role of radioluminescence and cherenkov emission,” *Frontiers in Physics*, vol. 8, Aug. 2020. DOI: 10.3389/fphy.2020.00328.

- [184] A. Hitachi, T. Doke, and A. Mozumder, “Luminescence quenching in liquid argon under charged-particle impact: Relative scintillation yield at different linear energy transfers,” *Physical Review B*, vol. 46, no. 18, pp. 11 463–11 470, Nov. 1992. DOI: [10.1103/physrevb.46.11463](https://doi.org/10.1103/physrevb.46.11463).
- [185] F. Di Martino et al., “Flash radiotherapy with electrons: Issues related to the production, monitoring, and dosimetric characterization of the beam,” *Frontiers in Physics*, vol. 8, Nov. 2020. DOI: [10.3389/fphy.2020.570697](https://doi.org/10.3389/fphy.2020.570697).
- [186] “PinPoint(R) Chamber Type 31015 PTW,” Accessed: Jul. 19, 2025. [Online]. Available: <https://www.ptwdosimetry.com/en/products/pinpoint-ion-chamber-31015>.
- [187] M. Togno et al., “Ultra-high dose rate dosimetry for pre-clinical experiments with mm-small proton fields,” *Physica Medica*, vol. 104, pp. 101–111, 2022.
- [188] H. K. Looe et al., “The role of radiationinduced charge imbalance on the doseresponse of a commercial synthetic diamond detector in small field dosimetry,” *Medical Physics*, vol. 46, no. 6, pp. 2752–2759, May 2019. DOI: [10.1002/mp.13542](https://doi.org/10.1002/mp.13542).
- [189] F. Gómez et al., “Development of an ultrathin parallel plate ionization chamber for dosimetry in flash radiotherapy,” *Medical Physics*, vol. 49, no. 7, pp. 4705–4714, Apr. 2022. DOI: [10.1002/mp.15668](https://doi.org/10.1002/mp.15668).
- [190] A. Subiel and F. Romano, “Recent developments in absolute dosimetry for flash radiotherapy,” *The British Journal of Radiology*, vol. 96, no. 1148, p. 20 220 560, 2023.
- [191] M. Bucciolini, F. Banci Buonamici, S. Mazzocchi, C. De Angelis, S. Onori, and G. A. P. Cirrone, “Diamond detector versus silicon diode and ion chamber in photon beams of different energy and field size,” *Medical Physics*, vol. 30, no. 8, pp. 2149–2154, Jul. 2003. DOI: [10.1118/1.1591431](https://doi.org/10.1118/1.1591431).
- [192] G. Milluzzo et al., “Comprehensive dosimetric characterization of novel silicon carbide detectors with uhdr electron beams for flash radiotherapy,” *Medical Physics*, vol. 51, no. 9, pp. 6390–6401, May 2024. DOI: [10.1002/mp.17172](https://doi.org/10.1002/mp.17172).
- [193] C. Angelou, I. S. Patallo, D. Doherty, F. Romano, and G. Schettino, “A review of diamond dosimeters in advanced radiotherapy techniques,” *Medical Physics*, 2024.
- [194] I. Ciancaglioni et al., “Dosimetric characterization of a synthetic single crystal diamond detector in clinical radiation therapy small photon beams: Dosimetric characterization of a synthetic single crystal diamond detector,” *Medical Physics*, vol. 39, no. 7Part1, pp. 4493–4501, Jul. 2012. DOI: [10.1118/1.4729739](https://doi.org/10.1118/1.4729739).
- [195] “microDiamond(R) PTW,” Accessed: Jan. 29, 2025. [Online]. Available: <https://www.ptwdosimetry.com/en/products/microdiamond>.
- [196] “flashDiamond(R) PTW,” Accessed: Feb. 3, 2025. [Online]. Available: <https://www.ptwdosimetry.com/en/products/flashdiamond-detector>.
- [197] M. Marinelli et al., “Dosimetric characterization of a microdiamond detector in clinical scanned carbon ion beams,” *Medical Physics*, vol. 42, no. 4, pp. 2085–2093, Mar. 2015. DOI: [10.1118/1.4915544](https://doi.org/10.1118/1.4915544).
- [198] M. Marinelli et al., “Design, realization, and characterization of a novel diamond detector prototype for flash radiotherapy dosimetry,” *Medical Physics*, vol. 49, no. 3, pp. 1902–1910, Jan. 2022. DOI: [10.1002/mp.15473](https://doi.org/10.1002/mp.15473).

-
- [199] G. Verona Rinati et al., “Application of a novel diamond detector for commissioning of flash radiotherapy electron beams,” *Medical Physics*, vol. 49, no. 8, pp. 5513–5522, Jun. 2022. DOI: 10.1002/mp.15782.
 - [200] T. Tessonnier, G. Verona Rinati, L. Rank, R. Kranzer, A. Mairani, and M. Marinelli, “Diamond detectors for dose and instantaneous dose rate measurements for ultrahigh dose rate scanned helium ion beams,” *Medical Physics*, vol. 51, no. 2, pp. 1450–1459, Sep. 2023. DOI: 10.1002/mp.16757.
 - [201] P. Cirrone and G. Petringa, Eds., “Monte Carlo in heavy charged particle therapy, new challenges in ion therapy” (Series in medical physics and biomedical engineering), First edition. Boca Raton ; London ; New York: CRC Press, Taylor & Francis Group, 2024, ISBN: 978-1-000-98761-4.
 - [202] M. Janson, L. Glimelius, A. Fredriksson, E. Traneus, and E. Engwall, “Treatment planning of scanned proton beams in raystation,” *Medical Dosimetry*, vol. 49, no. 1, pp. 2–12, 2024. DOI: 10.1016/j.meddos.2023.10.009.
 - [203] A. Kraan et al., “Charge identification of nuclear fragments with the foot time-of-flight system,” *Nuclear Instruments and Methods in Physics Research Section A: Accelerators, Spectrometers, Detectors and Associated Equipment*, vol. 1001, p. 165 206, Jun. 2021. DOI: 10.1016/j.nima.2021.165206.
 - [204] S. Muraro, G. Battistoni, and A. Kraan, “Challenges in monte carlo simulations as clinical and research tool in particle therapy: A review,” *Frontiers in Physics*, vol. 8, Nov. 2020. DOI: 10.3389/fphy.2020.567800.
 - [205] H. N. Tran et al., “Review of chemical models and applications in geant4dna: Report from the esa biorad iii project,” *Medical Physics*, vol. 51, no. 9, pp. 5873–5889, Jun. 2024. DOI: 10.1002/mp.17256.
 - [206] C. Karle et al., “Characterizing diamond detectors for various dose and dose rate measurements in scanned carbon and oxygen beams,” *Medical Physics*, vol. 52, no. 7, e17893, DOI: 10.1002/mp.17893.
 - [207] C. Karle et al., “First in vitro and in vivo experiments with ultra high-dose rate oxygen ion radiotherapy,” *Physics and Imaging in Radiation Oncology*, vol. 35, p. 100 803, 2025. DOI: 10.1016/j.phro.2025.100803.
 - [208] J. Li et al., “Tumor cell-intrinsic factors underlie heterogeneity of immune cell infiltration and response to immunotherapy,” *Immunity*, vol. 49, no. 1, 178–193.e7, Jul. 2018. DOI: 10.1016/j.immuni.2018.06.006.
 - [209] S. R. Hingorani et al., “Trp53r172h and krasg12d cooperate to promote chromosomal instability and widely metastatic pancreatic ductal adenocarcinoma in mice,” *Cancer Cell*, vol. 7, no. 5, pp. 469–483, May 2005. DOI: 10.1016/j.ccr.2005.04.023.
 - [210] U. Ratzinger et al., “A new rfq for the carbon therapy injector at hit heidelberg,” in *Proceedings of the 32nd Linear Accelerator Conference (LINAC2024)*, Chicago, IL, USA, 2024, pp. 25–30.
 - [211] Y. Simeonov et al., “3d range-modulator for scanned particle therapy: Development, monte carlo simulations and experimental evaluation,” *Physics in Medicine & Biology*, vol. 62, no. 17, pp. 7075–7096, Aug. 2017. DOI: 10.1088/1361-6560/aa81f4.

- [212] Y. Simeonov et al., “Development, monte carlo simulations and experimental evaluation of a 3d range-modulator for a complex target in scanned proton therapy,” *Biomedical Physics & Engineering Express*, vol. 8, no. 3, p. 035 006, Mar. 2022. DOI: 10.1088/2057-1976/ac5937.
- [213] S. Minohara et al., “Recent innovations in carbon-ion radiotherapy,” *Journal of Radiation Research*, vol. 51, no. 4, pp. 385–392, 2010. DOI: 10.1269/jrr.10028.
- [214] N. Hamatani et al., “Investigation of ionization chamber characteristics for ultrahigh-dose-rate scanned carbon-ion beams,” *In Vivo*, vol. 38, no. 5, pp. 2220–2227, 2024. DOI: 10.21873/invivo.13686.
- [215] M. Martíňková and O. Jäkel, “Dosimetric properties of gafchromic[®] ebt films in monoenergetic medical ion beams,” *Physics in Medicine and Biology*, vol. 55, no. 13, pp. 3741–3751, Jun. 2010. DOI: 10.1088/0031-9155/55/13/011.
- [216] V. Grilj and D. J. Brenner, “Let dependent response of gafchromic films investigated with mev ion beams,” *Physics in Medicine & Biology*, vol. 63, no. 24, p. 245 021, Dec. 2018. DOI: 10.1088/1361-6560/aaf34a.
- [217] “OCTAVIUS(R) Detector 1500XDR PTW,” Accessed: Aug. 6, 2025. [Online]. Available: <https://www.ptwdosimetry.com/en/products/octavius-detector-1500xdr>.
- [218] B. Ackermann, “Validierung eines 2d ionisationskammerarrays für die qualitätssicherung in der ionenstrahl-therapie,” ger, 2024. DOI: 10.11588/heidok.00035925.
- [219] S. Rossomme et al., “Response of synthetic diamond detectors in proton, carbon, and oxygen ion beams,” *Medical Physics*, vol. 44, no. 10, pp. 5445–5449, Aug. 2017. DOI: 10.1002/mp.12473.
- [220] S. Rossomme, J. Hopfgartner, S. Vynckier, and H. Palmans, “Under-response of a ptw-60019 microdiamond detector in the bragg peak of a 62 mev/n carbon ion beam,” *Physics in Medicine and Biology*, vol. 61, no. 12, pp. 4551–4563, May 2016. DOI: 10.1088/0031-9155/61/12/4551.
- [221] M. Marinelli, G. Prestopino, C. Verona, and G. VeronaRinati, “Experimental determination of the ptw 60019 microdiamond dosimeter active area and volume,” *Medical Physics*, vol. 43, no. 9, pp. 5205–5212, Aug. 2016. DOI: 10.1118/1.4961402.
- [222] P. Wardman, “Mechanisms of the flash effect: Radiation chemistry should not be ignored in developing models,” *Radiotherapy and Oncology*, vol. 184, p. 109 673, Jul. 2023. DOI: 10.1016/j.radonc.2023.109673.
- [223] M. El Khatib et al., “Direct measurements of flash-induced changes in intracellular oxygenation,” *International Journal of Radiation Oncology, Biology, Physics*, vol. 118, no. 3, pp. 781–789, 2024. DOI: 10.1016/j.ijrobp.2023.09.019.
- [224] P. Vaupel, A. B. Flood, and H. M. Swartz, “Oxygenation status of malignant tumors vs. normal tissues: Critical evaluation and updated data source based on direct measurements with po2 microsenors,” *Applied Magnetic Resonance*, vol. 52, no. 10, pp. 1451–1479, Jul. 2021. DOI: 10.1007/s00723-021-01383-6.
- [225] A. Mairani, T. T. Böhlen, I. Dokic, G. Cabal, S. Brons, and T. Haberer, “Modelling of cell killing due to sparsely ionizing radiation in normoxic and hypoxic conditions and an extension to high let radiation,” *International Journal of Radiation Biology*, vol. 89, no. 10, pp. 782–793, Jun. 2013. DOI: 10.3109/09553002.2013.800247.

-
- [226] B. P. Venkatesulu et al., “Ultra high dose rate (35 gy/sec) radiation does not spare the normal tissue in cardiac and splenic models of lymphopenia and gastrointestinal syndrome,” *Scientific Reports*, vol. 9, no. 1, Nov. 2019. DOI: 10.1038/s41598-019-53562-y.
- [227] E. J. Hall and D. J. Brenner, “The dose-rate effect revisited: Radiobiological considerations of importance in radiotherapy,” *International Journal of Radiation Oncology, Biology, Physics*, vol. 21, no. 6, pp. 1403–1414, 1991. DOI: 10.1016/0360-3016(91)90314-T.
- [228] M. Krämer, O. Jäkel, T. Haberer, G. Kraft, D. Schardt, and U. Weber, “Treatment planning for heavy-ion radiotherapy: Physical beam model and dose optimization,” *Physics in Medicine and Biology*, vol. 45, no. 11, pp. 3299–3317, Oct. 2000. DOI: 10.1088/0031-9155/45/11/313.
- [229] T. Tessonnier et al., “Dosimetric verification in water of a monte carlo treatment planning tool for proton, helium, carbon and oxygen ion beams at the heidelberg ion beam therapy center,” *Physics in Medicine & Biology*, vol. 62, no. 16, pp. 6579–6594, Jul. 2017. DOI: 10.1088/1361-6560/aa7be4.
- [230] T. T. Böhlen et al., “Normal tissue sparing by FLASH as a function of single-fraction dose: A quantitative analysis,” *International Journal of Radiation Oncology, Biology, Physics*, Jul. 2022. DOI: 10.1016/j.ijrobp.2022.05.038.
- [231] T. Tessonnier et al., “First dosimetric and biological verification for spot-scanning hadron arc radiation therapy with carbon ions,” *Advances in radiation oncology*, vol. 9, no. 12, p. 101611, 2024. DOI: 10.1016/j.adro.2024.101611.

SUPPLEMENTARY MATERIAL

E.1 Supplementary - 2nd Paper

Supplementary material corresponding to Sec. 6.2, “Oxygen consumption measurements at ultra-high dose rate over a wide LET range.” [67] For inclusion in this thesis, the original files were adapted through bycropping to accommodate the document layout. The scientific content remains unaltered.

1 Supplementary

2

3 [Figure Captions](#)

4

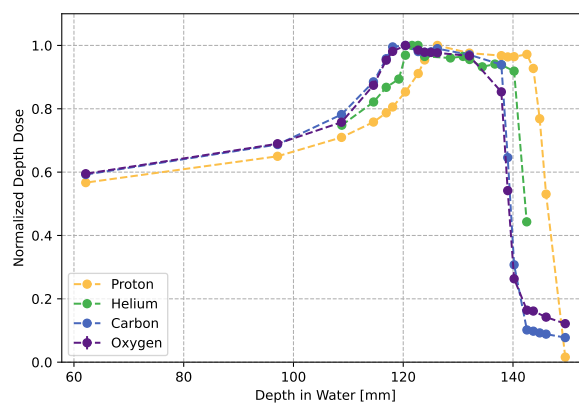
5 **Figure S 1:** Depth dose curves for the 2DRM obtained with the beam parameters mentioned in Tabel 2 for the UHDR irradiations.

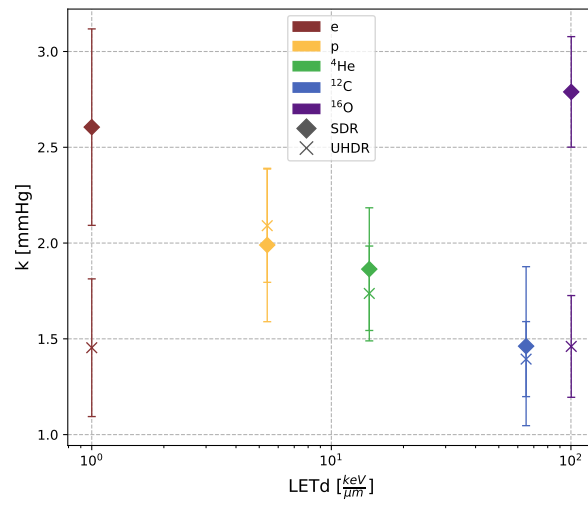
6 The normalized depth dose is plotted against the depth in water. Due to the different energies of the primary particles the curves

7 are shifted in depth, which is accounted for in the experiment by using different thicknesses of PMMA.

8 **Figure S 2:** Fitted k values and their standard deviations for every particle type against their LETd values. The SDR values are

9 marked with a diamond while the UHDR are represented by a cross.





E.2 Supplementary - 3rd Paper

Supplementary material corresponding to Sec. 6.3 “First in vitro and in vivo experiments with ultra high-dose rate oxygen ion radiotherapy.” [207]

For inclusion in this thesis, the original files were adapted through by cropping to accommodate the document layout. The scientific content remains unaltered.

Supplementary Material

Irradiation facility

The Heidelberg Ion Beam Therapy Centre (HIT) currently facilitates research using four particle beams: protons, helium, carbon and oxygen ions. The latter two are generated using a single electron cyclotron resonance ion source, with carbon dioxide (CO₂) as primary gas, yielding carbon ions (¹²C₄₊) or oxygen ions (¹⁶O₆₊) [1]. After acceleration in a synchrotron, the particles are extracted via a third-order resonant RF-knockout extraction system. The nozzle is equipped with a Beam Application and Monitoring System (BAMS), which integrates various ionization chambers and multi-wire proportional chambers. These components serve the dual purpose of monitoring and recording the spill structure to facilitate the raster scanning. Additionally, a feedback loop enables precise intensity-controlled application of raster-scanned pencil beams [2].

To achieve UHDR, specific synchrotron adaptations are required. These include tuning the extraction frequency closer to resonance and increasing sextupole magnet strength. Notably, these modifications facilitate UHDR application without compromising the functionality of the raster scanning or intensity control system [3].

Film Evaluation

To guarantee that the various field sizes and spot spacings employed in the active pencil beam scanning irradiation deliver a uniform dose to the samples, EBT3 Gafchromic Films (Ashland) were irradiated and scanned at a resolution of 1200 dpi. Horizontal and vertical line profiles through the center of the film were extracted with ImageJ. In Python, the profiles were normalized to the maximum greyscale value and smoothed with a Gaussian filter. From the central point of the profile, we identified a region spanning 50 % of the total area under the curve. Within this central region, we calculated a flatness index (F):

$$F = 100 * \frac{Y_{max} - Y_{min}}{Y_{max} + Y_{min}}$$

with Ymax and Ymin being the maximum and minimum normalized grey scale value in the central area. The profile was evaluated for one film per experiment and the profile with the largest F was displayed in Figure S1. As the index did not exceed 5 %, homogeneous irradiation of the samples is ensured. The fields were utilized exclusively for the evaluation of field homogeneity, rather than for absolute dosimetry.

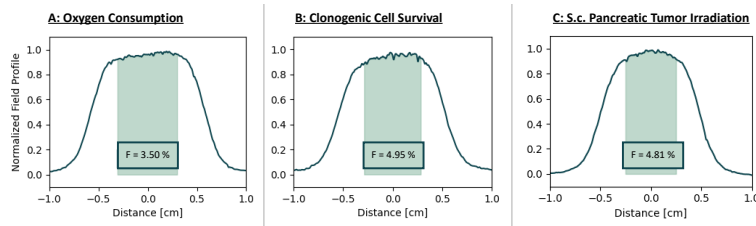


Figure S1: The film flatness graphs provide a representative line profile of an irradiated film with the calculated flatness index (F).

Spill Structure Information

Table S1: Spill structure information for all three experiments: The mean dose rate is calculated by dividing the total dose applied by the total irradiation time. The delivery time encompasses the interval between the initiation of the first spill and the conclusion of the final spill, whereas the spill time represents the temporal duration of a single spill. The interspill time, on the other hand, denotes the interval between the end of one spill and the subsequent onset of the next.

Experiment	Field Size [mm ²]	Spot Spacing [mm]	Mean LETd [keV/μm]	Mean Dose Rate [Gy/s]	Delivery Time [s]	Spill Time [ms]	Interspill Time [s]	Dose [Gy]
Oxygen Consumption	9 x 9	1.5	100 [range 88–235]	0.309 ± 0.010	48.5 ± 1.6	876 ± 154	4.39 ± 0.05	15.02 ± 0.04
				108 ± 10	0.137 ± 0.012	137 ± 12	-	14.86 ± 0.16
In Vitro	9 x 9	1.5	100 [range 88–235]	0.1912 ± 0.0027	41.8 ± 1.3	367 ± 9	4.23 ± 0.04	8.02 ± 0.05
				170 ± 4	0.047 ± 0.003	47 ± 3	-	8.01 ± 0.15
In Vivo	8 x 8	1	134 [range 106–162]	1.4467 ± 0.021	6.98 ± 0.03	1631.8 ± 99	4.3 ± 0.04	10.10 ± 0.14
				280 ± 11	0.0361 ± 0.0013	36.1 ± 1.3	-	10.17 ± 0.19

Supplementary Bibliography

- [1] Winkelmann T, Cee R, Haberer T, Naas B, Peters A, Scheloske S, et al. Electron cyclotron resonance ion source experience at the Heidelberg Ion Beam Therapy Center. *Rev Sci Instrum* 2008;79:A331. <https://doi.org/10.1063/1.2823952>.
- [2] Schömers C, Feldmeier E, Naumann J, Panse R, Peters A, Haberer T. The intensity feedback system at heidelberg ion-beam therapy centre. *Nucl Instrum Methods Phys Res A* 2015;795:92–9. <https://doi.org/10.1016/j.nima.2015.05.054>.
- [3] Schömers C, Brons S, Cee R, Peters A, Scheloske S, Haberer T. BEAM PROPERTIES BEYOND THE THERAPEUTIC RANGE AT HIT. *Proc. IPAC 23*, vol. THPM064, Venice, Italy: JaCoW; 2022. <https://doi.org/10.18429/JACoW-IPAC2023-THPM064>.

ACKNOWLEDGEMENTS

First and foremost, I would like to express my deepest gratitude to **Prof. Dr. Dr. Jürgen Debus** and **Prof. Dr. Dr. Amir Abdollahi** for giving me the opportunity to pursue this work and for providing all the necessary resources at DKFZ, HIT, and NCT. Your invaluable expertise, guidance during TAC meetings, and career support have been instrumental throughout my PhD journey. I would also like to thank **Prof. Dr. Michael Hausmann**, not only for being my second referee of this thesis but especially for your valuable comments and support throughout the PhD. It was a genuine pleasure to learn and teach under your friendly and encouraging guidance. I am grateful to **PD. Dr. Loredana Gastaldo** and **Prof. Dr. Jörg Jäckel** for their willingness to serve on the final examination committee.

Before I continue: I already want to apologize for the length of this acknowledgments section. The past years have been shaped by countless people, and I want to honor each one properly. Think of this section less like pages of thanks and more like the credits of a "FAST AND FURIOUS" movie about my PhD journey that now ends:

DIRECTOR

First of all, I want to thank **Prof. Dr. Andrea Mairani** for your unwavering support and encouragement. You believed in me, pushed my work forward, and were always there to listen when doubts crept in. I am truly grateful for the trust and freedom you gave me throughout my PhD and for the opportunities you opened up for me. I couldn't have asked for a better supervisor.

CO-DIRECTOR

Next, I want to thank **Dr. Thomas TessonnIER** (nope, this is not a typo). I am deeply grateful for all the night shifts we shared. You taught me not only technical skills, but also how to build resilience, and how to communicate efficiently – with people and the synchrotron alike. Those lessons will stay with me far beyond this PhD.

PERSONAL ADVISOR

Dr. Hans Liew: You were always by my side, from conferences on opposite sides of the world to my very first night shift. From the knowledge you shared to the many soft skills you patiently taught me along the way, your mentorship has shaped me. Today, I can only hope we get to raise a Dubbeglas together — cheers to that!

BIOLOGICAL CONSULTANT

As a physicist venturing into the field of biology, I couldn't have done this without expert guidance. I would like to sincerely thank **Dr. Ivana Dokic**, whose mentorship went far beyond radiobiology. You not only helped me navigate the science but also taught me how to write with confidence, respond thoughtfully to referees, and truly believe in my work. My thanks also to **Nora Schuhmacher**, who patiently taught me protocols and always jumped in when help was needed, but who also made long night shifts fun – with good music and good company.

TECHNICAL CONSULTANT

My heartfelt thanks to the **Accelerator Team at HIT** for accommodating my endless UHDR requests. Special thanks to **Dr. Christian Schömers**, **Dr. Stefan Scheloske**, and **Dr. Rainer Cee**, who dedicated night shifts to optimizing the UHDR settings. Christian, thank you for all the time you spent explaining the synchrotron to me – while I now understand the seperatrix and magnets, the 3rd-order knockout system remains magical. Thanks also to **Dr. Tim Winkelmann**, who never grew tired of my questions and explained the sources with great patience.

My gratitude extends to everyone who helped during the night shifts – whether it was with technical or mental support (including ice cream delivery).

A very special thanks goes to **Dr. Stephan Brons**. You supported me during night shift preparations and setups, you also always took the time for all my questions and gave me invaluable feedback.

Additional thanks go to the entire **HIT Medical Physics** team – it was a true pleasure to work alongside you all during the early quality assurance shifts, to learn from your expertise, and to share many enjoyable conversations and a ski trip along the way.

MANAGEMENT

Claudia Rittmüller, you literally guided me through the jungle of bureaucracy. Thank you for always being there, helping me find my way!

CREW

A huge thanks to all past and present members of the **BioPT group**! From funny coffee breaks and rainy hikes to Bavarian breakfasts and delicious cakes, you made this PhD journey truly memorable. I am so grateful to have amazing colleagues to whom I can always talk, share experiences with, and even go swimming alongside. You've made this adventure genuinely joyful.

STUNT DOUBLE

During this journey, I was truly blessed to have the best PhD buddy by my side: **Filipa Baltazar**. We started on the same day, shared the same ups and downs, and even vacations. I couldn't have asked for a better partner in (crime) this adventure. Obrigada for everything!

SUPPORTING CAST

Countless friends have supported me over these years. Though I can't list you all, I am grateful to all who endured my busy schedule and just came for a quick coffee, a proper Spaziergang, an inliner round, delicious dinner, or/and offered endless support. To all my friends from Mannheim, my physics Kommilitonen from the early semesters, and all who joined in the last years – thank you.

EXECUTIVE PRODUCER

Das Dankeschön an meine Familie lässt sich nicht quantifizieren. **Mama und Papa**, ihr habt mich schon immer vollkommen bedingungslos in wirklich allem unterstützt. Ich wusste immer, wo ich hingehen konnte, wen ich anrufen konnte und wer mir bei allem half – vom Umzug bis zum GFS-Schreiben. Eines muss ich noch besonders erwähnen: Papa, du hast nicht nur meine Liebe zur Technik immer weiter entfacht, sondern warst damals sogar direkt mit am Schwerionenbeschleuniger, wo ich mir nie hätte träumen lassen, dass ich einmal tatsächlich im HIT arbeiten würde. Ihr habt das möglich gemacht. Danke auch an meine **Oma**, meinen wohl größten Fan, für die unzähligen gedrückten Daumen und an **Onkel Erich**, der mich stets mit Schokolade und einem offenen Ohr in allen Lebenslagen unterstützt hat.

BEST SUPPORTING ROLE

Last but not least geht mein Dank an **Robert Hammann**. Danke, dass du immer für mich da bist – mit unendlicher Geduld, Unterstützung und Humor. All die Abenteuer, die wir gemeinsam erlebt haben, von privaten bis physikalischen, haben diese Zeit so besonders gemacht. Du bist mein Fels in der Brandung, und ich freue mich auf alle weiteren Fortsetzungen dieses Films die jetzt kommen – mit dir an meiner Seite.